ACOUSTO-ELASTIC INTERACTION IN COMBUSTION CHAMBERS

Rob Huls

This research project, NNE5/388/2001-DESIRE, was supported by the European Union.

De promotiecommissie is als volgt samengesteld:

Voorzitter en secretaris:	
Prof.dr.ir. H.J. Grootenboer	Universiteit Twente
Promotor:	
Prof.dr.ir. A. de Boer	Universiteit Twente
Assistent Promotor:	
Dr.ir. P.J.M. van der Hoogt	Universiteit Twente
Leden:	
Prof.dr.-Ing. habil. R. Rolfes	Universiteit van Hannover
Prof.dr.ir. N.B. Roozen	Technische Universiteit Eindhoven
Prof.dr.ir. T.H. van der Meer	Universiteit Twente
Dr. M. Huth	Siemens AG
Dr.ir. J.B.W. Kok	Universiteit Twente

Acousto-Elastic Interaction in Combustion Chambers
Huls, Rob Alexander
PhD thesis, University of Twente, Enschede, The Netherlands
May 2006

ISBN 90-365-2336-2
Subject headings: acoustics, vibro-acoustics, combustion, vibration

Printed by PrintPartners Ipskamp B.V., Enschede, The Netherlands

ACOUSTO-ELASTIC INTERACTION IN COMBUSTION CHAMBERS

PROEFSCHRIFT

ter verkrijging van
de graad van doctor aan de Universiteit Twente,
op gezag van de rector magnificus,
prof. dr. W.H.M. Zijm,
volgens besluit van het College voor Promoties
in het openbaar te verdedigen
op woensdag 17 mei 2006 om 13.15 uur

door

Rob Alexander Huls

geboren op 26 november 1977

te Hellendoorn

Dit proefschrift is goedgekeurd door de promotor

Prof.dr.ir. A. de Boer

en de assistent promotor

Dr.ir. P.J.M. van der Hoogt

Summary

Air pollution has become an important subject in the last few decades. An important component of the pollution is nitrogen oxide or NO_x, which is, amongst other things, formed during combustion of fossil fuels in gas turbines. To decrease this formation, lean combustion is applied in gas turbines, using an excess of air to combust the fuel. This leads to lower NO_x emissions, but also to increased acoustic pressure levels in the combustion chamber. Because of the high temperatures in the combustion chamber, the surrounding structure, the so-called liner, has to be thin and is therefore flexible. The acoustic pressure perturbations induce vibration of the structure, leading to fatigue problems. This thesis deals with the interaction between combustion, acoustics and vibrations with emphasis on frequencies below 500 Hz. Extensive literature is available on the interaction between combustion and acoustics and much work is also available on the interaction between acoustics and vibration. The work presented in this thesis attempts to combine these fields in order to calculate the vibrations of the liner.

A test rig with a thermal power of 500 kW at a maximum pressure of 5 bars has been built, in which measurements are carried out on the combustion process, the acoustic response in the combustion chamber and the resulting vibrations of the liner. The acoustic pressures in the combustion chamber are measured using sidetubes and a back pressure system, which enables the use of relatively cheap pressure transducers for measurements at high pressure and high temperature. Structural vibrations are measured using a laser vibrometer and a traverse system. Because the liner is surrounded by a pressure vessel, glass windows have been constructed in the pressure vessel in order to allow optical access to the liner. The test rig provides the geometry for all the models in this work. A step-by-step approach is adopted, in which the separate domains are first modeled and validated experimentally. Subsequently, they are coupled to form more complex models.

The acoustic response of the combustion chamber in absence of flow and combustion, is modeled using the finite element method. The model includes

upstream geometry (the burner and plenum) and downstream geometry (the water cooler). It is shown that these are necessary to accurately predict the acoustic response in the combustion chamber. For the acoustic behavior during combustion, the density and speed of sound are adjusted for the temperature field calculated with CFD. The predicted acoustic eigenfrequencies during combustion match very well with measurements.

The finite element method is also used to model the structural behavior of the liner. This structural model is validated by experimental modal analysis. The eigenfrequencies and mode shapes found with the model are similar to those found experimentally.

The acoustic and structural finite element model are subsequently combined in a fully coupled acousto-elastic model. The coupling between the acoustic and structural model is first successfully validated using a simple experiment. A simple coupled model of a section of the test rig shows that the acoustic properties of the combustion chamber and cooling passage have an influence on the structural behavior, although this is only substantial for structural modes that cause a change in the volume of the combustion chamber. The influence of structural vibrations on the acoustic behavior is small for the geometry and properties of the test rig. Furthermore, it is shown that the influence of temperature on the structural behavior of the liner is smaller than the influence of temperature on the acoustic behavior. A simple approximation of the liner temperature is therefore sufficient for modeling liner vibrations.

To predict the structural response caused by combustion, a flame model is needed. Several simplified models are therefore introduced. The flame is modeled as an acoustic volume source in the finite element code, which gives a prediction of the vibration level of the liner caused by the flame as an autonomous source of sound. A second approach investigated is using the pressures on the wall from a large eddy simulation as loads and then calculating the structural vibration in a transient analysis. Both methods give similar results, matching well with the measured vibration response. To include the response of the flame to the acoustic field it generates, transfer functions are extracted from the fully-coupled acousto-elastic finite element model, which are used in combination with a flame transfer function model to predict the influence of feedback. This model gives an explanation for some of the differences between the measurements and the calculations with the autonomous model.

In conclusion, an acousto-elastic modeling procedure has been developed to predict structural vibrations in combustion chambers. The procedure was successfully validated by experiments in a representative combustion system and can be applied to complex industrial combustion systems.

Samenvatting

Luchtvervuiling is de afgelopen decennia een belangrijk onderwerp geworden. De vervuilende stoffen bestaan onder meer uit zogeheten stikstofoxiden, ook wel NO_x genoemd, die onder meer tijdens verbranding van fossiele brandstoffen in gas turbines worden gevormd. Om de uitstoot te verminderen wordt brandstof verbrand met een overmaat aan lucht, de zogeheten arme verbranding. Dit leidt tot een lagere uitstoot van NO_x, maar ook tot een sterker geluidsveld in de verbrandingskamer. Vanwege de hoge temperaturen in de verbrandingskamer moet de omringende structuur, de liner, dun zijn en deze is daarom flexibel. Het sterkere geluidsveld brengt de liner sterker in trilling, wat leidt tot een kortere levensduur. Dit proefschrift behandelt de interactie tussen verbranding, akoestiek en trillingen met de nadruk op frequenties beneden de 500 Hz, waarbij bestaande kennis over interactie tussen verbranding en akoestiek en interactie tussen akoestiek en trillingen wordt gecombineerd.

Om metingen te doen aan een verbrandingsproces, de akoestische responsie in de verbrandingskamer en de resulterende trillingen van de liner is een testopstelling met een thermische vermogen van 500 kW bij een druk van 5 bar gebouwd. De akoestische druk in de verbrandingskamer wordt gemeten met behulp van pijpjes en een tegendruksysteem, waardoor relatief goedkope druksensoren kunnen worden toegepast bij hoge druk en temperatuur. De trillingen worden gemeten met een laser vibrometer op een traverseersysteem. Omdat de liner wordt omsloten door een drukvat, zijn er glazen vensters in dit drukvat gemaakt om de noodzakelijke optische toegang tot de liner mogelijk te maken. De geometrie voor de meeste modellen in dit proefschrift is afgeleid van de testopstelling. Elk fysiek domein (verbranding, akoestiek en trillingen) wordt eerst afzonderlijk gemodelleerd en experimenteel gevalideerd. Daarna worden ze gekoppeld tot complexere modellen.

De akoestische respons in de verbrandingskamer, wanneer er geen stroming en verbranding plaats vinden, wordt gemodelleerd met de eindige elementen methode. Het model omvat zowel de geometrie stroomopwaarts (de brander en plenum) als de geometrie stroomafwaarts (de waterkoeler). Er wordt aange-

toond dat deze nodig zijn om de akoestische responsie in de verbrandingskamer nauwkeurig te voorspellen. Voor het akoestische gedrag tijdens verbranding worden de dichtheid en de geluidssnelheid aangepast aan het temperatuursveld berekend met CFD. De gemeten en berekende akoestische eigenfrequenties tijdens verbranding komen uitstekend overeen.

De eindige elementen methode wordt ook gebruikt om het structurele gedrag van de liner te modelleren. Het structurele model wordt gevalideerd met behulp van experimentele modaal analyse op de liner. De eigenfrequenties en de trilvormen gevonden met het model en in het experiment lijken sterk op elkaar. De verschillen, die tijdens de productie door lassen worden veroorzaakt, zijn klein genoeg om het structurele model in de verdere berekeningen te kunnen gebruiken.

Het akoestische en structurele eindige elementen model zijn vervolgens samengevoegd in een volledig gekoppeld model. De koppeling tussen het akoestische en structurele model is succesvol gevalideerd met een vereenvoudigd experiment. Met een model van een deel van de liner en de verbrandingskamer wordt aangetoond dat de akoestiek van de verbrandingskamer en het koelkanaal invloed heeft op het structurele gedrag. Dit verschil is echter alleen wezenlijk voor trilvormen die het volume van de verbrandingskamer veranderen. Voor de testopstelling is de invloed van de trillingen van de liner op het akoestische gedrag minder belangrijk. Verder is de invloed van temperatuur op de trillingen van de liner kleiner dan de invloed van temperatuur op het akoestische gedrag. Een eenvoudige benadering van de temperatuur van de liner volstaat daarom voor berekeningen aan trillingen van de liner.

Om de structurele trillingen ten gevolge van verbranding te voorspellen is een model van de vlam nodig. Verscheidene vereenvoudigde modellen worden geïntroduceerd. De vlam wordt in de eindige elementen code gemodelleerd als akoestische volumebron. Hiermee wordt het trillingsniveau van de liner ten gevolge van de vlam als autonome bron van geluid berekend. Als alternatief wordt de druk op de liner uit een large eddy simulatie als belasting gebruikt om structurele trillingen in het tijdsdomein te berekenen. Beide methodes geven gelijksoortige resultaten, die goed met de gemeten trillingen overeen komen. Om de reactie van de vlam op het veroorzaakte akoestische veld mee te kunnen nemen, worden overdrachten uit het volledig gekoppelde acoustoelastische eindige elementen model gehaald die worden gebruikt in combinatie met de overdracht van de vlam om de invloed van terugkoppeling te voorspellen. Dit model geeft een verklaring voor enkele verschillen tussen de metingen en de berekeningen met het autonome model van de vlam.

Contents

Chapter 1

Introduction

1.1 Background

To make electricity generation by combustion cleaner than it already is, the European Union (EU) put stringent limits on the emission of NO_x (which is the short term for nitrogen oxides like NO and NO_2) from gas turbines. In modern gas turbines, most NO_x is formed by the reaction, at high temperatures, of oxygen (O_2) and nitrogen (N_2) from the combustion air [60]. In older combustion setups the ratio between air and fuel was near the stoichiometric ratio, which means that there is just enough oxygen in the air to fully combust the hydrocarbons in the fuel. This combustion results in very high temperatures and therefore high NO_x emissions, because the reaction speed of oxygen and nitrogen to form NO_x is a very strong function of temperature. The most effective method to decrease this so-called thermal NO_x is lean premixed combustion, meaning that there is an excess supply of air mixed with the fuel before it is combusted. There is more air to be heated by the same amount of fuel, leading to lower combustion temperatures and therefore lower NO_x emissions. This can continue until there is so much air that the fuel will not combust anymore (the lean blow-off limit). In general, the lower temperatures would lead to a lower efficiency. The inlet temperature of the turbine is limited though by the maximum allowable temperature of the first turbine stage. The hot combustion gasses from the flame zone are therefore cooled by adding relatively cold air to the hot combustion gasses. In lean combustion, less cool air is added after the flame and more air is led through the burner, leading to the same turbine inlet temperature and therefore the same efficiency.

The price for low NO_x emissions by lean premixed combustion is that the combustion becomes more unstable. This is a result of the lower combustion

temperatures and lower fuel concentrations. This unstable combustion results in pressure pulsations in the combustion chamber. These perturbations not only decrease the combustion efficiency, but also lead to vibration of the surrounding structure, the liner. The risk of failure due to high cycle fatigue therefore increases. In very lean combustion setups, the liner has therefore become a critical part in the lifetime of the combustor.

To comply with EU regulations requiring low NO_x emissions (below 10 parts per million) but still have a reliable combustor, a European project called DESIRE was initiated. The acronym DESIRE stands for *desi*gn and demonstration of highly *re*liable low NO_x combustion systems for gas turbines. In this project, research institutes (the University of Twente from The Netherlands, CERFACS from France, CIMNE from Spain), research establishments (DLR from Germany, KEMA from The Netherlands) and companies (Siemens from Germany, Powergen from Great Britain) cooperate to improve the reliability of gas turbine combustors and thereby allow a further decrease of NO_x emissions. Within workpackage 1 of the DESIRE project, the University of Twente built a test rig representative of a gas turbine combustion chamber to gain insight in the processes and mechanisms that are important in the liner vibration behavior of a combustion chamber. Numerical models were also built to support the insight and to predict the behavior of other setups.

1.2 The test rig

The test rig in workpackage 1 of the DESIRE project is an academic setup with facilities to perform detailed measurements on the flame, the acoustics and structural vibration. On the other hand, results obtained should be relevant for real gas turbines and therefore the test rig has to show behavior similar to a real gas turbine. The general properties of an industrial gas turbine are discussed in this section, as well as the boundaries this poses on the design of the test rig.

Air enters a gas turbine through the inlet (1 in figure 1.1) after which it is compressed in the compressor stage (2). The compressed air flows past the fairly thin walls of the combustion chamber (the liner) to cool these walls. Part of the air is leaked through the walls into the combustion chamber (3 and figure 1.2) to provide a cool air layer on the inside and to cool down the combustion gasses before they enter the first stage of the turbine. The air that is not leaked goes to the burners. In the burners fuel is mixed with the compressed air to form a combustible mixture, which is forced into a swirling motion. The swirling mixture is combusted in the combustion chamber, with

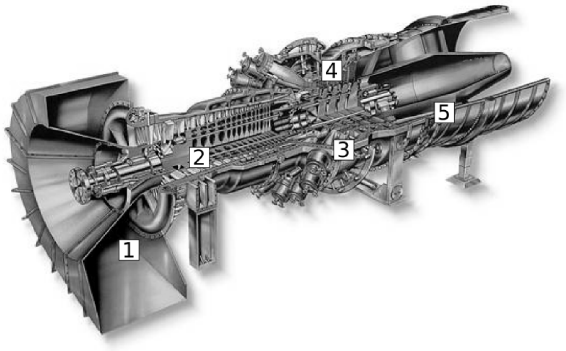

1 = Inlet
2 = Compressor
3 = Combustor
4 = Turbine
5 = Outlet

Figure 1.1: Example of an industrial gas turbine (Siemens SGT6-6000G).

a strong increase in gas temperature as a result. Because the mixture swirls, recirculation zones develop, in which a part of the combusted mixture is fed back to the flame zone. The rest of the combusted gasses are mixed with leakage air and enter the turbine (4) in which they are expanded to atmospheric pressure under generation of power. Finally, they are discharged through the outlet (5).

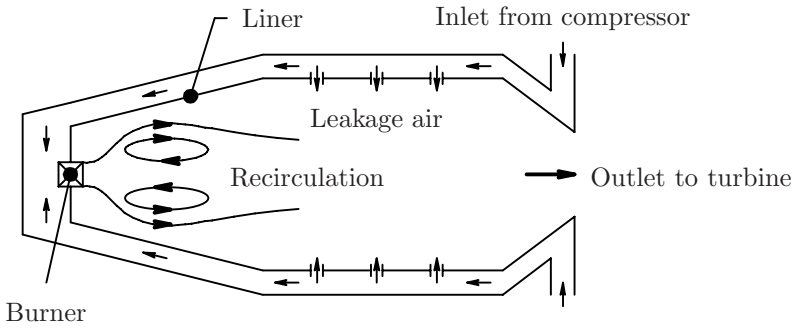

Figure 1.2: Schematic figure showing the air flow in and around an industrial combustion chamber.

The subject of the DESIRE project is the combustion chamber, as depicted in figure 1.2. One of the combustion chamber designs currently used in gas turbines is the so-called annular combustor (figure 1.3). In this design the combustion chamber is shaped as an annulus in which multiple burners (for instance 24) cause multiple swirling flames. It is very expensive to build a full annulus as a test rig, and therefore one section, containing one burner, is taken from the annulus. The interaction between flames from different burners is

therefore not present in the test rig.

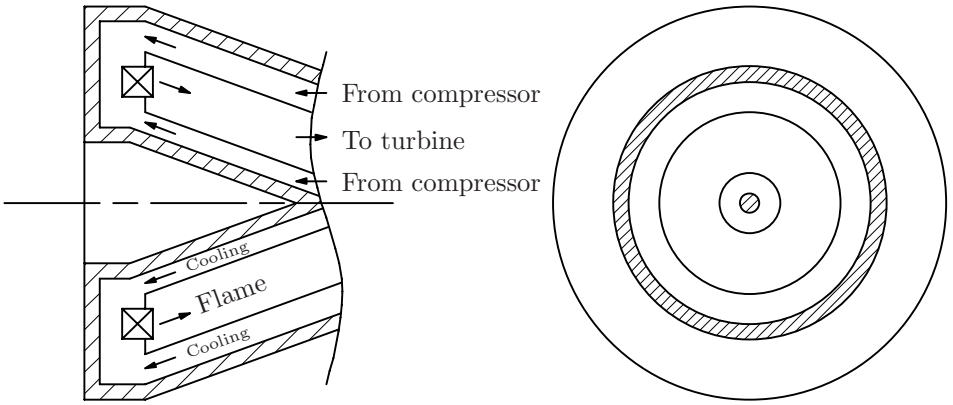

Figure 1.3: Schematic figure of an annular combustor.

A requirement for the test rig to be relevant to industrial combustors is that it should have acoustic and structural behavior that is similar to that of a real gas turbine. This thesis is focused on the lower frequencies, below 500 Hz, because experience has shown that this is one of the more problematic frequency regions with respect to fatigue. In this region, annular combustion chambers exhibit two types of acoustic modes. The first are axial modes, which have a changing pressure in the axial direction and constant pressure in the circumferential direction. The second type are circumferential modes, which have a more or less constant pressure in the axial direction and a changing pressure in the circumferential direction. The circumferential modes are not present in the test rig, but the axial modes, which have constant pressure in the circumferential direction, are. To obtain similar acoustic eigenfrequencies, the length of the test rig has to resemble the length of an industrial combustor, which is approximately 2 meters. For the structural behavior, the resonances of an industrial combustor start somewhere near 200 Hz, which should also be obtained in the test rig. Because the dimensions of the annulus are much larger than those of the section used for the test rig, this means that the test rig structure has to be more flexible than the annulus.

The conclusion reached from the above is that to achieve results in a test rig which also apply to a real gas turbine engine, the test rig should have a combustion chamber with a fairly thin liner, around which cooling air flows. It has to be capable of operating at elevated pressures and have a lean, swirling flame. Furthermore, it should have a length of around 2 meters and structural resonances starting in the region of 200 Hz. These requirements are fullfilled

by the test rig built. The experimental results are therefore also relevant for industrial scale combustion chambers. Because the geometry is relevant to gas turbines, the numerical models made using this geometry also give information relevant to industrial scale applications.

1.3 Combustion, acoustics and vibration

This section introduces the basic phenomenology, which is schematically depicted in figure 1.4, starting with the flame. The most characteristic influence of the flame is that it generates a temperature field (1), which strongly influences the acoustics of the system. This is mostly a static influence. The steady state temperature field created by the flame determines the steady state temperature field for the acoustics of the system. Unsteady combustion can give time-dependent temperature differences. When the flame moves, the local temperature field in the flame zone changes, but these perturbations have no global influence. When the amount of fuel that comes to the flame changes, the temperature of the total flame changes. These perturbations propagate through the combustion chamber with the flow velocity and are called entropy waves [78]. These are not taken into account in this thesis. Besides the steady influence, the flame also has unsteady components. Because the combustion is turbulent, the combustion speed constantly changes around the mean value. These changes generate an acoustic volume source (2), which gives an acoustic field in the combustor (this is commonly called *combustion roar*). This acoustic field in turn generates perturbations in the fuel and air flow to the burner and to the mixture coming to the flame (3), which again generates perturbations in the speed of combustion. This loop can become unstable, which is known as a combustion instability. This behavior is studied extensively in the literature [23, 62, 69]. Another well-known example of an unstable feedback loop between heat and acoustics is the so-called Rijke tube [82].

Vibration of the structure is influenced directly by the flame through the temperature field (1). This is again a steady phenomenon, the steady flame determines the temperature of the liner and therefore its material properties. Changes in operating conditions cause changes in thermal expansion of components and therefore cyclic thermal stresses, which can directly lead to relatively low cycle fatigue [95]. The interaction between acoustics and vibration is similar to that between combustion and acoustics. The acoustic field acts as a pressure load on the structure (4), which vibrates in response. This vibration imposes a velocity boundary condition on the acoustic domain (5), which generates an acoustic field. This loop does not become unstable, because there

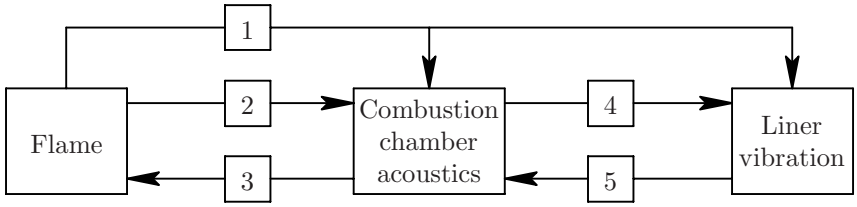

1 = Temperature field
2 = Volume source
3 = Burner velocity
4 = Pressure load
5 = Boundary velocity

Figure 1.4: Diagram of the interaction between combustion, acoustics and vibration.

is no energy source involved, as opposed to the interaction between flame and acoustics, where the flame can add energy to the system making it unstable. The interaction can cause strong amplification though.

1.4 Modeling

The interaction between combustion, acoustics and vibration discussed in the previous section can be studied using relevant experiments. Another method is to build numerical models. Due to the complex geometries involved, numerical methods are most appropriate to obtain accurate results. For the combustion part, Computational Fluid Dynamics (CFD) models are often used [105], which are able to include the effects of turbulence and combustion on the flow field. For acoustic modeling, two methods are common, being the Finite Element Method [106] (FEM) and the Boundary Element Method (BEM) [19]. Simplified methods, for instance based on one-dimensional acoustics, are also often used. Finally, for structural models the method of choice is often the finite element method.

Typically, the methods for the different domains are implemented in different software packages. These packages therefore have to be coupled using interfaces. Because there are three different domains (combustion, acoustics and structural vibration), there can be two code interfaces, one between the flame model and the acoustic model and one between the acoustic model and the structural model. It is also possible to include several domains in one model. Figure 1.5 shows several ways to do this.

The most complete method is to solve the full fluid, structure and reaction equations in one monolithic model (method 1 in figure 1.5). This evidently

includes all coupling mechanisms. An entire code needs to be developed to do this. If existing codes are coupled together, advantage can be taken from the work already done on these codes. To obtain a full model, including all coupling effects, all relevant data has to be exchanged over the boundaries, for instance between fluid and structure. Moreover, several iterations are needed within a time step. If, for instance, the fluid result is imposed as boundary condition on the structural model, the structural code generates a new boundary condition for the fluid domain and therefore the fluid calculation has to be redone using the new boundary conditions. Exchanging all data over the boundary is therefore difficult to implement and computationally expensive. Partial coupling, only exchanging data for the most relevant effects, can therefore be an attractive alternative.

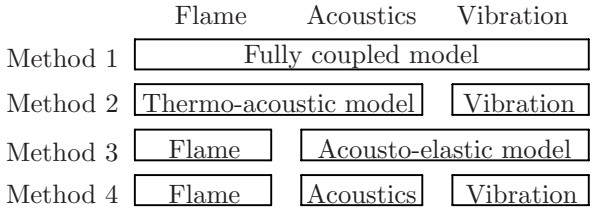

Figure 1.5: Different types of coupling.

There are three ways in which the different domains can be split. Acoustics and combustion can be combined in a thermoacoustic model and then coupled to a structural model (method 2) , acoustics and structural vibration can be combined in an acousto-elastic model which is coupled to a flame model (method 3) and all domains can be calculated separately (method 4).

In method 2 acoustics and combustion are solved simultaneously. Time integration for solving the non-linear fluid equations requires very high computational effort, because solving the acoustic part of the equations demands very small time steps. The acoustic pressure on the wall of the combustion chamber is transfered to a structural model to calculate the resulting vibration, neglecting the influence that this vibration has on the acoustic behavior.

Method 4 uses a separate acoustic model, which removes the time step restriction on the combustion model. The flame model generates an equivalent acoustic source for the acoustic model. The acoustic model subsequently generates the unsteady pressures on the wall which are transfered to a structural model. The acoustic model can also generate acoustic particle velocities, for instance at the burner outlet, that couple back to the flame model as an unsteady supply of mixture to the flame. This method is used in industry without

any feedback mechanisms.

Method 3 combines the structural and acoustic model in one code, giving full coupling for fluid-structure interaction. The acoustic model is driven by an equivalent source from a flame model, and acoustic particle velocities can be coupled back to the flame model.

This thesis mainly studies the third method, with a focus on the fluid-structure model. A companion thesis by Jaap van Kampen [48] focuses on thermoacoustic interaction. Purely acoustic or structural models are also discussed, but more for the purpose of validation than for their use in a fashion such as method 4.

1.5 Objective

The objective of this research is:

- To develop and build an experimental setup in which the interaction between combustion, acoustics and vibration can be studied.
- To use the experimental setup to get insight in the interaction between combustion, acoustics and vibration.
- To develop and experimentally validate models that facilitate the understanding of the interaction between combustion, acoustics and vibration and can as such be used as a design tool.

1.6 Outline

In chapter 2 the experimental facility built for this work is discussed. This is also the geometry for most of the models. Chapter 3 starts with an introduction to combustion and explains how a flame acts as acoustic source. It subsequently treats the acoustic models. Attention is also paid to acoustic measurement methods in the test rig and the experimental validation of the acoustic models. Chapter 4 explains the structural model and the interaction between structural vibration and acoustics. For this purpose, a simplified setup is first modeled and experimentally verified. A model for the structural vibration properties of the liner is developed and also experimentally verified. Fluid-structure interaction, without combustion, is then studied both numerically and experimentally for the test rig. Chapter 5 brings the flame model and the coupled acousto-elastic model together to form a full model of the fired setup. Experimental and numerical results are compared for the fired setup in

this chapter. Finally, conclusions and recommendations are given in chapter 6.

Chapter 2

The test rig

2.1 Introduction

This chapter deals with the test rig that was built for the research at the University of Twente. The geometry of this rig is used in many of the calculations in the next chapters. Major decisions that were made in the design are discussed first. Subsequently, the auxiliary components needed to operate the resulting design are treated to give an overview of the flows through the rig. This work mainly deals with the combustion chamber, of which the global properties are treated first. The different parts of the combustion chamber, which are the combustion section, the structural section and the cooler section, are treated in more detail next. The chapter ends with an overview of properties that are measured on the test rig and the locations where these measurements are made.

2.2 General considerations

The test rig is a scaled down representation of a real annular combustor, because a full annular combustor would be much too expensive, both to build and to use. The basic physics of the annular combustor should, however, be retained in the test rig. Two principle downscalings are done. Firstly, one burner section (from a total of 24 burners) is used. Secondly, the thermal power of the burner is scaled down.

To obtain a burner that can operate at this limited power (100 kW/bar for this test rig), the size of the burner is decreased (because the flow speed must be high enough to obtain a stable recirculation area). The burner needs a cross-sectional diameter of 50 mm. For a stable recirculation area, the expansion

from burner to combustion chamber needs to be a factor of around 3, giving a combustion chamber diameter of 150 mm. The chamber is made square to facilitate the creation of glass windows in the rig (to make measurements on the flame and on the vibration of the liner). If an industrial combustor would be scaled down using this diameter, the length of the combustion chamber would be in the region of 300 mm. To obtain acoustic eigenfrequencies in the range of those in an industrial combustor, the combustor length is taken similar to an industrial combustor, in this case 1.8 meter. A big difference that arises is that, where in an industrial combustion system the flame occupies a substantial part of the combustion chamber, the test rig has a relatively small flame zone in the most upstream part of the combustion chamber (see also section 3.3.8). In this respect, upstream means the part where the flow goes first, so the 'start' of the combustion chamber. This is also seen in the literature, where more or less small scale test setups are long and slender when thermoacoustics is studied [25, 31, 66]. It should be noted that circumferential acoustic modes, which exist in an annular combustor, are not present in this test rig.

2.3 Layout of the auxiliary components

The general layout of the test rig is depicted in figure 2.1. Air is drawn from the atmosphere and compressed using an air compressor. The air is then supplied to two mass flow controllers (MFCs). One MFC controls the air mass flow to the electrical heater and subsequently to the burner. The heater is needed to reheat the compressed air - which is first cooled down after compression and then transported to the test rig - to simulate true combustion conditions. This reheated air goes through the combustion channel to the water cooler. The other controls the mass flow entering the cooling passage. This is the passage between the liner, the thin structure around the combustion channel, and the pressure vessel. Natural gas is compressed using a gas compressor, which supplies pressurized gas to a mass flow controller. This MFC controls the mass flow of natural gas to the burner and therefore the thermal power the test rig operates on. In the burner, natural gas and air mix partially to form the combustible mixture, which is combusted in the combustion chamber. The hot flue gasses are first cooled down in a water cooler, where the cooling air which passed through the cooling channel is also merged with the combustion flow. The gasses subsequently go through a throttle valve, which controls the pressure inside the combustion system. The properties of the combustion chamber will be discussed in the remainder of this chapter.

The test rig is depicted in figure 2.2. Combustion air enters the rig in the

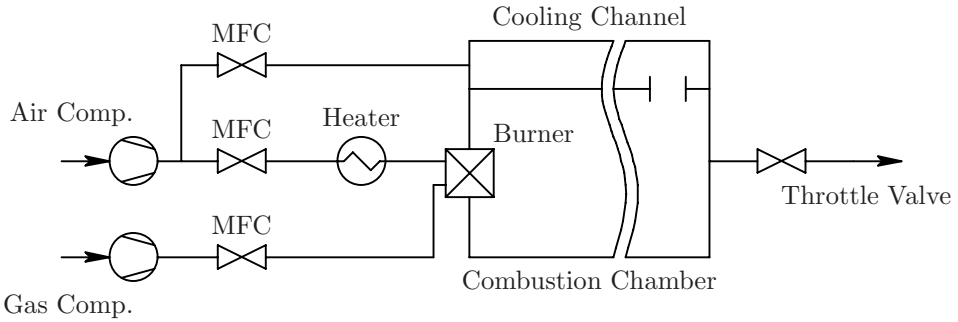

Figure 2.1: Layout of the main components of the test rig.

air supply box (1) from which it flows through a contraction to the plenum (2). From the plenum it goes through the burner (3), where natural gas is mixed with the air, to the combustion chamber (4). Here the mixture is combusted. The combustion products pass the structural section (5), where structural liner vibrations are measured, and flow through a contraction (the CFD tube, 6, the name comes from one of its functions, which is to provide a well defined boundary condition for CFD simulations) to the water cooler (7), where water sprays are used to cool the combustion product. The gasses then leave the combustor through the outlet (8) to a throttle valve controlling the pressure in the test rig.

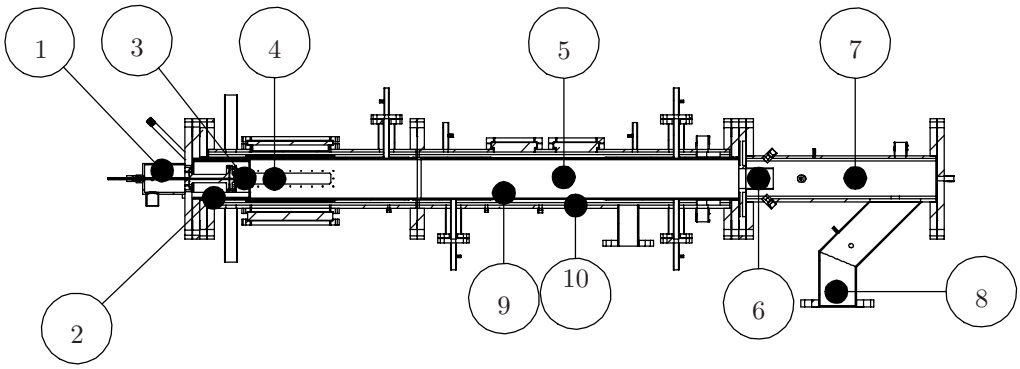

Figure 2.2: Cross section of the test rig.

The wall of the combustion channel, called the liner (9), is very thin to keep thermal stresses low. Measurements can be made under atmospheric conditions, but also during combustion at elevated pressures, as they are in a real combustor. A pressure vessel therefore surrounds the liner. The liner is

cooled by a separate air flow between the liner and the pressure vessel (10). This flow is added to the main flow in the water cooler. Because the cooling air remains relatively cool (below 300 °C), the thermal stresses are also low and therefore the pressure vessel can be thick enough to withstand the pressure loads. Contactless vibration measurements are made on the liner, and therefore windows are available in the pressure vessel through which a laser vibrometer can measure the liner vibration.

2.4 Combustion chamber

A cross section of the combustion chamber is depicted in figure 2.3. The test rig is mounted vertically, with combustion gasses flowing from the top to the bottom, but for compactness it is depicted horizontally here, with combustion gasses flowing from left to right. The test rig consists of three parts. The left part is the combustion section, consisting of the plenum (the last chamber upstream of the burner), the burner itself (in which the air gets a swirling motion and fuel is added) and the first part of the combustion chamber (where the combustion takes place). The middle section is the structural section, in which the vibration of the wall can be measured. The most right part is the water cooler in which the cooling air is mixed with the combustion air and the hot gasses are cooled down by water injection to temperatures that the throttle valve can withstand. The combustion channel in the structural section and the water cooler are separated by a tube which is referred to as the CFD tube. This tube serves two purposes. Firstly, it separates the acoustics of the water cooler and the rest of the system to a certain degree, because acoustic waves hardly travel from the structural section through the CFD tube to the water cooler and back again to the structural section (see also section 3.3.4). Secondly, it provides a well defined end for CFD calculations (hence its name). The three sections will now be discussed separately.

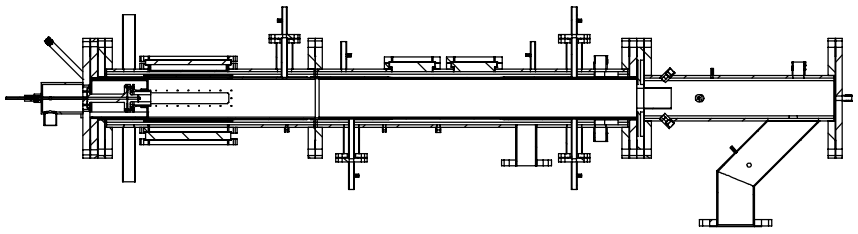

Figure 2.3: Cross section of the test rig.

2.4.1 Combustion section

The combustion section is depicted in figure 2.4. Air enters the test rig in an air supply box (1). It is forced through a flange containing small holes (2) to the plenum (3). Acoustic waves in the downstream part (in the direction of the flow) of the test rig hardly travel upstream (in the direction against the flow) of this flange due to the large decrease in cross-sectional area and the high velocity in these holes. This ensures a proper acoustic end condition for acoustic models (see also section 3.3.4). From the plenum, the air is swirled in the axial vanes of the burner (4). It then enters a swirl tube (5) around a central core (6). This central core has a central hole with radial injection holes, through which the fuel is injected (7). This results in a partial mixture of air and natural gas. This partial mixture enters the combustion chamber (8) through the end of the burner (the burner outlet). In the combustion chamber the mixture is ignited with a spark plug (or by the flame itself if it is already present). The first section of the combustion chamber is equipped with windows (9) in both pressure vessel and liner, which are used for chemilumniscence and Planer Laser Induced Fluorescence (PLIF) measurements [54]. To cool the liner (10), cooling air enters through four pipes (11) to the cooling passage between pressure vessel (12) and liner.

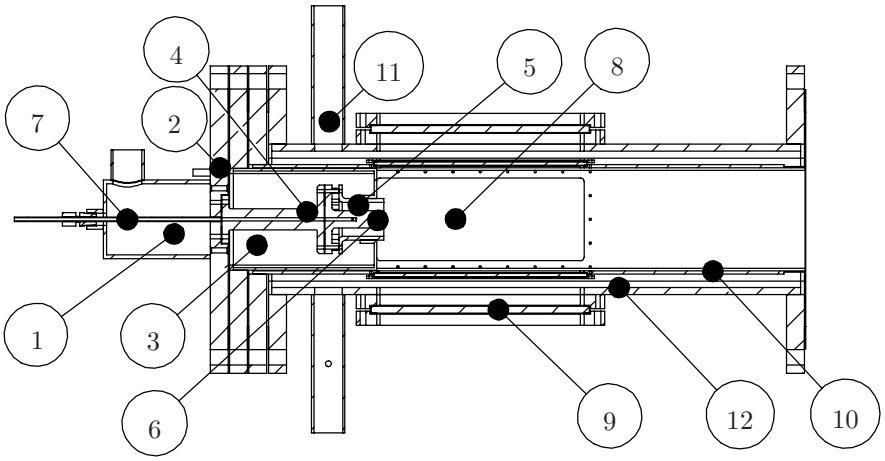

1 = Air supply box	2 = Decoupler plate	3 = Plenum
4 = Burner	5 = Swirl tube	6 = Central core
7 = Fuel supply	8 = Combustion chamber	9 = Windows
10 = Liner	11 = Cooling inlet	12 = Pressure vessel

Figure 2.4: Cross section of the combustion section of the test rig.

2.4.2 Structural section

Figure 2.5 shows the structural section of the test rig, which is located downstream of the combustion section. The mixture is fully combusted when it enters this section. Like the combustion section, the structural section consists of a flexible liner (1,2) inside a stiff pressure vessel (thickness 10 mm), between which cooling air flows, similar to the combustion section. The cooling air leaves the passage at the end of the structural section through four hoses (3).

The liner can be easily replaced, because of its simple construction. It is made as a thin (1.5 mm) square tube (1) with thicker (4 mm) end sections (2). By making a thin section between thicker parts, the vibration level of the thin section is much higher than that of the thick parts and therefore the thick parts approximate a clamped boundary condition for the thin part. This is a much more simple boundary condition than for an entirely thin liner, because this has flanges and connections as boundary conditions.

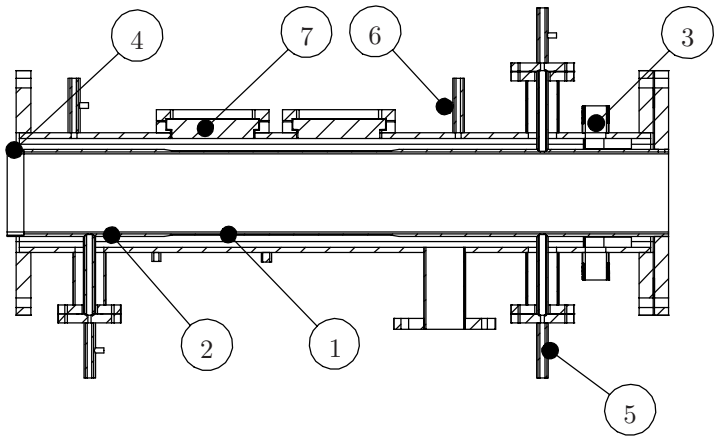

1 = Thick part liner 2 = Thin part liner 3 = Sliding connection
4 = Cooling pressure 5 = Combustion pressure 6 = Optical access

Figure 2.5: Cross section of the structural section of the test rig.

The radial thermal expansion of the thin and thick parts of the tube are approximately the same, which results in low thermal prestresses due to this direction. If in the other direction, the liner is approximated as a beam, clamped on both sides, the stresses σ arising when temperature is increased by ΔT are given by:

$$\sigma = E\alpha\Delta T\,, \tag{2.1}$$

in which E is the Young's modulus, α is the coefficient of thermal expansion and ΔT is the temperature difference. Subsection 4.4.5 will show that the

liner temperature is approximately 800 °C. The average modulus of elasticity E in this temperature region is 175 GPa and the average coefficient of thermal expansion α is 17 μm/mK. These values result in a thermal stress of 2380 MPa, which is far above the yield stress of 240 MPa at 800 °C. The sliding connection with the liner in the combustion section (4) alleviates this problem, but some stresses can still exist, because of friction in the sliding connection.

In a gas turbine the liner is made as stiff as possible, until thermal stresses become too high, to keep structural vibration low and therefore avoid fatigue. This results in a lowest structural eigenfrequency in the region of 200 Hz. Because the test rig is a downscaled version of an industrial gas turbine, the structural eigenfrequencies are higher and therefore the behavior is very different. Furthermore, below the first eigenfrequency, the vibration amplitudes are very low and therefore difficult to measure. Lower eigenfrequencies are therefore desirable. Three measures were taken to decrease the structural eigenfrequencies to the range in which they occur in an industrial turbine. Firstly, the walls were made flat (opposed to the curved walls in an industrial turbine). Secondly, the liner thickness was decreased. This decrease is limited by the strength required to withstand a pressure difference between the combustion channel and the cooling passage and the loads imposed during ignition. Thirdly, given the 0.15x0.15 m cross section, the eigenfrequencies can be decreased by making the flexible section longer. This has the disadvantage that larger windows are needed to measure the vibration level over the full length of the flexible section. The length of the flexible part of the liner is 400 mm. A longer flexible section only gives a small further decrease in eigenfrequency, which no longer justifies the added costs of the bigger windows needed.

Figure 2.5 also shows several pressure pickups (5,6). Pressure transducers measuring the pressure in the combustion chamber (5) use a tube through the pressure vessel and cooling passage onto a small hole in the liner. For measuring the acoustic pressures in the cooling passage only a small sidetube is needed. The working of the sidetubes as well as the necessary back pressure facility for the pressure transducers is explained in section 3.4. Structural vibration is measured using a laser vibrometer through glass windows (7) in the pressure vessel (see also section 2.5.3).

2.4.3 Cooling section

The cooling section is depicted in figure 2.6. The purpose of the cooling section is to cool down the hot flue gasses before they leave the combustor through the throttle valve. This is done by means of water injection through spray nozzles. The hot gasses enter the water cooler through the CFD tube. An attachment

point with a diameter of 50 mm is available. This is used to mount a circular tube with a speaker in a box at the end, used to acoustically excite the system (see also chapter 3). Furthermore, there is a sidetube (which is not visible in the figure) to which the four hoses coming from the cooling passage connect. Through this sidetube the cooling air is mixed with the combustion air before it enters the throttle valve and therefore the pressure in the combustion chamber and the pressure in the cooling air passage is always almost equal.

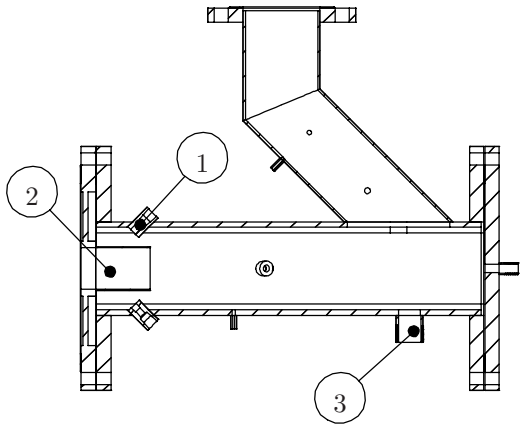

1 = Spray nozzle 2 = CFD tube 3 = Excitation point

Figure 2.6: Cross section of the cooler section of the test rig.

2.5 Measurements

This section discusses the measurement methods that are used to perform measurements on the setup. Operational parameters are discussed first, after which dynamic measurements like pressure and vibration are treated. Results of these measurements can be found in the other chapters of this thesis.

2.5.1 Operational parameters

To accurately monitor the behavior of the test rig, the operational parameters are measured. With operational parameters the steady parameters which only change slowly over time are meant. These parameters determine the combustion situation in which the rig operates and also show whether the system is in a stable or transient state. The following physical parameters are monitored:

- Mean air mass flow for combustion and for cooling
- Mean fuel mass flow
- Mean pressure inside the combustion channel
- Mean pressure difference over the liner
- Mean temperature at several points

The mean air and fuel flow to the burner determine the operating power and are measured using Bronkhorst Mass Flow Controllers. Together with the mean pressure in the combustion channel (measured using a Special Instruments Clic pressure transducer), they give the operating condition. The different operating conditions are numbered. The cases used in this thesis are listed in table 3.1. The cooling air flow is also measured. The measurements in this thesis are always made using a cooling air factor of 1.0, meaning that the amount of air that flows to the burner is equal to the amount of air that flows through the cooling passage.

The pressure difference over the liner is monitored using a Special Instruments Clic pressure transducer mounted with one port on the combustion chamber and with one on the cooling passage. This measurement is made for two reasons. Firstly, if the pressure difference becomes too high, the liner can fail or the windows in it can break. Secondly, a pressure difference causes a prestress in the liner, changing the structural behavior (see section 4.4.5).

The liner temperature is measured using thermocouples on the liner just before and after the thin flexible section. Mounting thermocouples on the flexible section would influence the structural behavior of it too much and the difference in liner temperature is not large. It is measured for two reasons. Firstly, if the liner becomes too hot, it can melt and secondly, the liner temperature can influence the material properties of the liner (see section 4.4.5). Beside the thermocouples, the liner temperature is also measured using a pyrometer through the square laser vibrometer window in the structural section. Furthermore, the inlet and outlet temperature of the cooling air is measured to determine the heat loss, and the inlet and outlet temperature of the combustor is measured to determine whether the temperature profiles used are reasonable.

The output of all sensors for operational parameters are digitized using a National Instruments Fieldpoint interface and the control is done using LabVIEW.

2.5.2 Acoustic measurements

The subject of the project is the interaction between unstable combustion and structural vibrations, which are coupled by acoustics. The acoustic field inside

the combustion chamber is therefore measured. Moreover, the acoustic field in the cooling passage is measured, because the excitation on the structure is the difference between the pressure on the inside (where the combustion takes place) and the outside (which is the cooling air between the liner and the pressure vessel). The measurements are performed using Kulite pressure sensors. The construction to mount the transducers, using semi-infinite tubes and a back pressure facility is discussed in section 3.4. The lowest acoustic level the Kulite pressure transducers can measure is 60 dB, or 0.02 Pa.

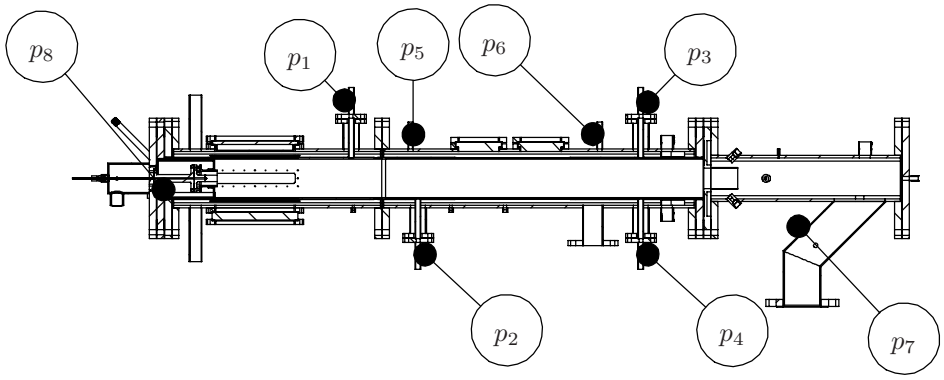

$p_1 = 506$ mm $\quad p_2 = 754$ mm $\quad p_3/p_4 = 1579$ mm
$p_5 = 716$ mm $\quad p_6 = 1416$ mm

Figure 2.7: Location of the pressure sensors.

The locations of the pressure transducers, numbered from p_1 to p_8, are depicted in figure 2.7. The distances from the burner outlet are listed below the figure. Sensors p_1 to p_6 are located in sidetubes. Sensor p_7 is located in the outlet towards the throttle valve (figure 2.6). Sensors p_3 and p_4 are located opposite each other. If the acoustic field in the test setup is one-dimensional, both sensors give the same measurement. The arrangement is also used to check to accuracy of the infinite tube arrangement (section 3.4).

2.5.3 Structural measurements

Structural vibration is measured using laser vibrometry [79]. This technique was chosen because it can measure on the hot (up to 800 °C) surface of the liner. Furthermore, because it is a contactless measurement, it does not influence the structural behavior of the liner.

Because the flexible liner is contained inside a pressure vessel, windows are needed in this vessel to allow laser vibrometry on the flexible liner. Two types

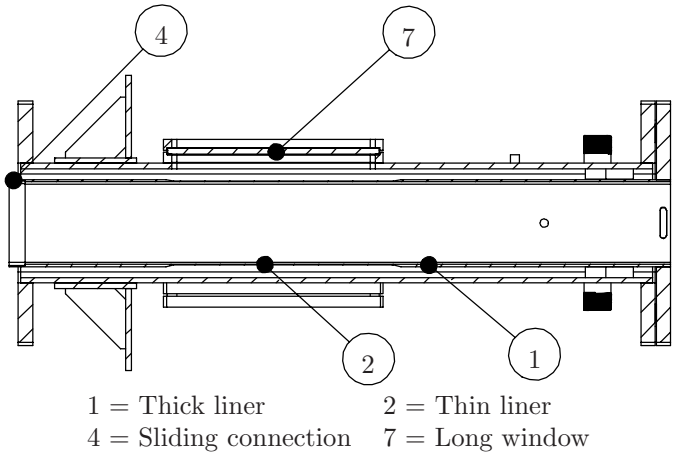

Figure 2.8: Cross section of the structural section of the test rig.

of windows are used, square windows (two on one side, figure 2.5) and slit windows (two on opposite sides, figure 2.8). The slit window is located 50 mm from the edge of the liner, so 100 mm from the other edge (figure 2.9). It has a length of 370 mm. The start of the slit window is located at the connection between the thick and the thin part of the liner, so measurements can be made up to 30 mm before the connection to the other thick part. The locations of the square windows are also shown in the figure. The recognizability of different structural modes through the available windows is discussed in appendix E.

Most results shown in this thesis were made on one of the slit windows, because information is obtained over almost the entire flexible section of the liner. The structural modes almost always have only one half wave over the width and therefore that information is less useful. Furthermore, obtaining good data on a two-dimensional grid covering the square windows takes much time, in the range of hours due to the averaging needed to filter out turbulent effects. These measurements are therefore much more expensive than those on the one-dimensional slit window.

2.5.4 Flame measurements

The pressure vessel and the liner contain windows in the combustion section. These windows are used to make Chemiluminescence and Planer Laser Induced Fluorescence (PLIF) measurements. These methods are quantitative methods to measure the presence of different species. With PLIF the measurements can be made in a plane, where chemiluminescence provides an integrated value

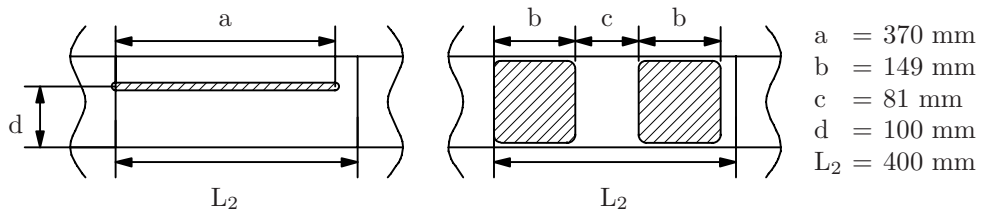

Figure 2.9: Location of the laser vibrometer windows with respect to the thin part of the liner.

over the flame. Both techniques are used for validating flame models and are therefore not discussed here, results can be found in Harleman [38].

Finally, figure 2.10 shows an overview of the test rig. It contains the names of the different sensors and some global properties. This figure is used as a reference in the remainder of this thesis.

2.6 Concluding remarks

This chapter dealt with the test rig that will be used in this thesis. The test rig is representative for an industrial combustion system. Static parameters, such as air factor, operating pressure and thermal power, can be chosen. Furthermore, the temperature of the gasses as well as the structure can be measured at different locations. Measurements can be made on the behavior of the flame using chemilumniscence and LIF. The acoustic behavior can be monitored at different locations using pressure transducers and the vibration behavior of the liner can be measured using laser vibrometry through windows in the pressure vessel. The test rig can therefore provide sufficient data for the validation of the models that will be developed in this thesis as well as models developed by others [48, 88].

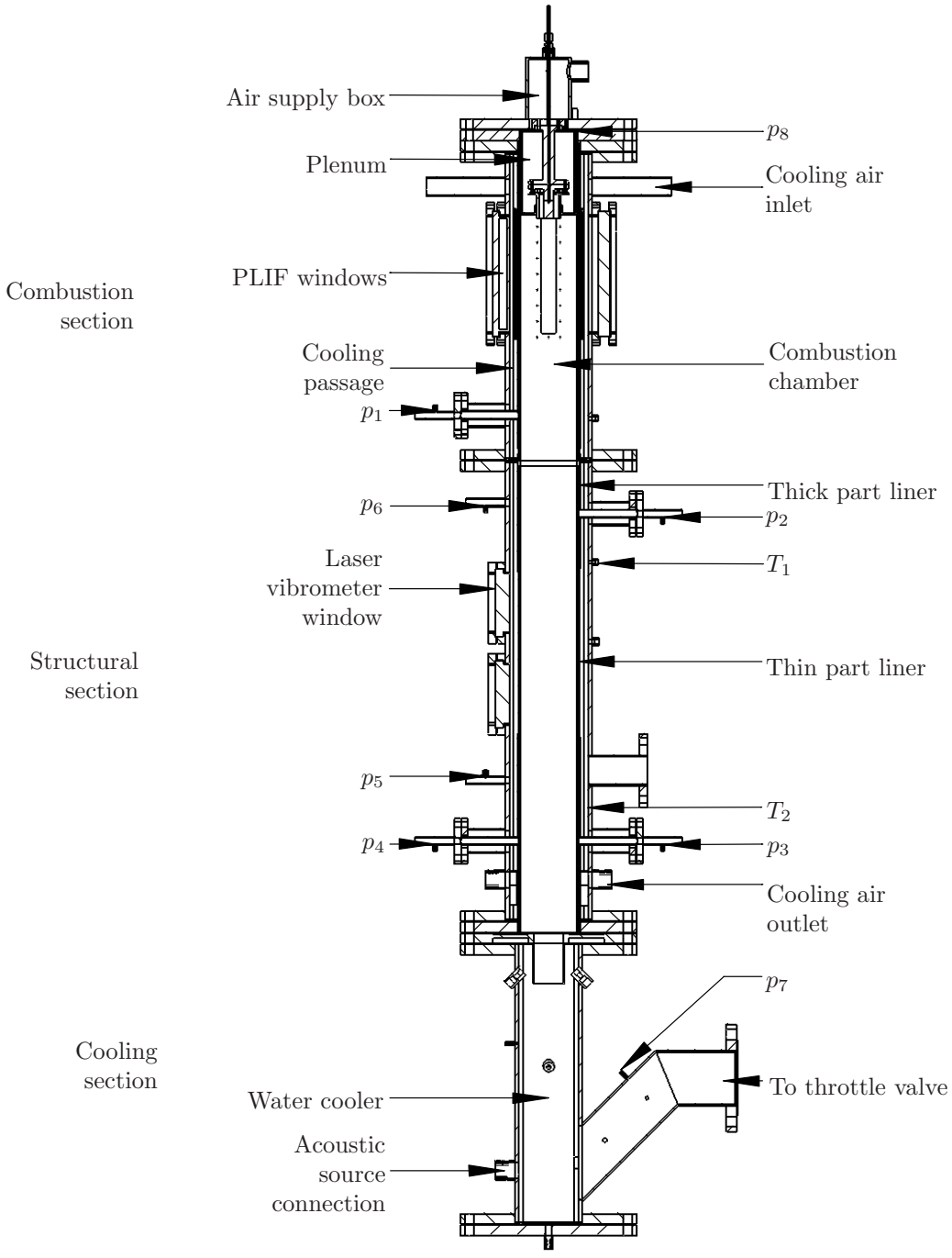

Figure 2.10: Reference overview of the test rig.

Chapter 3

Acoustics

3.1 Introduction

In the previous chapter, the test rig used for this thesis was discussed. This chapter deals with acoustics and the flame as acoustic source. An introduction to the field of combustion is therefore given first, after which the flame as acoustic source is treated. Acoustic models are described next. Two types of models are presented: finite element models and models based on one-dimensional acoustics. The first type has the advantage that complex geometries can be included, whereas the second type is often faster in computation and is widely used for thermoacoustic calculations [25, 62]. For the calculations, the geometry of the test rig at the University of Twente is used. The models are used to investigate the influence of different components of the rig on the acoustic behavior and the influence of temperature distribution. Furthermore, the burner impedance is evaluated as an indication of thermoacoustic stability. To validate the acoustic models for the case that there is no combustion, acoustic pressure measurements on the test rig are performed. To allow measurements under high temperature conditions, so-called semi-infinite tubes are used. The working of these tubes is explained and validated. For measurements in which the test rig is operated above atmospheric pressure, a second technique called back pressure tubes is used, which is also validated. Acoustic measurements, which are made with an acoustic source and without combustion and flow, are subsequently treated. Acoustic eigenfrequencies and transfer functions are compared with results from the numerical models. Furthermore, some experimental results on the influence of mean flow on the acoustic behavior are described. Chapter 4 treats the structural behavior and fluid-structure interaction and in chapter 5 models and experiments with combustion are discussed.

3.2 The flame as acoustic source

This section deals with the flame, being one of the three physical domains that are important for the subject of this thesis. Reference should first be made to the thesis of Van Kampen [50], which was written in the same project as this one and focuses on the thermoacoustic behavior of the combustion process. In this section, an introduction is given to combustion and the terminology used in the rest of this thesis is introduced. The relation between combustion and acoustics is then treated. Subsequently, sound generation by combustion and the subject of thermoacoustic feedback are treated. Flame models are needed to model this feedback, hence the introduction of several basic flame models, both analytical and numerical, that are used in this and later chapters. Finally, some concluding remarks are given. Further information on combustion can be found in, amongst others, Lefebvre [60] and Warnatz [104].

3.2.1 An introduction to combustion

Combustion is basically the oxidation of fuels. Oxygen is commonly taken from air, so fuel is combusted using air from the environment. The combustion gasses are subsequently discharged back into the environment. The combustion processes in this thesis are characterized by three parameters:

- Pressure
- Thermal power
- Preheat temperature
- Equivalence ratio

Thermal power is the power released from the fuel by the reaction with oxygen, which is released as heat. The word thermal is used in this respect because only a part of the thermal power is converted into mechanical work by a turbine. This mechanical work can, for instance, be used to generate electricity with a generator. In a gas turbine engine, the rest of the thermal power is discharged through the outlet, where it can be used in, for instance, a steam cycle. The preheat temperature is the temperature with which the air enters the air supply box (see also chapter 2).

The equivalence ratio represents the ratio between fuel and air mass flow. When there is exactly enough oxygen in the mixture to oxidize all the fuel, leaving no oxygen in the combustion products, the mixture is called stoichiometric[1]. If there is too little oxygen present, the fuel is only partially oxidized,

[1]For combustion of natural Groningen gas, the stoichiometric ratio is 0.0771 [36].

Operating point	Thermal power	Pressure	Air factor	Preheat temperature
15.4	125 kW	1.5 bar	1.8	300 °C
15.7	150 kW	1.5 bar	1.8	300 °C
20.4	200 kW	2.0 bar	1.8	300 °C
20.5	150 kW	2.0 bar	1.8	300 °C
30.5	250 kW	3.0 bar	1.8	300 °C

Table 3.1: Operating points.

which typically causes the generation of soot and carbon monoxide (CO). For clean combustion, an excess supply of air should therefore be used. The ratio between fuel and air that is used, compared with the stoichiometric ratio, is called the equivalence ratio, given by:

$$\phi_0 = \frac{y_{f,0}/y_{a,0}}{[y_{f,0}/y_{a,0}]^{st}}\,, \tag{3.1}$$

in which ϕ_0 is the mean equivalence ratio, $y_{f,0}$ is the mean fuel mass flow, $y_{a,0}$ denotes the mean air mass flow and a superscript st denotes the stoichiometric ratio. A term that is also commonly used in this respect is the air factor, which is the reciprocal of the equivalence ratio. Using an air factor bigger than one, so using more air than strictly needed, is called lean combustion.

For the tests and models described in this thesis, standard combinations of pressure, thermal power and air factor are used, which are called operating points. These operating points are listed in table 3.1. The operating points have been numbered to facilitate communication between different partners in the DESIRE project and this numbering is maintained throughout this thesis.

Clean combustion

To decrease the NO_x emissions of combustion, the air factor is increased. Since more air is available for the same amount of fuel, the same amount of energy has to heat up larger amounts of air. This leads to a lower combustion temperature. This lower temperature decreases the rate at which nitrogen and oxygen from the combustion air react to form thermal NO_x. If the fuel is not evenly mixed with air, hot spots arise where the air factor is locally low, leading to higher combustion temperatures and therefore higher NO_x production. To obtain low NO_x emission it is therefore necessary to use a high air factor and a good premixing. This has led to the development of lean premixed combustors giving very low NO_x emission levels. Typical air factors used in industrial

combustors are approximately 2.0 with almost perfect premixing. The experimental combustor used in the DESIRE project uses partial premixing and an air factor of 1.8, because the combustion is still very stable at that air factor.

3.2.2 Sound generated by combustion

The flame as acoustic source can be conveniently described using the Lighthill analogy [67]:

$$\frac{\partial^2 p'}{\partial x_i^2} - \frac{1}{c_0^2}\frac{\partial^2 p'}{\partial t^2} = \frac{\partial^2}{\partial x_i \partial x_j}(\tau_{ij} - \rho v_j v_i) + \frac{\partial f_i}{\partial x_i} + \frac{\partial^2}{\partial t^2}\left(\rho' - \frac{p'}{c_0^2}\right), \tag{3.2}$$

in which an $'$ denotes a perturbation, p is the pressure, x_i is the coordinate, c_0 is the speed of sound, t is the time, τ_{ij} is the viscous stress tensor, ρ is the density, v_i is the velocity in direction i and f_i is the force exerted on the fluid in direction i. All terms on the right-hand side are acoustic sources, with the first representing quadrupole sources, the second dipole sources and the third monopole sources. An unsteady heat release rate of the flame acts as a monopole source for the acoustic field in the combustor. Leaving out other source types and rewriting (appendix B) gives:

$$\frac{1}{c_0^2}\frac{\partial^2 p'}{\partial t^2} - \frac{\partial^2 p'}{\partial x_i^2} = \frac{\rho_0(\gamma - 1)}{c_0^2}\frac{\partial^2 q'}{\partial t^2}, \tag{3.3}$$

in which γ is the ratio of specific heats and q is the heat release. Two types of combustion as acoustic source are usually distinguished. Firstly, the flame as autonomous source of sound, referred to as flame noise and secondly the flame as an active source, when it responds to an acoustic field, which is important for thermoacoustic feedback.

In the finite element models, the nodal flow rate Q is used in harmonic analysis to model the flame as acoustic source. If the volume integrated heat release rate $\bar{q}$ is expressed as:

$$\bar{q} = \hat{q}e^{\mathrm{i}\omega t}, \tag{3.4}$$

in which ω is the angular frequency, $\hat{q}$ is the amplitude of the volume integrated heat release rate and i is the imaginary unit, then the nodal flow rate Q can be expressed as:

$$Q = \frac{\mathrm{i}\omega(\gamma - 1)}{\rho_0 c_0^2}\hat{q}, \tag{3.5}$$

in which ρ_0 is the mean density at the adiabatic flame temperature. The derivation of this relation can be found in appendix B.

Flame noise

Because this thesis concerns turbulent flames, the combustion is by definition unsteady due to turbulent fluctuations in the flow and therefore the combustion acts as an acoustic source. This is known as *the flame as autonomous source* [92] or simply *flame noise*. Flame noise together with the acoustic resonances of the combustion chamber determine the acoustic spectrum in the combustion chamber when combustion is taking place.

The unsteady combustion has typical frequencies that are the same as the typical turbulent frequencies in the combustor. For the test rig in this thesis, these frequencies generally range up to 300 Hz and in the flame zone up to 1000 Hz. It should be stressed that flame noise does not depend on the acoustic field that is generated in the combustion chamber. The reaction of the flame on acoustic fluctuations is called thermoacoustic feedback and will be treated next.

Thermoacoustic feedback

As discussed, unsteady combustion in the flame acts as a source of sound. If the flame burns in a confined environment, such as a tube or combustion chamber, the generated acoustic waves reflect from the boundaries. The flame reacts to these acoustic waves and can therefore either amplify these waves further, or reduce them. The condition under which the flame amplifies the sound at a certain location was described by Lord Rayleigh [82] as:

$$\int_{t=0}^{t_{max}} p'(t)\bar{q}(t)dt > 0\,, \tag{3.6}$$

which simply means that when local heat release perturbations and pressure perturbations are in phase, sound is amplified and vice versa, if they are out of phase, the sound is attenuated. Information on the phase behavior of the flame with respect to the sound field in the combustion chamber is therefore very important when evaluating unstable behavior. The heat release distribution can also be very important, because it determines the location in the pressure field of the heat release and therefore it influences the phase relation between pressure and heat release [85]. Equation (3.6) indicates whether or not the combustion process adds energy to the acoustic field. In practical situations acoustic energy is absorbed at inlets, outlets, through vibrations of the wall and in boundary layers. The energy input by the flame must be higher than the energy absorbed at the boundaries for an instability to develop [25]. This means that information on the amplitude behavior of the flame is also important.

3.2.3 Flame models

In the previous section it was discussed that a flame generates an acoustic field and can also react to an acoustic field. This section gives an overview of the modeling techniques that are used to determine how the flame reacts to acoustic perturbations, which can be analytical, numerical and experimental. How a flame can react to an acoustic field is subsequently discussed and a simple flame model is presented that is used in chapter 5. This model is fitted to numerical data from a CFD model.

Analytical models

The advantage of an analytical model is the insight it provides in the process that makes the system unstable and that it can be evaluated very rapidly. The most well-known models in this category are the so-called n-τ models. These models assume that the flame is excited by acoustic velocity perturbations which convect towards the flame. Parameter n describes the amplitude of the flame response and τ the convective time delay and therefore the phase [9]. These parameters can be obtained by measurements, CFD calculations or analytical approximations. A non-linear extension can be made to calculate the resulting pressure amplitude under unstable conditions [24].

A second more or less analytical method that is often used is the unsteady well stirred reactor model [31]. This model gives a basic description of the combustion process if the mixing process is much faster than the reaction rate of the components to combust. This means that the combustion takes place homogeneously in the flame zone.

Numerical models

Numerical models use a Computational Fluid Dynamics (CFD) model to derive a transfer from an acoustic quantity to flame behavior (a so-called flame transfer function), similar to that of the analytical methods. The most common procedure is to excite the numerical model of the flame by an impulse and then monitor (numerically) the response of the flame. Different methods to describe turbulence are used, such as Reynolds averaged Navier Stokes (RaNS) [10, 13, 84] and Large Eddy Simulation (LES) [100]. It is also possible to linearize the entire CFD model and in this way obtain the linear flame response [51].

Experimental models

Experiments can be used to validate analytical and numerical models. But experimental data can also be used to supply information on the flame transfer function. The most common method used is to force the acoustics in the combustion chamber, for instance with a siren, and then measure the flame response [6, 15, 63, 76].

Flame excitation mechanisms

Many types of interaction between acoustics and combustion are suggested in the literature. Three main categories of interaction can be distinguished: vortical modes, acoustical modes and entropy modes. The first, vortical modes, is related to vortex shedding. When these vortices reach the flame zone they cause unsteady combustion. The second, acoustical modes, originates in direct interaction between acoustic waves and the flame front. The third, entropy modes, is related to differences in mixture convecting to the flame front. An overview of the interaction between combustion and acoustics can be found in, for instance, Lieuwen [62] or McManus [69]. The simple model described in the next section is of the entropy type, because this type of interaction is well understood and there exists good agreement between calculations and measurements in the literature.

A simple flame model

A relatively simple model of a flame can be constructed by assuming that the heat release rate from the flame responds to the acoustic particle velocity perpendicular to the burner outlet. The physics behind this assumption is that a velocity perturbation at the burner outlet causes a modulation in the supply of the components of the combustible mixture to the flame. This causes an equivalence ratio perturbation that is convected towards the flame front, which causes a time delay. The low pass behavior is governed by the Strouhal number [62]:

$$St = \frac{f L_{FL}}{v_f}\,, \tag{3.7}$$

in which L_{FL} is the length of the flame, f is the frequency and v_f is the convection speed through the flame. Figure 3.2 shows the reaction rate of methane (which is an indication of the heat release rate) and the temperature field for a flame in the test rig. For this flame, the length of the flame is 0.10 meter. The Strouhal number is the time it takes for the perturbation to travel through the flame compared with the period of oscillation. When $St = 1$ a full

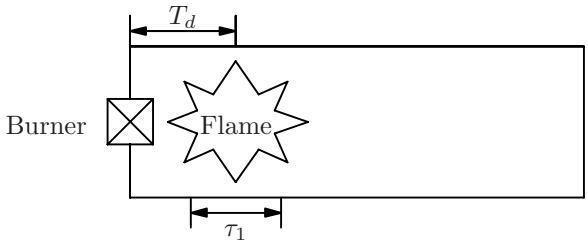

Figure 3.1: Schematic depiction of time delays in an n-τ model.

cycle fits into the flame. Therefore, the acoustic source originating from it has a phase spectrum that is equally distributed between 0 and 2π radians, making it cancel itself out (assuming that the flame is acoustically compact, so its dimensions are much smaller than the acoustic wavelength). This means that for low Strouhal numbers the source is almost entirely in phase and is therefore strong and for high Strouhal numbers the source is weak due to phase effects. This leads to a low pass behavior, in which the reaction of the flame to acoustic fluctuations decreases in strength with increasing frequency.

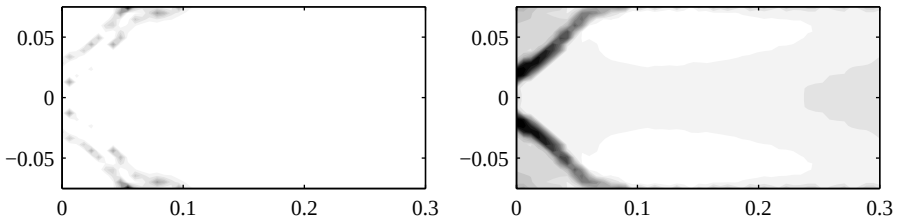

Figure 3.2: Numerical results for case 15.7, left shows the reaction rate of methane (black is high) and right the temperature field (white is high). Only the first 0.3 meter of the almost 2 meter long combustion chamber is shown.

A model with these two effects, a low pass filter combined with a convective time delay, is often referred to as an n-τ model and can be written as:

$$\frac{\hat{q}}{q_0} = \left[\frac{1}{1+\mathrm{i}\omega\tau_1}\right]\left[\frac{\hat{v}_B}{v_{B,0}}\right]\mathrm{e}^{\mathrm{i}\omega T_d}\,, \tag{3.8}$$

in which $\hat{v}_B$ is the velocity at the burner outlet, τ_1 determines the cut-off frequency of the low pass filter, T_d is the time delay and ω the angular frequency. The cut-off frequency is given by $St = 1$ or:

$$\tau_1 = \frac{L_{FL}}{2\pi v_f}\,. \tag{3.9}$$

The choice of a first order low pass filter is quite arbitrary. Higher order filters might be used as well, if experimental or numerical data show that a higher order transfer function fits better. A more general formulation is therefore used, given by:

$$\frac{\hat{q}}{q_0} = \left[\frac{1}{1+\mathrm{i}\omega\tau_1}\right]^m \left[\frac{\hat{v}_B}{v_{B,0}}\right] \mathrm{e}^{\mathrm{i}\omega T_d}, \tag{3.10}$$

in which m is the order of the low pass filter. Sometimes several time delays are used [65], a technique that is not applied here.

3.2.4 Numerical flame model results

The numerical flame models that are available for the setup of this thesis are of two different types, RaNS models [50] and LES models, which essentially differ in the manner in which turbulent eddies are taken into account [101]. They are discussed because they are used in obtaining temperature fields for acoustic calculations and also to fit the parameters of the n-τ model.

RaNS models

In the RaNS method, the flow field parameters are split in a mean value and the perturbations around it, so for velocity $v = v_0 + v'$. The effect of the turbulent part v' (which is a perturbation of a mean value, but not an acoustic perturbation) is then modeled by a closure model and the transport equations for the mean flow field v_0 are solved on the numerical grid. The results are taken from the thesis of Van Kampen [50]. A k-ϵ model is used as turbulence model. Combustion was modeled using a one-step combustion model. More information on turbulent combustion modeling can be found in Veynante [101]. The equivalence ratio of the supplied mixture is perturbed by an impulse on the fuel supply and the response is measured as the unsteady heat release rate by the flame. An experimentally validated result is depicted in figure 3.3. The response is calculated for case 15.7 (table 3.1), which is at 125 kW, equivalence ratio 1.8, pressure 1.5 bar and preheating at 300 °C.

LES models

The essential difference between RaNS models and LES models is that in LES models the unsteady instantaneous flow and its larger turbulent eddies are solved down to the scale of the computational grid, where RaNS only solves the quasi-steady mean flow. This improves flow modeling and can improve the prediction of phenomena like turbulent mixing and turbulent properties

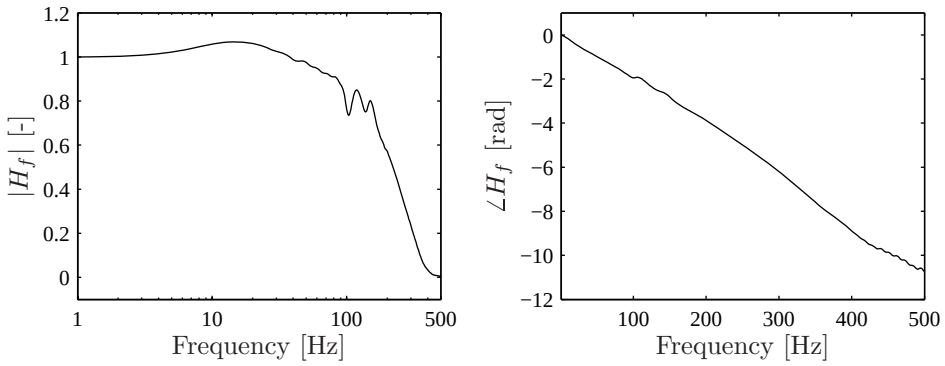

Figure 3.3: Amplitude (left) and phase response (right) of a RaNS numerical flame.

and therefore also the properties of the flame transfer function. The LES calculations were performed by the CFD team of CERFACS (Centre Européen de Recherche et de Formation Avancée en Calcul Scientifique). They are available for one excitation frequency only though, because the calculations take very long.

Properties of the simplified flame model

The flame model in equation (3.10) still needs values for the order of the low-pass filter m, the time delay τ and parameter τ_1, which determines the cut-off frequency. These can be extracted from a flame transfer function, determined with the RaNS models, which is defined as:

$$H_f = \frac{\bar{q}'/\bar{q}_0}{\phi'/\phi_0}\,, \tag{3.11}$$

in which $\bar{q}'$ is the perturbation in the volume integrated heat release rate and ϕ' is the perturbation in the equivalence ratio. The equivalence ratio perturbation is achieved by perturbing the fuel flow and can therefore, according to equation (3.1), be written as:

$$\phi' = \frac{y_f'/y_{a,0}}{[y_{f,0}/y_{a,0}]^{st}}\,, \tag{3.12}$$

and therefore:

$$\frac{\phi'}{\phi_0} = \frac{y_f'}{y_{f,0}}\,, \tag{3.13}$$

giving a flame transfer function of:

$$H_f = \frac{\bar{q}'/\bar{q}_0}{y'_f/y_{f,0}}\,, \tag{3.14}$$

The flame transfer function definition in equation (3.11) therefore defines the response of the volume integrated heat release rate to a relative perturbation in the fuel supply. In the n-τ model in equation (3.10), the response in heat release rate to a fluctuation in the burner outlet velocity was used. Because linearity is assumed, the heat release rate perturbations are only determined by the fuel flow perturbations and therefore the only relevant effect induced by a velocity perturbation at the burner outlet is a change in fuel supply. The parameters of the n-τ model can therefore be fitted to the results of the RaNS model.

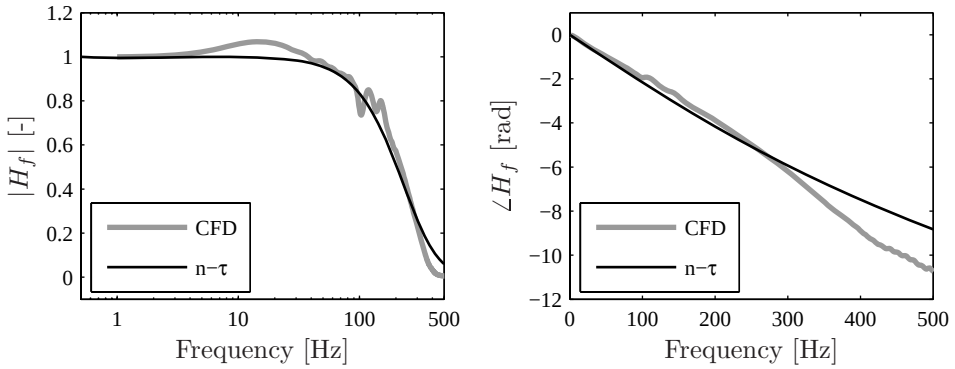

Figure 3.4: Amplitude (left) and phase (right) of the flame transfer function.

The fitted n-τ model is depicted in figure 3.4. The transfer function is fitted on the numerical results to obtain correct values for time delay, low pass cut-off frequency and order of the low pass filter. The result is a sixth order low pass filter with a cut-off frequency of 400 Hz, combined with a time delay of 1.1 ms. Figure 3.4 shows that the amplitude match is quite good. The match in phase shows some deviation above 300 Hz. The time delay is not fully responsible for the phase plot, because the low pass filter has a substantial phase delay due to its relatively high order. The time delay found using particle tracking in a CFD calculation is therefore higher [48] than the time delay constant in the n-τ model.

3.3 Acoustic modeling

3.3.1 Introduction

Two acoustic modeling techniques are used in this section, one-dimensional acoustics and the finite element method. In thermoacoustic research, one-dimensional acoustic models are often used [25, 62]. More recently, finite element models are also used [72, 75]. A finite element model has advantages over a one-dimensional model. Complex geometries do not have to be approximated using one-dimensional elements and an accurate temperature distribution can be included. Furthermore, two-way coupling with structural vibration can be added easily. On the other hand, including the influence of flow on acoustics and accurately adding combustion as acoustic source is more difficult (appendix B describes the method used in this thesis to add a thermoacoustic source, flow is not included in the finite element models in this thesis). An acoustic finite element model is developed. Because complex geometries can be modeled, the influence of different components of the test rig, such as the plenum, air supply box and preheater on the acoustic response of the rig is evaluated using different finite element models. With this knowledge, a one-dimensional model is made, as numerical validation and to evaluate the different methods, based on the real dimensions of the rig and some fitting to finite element results. The results of the one-dimensional and finite element model are compared. The main model used in this thesis is the finite element model. Burner impedance and the influence of temperature and its distribution are studied using this model. An experimental validation of the model is presented in section 3.5. In chapter 4 the finite element model is extended with a structural model to study fluid-structure interaction. A method to use the finite element model in combination with a flame as acoustic source is discussed in chapter 5.

3.3.2 The finite element model

A finite element model of the internal part of the test rig has been constructed. Linear acoustic tetrahedral elements are used. As a general rule six elements per wavelength are needed, which means that at ambient temperatures and up to 500 Hz, the elements should not be larger than 10 cm. This is only slightly less than the width of the combustor and therefore the mesh size is dictated by the geometry. The mesh that is used for the purely acoustic calculations is depicted in figure 3.5 and was made using Femap. It includes the tube to the throttle valve, the tube used for acoustic excitation (see also section 3.5) and a representation of the cooling tubes. The figure shows that there is substantial

Frequency	Description
43.4 Hz	Water cooler Helmholtz
107.5 Hz	Water cooler 1
198.2 Hz	Water cooler 2
265.8 Hz	Water cooler 3
289.0 Hz	Water cooler 4
421.1 Hz	Water cooler 5
490.5 Hz	Water cooler 6

(a) Water cooler

Frequency	Description
85.1 Hz	Plenum Helmholtz
131.7 Hz	Combustion 1
213.2 Hz	Combustion 2
305.2 Hz	Combustion 3
391.4 Hz	Combustion 4
484.0 Hz	Combustion 5
581.5 Hz	Combustion 6

(b) Combustion chamber

Table 3.2: Acoustic eigenfrequencies calculated with the finite element model.

refinement in the burner region, to accurately represent the internal geometry of the burner (figure 2.4). Furthermore the elements are refined in the burner outlet region to accurately calculate the acoustic particle velocity for burner impedance calculations (section 3.3.9). The semi-infinite tubes are treated in section 3.4.2. The commercial finite element solver Ansys is used.

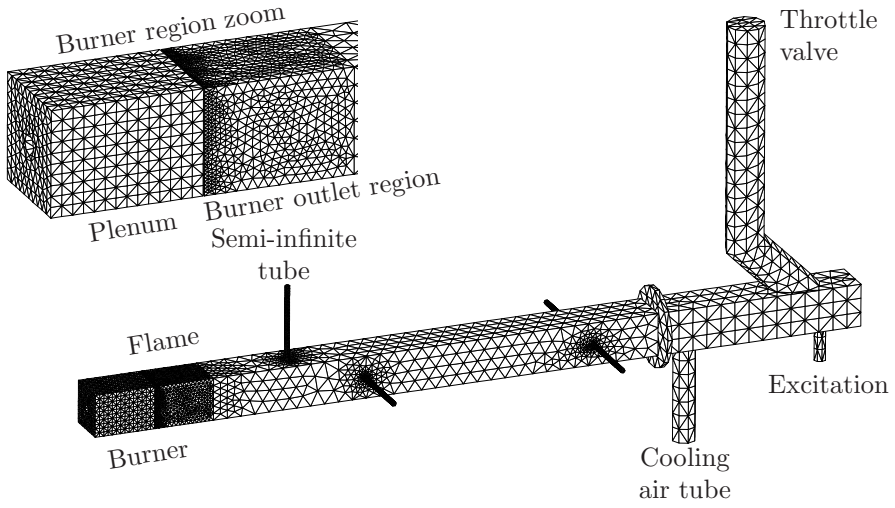

Figure 3.5: Mesh for the acoustic calculations.

3.3.3 Finite element model results

For a first indication of the behavior of the acoustic model, a modal analysis is performed. The resulting eigenfrequencies are listed in table 3.2 and the corresponding pressure at the centerline of the test rig is depicted in figure 3.6. It can be seen that several types of acoustic eigenmodes are present. The first two are Helmholtz-like modes[1] (water cooler Helmholtz and plenum Helmholtz), in which the three parts of the setup (plenum, combustion chamber and water cooler) interact through the contractions between them (the burner and the CFD tube, respectively, see chapter 2, which are inside the mesh of figure 3.5 and therefore not visible). After these two Helmholtz-like modes, a range of acoustic modes of the combustion chamber and the water cooler follow. These modes more or less alternate, where with increasing frequency, a combustion chamber mode is found, followed by a mode of the water cooler. This is caused by the similar effective length of the two components when the effective length of the water cooler is taken from the throttle valve via the water cooler to the cooling air tube. The pressure pattern in the water cooler is not clearly visible in figure 3.6, because the mode shapes extend off-axis to the cooling air tube and towards the throttle valve. In the acoustic experiments (section 3.5) the acoustic excitation takes places in the water cooler, and therefore these modes have to be taken into account. The more complex geometry of the water cooler causes the less regular interval between two cooler modes, compared with modes in the combustion chamber.

3.3.4 Acoustic influence of different components

The full geometry of the setup can be included in the finite element model. In this section a sensitivity analysis is described to analyze how sensitive the eigenfrequencies are to including the water cooler, the plenum and the air supply system upstream of the plenum. These calculations are performed at ambient conditions, so pressure is 1 bar, temperature is $20°C$ and density is 1.21 kg/m^3.

The idea behind the design of the setup is that the water cooler and all parts upstream of the decoupler plate do not influence the acoustics of the setup. This is caused by two effects. Firstly, without flow the decoupler plate and the CFD tube cause decoupling by the area contraction. This effect can

[1] The name Helmholtz mode is commonly used in the literature for modes in which different parts of the setup interact as volumes through a contraction. In this case, the plenum volume and the combustion chamber volume can interact through the burner contraction causing the plenum Helmholtz mode

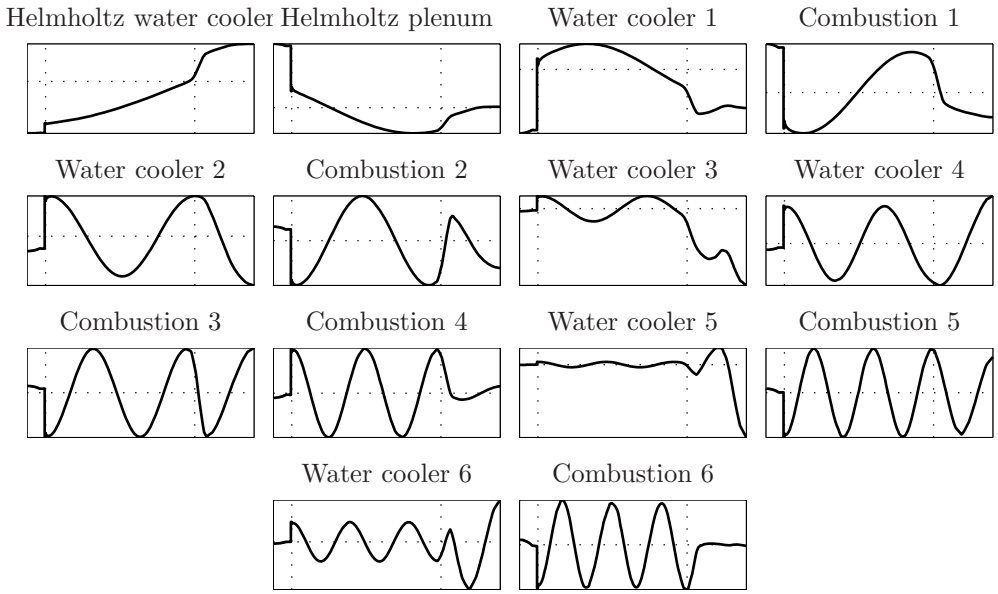

Figure 3.6: Pressure at the centerline of the test rig for different modes. The horizontal dotted line is zero, the vertical dotted lines are the start of the plenum and the water cooler.

be studied using stationary FEM models like those used here. A second effect is the high flow speed at the location of the decouplers, which causes extra decoupling [26]. This section only includes the first effect.

Several different configurations are compared. Firstly, only the combustion chamber has been modeled, between the burner outlet and the CFD decoupler tube (figure 3.7). A second model includes the plenum chamber and a third also some basic behavior of the component upstream of the decoupling flange of the plenum (upstream is left in figure 3.7). To evaluate the cooler influence, a model is made without the water cooler, but including all upstream geometry (the plenum and air supply, including the preheaters which are several meters in length).

The differences between the acoustic eigenfrequencies for the different models are depicted in figure 3.8. It had been already observed in the previous section that, in the low frequency range, Helmholtz-like modes arise. These modes only show up if the participating components are actually present in the model. Beside these global Helmholtz modes, almost all other modes can be attributed to a separate component, either the combustion chamber, the water cooler or the air supply system. The components outside this basic com-

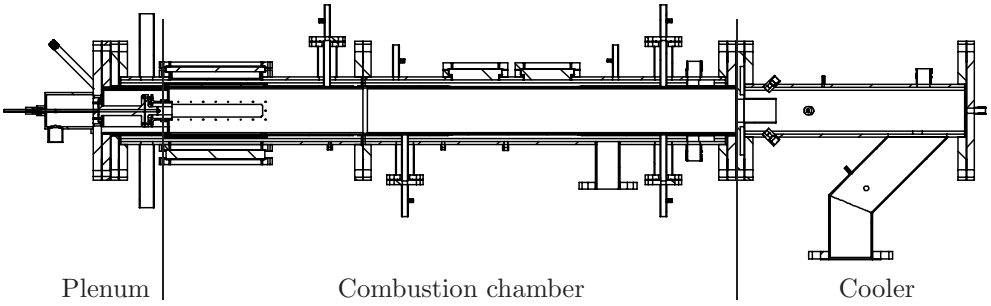

Figure 3.7: Cross section of the test rig.

ponent determine the exact boundary conditions and therefore influence the eigenfrequencies.

The most important modes are those of the combustion system itself. When the components upstream of the combustion chamber (plenum and air supply) and downstream (water cooler) are not included in the model, the eigenfrequencies of the system decrease (the triangles in figure 3.8). Figure 3.6 shows the first acoustic mode shape of the combustion chamber. A little more than half a sine wave is observed in the combustion chamber and therefore the frequency is a little higher than without plenum and water cooler, when exactly half a sine wave fits in. For the first acoustic mode the difference is almost 27 percent, but the difference obviously decreases rapidly when the mode number and frequency increase. For combustion chamber mode 4 and higher, the differences in eigenfrequencies have almost disappeared. Furthermore, it can be seen that the water cooler has the strongest influence on the eigenfrequency. The

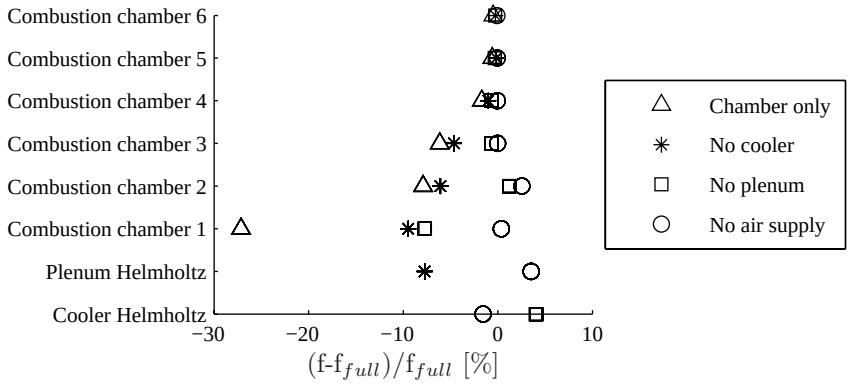

Figure 3.8: Acoustic eigenfrequencies, normalized with the full geometry calculation, when adding different components of the setup to the model.

changes due to the plenum (squares in figure 3.8) are less and the air supply upstream of the plenum (circles) hardly changes the frequencies. In conclusion, at lower mode shape numbers (up to the fourth) it is important to include the plenum and especially the water cooler to get an accurate prediction of the eigenfrequencies.

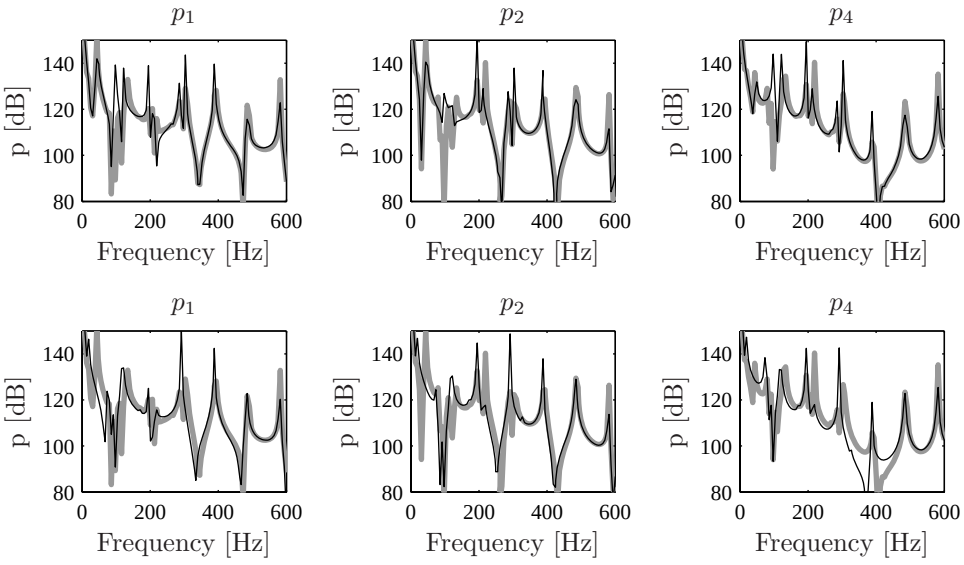

Figure 3.9: Comparison of the acoustic response at the pressure sensors in the combustion chamber for a full model (gray) and one without upstream geometry (black, top) and downstream geometry (black, bottom).

Figure 3.9 shows the acoustic response in the combustion chamber at sensors p_1, p_2 and p_4 to a volume source at the approximate flame location (in this case 10 centimeters from the burner outlet). In the top row the response of the full model is compared with a model without upstream acoustic geometry. It can be seen that the response remains largely the same above 300 Hz. Below 300 Hz there are significant differences, because the Helmholtz modes of the plenum and the water cooler are no longer present and the eigenfrequencies of the combustion chamber modes become inaccurate.

The bottom row of figure 3.9 shows the same comparison when leaving the downstream geometry (the water cooler) out. Again the response above 300 Hz is quite good, but there seems to be a large difference around 400 Hz at sensor p_4. The reason is that sensor p_4 is located near the end of the combustion chamber. When the water cooler geometry is removed, the local response here changes strongly, because the exact frequency at which the pressure node is at

the sensor location changes from just before to just after the eigenfrequency. This hardly influences the more global pressure response in the combustion chamber, as can be seen in the other two figures at the bottom row of figure 3.9.

As a conclusion, it can be said that the pressure response of the combustion chamber above 300 Hz can be predicted accurately with a model that only contains the combustion chamber. The rest of the geometry has to be included when calculating at lower frequencies. It should be noted that the results are for the cold case. When temperatures are higher, the frequency range in which the results are accurate moves upwards.

3.3.5 One-dimensional models

One-dimensional acoustic models are widely used in the field of the interaction between combustion and acoustics [25, 49]. The main reasons are that they are fast and easy to use and can be extended with phenomena like asymmetric sound propagation due to a mean flow (in which the speed of sound depends on the travel direction, upstream or downstream), inhomogeneous speed of sound due to temperature differences [93] and dissipation due to the mean flow [46, 47]. Furthermore, parts of the acoustic behavior of the combustion chamber are often one-dimensional for frequencies up to 500 Hz. In this section the theory behind one-dimensional acoustic models is introduced. In the following section a model of the test rig is developed.

The basic equation used in thermoacoustics, giving the relation between unsteady heat release and acoustic wave propagation (neglecting viscothermal effects [94]), was given in equation (3.3) and reads:

$$\frac{1}{c_0^2}\frac{\partial^2 p'}{\partial t^2} - \frac{\partial^2 p'}{\partial x_i^2} = \frac{\rho_0(\gamma-1)}{c_0^2}\frac{\partial^2 q'}{\partial t^2}\,. \tag{3.15}$$

In the special case of harmonic time dependence ($p' = \hat{p}e^{i\omega t}$) and using the previously introduced notation of $\hat{q}$ as the harmonic amplitude of the volume integrated heat release rate (equation (B.24)), this equation simplifies to the inhomogeneous Helmholtz equation:

$$k^2\hat{p} + \frac{\partial^2 \hat{p}}{\partial x_i^2} = \frac{\mathrm{i}\omega(\gamma-1)}{c_0^2}\hat{q}\,, \tag{3.16}$$

in which $k = \omega/c_0$ is the wavenumber. If one of the dimensions of the setup is much larger than the other two, a frequency range exists in which the acoustic behavior of the setup can be described accurately with a one-dimensional

model. The highest frequency for which this occurs is called the cut-off frequency f_c, which is the frequency of the first transverse resonance if the tube is square [83], given by:

$$f_c = \frac{c_0}{2d}\,, \tag{3.17}$$

in which d is the cross-sectional dimension of the tube. Equation (3.16) then reduces to:

$$k^2\hat{p} + \frac{\partial^2\hat{p}}{\partial x^2} = k^2\rho_0(\gamma-1)\hat{q}\,, \tag{3.18}$$

in which x is the axial coordinate. Without external sources, the homogeneous wave equation remains and it has a solution of the form:

$$\hat{p} = p_A e^{\mathrm{i}kx} + p_B e^{-\mathrm{i}kx}\,, \tag{3.19}$$

in which p_A and p_B are the amplitudes of the waves traveling in the positive and negative direction (figure 3.10). The acoustic particle velocity is given by

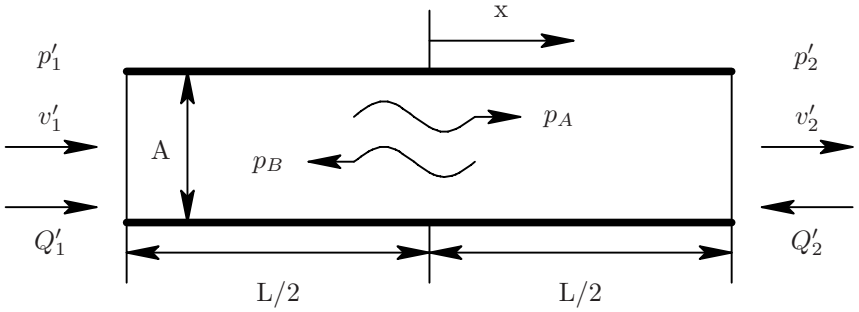

Figure 3.10: Schematic drawing of one-dimensional wave propagation in a tube.

the relation of Euler:

$$\hat{v} = \frac{\mathrm{i}}{\omega\rho_0}\frac{\partial\hat{p}}{\partial x}\,. \tag{3.20}$$

From equation (3.19) it follows that:

$$\hat{v} = -\frac{1}{\rho_0 c_0}\left(p_A e^{\mathrm{i}kx} - p_B e^{-\mathrm{i}kx}\right)\,. \tag{3.21}$$

For one-dimensional wave propagation in a tube, the pressure and acoustic particle velocity at location x are now known as functions of p_A and p_B. The basic idea of the so-called transfer matrix formulation (TMF) is to couple one-dimensional tube elements of finite dimensions, to obtain a larger model [27]. Volume sources can be added at the tubes' interfaces.

A relation between the pressure and acoustic particle velocity at nodes 1 and 2 of a tube of length L (figure 3.10) can be derived using equations (3.19) and (3.21) as:

$$\begin{Bmatrix} \hat{v}_1 \\ \hat{v}_2 \end{Bmatrix} = \frac{1}{c_0 \rho_0 \sinh(\mathrm{i}kL)} \begin{bmatrix} \cosh(\mathrm{i}kL) & -1 \\ 1 & -\cosh(\mathrm{i}kL) \end{bmatrix} \begin{Bmatrix} \hat{p}_1 \\ \hat{p}_2 \end{Bmatrix} . \tag{3.22}$$

To allow coupling of tubes with different cross-sectional areas, it is beneficial to write these equations in terms of the mass flow, given by:

$$\begin{Bmatrix} \hat{Q}_1 \\ \hat{Q}_2 \end{Bmatrix} = A\rho_0 \begin{Bmatrix} \hat{v}_1 \\ -\hat{v}_2 \end{Bmatrix} , \tag{3.23}$$

in which A is the cross-sectional area of the tube and $\hat{Q}_i$ is the mass flux on node i. Using this expression gives:

$$\begin{Bmatrix} \hat{Q}_1 \\ \hat{Q}_2 \end{Bmatrix} = \frac{A}{c_0 \sinh(\mathrm{i}kL)} \begin{bmatrix} \cosh(\mathrm{i}kL) & -1 \\ -1 & \cosh(\mathrm{i}kL) \end{bmatrix} \begin{Bmatrix} \hat{p}_1 \\ \hat{p}_2 \end{Bmatrix} . \tag{3.24}$$

The mass flux $\hat{Q}_i$ is related to the volume flow rate Q used in the finite element model (section 3.2.2) by:

$$\hat{Q}_i = \frac{\rho_0}{\mathrm{i}\omega} Q \, . \tag{3.25}$$

It is now possible to couple tubes with different properties and obtain a transfer matrix formulation for the acoustic response of the system, because the pressure on a node should be the same irrespective of the element and the total mass flux should be zero. This leads to a system that, when solved, gives the (complex) nodal pressures. The pressure at any other location in the system can be calculated with equation (3.19) by evaluation of the nodal pressures p_1 and p_2:

$$p_A = \frac{\hat{p}_2 e^{-\frac{ikL}{2}} - \hat{p}_1 e^{-\frac{3ikL}{2}}}{1 - e^{-2ikL}} , \tag{3.26a}$$

$$p_B = \frac{\hat{p}_1 e^{-\frac{ikL}{2}} - \hat{p}_2 e^{-\frac{3ikL}{2}}}{1 - e^{-2ikL}} . \tag{3.26b}$$

When these pressure amplitudes are substituted back into equation (3.19), the pressure as a function of position x is found:

$$\hat{p} = \frac{\hat{p}_1 + \hat{p}_2}{2\cos\left(\frac{kL}{2}\right)} \cos(kx) - \frac{\hat{p}_1 - \hat{p}_2}{2\sin\left(\frac{kL}{2}\right)} \sin(kx) \, . \tag{3.27}$$

Because the pressure is assumed constant in the other directions (y and z) this suffices to calculate the acoustic pressure in the setup.

3.3.6 One-dimensional model of the test rig

A schematic representation of the one-dimensional model of the test rig is depicted in figure 3.11. The inlet (node 1) is located at the upstream acoustic decoupler and is assumed to be acoustically hard (which means that all acoustic waves are reflected). The finite element results in section 3.3.4 showed that results are accurate with this assumption. The outlet is located at the throttle valve (node 21), which is also assumed to be acoustically hard. The sidetubes are perfect semi-infinite tubes, meaning that they have full absorption at the end (the prescribed dimensionless impedance is one at nodes 15, 17 and 19). The burner is simplified to two tubes, representing the swirler and the swirl tube where the fuel injection takes place. Two other side-branches are present at the water cooler, which represent the excitation tube and the part of the water cooler downstream of the sidetube leading to the throttle valve.

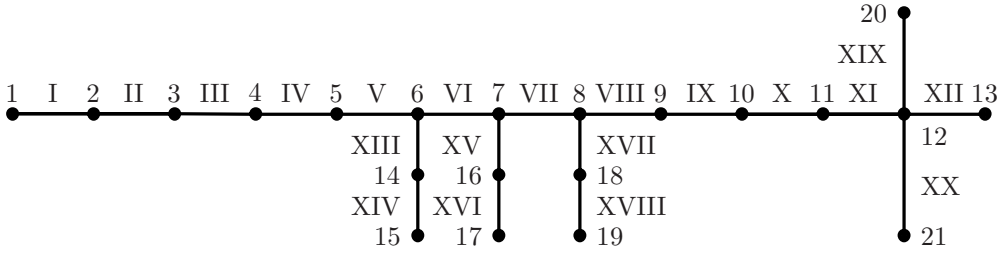

I	Plenum
II	Swirler
II	Swirl tube
IV to VIII	Combustion chamber
IX	CFD tube
X to XII	Water cooler
XIII to XVIII	Sidetubes
XIX	Excitation tube
XX	Exit tube

1	p_8
5	Flame
12	p_7
14	p_1
16	p_2
18	p_3/p_4
20	Acoustic excitation plug
21	Throttle valve 11

Figure 3.11: One-dimensional model of the full setup.

3.3.7 Comparison of one- and three-dimensional model

In the previous sections two different types of models were constructed, the analytical one-dimensional TMF model and the three-dimensional finite element model. In this section the results of these two models are compared. The calculations are done for the case without flow, at a temperature of 300 K, which gives, with a ratio of specific heats γ of 1.4 and a gas constant R of

287 J/kgK, a speed of sound c_0 of 347 m/s. Figure 3.12 shows the acoustic response to a volume source located at the flame position.

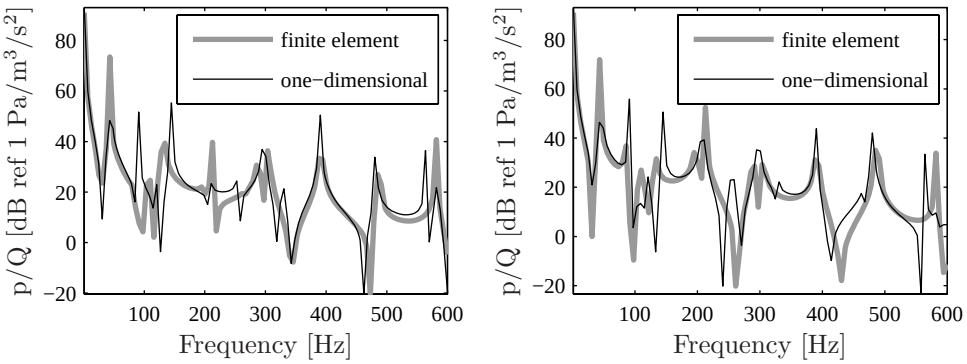

Figure 3.12: Acoustic response at the location of sensor p_1 (left) and p_2 (right) to a volume source.

It can be seen that for the most important modes, i.e. those of the combustion chamber, the results match well between the two models. Furthermore, if the local distortions near the up and downstream components are disregarded, the response shape is also similar. This is, of course, a direct consequence of the highly one-dimensional nature of the combustion chamber.

3.3.8 Influence of temperature on acoustic behavior

Temperature has a very direct influence on the acoustic properties, because the speed of sound is a function of temperature as $c_0 = \sqrt{\gamma RT}$ and density as $\rho_0 = p_0/RT$. It is therefore important to include temperature effects in the model. Several approaches found in the literature are first given.

Literature review

The influence of temperature on the acoustic properties in a combustion chamber was studied by several people. Kim [52] used a variational principle to investigate the effects, drawing general conclusions about the possible influence of temperature. To include temperature effects in a model, several different approaches are found. A first method is to divide the setup in two parts, a cold part upstream and a hot part downstream of the burner [9]. This method is often used in combination with one-dimensional models, because these do not allow for three-dimensional detail. As a refinement, a temperature gradient can be used over the length of the combustion chamber to account for heat losses

and cooling. When using the finite element method, a more detailed temperature field can be used (see for instance figure 3.2). This temperature field can be obtained using a reacting flow CFD calculation [31, 72]. Fannin [31] and Nowak [72] both use a finite element approach. Nowak splits the fluid in two regions, upstream of the flame front, where the gas is cold, and downstream, where it is hot. It depends on the test rig whether this approach works well. When there is little heat loss of the hot gasses before they leave the combustor, this approach works well. This is caused by the fact that the flame front, which is the zone in which fuel combusts with air to form the combustion products, is very thin, which means that the temperature almost instantly jumps from low to high. Appendix A contains a basic calculation of the flame temperature for combustion of methane with air. The result of this calculation can be used to approximate the temperature of the hot region. However, in the test rig used in this project, the combustion chamber is very long compared with the size of the flame (chapter 2) and the gasses are cooled substantially by the relatively cold liner walls before the flue gasses leave the combustion chamber. Although this is not truly similar to an industrial combustor, this has to be taken into account to obtain accurate predictions of the acoustic behavior of the test rig. Fannin uses four temperature regions to account for such temperature differences in the combustion chamber. In this thesis a similar approach is used, in which temperatures from a CFD calculation of the DESIRE test rig [50] are transfered to the finite element model, but the temperature, density and speed of sound are determined for every node in the mesh by interpolating the CFD data onto the finite element mesh. The finite element code used then uses these nodal data in building the system matrices. It should be noted that the temperature field is assumed to be stationary. When combustion instabilities occur, the heat release may become a very strong function of time and space, which results in a transient temperature field. Because this thesis deals only with linear theory and the onset of instability, this does not have to be included.

Temperature fields from CFD

The temperature data used in this section are taken from the RaNS CFD model (section 3.2.4) for case 15.7 (table 3.1). A cross section of the CFD temperature field is shown in figure 3.13 with a zoom around the burner exit in figure 3.14. The maximum temperature found using CFD is 1680 K. The difference with the estimate made in appendix A of 1808 K is mainly caused by heat losses, which are included in the CFD model. Figure 3.13 also clearly shows the thermal gradient in the combustion chamber, giving an exit temperature in

the region of 1200 K. Figure 3.14 shows that the thermal gradient is very steep and well-defined areas with different temperatures appear, such as the inner and outer recirculation zones, the zone after the flame and the zones with unburned mixture.

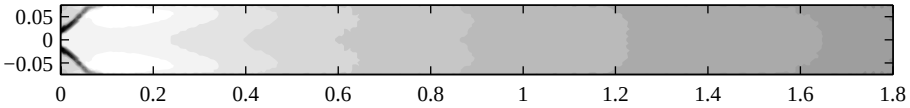

Figure 3.13: Temperature field from CFD calculation in the entire combustion chamber. The discrete gray levels are only for visualization.

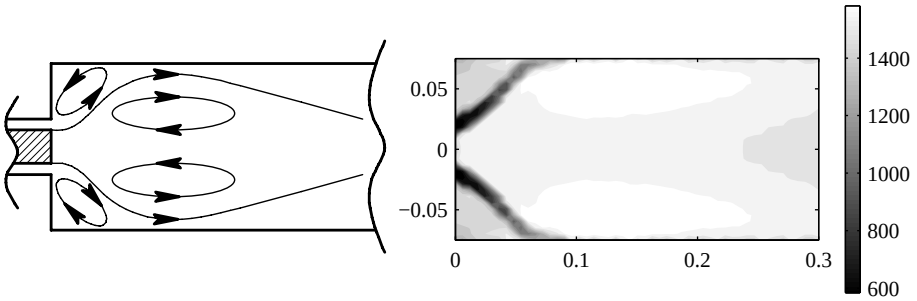

Figure 3.14: Schematic flow pattern (left) and temperature field [K] from a CFD calculation (right) in the flame region.

The mesh size of the CFD model is prescribed by the smallest flow details to be resolved, where the acoustic mesh size is prescribed by the geometry and the smallest acoustic wavelength to be solved. The acoustic mesh is much coarser than the CFD mesh, because the mixing of fuel and air as well as the combustion process require high spatial detail. The temperature data of the CFD mesh are therefore interpolated on the acoustic mesh. A Delaunay triangulation is first made of the nodes from the CFD mesh. This makes a set of tetrahedral elements from the given nodes, in which no datapoints are contained in each tetrahedral. These tetrahedral elements are subsequently used to find the point in the CFD mesh nearest to the node in the FEM mesh, from which the temperature is taken. Because the CFD mesh is much finer than the FEM mesh, especially in regions of high thermal gradients, a more accurate interpolation is not needed.

Now the temperatures of the nodes in the acoustic mesh are known, there are several methods to include this in the model. As said previously, a division in 2 or 4 regions has been made in the literature. Moreover, in the code used

in this thesis, the temperature of each element individually can be included in the model as the average of the temperature of the nodes. To evaluate these different strategies, results are obtained for all three.

For the division in temperature zones, the temperature ranges of these zones should be defined. Dividing in two regions is straightforward, because there is a very sharp temperature increase in the flame zone. An element has either the inlet temperature (573 K in this case) or the maximum temperature in the CFD result (1680 K). The division is made at the average temperature of the two (1127 K). For the division in 4 regions, it is not good to equally split the region between the minimum and maximum temperature in 4 sections, because the temperature increases almost instantly to the maximum temperature at the flame front and then goes down slowly over the length of the combustion chamber, but evidently not to temperatures as low as the inlet temperature. Of the four levels the first is therefore taken as the inlet temperature and the other three between the maximum temperature and the temperature at the outlet (1200 K), which gives the following ranges:

$$
\begin{array}{llll}
\text{T=573} & \text{for} & & \text{T} < 1200\ \text{K} \\
\text{T=1280} & \text{for} & 1200\ \text{K} < & \text{T} < 1360\ \text{K} \\
\text{T=1440} & \text{for} & 1360\ \text{K} < & \text{T} < 1520\ \text{K} \\
\text{T=1600} & \text{for} & & \text{T} > 1520\ \text{K}
\end{array}
$$

The resulting temperature fields for the different CFD divisions are shown in figure 3.15.

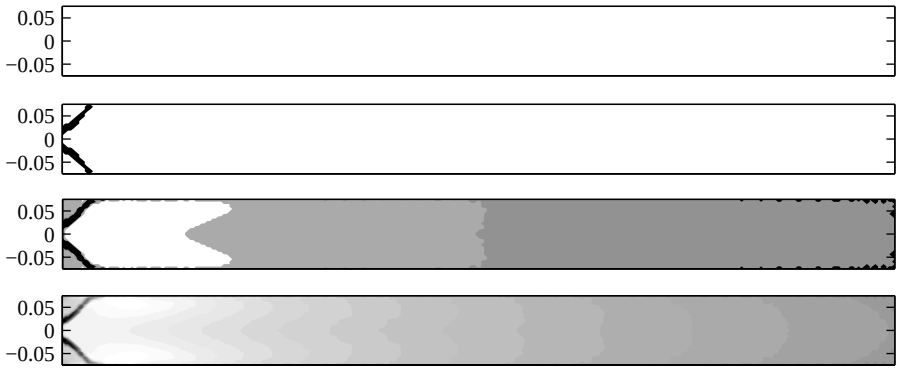

(d) Full temperature field, levels only for visualization.

Figure 3.15: Temperature field divisions for use in FEM.

To compare the different strategies, the eigenfrequencies of the acoustic finite element model (section 3.3.2) are listed in table 3.3. For brevity, the

acoustic modes of the combustion chamber are now numbered, so combustion 1 becomes $(100)_a$. It is evident that temperature should be taken into account; the eigenfrequencies using the cold data at 573 K are 50% wrong. The differences between using one or two regions are quite small. The second region only includes a small zone where the cold, swirling combustion gasses enter the combustion chamber. It should be noted that in the model with one region, the plenum is still kept at the inlet temperature and the maximum temperature from the CFD model is used as temperature. Using for regions substantially lowers the eigenfrequencies, because large zones downstream of the flame front are now kept at a lower temperature. The differences between the four zone approach and including the full temperature field are approximately 2.5 percent, which is reasonable.

Mode	Cold	Full	4 Regions	2 Regions	1 Region
$(100)_a$	178.0	257.9	248.2	281.1	286.36
$(200)_a$	295.3	436.0	404.9	481.5	495.78
$(300)_a$	419.6	626.9	607.4	695.8	709.84
$(400)_a$	541.4	818.4	797.8	914.6	917.23
$(500)_a$	672.2	1017.4	991.7	1139.0	1142.5

Table 3.3: Numerically calculated acoustic eigenfrequencies of the combustion system using different temperature distribution methods.

3.3.9 Burner impedance

An important property that is used in the analysis of thermoacoustic stability is the so-called burner impedance [57], which is defined as:

$$Z = \left(\frac{\hat{p}}{\hat{v}}\right)_B , \tag{3.28}$$

in which $()_B$ stands for the location of the burner outlet. It is preferable to have a high burner impedance, because high pressure amplitudes will then lead to only minor velocity perturbations on the burner outlet. In the previous chapter it was discussed that the flame as an active acoustic source becomes stronger when the acoustic particle velocity at the burner outlet increases. Therefore, a high burner impedance will make the gain in the thermoacoustic feedback loop lower and improve the stability of the combustion system (see also chapter 5). Because the source is downstream of the burner, the burner impedance as seen from the combustion chamber is used.

Two different methods for calculating the burner impedance are presented. The first is the so-called direct method using calculated pressure and velocity perturbations on the burner outlet and the second is the indirect method using the two microphone method applied to the numerical model. After the two methods have been described, the results of both methods are discussed.

Direct impedance calculation

The burner impedance can be predicted using finite element calculations. The variable solved in the finite element formulation is the pressure. The acoustic particle velocity can be calculated using the Helmholtz equation:

$$-\rho_0 \mathrm{i}\omega \hat{v}_i = \frac{\partial \hat{p}}{\partial x_i}\,, \tag{3.29}$$

in which $\hat{v}_i$ is the amplitude of the acoustic particle velocity in direction i. For the linear, isoparametric, tetrahedral elements used in this thesis this results in:

$$\begin{Bmatrix} \frac{\partial \hat{p}}{\partial x_1} \\ \frac{\partial \hat{p}}{\partial x_2} \\ \frac{\partial \hat{p}}{\partial x_3} \end{Bmatrix} = \left[\begin{bmatrix} -1 & 1 & 0 & 0 \\ -1 & 0 & 1 & 0 \\ -1 & 0 & 0 & 1 \end{bmatrix} \cdot \begin{bmatrix} x_1^{(1)} & x_2^{(1)} & x_3^{(1)} \\ x_1^{(2)} & x_2^{(2)} & x_3^{(2)} \\ x_1^{(3)} & x_2^{(3)} & x_3^{(3)} \\ x_1^{(4)} & x_2^{(4)} & x_3^{(4)} \end{bmatrix} \right]^{-1} \begin{bmatrix} -1 & 1 & 0 & 0 \\ -1 & 0 & 1 & 0 \\ -1 & 0 & 0 & 1 \end{bmatrix} \begin{Bmatrix} \hat{p}^{(1)} \\ \hat{p}^{(2)} \\ \hat{p}^{(3)} \\ \hat{p}^{(4)} \end{Bmatrix}, \tag{3.30}$$

in which $\hat{p}^{(i)}$ is the amplitude of the acoustic pressure at node i and $x^{(i)}$ is the coordinate of node i. The derivation of this relation can be found in appendix C. It can be seen that the pressure gradient is independent of the location in the element, which is because it is a linear element. To obtain the acoustic particle velocity on the burner exit plane, the velocity perpendicular to that plane is calculated on the nodes of the elements, using the average from the adjacent elements. Because the differences in acoustic particle velocity are not very large, further weighing for the size of the elements was not applied.

Indirect impedance calculation

A second method that is widely used to either calculate or measure impedances is the so-called two microphone method. It is based on measuring pressure at two locations. When the pressure field can be taken as one-dimensional, there is no damping and there are no sources between the sensors and the burner plane, the burner impedance can be calculated from [17]:

$$\zeta_B = \mathrm{i}\frac{H_{12}\sin(kl_b) - \sin(k[l_b - l_s])}{\cos(k[l_b - l_s]) - H_{12}\cos(kl_b)}\,, \tag{3.31}$$

in which ζ_B is the dimensionless impedance at the burner outlet, H_{12} is the transfer function from sensor p_1 to sensor p_2, l_b is the distance from sensor p_1 to the burner outlet and l_s is the distance between the sensors (figure 3.16). A condition that should be satisfied is that the distance between the sensors is less than half the acoustic wavelength and also that they are not too close together with respect to the acoustic wavelength. This is expressed by [90]:

$$0.1\pi < kl_s < 0.8\pi\,. \tag{3.32}$$

The pressure at the sensor locations can be measured in an experimental setup, for instance in an impedance tube [18], but it can also be taken from a numerical calculation, which is done here.

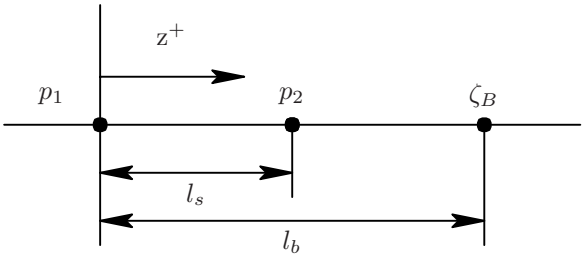

Figure 3.16: Symbols used for the indirect impedance calculation.

Calculation and results

The burner impedance is not a property of the burner alone, but of the entire acoustic system upstream of the burner. When the burner impedance is therefore calculated from a numerical model, the relevant parts of the geometry upstream of the burner should be included. In this section, the finite element model including the plenum is therefore used to perform a harmonic analysis for a range of frequencies between 20 and 500 Hz. The model is excited at the acoustic excitation plug in the water cooler (see chapter 2 and figure 3.11). For the indirect burner impedance calculation, the pressure at the locations is used where the sensors are also located in the test rig. For the low frequencies sensors p_1 and p_3 are used (which are 1.07 meter apart, giving an accurate frequency range from 16 to 128 Hz) and for the higher frequencies sensors p_1 and p_2 are used (which are 0.248 meter apart, giving an accurate frequency range from 69 to 554 Hz). In the overlapping region they are both used and give the same result. The burner impedance is also calculated using the one-dimensional model from section 3.3.6. The results are depicted in figure 3.17,

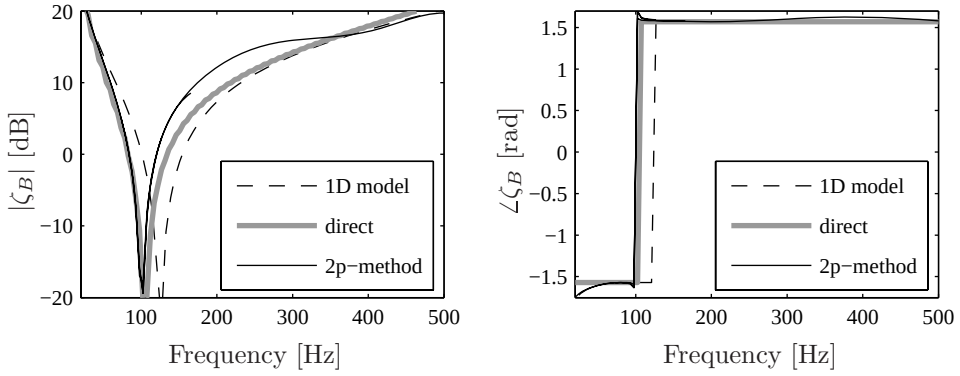

Figure 3.17: Dimensionless burner impedance amplitude (left) and phase (right).

which shows the impedance at the burner outlet. The impedance at very low frequencies is very high. In the low frequency limit, any pressure increase will only generate a very small velocity in the burner, because the plenum has a finite volume and therefore only a limited amount of air can be added to it. This explains the high start and rapid roll-off in the low frequency region. The burner impedance is minimal around 100 Hz. The burner impedance only depends on the upstream geometry. Due to this geometry, which consists of a 'neck' (the burner passage, cross section A in figure 3.18) and a volume (the plenum, V in figure 3.18), the first interesting frequency can be expected to approximate the Helmholtz frequency of this system, given by:

$$f = \frac{c_0}{2\pi}\sqrt{\frac{A}{LV}}\,, \tag{3.33}$$

in which A is the cross-sectional area of the neck, L is the length of the neck and V is the volume (figure 3.18). For the burner plenum configuration of the test rig, the approximate dimensions are listed in the same figure. The Helmholtz frequency of the plenum and burner configuration becomes approximately 95 Hz, which is very close to the 100 Hz where minimum impedance is found. After 100 Hz the burner impedance increases monotonically. This is because the plenum has no acoustic resonances in the frequency range below 500 Hz other than the Helmholtz frequency. Therefore, the impedance is still increasing towards the first resonance of only the plenum.

Besides the burner impedance, the transfer from acoustic waves to the acoustic cavities upstream of the burner can be important. If the air flow upstream of the burner becomes perturbed, the equivalence ratio of the mix-

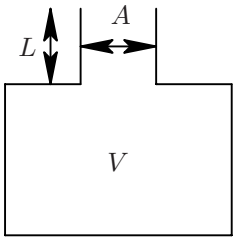

Symbol	Value
c_0	343 m/s
A	1473 mm^2
L	100 mm
V	4.6·10^6 mm^3
f	95.5 Hz

Figure 3.18: Helmholtz resonator and the approximated parameters for the plenum and burner configuration.

ture coming to the flame front changes (assuming a stationary fuel flow, for instance because the fuel supply is choked). This leads to heat release perturbations, which give rise to new acoustic waves, generating a potentially unstable thermoacoustic feedback loop [64]. This is essentially determined by the impedance of the air supply. Figure 3.19 shows the impedance for a tube of 1 meter mounted upstream of the acoustic decoupler when there is no flow, determined with the one-dimensional model. This tube represents the geometry upstream of the plenum.

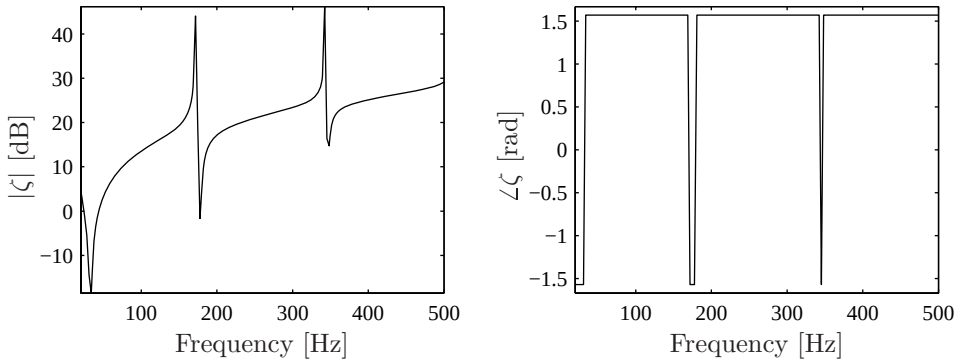

Figure 3.19: Dimensionless impedance of the schematic geometry upstream of the plenum.

At very low frequencies, there is a sharp dip in the impedance, which is caused by a Helmholtz-like mode between plenum and air supply. After this, the impedance is always high, except very near eigenfrequencies of the air supply system. These sharp peaks are in practice flattened by damping effects and therefore their influence is small. This is caused by the acoustic decoupler between the plenum and the other upstream air supply components. This high impedance is the reason why the acoustic response of the system with and

without the air supply is very similar (section 3.3.4).

As a conclusion it can be said that the air supply is only susceptible to perturbations at low frequencies. The supply of mixture to the flame front is easily perturbed around 100 Hz, after which susceptibility to perturbation becomes lower.

3.4 Acoustic pressure measurements

3.4.1 Introduction

In the experimental setup, acoustic pressure perturbations in the combustion chamber are measured. It is possible to do this directly using water cooled pressure transducers that can withstand the high static pressure, but this has substantial disadvantages, most notably the high costs and limited measurement accuracy of such sensors. A method to avoid the temperature problem is to use small tubes that are attached to the combustion chamber. Some distance away from the hot combustion chamber, where temperatures are substantially lower, the pressure transducer is mounted flush to the wall of these small tubes. This construction is called a sidetube in this thesis and is described in section 3.4.2. To diminish the static pressure difference over the sensor, a steady pressure at the back side of the sensor is used. The way in which this is achieved is described in section 3.4.3. When using these two techniques, temperatures are much lower and no high static pressure difference exists over the sensor and therefore, cheaper and more sensitive sensors can be used.

3.4.2 Semi-infinite tubes

The standard method to mount a pressure transducer, flush with the wall of the combustion chamber, is shown schematically in figure 3.20(a). For the measurements described in this thesis, a sidetube construction was used. In the literature, several methods can be found to construct such a sidetube [32].

The most basic one is to mount a microphone at the end of the tube (figure 3.20(b)), but this may induce strong resonances in the sidetube if the first eigenfrequency of the tube lies in or near the measurement range. For the DESIRE setup, the sidetube has to go through the cooling passage first and therefore the length is always such that the first acoustic resonance lies in the measurement range, which is up to 500 Hz. This resonance can be avoided by filling the sidetube with isolation material, but this also lowers the signal level substantially and it introduces uncertainties in the transfer function

from the inlet to the microphone, making accurate calibration and constant measurement conditions necessary [35].

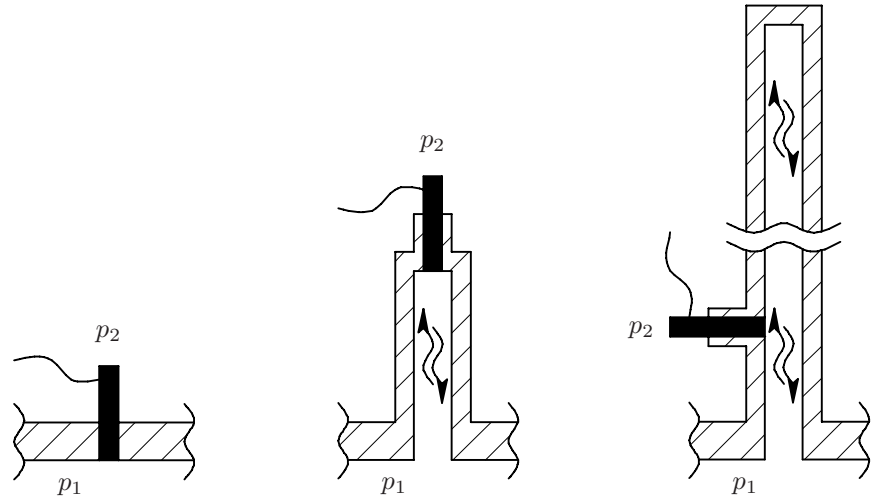

(a) Flush with the wall. (b) Sidetube. (c) Semi-infinite tube.

Figure 3.20: Schematic drawings of pressure pickup mounting configurations.

A second method consists of moving the pressure sensor flush to the wall of the sidetube and providing a long tube at the end of the sidetube (figure 3.20(c)). A drawback of this concept is that resonance may occur in the sidetube, which means that both the amplitude and the phase of the pressure at the location of the sensor differs from the values at the inlet of the tube, where pressure information is desired. The pressure at the inlet can be reconstructed by inverting the transfer from the pressure at the inlet of the tube to the pressure at the location of the sensor, but this is no trivial matter due to the unknown temperature gradient in the sidetube. Several solutions to this problem exist.

A first solution is to use a very long tube with a closed end. Because the tube is closed, there is no flow of hot gasses into the tube, and therefore only the first part of the tube is hot. The setup is calibrated without combustion, measuring the transfer function from the inlet of the tube (p_1 in figure 3.20) to the sensor (p_2). Using the inverse of this transfer function makes it possible to reconstruct the pressure at the inlet of the sidetube. A disadvantage of this method is that this transfer function should remain the same during an experiment, which generally is not the case. The speed of sound in the tube, for instance, may change because the room in which the setup is located heats

up. This is the case for the setup used in this thesis, because the preheaters and test rig have substantial heat loss to the relatively small surrounding room. A second disadvantage is that a pressure sensor has to be placed at the inlet of the sidetube, so access to this location needs to be available.

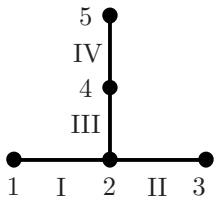

Number	Description
1	Prescribed pressure
2	Connection to the sidetube
3	Hard end
4	Sensor location
5	Anechoic end

Figure 3.21: One-dimensional model for the infinite tube test.

A second solution to overcome the resonance problem is to eliminate all acoustic reflections from the end of the sidetube. This can be done by adding acoustic absorption material at this end, because then there is only a wave traveling inwards in the tube. The pressure measured by the sensor therefore has the same amplitude as the signal at the entrance of the tube and a phase given by a constant time delay. To illustrate this, the one-dimensional model shown in figure 3.21 is used. A 1.25 meter tube is modeled with a prescribed pressure of 1 Pa at one side and a perfectly anechoic sidetube at a distance of 0.6 meter from the excitation end. The sensor is located at a distance of 208 mm in the sidetube. The results in figure 3.22 show that the only difference between a sensor flush with the wall (the pressure at the inlet of the sidetube or node 2) and the one in the sidetube (node 4) is a constant time delay.

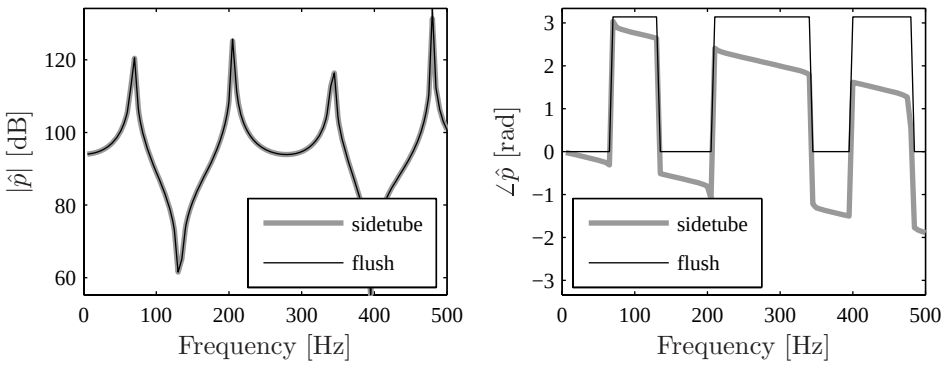

Figure 3.22: Calculated amplitude and phase for a sensor flush with the wall and one in a perfectly anechoic sidetube.

The semi-infinite tube is constructed by connecting a copper tube to several meters of hose. The copper tube is filled with absorbing material. To test the performance of this absorption system, a small setup is used in which an acoustic source (a speaker in a box) is placed at the inlet of the semi-infinite tube (figure 3.23). The pressure signal is measured at approximately the same location in the semi-infinite tube as in the test rig.

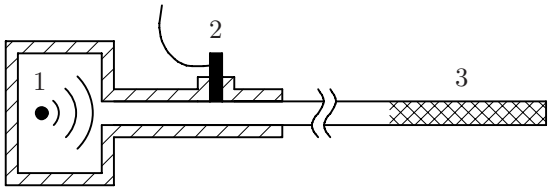

No.	Description
1	Acoustic source
2	Pressure transducer
3	Absorption material

Figure 3.23: Experimental setup to validate the working of the absorption material.

Figure 3.24(a) shows the signal that is measured when a white noise signal is fed to the acoustic source. It can be seen that adding the absorption material at the end of the tube decreases the amplitude of the oscillations to a level below 2 dB. The roll off at higher frequencies is caused by the characteristics of the source.

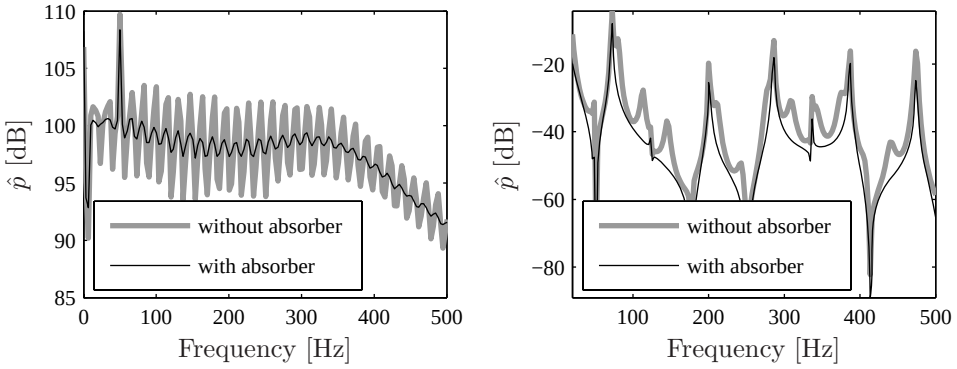

(a) Experimentally determined response of a simplified setup.

(b) Numerically determined response of the full setup.

Figure 3.24: Effect of an acoustic absorber at the end of the semi-infinite tube.

Figure 3.24(b) shows a numerical result of what can be expected when acoustic absorbers at the end of the semi-infinite tubes are not used in the full setup. The calculations were done using the one-dimensional model, excited by

a prescribed pressure at the end of the first semi-infinite tube (section 3.3.6). The transfer to the pressure sensor in the second semi-infinite tube is plotted with acoustically hard and with anechoic boundaries on the end of the semi-infinite tube. It can be seen clearly that the acoustically hard end causes many resonances which hide the desired signal.

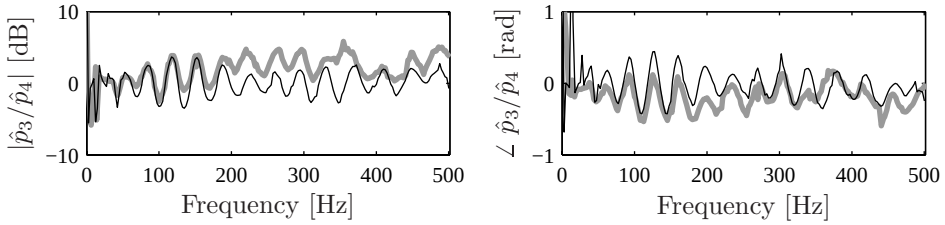

(a) Measured amplitude (gray during combustion, black cold).

(b) Measured phase (gray during combustion, black cold).

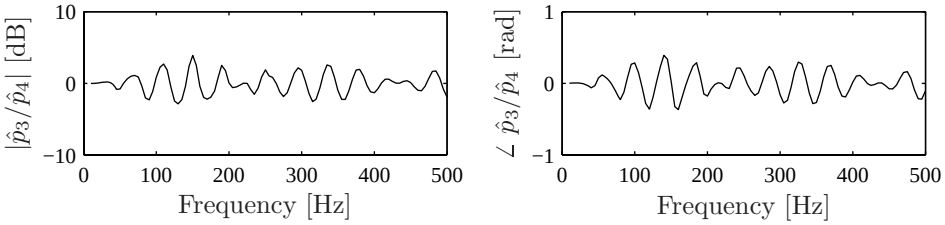

(c) Calculated amplitude.

(d) Calculated phase.

Figure 3.25: Amplitude and phase between the signals measured by sensors p_3 and p_4 in the test rig due to acoustic excitation. The sensors are opposite to each other and should therefore give the same signal.

A further check for the effect of the semi-infinite tubes is the comparison between the signals from pressure sensor p_3 and p_4 in the test rig. These are located on opposite sides of the rig and should therefore, if the pressure field is indeed one-dimensional, give the same signal. The transfer function should thus have an amplitude of 0 dB and a phase of 0 degrees. The transfer function that is measured using acoustic excitation in the water cooler is depicted in figure 3.25. It can be seen that there is quite some difference between the signals, with amplitude differences of 3 dB and phase differences of 0.4 radians. The differences are caused by the imperfect anechoic end conditions. Figures 3.25(c) and 3.25(d) show the calculated transfer functions using the same model as for figures 3.22. Two sensors with two semi-infinite tubes are now used, which have lengths 3.63 and 4.43 meters, the same as the lengths on the test rig. The end

condition describing the absorption material is now not full absorption, but an absorption coefficient of 0.65 below 250 Hz and 0.85 above (these values are assumed because the absorption material is known to absorb better at higher frequencies). A transfer function that is very similar to the measured one is now found. This proves that the imperfect absorption at the end of the semi-infinite tube results in measurement errors of up to 0.4 radians in phase and 3 dB in amplitude.

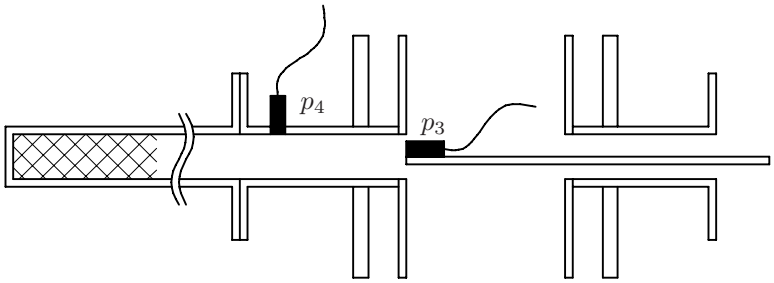

Figure 3.26: Schematic drawing of the semi-infinite tube influence measurement.

Another measurement was made on the test rig with a pressure sensor at the inlet of the sidetube of pressure sensor p_3, which was placed there through the sidetube of pressure sensor p_4 (figure 3.26). The amplitude and phase of the transfer function from the inlet to the normal sensor location (p_4) are shown in figure 3.27. The amplitude again shows the imperfect anechoic end condition, giving measurement errors up to 2 dB. The phase plot shows a continually declining phase caused by the distance between the inlet and pressure sensor p_3. The phase difference of 2.0 radians at 500 Hz corresponds to the time delay caused by the distance between the inlet and the sensor, which is 212 mm. The imperfect end condition again leads to additional phase errors. The errors can be corrected, because they are now known for this sensor. There are two problems though. Firstly, similar measurements are difficult to make for the other pressure sensors, because there is no easy way to locate a pressure sensor at the inlet of the sidetubes. Secondly, the transfer is measured in a cold state. When the setup is fired, the first part of the sidetube will have a different temperature profile, thereby changing the transfer, especially the phase of this transfer function.

Figure 3.28 shows the measured transfer function from sensor p_1 in the test rig to the pressure measured at the inlet of the sidetube going to sensor p_4 and the pressure measured by the sensor in the sidetube. It can be seen that the remaining resonances in the sidetube due to the imperfect end condition have

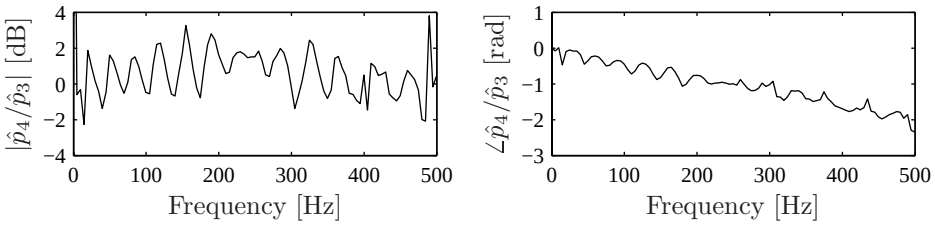

Figure 3.27: Measured transfer from the inlet of the sidetube to the sensor location.

little influence on both the phase and amplitude of this transfer function.

The sidetubes are also implemented in the finite element model of the full rig. The semi-infinite tube is modeled by imposing full absorption at the end of the tube. This is done in ANSYS by adding a term to the acoustic wave equation as:

$$\frac{1}{c_0^2}\frac{\partial^2 p'}{\partial t^2} + \left[\frac{r}{\rho_0 c_0}\right]\frac{1}{c_0}\frac{\partial p'}{\partial t} - \nabla^2 p' = 0\,, \tag{3.34}$$

in which r is called the characteristic impedance. This modified equation is used for the elements at the end of the sidetubes. A value of one is imposed for r, giving no reflections.

3.4.3 Back pressure facility

As mentioned previously, two problems have to be solved when using low cost pressure transducers in a high temperature and high pressure combustion setup. A solution for the first, the high temperatures, was discussed in the previous section. The second, high pressures, can be solved by using a back pressure system.

The Kulite pressure sensors (figure 3.29) measure the dynamic pressure

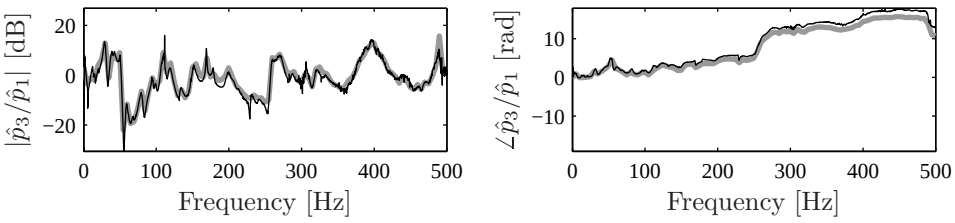

Figure 3.28: Transfer from sensor p_1 to sensor p_3 (gray) and to the inlet of the sidetube of p_3 (black).

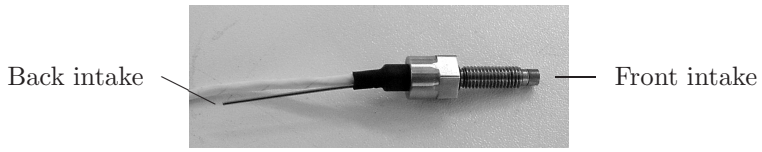

Figure 3.29: Photograph of the Kulite XCS-190M sensor, showing the front and back intake.

difference between the front and back intake of the sensor. In a pressurized setup, the mean pressure at the front intake is above atmospheric and therefore the mean pressure at the back intake should be equally high. This can be done by also connecting the back intake to the pressurized setup. A requirement is then that the pressure at the back intake no longer contains fast dynamic components, because these would generate noise on the signal measured at the front. The back intake is connected to the setup itself, because the static pressure should be the same. This means that all dynamic components should be removed between the intake point on the setup and the back intake of the Kulite sensor.

Two mechanisms are applied to achieve this. Firstly, a long thin hose is used as a connection between the setup and the back intake, which causes viscothermal losses. Secondly, an expansion volume is placed in this hose, which further decreases acoustic pressure perturbations.

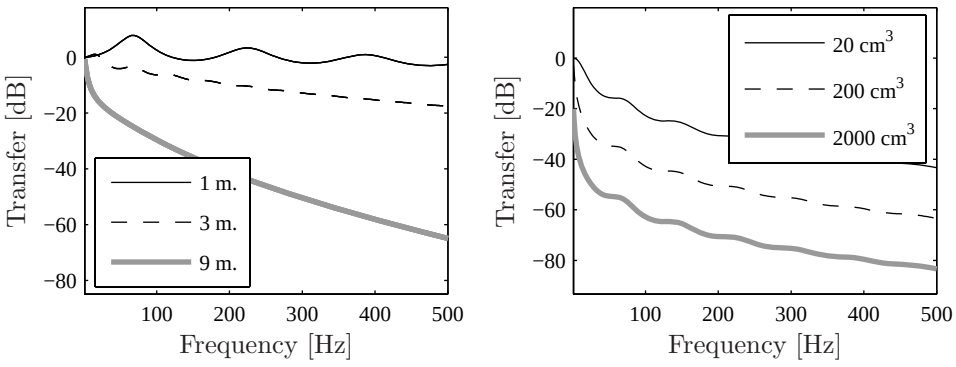

Figure 3.30: Transfer from inlet to outlet for a thin hose (left), showing acoustic attenuation by viscothermal effects and the attenuation by a volume (right).

To evaluate the damping inside the thin hose, one-dimensional viscothermal wave propagation theory is applied [27]. Figure 3.30 shows the transfer from the inlet to the outlet of a thin tube (diameter 0.8 mm) for different tube lengths.

Two things can be noticed. Firstly, the damping of pressure perturbations, which is caused by viscothermal effects, is higher for longer hoses. For short tubes the resonances of the tube are even still clearly visible. Secondly, the damping is lower for lower frequencies. In the static limit, for frequencies going to zero, there is no attenuation, so changes in the static pressure of the setup are followed.

The attenuation by a volume, calculated using the same theory, is also shown in figure 3.30. It can be seen that it has the same characteristics in the frequency domain; the attenuation becomes higher for higher frequencies. Furthermore, the attenuation is higher for larger volumes.

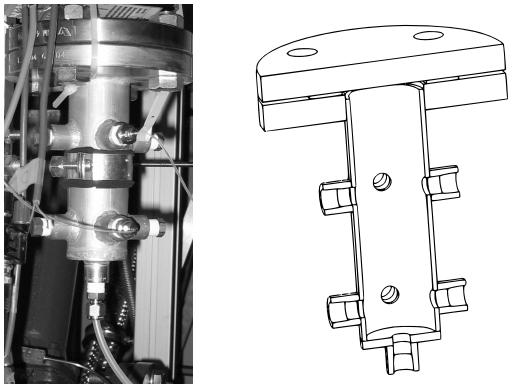

Figure 3.31: Volume used for decoupling in the acoustic back pressure system.

The two decoupling mechanisms, damping by the thin hose and a volume, are both present in the test rig. From figure 3.30 it can be concluded that the damping mechanisms do not work well at very low frequencies. This is necessary, because changing the pressure in the test rig is just a low frequency perturbation, which should be followed. For the dynamic signals that are measured, the lowest frequency of interest is 20 Hz. The volume in the back pressure tube in the test rig (figure 3.31) has a size of approximately 270 cm^3 and the thin hoses are at least three meters long (differs somewhat between the sensors), which gives an attenuation of almost 30 dB due to the volume. At a frequency of 20 Hz, the signal (front of the sensor) to noise (back of the sensor) ratio can therefore be 30dB, and this improves for higher frequencies, where it reaches 80 dB at 500 Hz. Measurements on the thin hoses used indicate that the actual damping is even higher [56].

3.5 Experiments on the test rig

In the previous section two experimental techniques used in the pressure measurements were discussed. This section will discuss the acoustic experiments that were conducted on the test rig. The results are compared with the numerical models developed in this chapter. It has to be stressed that all experiments described in this chapter are for the cold setup. There is no airflow, no preheating and no combustion.

3.5.1 Acoustic experiments

For the acoustic experiments, a normally unused plug is provided in the wall of the water cooler section of the test rig (see also chapter 2). The cross-sectional diameter is 50 mm. A box with a speaker inside is connected to this plug using an aluminum tube (figure 3.32). The source is driven by a random signal generated by a SIGLAB dynamic signal analyzer, which is amplified by a Brüel and Kjaer 2706 amplifier. The Kulite sensors are used as pressure transducers, mounted with the semi-infinite tube assemblies and back pressure facilities. Besides the normal pressure sensors, a reference sensor is mounted in the acoustic supply tube. The root mean square (rms) value of the sound pressure level was about 120 dB for all pressure sensors, which is well above the noise floor of the sensors, which is 60 dB. A Hanning window [81] and 20 averages were applied. The sampling rate was 2560 Hz. The measured autospectra are depicted in figure 3.33.

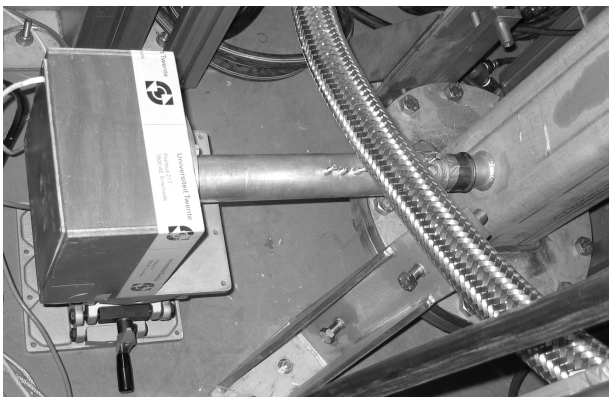

Figure 3.32: Acoustic source for acoustic experiments on the test rig.

Figures 3.33(a) and 3.33(b) show that the pressure levels in the cooling passage are of the same magnitude as those in the combustion chamber. This

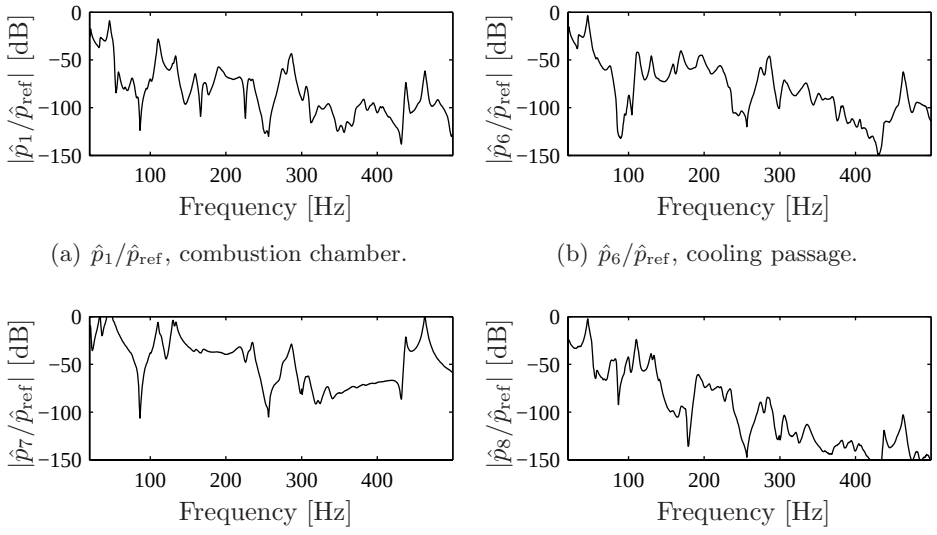

(a) $\hat{p}_1/\hat{p}_{\mathrm{ref}}$, combustion chamber.

(b) $\hat{p}_6/\hat{p}_{\mathrm{ref}}$, cooling passage.

(c) $\hat{p}_7/\hat{p}_{\mathrm{ref}}$, water cooler.

(d) $\hat{p}_8/\hat{p}_{\mathrm{ref}}$, plenum.

Figure 3.33: Measured autospectra for different sensors with acoustic excitation.

is because there are two acoustic paths from the acoustic source to the cooling passage in this configuration. The first is through the CFD tube to the combustion chamber and then through vibrations of the liner (which are treated in the next chapter, but they are evidently always present in the test rig) to the cooling channel. The second is through the cooling air bypass to the cooling passage. These paths give rise to similar pressure amplitudes.

Figure 3.33(c) shows the pressure spectrum in the water cooler. Because excitation takes place here, the acoustic pressure amplitudes are higher. Furthermore, less resonances are clearly visible because the resonances of the upstream components, most notably the combustion chamber, have little influence on the spectrum. Figure 3.33(d) shows that the acoustic pressures in the plenum are smaller than in the combustion chamber, which is caused by the contraction imposed by the burner.

It should be noted that the pressure spectra measured in this experiment are not the same pressure spectra observed during combustion. Excitation during combustion is mainly in the combustion chamber, whereas combustion in this experiment is in the water cooler. The excitation coming to the combustion chamber through the CFD tube is therefore already colored by the acoustic properties of the water cooler (which is evident from the pressure

signal measured with sensor 7 in the water cooler).

3.5.2 Model comparison

The cold acoustic measurements were made for two main reasons. Firstly, they provide direct insight in the acoustic behavior of the test rig, which facilitates the interpretation of data obtained while there is a flame in the test rig. This purpose was served in the previous section. Secondly, the data can also be used to validate the acoustic models of the setup. This is described in this section.

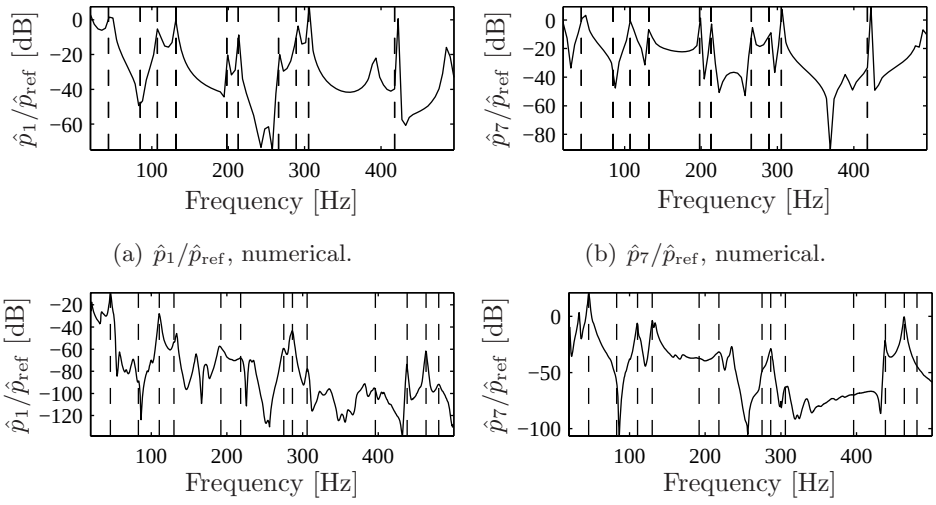

(a) $\hat{p}_1/\hat{p}_{\mathrm{ref}}$, numerical.

(b) $\hat{p}_7/\hat{p}_{\mathrm{ref}}$, numerical.

(c) $\hat{p}_1/\hat{p}_{\mathrm{ref}}$, experimental.

(d) $\hat{p}_7/\hat{p}_{\mathrm{ref}}$, experimental.

Figure 3.34: Transfer functions from the reference sensor (at the acoustic excitation point) to pressure sensors p_1 (combustion chamber) and p_7 (water cooler). Dashed lines are acoustic eigenfrequencies.

Figure 3.34 shows the measured transfer function from the excitation tube to pressure sensors 1 and 7. Moreover, the transfer functions calculated with the finite element model are shown. To calculate these, the excitation tube is added to the acoustic finite element model. Pressure is prescribed at the end of this tube and in this way the transfer function between the pressure sensor in the test rig and the reference pressure sensor is obtained. In the calculated results, the acoustic eigenfrequencies calculated by modal analysis are also shown. In the experiment, the eigenfrequencies are identified from the acoustic spectra. Because it is not obvious whether a peak in the measured spectrum is caused by a resonance of the system considered or by upstream components like

the air supply, the acoustic eigenfrequencies are determined by comparing the shape of the measured and calculated spectrum and then picking the correct peaks. The resulting eigenfrequencies are shown in the figure and the values are listed in table 3.4. The agreement for the combustion chamber modes is good. For the water cooler dominated modes, the distance between the water cooler and the throttle valve, which is the end of the acoustic system, is tuned to the measured results, because this distance is not accurately known. The frequencies of the cooler dominated modes also agree well for measurement and calculation. These modes are less visible when the excitation is in the combustion chamber (for instance with the flame as excitation).

Description	**FEM [Hz]**	**Meas. [Hz]**	**Diff. [%]**	**Description**	**FEM [Hz]**	**Meas. [Hz]**	**Diff. [%]**
Plenum H.	85.1	83.0	2.5	Cooler H.	43.4	46.0	6.0
$(100)_a$	131.7	130.0	1.3	Cooler 1	107.5	110.5	2.8
$(200)_a$	213.2	218.0	2.3	Cooler 2	198.2	192.0	-3.1
$(300)_a$	305.2	306.1	0.3	Cooler 3	265.8	275.0	3.5
$(400)_a$	391.4	396.0	1.2	Cooler 4	289.0	286.5	-0.9
$(500)_a$	484.0	463.0	4.4	Cooler 5	421.1	438.0	4.0

Table 3.4: Comparison of measured eigenfrequencies and those calculated with the full model.

3.5.3 Influence of flow on acoustic behavior

The proper choice of boundary conditions for the acoustic model is essential to obtain a good approximation of the acoustic behavior. In a real gas turbine, the outlet condition is defined by the first stage of the turbine. Because the flow speed is almost sonic there, the end condition is almost acoustically hard. This has the advantage that the acoustics are not influenced by the system downstream of the first turbine stage. The inlet condition is more difficult, because there is no clear acoustic decoupler there. An approach often taken is to aggregate all components upstream of the burner into a burner impedance [57], such as discussed in section 3.3.9.

Academic test setups often have specifically designed up- and downstream acoustic boundary conditions. Nowak [72] used acoustically hard boundaries on both the inlet and the outlet, reasoning that the flow speeds are high enough there to justify such an approximation. Bloxsidge [9] used a choked premixed inlet and therefore had an acoustically hard upstream condition. The down-

stream condition was an open end. A quite complicated equation related to nozzle flow was used as approximation of the acoustic behavior of an open end with flow, but the result was almost identical to prescribing constant pressure at the exit. Fannin [31] modeled the section upstream of the burner up to the choked inlets, which gave an acoustically hard condition. For the downstream section, the experimental setup used a long exhaust tube, which was modeled as a semi-infinite tube by prescribing a characteristic impedance of $\rho_0 c_0$ where the tube starts. The reasoning behind this is that acoustic waves are dissipated in the pipe and at the open end before they have traveled back to the combustion chamber. Fannin correctly noted that this semi-infinite tube model adds acoustic damping to the system, because acoustic energy traveling into the tube is lost, which is not the case in a real gas turbine. Lieuwen [66] used a perforated plate as the upstream boundary condition. He used the static relation between pressure and velocity for the plate (the flow resistance) to obtain the reflection coefficient. This leads to a reflection coefficient between 0.1 for high combustor pressure (8 bar abs) and 0.6 for atmospheric pressure. Both fuel and air were choked upstream of this perforated plate and therefore the flow rates of fuel and air were fixed. The downstream end condition was again a choked nozzle, which gives an acoustically hard end.

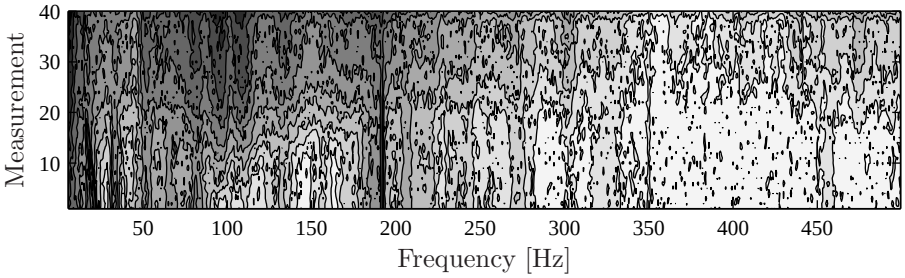

Figure 3.35: Noise levels when the flow is increased, darker colors denote higher pressures, the flow increases with increasing measurement number.

For the test rig built in the DESIRE project, the upstream end is designed as a perforated plate, which is assumed to provide an acoustic hard end. Between the combustion chamber and water cooler, a contraction is placed. This should also give an acoustically hard end. Subsection 3.3.4 on component influence showed that, without flow, this end has substantial influence on the acoustic behavior of the test setup. To gain some insight in what happens when flow is present, the noise levels upon increasing the cold flow in the setup are depicted in figure 3.35. The airflow was increased from the equivalent of 10 kW

thermal power at atmospheric pressure to 100 kW. The noise levels are higher at acoustic eigenfrequencies. When the boundary conditions change due to the flow, these eigenfrequencies would change too, and this would show up as lines changing location. This does not really seem to be the case. It must be noted that the pressure is always atmospheric and the flow is also not very high. Furthermore, the only excitation is flow noise, which does not give very clear resonance peaks. Still, the acoustic spectrum increases, but the peaks do not change much. Kruger [57] found that the burner impedance did not change much due to flow either.

3.6 Concluding remarks

This chapter first introduced the basics of the interaction between acoustics and combustion. The relation between unsteady heat release and an acoustic volume source was derived based on the theory of Lighthill. But the flame not only acts as a source of sound, it also reacts to the sound it is exposed to. Numerical models were shortly introduced and a simplified model that can be used later was derived and compared with numerical calculations made on the DESIRE rig. The relations established between combustion and acoustics are used in the rest of this chapter, in which the focus is on the acoustic domain.

A three-dimensional acoustic model of the test setup was made using the finite element method. This model was subsequently used to study the influence of different components of the test rig. Below 400 Hz the plenum and water cooler have to be included to obtain accurate results, whereas above 400 Hz the results from only modeling the combustion chamber are accurate. A one-dimensional model of the setup was also developed for comparison, which gives results that are similar to the finite element modes, though not exactly the same. The finite element model was used to determine the burner impedance. Two methods were introduced to calculate the burner impedance. The direct method, using acoustic pressure and particle velocity data on the burner outlet and an indirect method using a numerical implementation of the two microphone method. They both show that at the Helmholtz eigenfrequency of the burner and plenum, the impedance is very low. This frequency can be susceptible to thermoacoustically unstable behavior. The model is also used to study the influence of temperature and how this can be included in the model. The most dominant influence of temperature on the acoustic properties comes from the flame temperature. The local temperature field in the flame region is, due to the length of the combustion chamber, of much less influence than the heating of the combustion gasses. Because the setup is long, combustion gasses

are substantially cooled before reaching the end of the combustor, which makes it necessary to include this thermal gradient in the model. Including the full temperature field from a CFD calculation is the most accurate, but dividing the model in four temperature zones already gives less than 2.5% deviation in the eigenfrequencies.

To do acoustic measurements on the pressurized combustion setup, two constructions are used. The first is a back pressure system which uses long thin tubes and a volume to provide a steady back pressure to the pressure sensors, so they can measure the dynamic pressure perturbations in the combustion chamber. The second is a semi-infinite tube, which is an anechoic sidetube mounted to the setup. This makes it possible to measure the acoustic pressures in a region that is much cooler than the combustion setup itself. It was shown that accurate measurements can be made using these two techniques, with errors of less than 2 dB.

To validate the acoustic models, measurements were made without combustion but with an acoustic source connected to the setup. The acoustic eigenfrequencies were predicted very well by the finite element model. The acoustic transfer functions between the acoustic excitation and the pressure sensors in the test rig are also of similar shape. Flow does not seem to change these characteristics much.

Chapter 4

Interaction with the structure

4.1 Introduction

The previous chapter dealt with flame models and acoustic models, which were validated with experiments (chapter 3). This chapter focuses on the structural part and the coupling between the structure and the acoustics. An introduction to the different methods to couple structural and acoustic calculations is given in section 4.2. Section 4.3 studies a simplified model, which consists of a stiff aluminum box covered by a relatively flexible clamped aluminum plate. Experimental results are compared with finite element calculations for this configuration. The flexible part on which the measurements were made in the test rig, the so-called structural liner, is the subject of section 4.4 (interaction between acoustics of the combustion chamber and downstream components is not studied in this thesis [12]). It is modeled using finite elements and experiments are performed to validate these models. The influence of air in the cooling passage and combustion chamber on the structural behavior of the liner is subsequently studied in section 4.5, using simplified two-dimensional and three-dimensional models and a model that is close to the real setup.

4.2 Basics of fluid-structure interaction

In this section, the different methods to couple structural and acoustical analysis methods are introduced. This is followed by a description of the finite element formulation used in the remainder of this chapter.

4.2.1 One-way and two-way coupling

The different methods to couple combustion models, acoustic and structural models were introduced in section 1.4. This section focuses on the fluid-structure interaction part. For fluid-structure interaction, one-way coupling and two-way coupling can be distinguished. In one-way coupling, the acoustic pressure perturbations excite the structure, but the vibrating structure does influence the exciting pressure field (or the other way around). In two-way coupling, both mechanisms are included simultaneously, such that both mechanisms can influence each other.

For one-way coupling, pressure perturbations can be generated and transfered to the structural model. For two-way coupling, two approaches exist. The first is to create one monolithic model that contains a full description of the problem, including the interaction between the fluid and the structure. The second is to calculate the vibration response to the acoustic field and feed this vibration back as a boundary condition to the acoustic model. Iteration is then performed to find a solution. A monolithic approach is used in this thesis.

4.2.2 Finite element formulation

The finite element code Ansys is used in this thesis. This section explains the way in which coupling between fluid and structure is achieved in this code. For the acoustic domain, discretization of the wave equation without source term leads to the following system of equations:

$$\mathbf{M^p}\ddot{\mathbf{p}} + \mathbf{K^p}\mathbf{p} = \mathbf{0}\,, \tag{4.1}$$

in which $\mathbf{M^p}$ is the acoustic mass matrix, $\mathbf{p}$ is the vector containing the nodal pressures and $\mathbf{K^p}$ is the acoustic stiffness matrix. Euler's equation (3.20) states that pressure gradients are a function of the time derivative of the velocity and therefore of the second time derivative of displacement, which is the parameter solved in structural calculations. It is therefore logical that the fluid-structure interaction gives a term that depends on the accelerations from the structural problem and comes into the mass matrix:

$$\mathbf{M^p}\ddot{\mathbf{p}} + \mathbf{K^p}\mathbf{p} + \mathbf{M^{fs}}\ddot{\mathbf{w}} = \mathbf{0}\,, \tag{4.2}$$

where $\mathbf{w}$ is the vector containing the nodal displacements and $\mathbf{M^{fs}}$ is the mass coupling matrix. For the structural problem, the discretized equations are:

$$\mathbf{M^w}\ddot{\mathbf{w}} + \mathbf{K^w}\mathbf{w} = \mathbf{F^t}\,, \tag{4.3}$$

in which $\mathbf{M^w}$ is the structural mass matrix, $\mathbf{K^w}$ is the structural stiffness matrix and $\mathbf{F^t}$ is the vector containing the external loads. These external loads consist partially of the loads imposed by the acoustic pressure $\mathbf{F^p}$ and partially of structural external loads $\mathbf{F}$. Because the loads imposed by the acoustic domain on the structure are related to pressure times area, they generate a term depending on the acoustic pressure and therefore come back as a stiffness matrix:

$$\mathbf{M^w}\ddot{\mathbf{w}} + \mathbf{K^w}\mathbf{w} + \mathbf{K^{fs}}\mathbf{p} = \mathbf{F}\,, \tag{4.4}$$

in which $\mathbf{K^{fs}}$ is the stiffness coupling matrix. If the acoustic and structural mesh on the interface coincide, equations (4.2) and (4.4) can be assembled into one set of equations as:

$$\begin{bmatrix} \mathbf{M^w} & \mathbf{0} \\ \mathbf{M^{fs}} & \mathbf{M^p} \end{bmatrix} \begin{Bmatrix} \ddot{\mathbf{w}} \\ \ddot{\mathbf{p}} \end{Bmatrix} + \begin{bmatrix} \mathbf{K^w} & \mathbf{K^{fs}} \\ \mathbf{0} & \mathbf{K^p} \end{bmatrix} \begin{Bmatrix} \mathbf{w} \\ \mathbf{p} \end{Bmatrix} = \begin{Bmatrix} \mathbf{F} \\ \mathbf{0} \end{Bmatrix}. \tag{4.5}$$

The asymmetric matrices are only created at interfaces that are marked as fluid-structure interfaces. For the determination of the matrices reference is made to the ANSYS manual [2]. The total $\mathbf{M}$ and $\mathbf{K}$ matrices in this equation are asymmetric due to the off-axis $\mathbf{M^{fs}}$ and $\mathbf{K^{fs}}$ parts[1], and therefore an asymmetric solver is required that is in general substantially slower than a symmetric solver. Furthermore, modal superposition is more difficult and cannot be applied in the ANSYS package used. Full harmonic analysis is therefore used to generate the frequency dependent responses.

4.3 Simplified model

The geometry of the test rig is complex and therefore the models will also be complex. To validate the acousto-elastic coupling in the numerical code, a simplified model is therefore developed first, which has a simple geometry and well defined boundary conditions [41, 45]. The combustion chamber is simplified to an acoustic cavity covered by a flexible plate. The acoustic cavity is the simplified combustion chamber and the flexible plate represents the flexible liner. A speaker is used as representation of the source, which is the flame in the combustion experiments. After discussion of the properties of this setup, an analytical model of the flexible plate is given. Subsequently, the finite element model of the experimental setup is explained. This is followed by a comparison of measured and calculated results for the first several structural modes

[1] Symmetric finite element formulations are also possible [28, 73], but they are not applied here.

and acoustic modes. The eigenfrequencies belonging to these modes define the frequency range of interest, which should include these frequencies, at 200 to 1200 Hz.

4.3.1 Test setup

The experimental setup is shown in figures 4.1 and 4.2. It consists of a stiff aluminum box covered by a flexible aluminum plate with a thickness h of 1.1 mm. The plate is fixed using aluminum beams of thickness 5 mm, which are clamped with bolts. The part of the plate that can vibrate has dimensions 160 x 210 mm. The depth of the cavity behind the plate is 140 mm. The material properties are: a Young's modulus E of 70.5 GPa, a Poisson's constant ν of 0.3 and a density ρ of 2700 kg/m^3. All bolts are tightened with a torque of 20 Nm. The properties of the air are: a density ρ_0 of 1.22 kg/m^3 and speed of sound c_0 of 343 m/s.

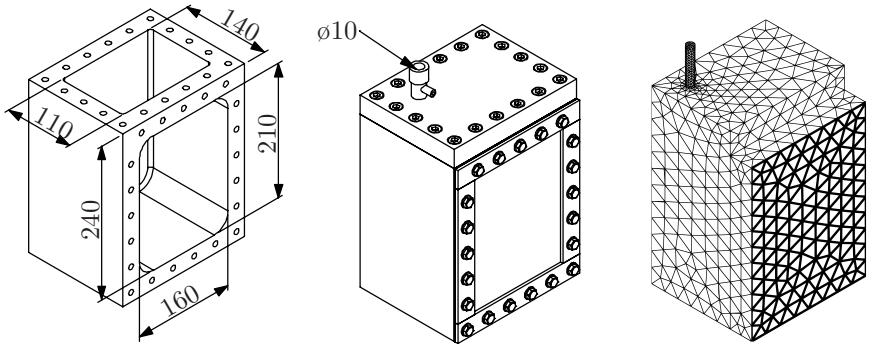

Figure 4.1: The test setup, left is the open box, middle is the box covered by a flexible plate and with the acoustic supply plug, right shows the finite element mesh with structural elements in thick lines.

A laser vibrometer (Polytec OFV-303 optics head combined with an OVD-01 velocity decoder in an OFV-3001 vibrometer controller) mounted on a traverse system is used to measure the vibration of the flexible plate (figure 4.2(b)). This allows for automated measurement of the vibration shapes. The pressure inside the box is measured using an electret microphone which is mounted in the upper right corner in the back (figure 4.2(d)). No acoustic mode shape of the box has a nodal plane at this location in the frequency range of interest and therefore the microphone should be able to detect all these acoustic mode shapes. The signal of this microphone is amplified using a custom-made amplifier with an amplification factor of 100. The acoustic field is excited by a point source. To create this source a speaker is mounted

in a box (figure 4.2(c)). A flexible hose transfers the sound towards the box with the flexible plate. Close to the point where the hose ends on the box a Kulite pressure transducer is mounted to measure the excitation pressure (figure 4.2(a)). The signals from the laser vibrometer, the microphone and the Kulite transducer are digitized using a SIGLAB 20-24 data acquisition unit and post processed using MATLAB. The speaker is driven by a Bruël and Kjær amplifier which is connected to an output channel of the SIGLAB unit.

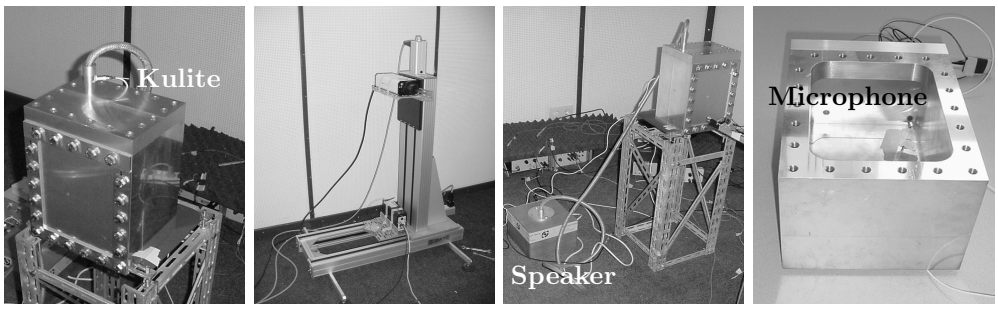

(a) The box with flexible plate. (b) Laser on traverse system. (c) The acoustic source. (d) Position of the microphone.

Figure 4.2: Several images of parts of the test setup.

4.3.2 Analytical model

The structural properties of the flexible plate can be obtained from an analytical model. These properties can be used to validate the finite element model. If the assumption is made that the air does not influence the vibration of the front plate, the uncoupled modes and eigenfrequencies of the flexible plate can be used. The eigenfrequencies of a rectangular plate are given by [8]:

$$f_{ij} = \frac{\lambda_{ij}^2}{2\pi a^2}\sqrt{\frac{Eh^3}{12m_p(1-\nu^2)}}\,, \tag{4.6}$$

in which a is the width of the plate, m_p in the mass per unit area of the plate and λ_{ij} is a factor tabulated for different length to width ratios. For the geometry used here, with a length to width ratio of 0.762, the values are interpolated between the values for a plate with clamped boundary conditions and a ratio of 2/3 and those for a ratio of 1.0. The interpolated values are given in table 4.1. The resulting eigenfrequencies are listed in table 4.2 in the column under analytic.

	$(11)_s$	$(12)_s$	$(21)_s$	$(22)_s$	$(13)_s$
λ_{ij}	29.58	50.77	68.51	87.98	85.31

Table 4.1: Values for λ_{ij} for a plate that is clamped on all sides and with an aspect ratio equal to 0.762.

The first acoustic eigenfrequencies can be approximated by considering the box as a rectangular cavity with acoustically hard walls. The acoustic eigenfrequencies then become [8]:

$$f(k_h, l_h, m_h) = \frac{c_0}{2}\sqrt{\left(\frac{k_h}{a_c}\right)^2 + \left(\frac{l_h}{b_c}\right)^2 + \left(\frac{m_h}{c_c}\right)^2}, \tag{4.7}$$

in which k_h, l_h and m_h are the number of half waves in the three directions and a_c, b_c and c_c are the associated dimensions (160 x 240 x 140 mm). The resulting eigenfrequencies are again listed in table 4.2 in the column under analytic.

4.3.3 Numerical model

In this section, the acoustic and structural eigenfrequencies are calculated using the finite element package ANSYS with the full coupling implementation described in section 4.2.2. The model consists of linear shell (SHELL63) and linear acoustic (FLUID30) elements. An unstructured mesh made of triangular and tetrahedral elements is used. The clamping is assumed to be perfect and therefore all translational and rotational degrees of freedom are suppressed on the clamped edges of the plate. The pressure is prescribed at the location where the Kulite pressure transducer is mounted. The acoustic mesh is shown in figure 4.1.

4.3.4 Results

This section describes the results of the simple setup. First, eigenfrequencies and eigenmodes are compared. Then the pressure response is validated with the experimental results and finally the accuracy of the predicted structural response to acoustic excitation is discussed.

Acoustic and structural eigenfrequencies

The calculated and measured eigenfrequencies of the system are listed in table 4.2. The differences between the analytic and finite element structural eigen-

frequencies are mostly caused by the interpolation of the values for λ_{ij} from the values known in the literature. For the acoustic eigenfrequencies, the difference is caused by the deviation of the test setup from a square box. This is why the vertical acoustic mode $(100)_a$, which is influenced by the beam on top (figure 4.1), has an analytical eigenfrequency which is slightly lower than the eigenfrequency found with the finite element model. Results are also listed for an uncoupled FEM model. The only difference with the coupled FEM model is that the off-diagonal coupling matrices ($\mathbf{M^{fs}}$ and $\mathbf{K^{fs}}$ in equation (4.5)) are not generated. The results are highly similar to those of the coupled model. Finally, the frequency match between the coupled finite element model and the measurements is excellent.

Mode	**Analytic**	**FEM uncoupled**	**FEM coupled**	**Measure**	**Deviation of coupled FEM**
$(11)_s$	312.8	303.4	307.4	306.2	0.39 %
$(21)_s$	537.0	511.8	506.9	505.0	0.38 %
$(12)_s$	724.5	707.7	702.7	702.5	0.03 %
$(100)_a$	714.6	731.8	736.2	742.5	-0.85 %
$(31)_s$	902.2	853.6	850.2	851.3	-0.13 %
$(22)_s$	930.4	889.8	885.4	895.0	-1.07 %
$(010)_a$	1071.9	1077.6	1080.3	1086.2	-0.54 %

Table 4.2: Eigenfrequencies (Hz) of the setup, index s denotes structurally dominated, index a denotes acoustically dominated.

Figure 4.3 shows the vibration patterns of the front plate for the different modes, both for measurements and calculations. The results match very well. The structural response due to the acoustic modes is also predicted well, indicating that the spatial prediction of the pressure field is also correct.

Pressure signals

The sound pressure level at the end of the supply hose is depicted in figure 4.4(a). It shows peaks at intervals of 62 Hz, which are the resonances of the 2.67 meter supply tube. The acoustic excitation level p_s is between 95 and 115 dB at the inlet, with decreasing pressure for increasing frequencies. This is caused by the properties of the speakerbox used. The excitation pressure produces enough excitation over the entire frequency range of 200 to 1200 Hz to measure structural vibrations on the plate using the laser vibrometer. The transfer from the pressure at the location of the Kulite in the supply hose to the

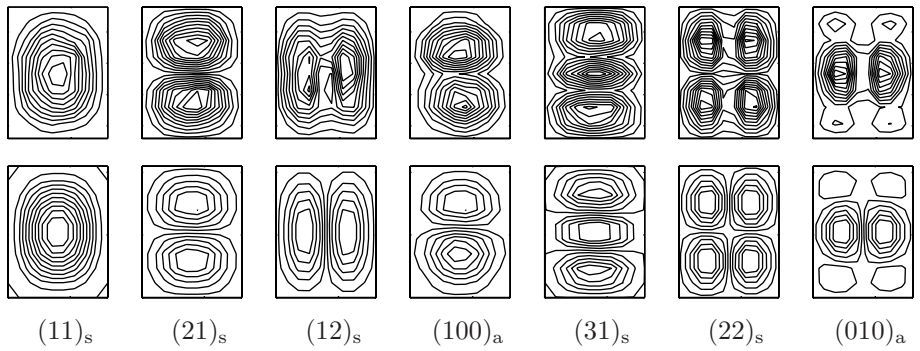

Figure 4.3: Calculated (top) and measured (bottom) mode shapes corresponding to table 4.2.

pressure in the box p_b is depicted in figure 4.4(b). A harmonic calculation with the numerical model was performed and the result is also shown in this figure. Furthermore, an uncoupled calculation was made to investigate the importance of the coupling for the acoustic response. The results of the measurement and the coupled calculation match very well. The first two acoustic eigenfrequencies are clearly visible. Furthermore, the first two structural modes show up as disturbances on the general shape of the curve, which are evidently not present in the decoupled calculation. The influence of the first structural mode on the acoustic behavior is substantial. The second one is slightly visible and higher structural modes are not visible at all, which is also caused by the location of

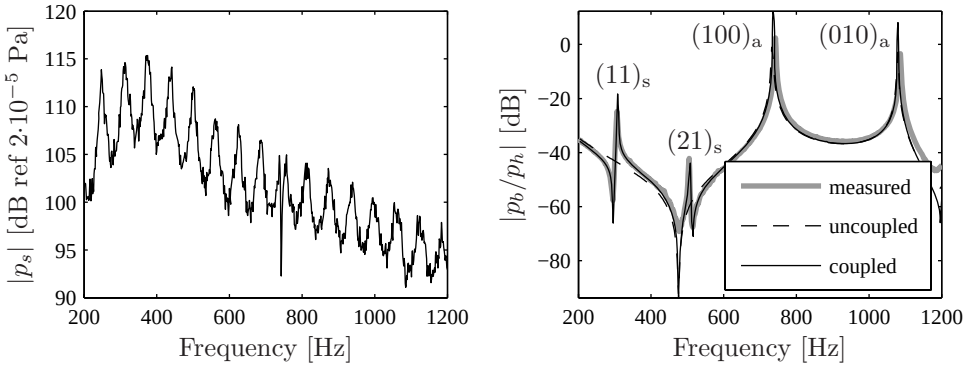

(a) Measured pressure at the end of the supply tube.

(b) Transfer from supply pressure to pressure in the box.

Figure 4.4: Transfer functions for the coupled model.

the pressure sensor, which is relatively far from the structure. Local pressure changes due to the structure are therefore hardly measured. The acoustic modes do not change in frequency either by adding the flexible plate to the model. For higher frequencies, acoustic predictions can therefore be made by only using an acoustic model with acoustically hard walls, whereas for lower frequencies the structure should be included.

Structural vibration

Figure 4.5(a) shows the transfer H_{L2} from the supply pressure to the spatial L_2 norm of the normal velocity of the front plate, which can be written as:

$$H_{L2} = \frac{1}{N_n} \frac{\sqrt{\sum_{i=1}^{N_n} \left(v_n^{(i)} \right)^2}}{p_s}, \tag{4.8}$$

in which $v_n^{(i)}$ is the velocity normal to the plate of a node of the mesh and N_n is the number of nodes on the flexible plate. The value is used as a global indication of the vibration level of the plate.

The results of the coupled finite element calculation and the measurement again agree very well. The graph shows more resonances than the one for the pressure in the box (figure 4.4(b)). At the acoustic eigenfrequencies the acoustic pressure becomes high which leads to high excitation levels and therefore high vibration levels. At the structural eigenfrequencies the excitation is rather low, but the structure is very compliant and therefore the vibration levels are still very high. Figure 4.5(b) shows the transfer from the pressure in the box (measured by the sensor in the corner, figure 4.2(d)) to the vibration of the plate. The acoustic eigenfrequencies have disappeared in this plot because the high vibration response is divided by the high pressure level. In both plots the third structural mode $(12)_{\mathrm{s}}$ does not show up strongly. This is because the pressure field generated is dominated by the nearby acoustically dominated $(010)_{\mathrm{a}}$ mode. This mode does not couple well with the structural vibration pattern of the $(12)_{\mathrm{s}}$ mode and therefore the structural mode is hardly visible in the transfer between pressure and vibration of the plate.

The transfer from the pressure in the supply tube to the velocity of a point on the plate is plotted in figure 4.6. The points for which the transfers are calculated are also shown. Points 1 and 3 show that the transfer is accurately predicted. Point 2 is very close to the vertical middle of the plate. The second structural mode has a nodal line here and therefore this mode is almost invisible in the vibration spectrum. Point 4 is very close to the clamping of the plate.

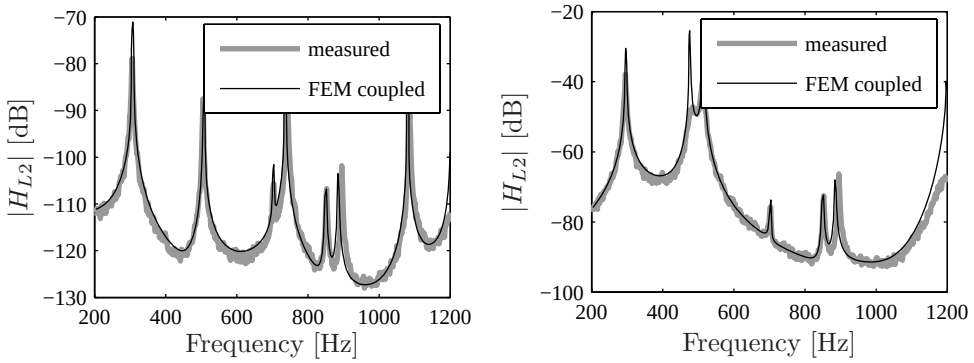

(a) From supply pressure.

(b) From pressure in the box.

Figure 4.5: Transfer from pressure to the spatial L_2 norm of velocities on the plate.

The vibration levels are therefore much lower and there is a lot of noise on the signal, because the measurement accuracy of the laser vibrometer becomes insufficient.

4.3.5 Conclusions

A finite element model of an acoustic cavity covered by a flexible plate has been made. The FEM model was successfully validated with an experimental setup. A point source was used constructed from a box with a speaker in it to which a long tube is connected. This tube transports the acoustic pressure to the box with the flexible plate. The mode shapes and eigenfrequencies can be predicted accurately. The transfer from the pressure at the end of the tube to the velocities on the plate are also predicted accurately. Beyond the first few eigenmodes of the structure, the prediction of the acoustic pressure in the upper corner of the box is accurate if the structure is not included in the model, whereas the first few eigenmodes do influence the pressure response in the box. If accurate models of the acoustic and structural behavior of the test rig can be made, the coupling used here will give an accurate prediction of the behavior of the coupled system when there is no flow. Because the flexible structure can influence the acoustic behavior and vice versa, the full coupling applied here also has advantages for modeling the acousto-elastic interaction in the test rig. The next section treats the necessary structural model for the liner.

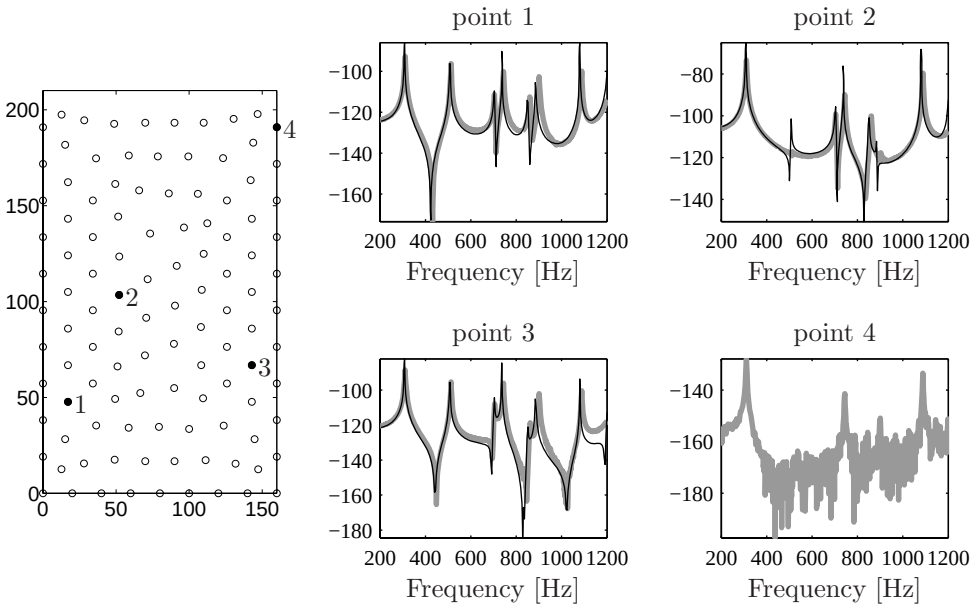

Figure 4.6: Transfer from supply pressure to velocity on points on the plate ($|v_i/p_s|$). Black is calculated, gray is measured.

4.4 Structural properties of the liner

4.4.1 Introduction

In chapter 3, the acoustic behavior of the test rig was modeled, without the influence of the flexible structure, and the model was validated with experiments. This chapter deals with the interaction between the acoustic field and the flexible structure. This requires more knowledge of the structural behavior of the flexible part of the test rig first. The design of the most important flexible part, called the structural liner, is discussed first. A three-dimensional finite element model is made, which is validated by experimental modal analysis. Two other important structural effects, the influence of temperature and the influence of prestress, are discussed at the end of the section.

4.4.2 Design of the structural liner

The design of the structural liner is based on several requirements:

- The structural behavior should be predictable to facilitate the comparison of numerical models with experiments. A real gas turbine construction is

of course more difficult to model, but the primary objective of this thesis is not to stay as close as possible to a real combustor, but to gain insight in fluid-structure interaction in a gas turbine.

- The structure should have low eigenfrequencies. Because the experimental setup is scaled down from a full size combustor (chapter 2), the liner becomes stiffer. When it is too stiff, the eigenfrequencies lie above the typical excitation frequencies of the flame (section 3.2) and little response is measured, which is not the case in a real gas turbine.
- The liner should be replaceable. This makes it possible to adapt the liner for future research projects.

The requirements mentioned resulted in the design of the test rig discussed in chapter 2, consisting of a section for combustion, one for structural measurements and one for cooling. A schematic drawing of the structural part is given in figure 4.7.

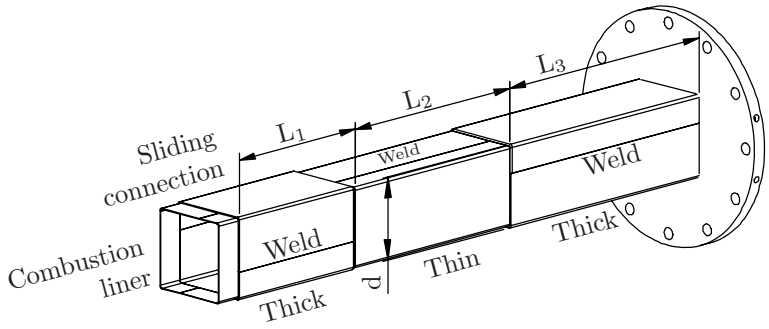

Figure 4.7: General shape of the liner in the structural section, gasses flow from left to right.

The liner consists of two parts, one in the combustion section and one in the section for structural measurements. These two liners are connected by a sliding connection. The liner in the structural section consists of a thick part, a thin part on which the vibrations are measured and again a thick part (figure 4.7). The design essentially decouples the boundary conditions at the flange and the sliding connection from the vibration, because for lower frequencies the vibration pattern will be located entirely in the thin part (see also the rest of this section). This makes the behavior of the liner more predictable. The small liner thickness ensures low eigenfrequencies and the simple and relatively cheap construction makes it possible to easily replace the liner without changing the rest of the test rig. Because the thick parts hardly vibrate in the relevant

frequency range, they can be used for mounting pressure transducers, for which holes are provided. The thermal expansions of the liner in the combustion section and the liner in the structural section, which are larger than that of the pressure vessel (because the pressure vessel remains cooler), can be taken by the sliding connection. It therefore decreases thermal stresses in the structural liner and their influence on the structural behavior. The dimensions of the structural liner, which is made of stainless steel 310, are listed in table 4.3.

Property		**Value**	**Property**		**Value**
Begin section	L_1	0.30 m	Young's modulus	E	210 GPa
Flexible section	L_2	0.40 m	Poisson's ratio	ν	0.3
End section	L_3	0.50 m	Density	ρ	7800 kg/m^3
Liner width	d	0.15 m			
Thickness (ends)	t_1	4.0 mm			
Thickness (middle)	t_2	1.5 mm			

Table 4.3: Dimensions and material properties of the liner in the structural section.

The three parts of the structural liner (a thick, a thin and again a thick section) are all made of two plates which have been bent in a U-shape (figure 4.7). These two plates are welded together, after which the three square tubes are welded together. This means that there are welds on the connection between the thin part and the thick parts of the structural liner and also on two of the four faces of the tube. Furthermore, the corners are not sharp but rounded. All these effects influence the structural behavior of the liner.

4.4.3 Finite element model of the liner

In this section, a finite element model of the structural liner (figure 4.7) is constructed. The model consists of only the flexible section, because this section dominates the dynamic behavior of the liner and all structural measurements are made on this section. The section is clamped at the inlet and outlet sides (figure 4.8) to approximate the influence of the thick parts. The elements applied in the finite element model are linear shells (SHELL63). The element size is again 10 mm.

The calculated mode shapes are depicted in figure 4.9. The names of the mode shapes are listed below them. The part of the mode name between brackets refers to the shape on one side. The $(11)_{ss}$ therefore shows one half wave in both directions on one side. The subscript of the mode refers to the

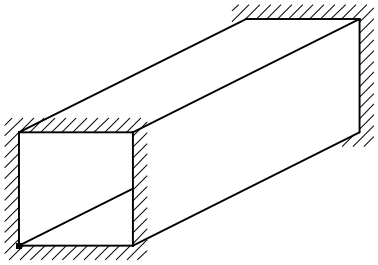

Figure 4.8: Boundary conditions of the three-dimensional model.

boundary conditions. For the $(11)_{ss}$ mode, one side moves outwards, the neighboring side moves inwards, the third outwards and the last one inwards again. Two sides that are connected to each other therefore move out of phase. The corners between the sides rotate, and therefore the corners behave much like a simply supported boundary condition. Hence the name 'simply supported-simply supported' or ss. In the $(11)_{cc}$ mode, all sides vibrate in phase, the corners behave like clamped boundary conditions and therefore they are named clamped-clamped or cc. For the third type of mode the vibration is located on two of the four sides and therefore they are referred to as 'half' or h. These modes appear in pairs of two because of their asymmetric nature. An analytical approximation of the ss and cc modes is given in appendix D.

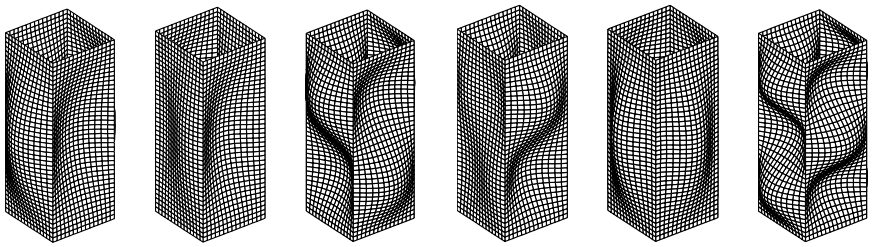

Figure 4.9: Modes shapes calculated with the finite element model.

4.4.4 Experimental liner modal analysis

For validation of the numerical models of the structural liner, modal analysis was performed. The liner part was placed on rubber mounts to obtain a free boundary condition at the location of the flange. To reduce residual stresses due to the welding, the liner was annealed before the measurements were made.

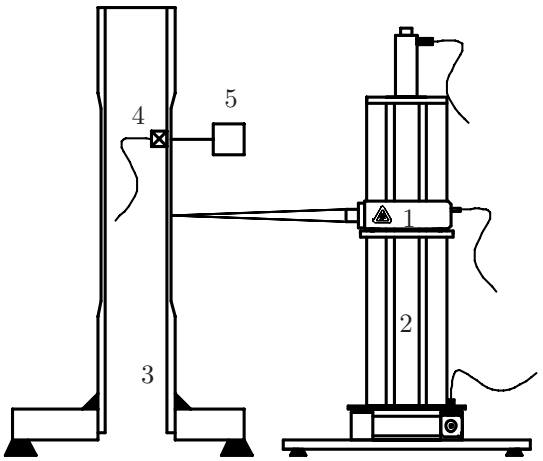

1 = Laser vibrometer
2 = Traverse system
3 = Liner
4 = Accelerometer
5 = Shaker

Figure 4.10: Structural measurements.

A white noise signal was created with a SIGLAB data acquisition system. This signal was amplified by a Bruël and Kjær amplifier. This signal drives a shaker that was mounted on the same side of the liner as the one on which the velocities were measured, to obtain sufficient vibration level on the flexible part for laser vibrometer measurements. The location of the shaker was 95 mm from the left side of the liner and 50 mm below the connection between the upper stiff part and the flexible part of the liner. A force sensor was placed between the shaker and the structure as reference sensor to obtain phase information. The vibration was measured by traversing a Polytec laser vibrometer, using a Dantec traverse system, over one side of the square liner, sequentially making measurements on different points (figure 4.10). The measurement grid and its location with respect to the thin section of the structural liner is depicted in figure 4.11. Furthermore, an accelerometer was mounted on the inside of the

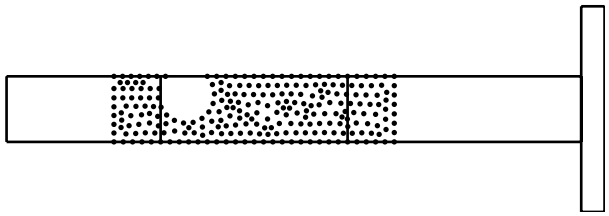

Figure 4.11: The measurement grid and its location on the liner.

liner at the same location as the shaker for additional validation. The force

sensor and the acceleration pickup were connected to a B&K Nexus signal conditioner. The signals from the laser vibrometer, acceleration pickup and force sensor were acquired with the same SIGLAB system.

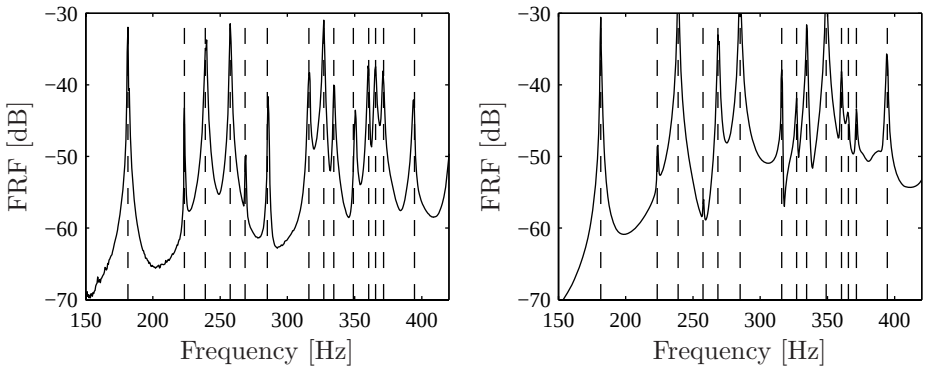

Figure 4.12: Measured spatially averaged force to velocity transfer for the liner. Left is the welded side, right is the unwelded side.

Description	**FEM**	**Measured**	**Improved FEM**
$(11)_{ss}$	196.8	181.5	182.5
Squeeze 1	-	223.5	220.0
$(12)_{ss}$	287.0	239.0	243.6
$(11)_{h1}$	280.5	257.5	269.0
$(11)_{h2}$	280.5	269.0	279.1
$(12)_{h1}$	355.3	285.0	318.0
$(13)_{ss}$	426.9	316.5	321.2
$(12)_{h2}$	355.3	327.0	337.6
$(11)_{cc}$	390.3	-	394.8

Table 4.4: Measured and calculated structural eigenfrequencies in Hz.

In figure 4.12 the amplitude of the transfer function from force to velocity, averaged over all measurement points, is shown (see also section 4.3.4 for this method). The reason that spatial averaging is applied is that all modes should become clearly visible. The figure shows that the results differ significantly, depending on the side of the liner on which the measurements are made (left and right in figure 4.12). Asymmetric modes (the $(11)_h$ and $(12)_h$ modes, table 4.4) split up in two different modes, which proves that the welds significantly influence the structural behavior of the liner. The two different modes will be

denoted with two different subscripts as $(11)_{h1}$ and $(11)_{h2}$. The behavior is also seen in the numerical calculations when an approximation is used for the weld (appendix F).

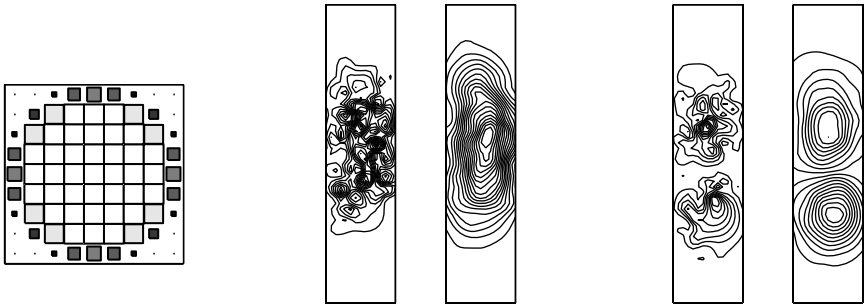

Figure 4.13: Graphical representation of the spatial smoothing filter (a white box represents a one) and the effect on two modes, where left is original and right is smoothed.

The eigenfrequencies derived from figure 4.12 are shown in table 4.4. Numerical results from the previous section are also included. The mode called 'squeeze 1' is not found in the calculations, because it is a mode in which the entire flexible liner, including the thicker end parts, is squeezed. The eigenfrequencies do not match really well. An improved model, including the thicker end parts and an approximation of the welds, is presented in appendix F. The results of this model are also listed in the table. The agreement with this model is good, considering the still coarse approximation of the welds in the construction.

Signal loss of the laser vibrometer is sometimes observed for some measurement points. Because a large number of points is measured, points which show poor coherence between laser vibrometer measurement and excitation force can be skipped. The measurements are replaced by a result that is linearly interpolated from neighboring measurement points, which eliminates this so-called outliers problem [99].

Because the shaker was mounted on the same side as where the measurements were performed, there are no measurements on the area behind the shaker (because the laser vibrometer has no line of sight with the surface of the liner). To eliminate the resulting gap in the measurement data, the data, already containing the interpolated data points, are remapped on a regular grid of 15x55 points. In the region behind the shaker, the vibration pattern is then interpolated between the boundaries of the region by this remapping.

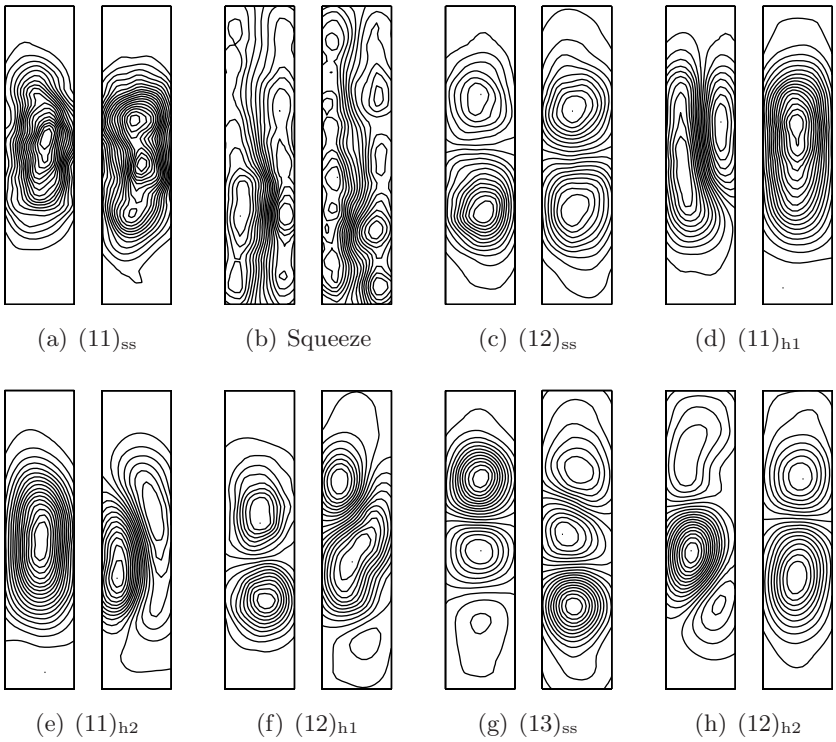

(a) $(11)_{ss}$ (b) Squeeze (c) $(12)_{ss}$ (d) $(11)_{h1}$

(e) $(11)_{h2}$ (f) $(12)_{h1}$ (g) $(13)_{ss}$ (h) $(12)_{h2}$

Figure 4.14: Measured mode shapes on two sides of the liner, left is the side without the weld, right with.

The length of the measurement, which takes over an hour, causes eigenfrequencies and vibration amplitudes to differ somewhat between the sequential measurements. This gives very irregular mode shapes. To decrease this irregularity, a circular filter (a so-called pill box filter) is applied on the remapped data, which averages the amplitude over an approximately circular area. The data must be on a regular grid to be able to do this, which is a second reason to apply the remapping. A graphical representation of the elements in the matrix used in this filter is shown in figure 4.13, where white boxes denote ones and empty spaces zeros. The radius of the filter is 50 mm, as a compromise between maintaining spatial detail and measurement differences dominating the visualization. The effect of the smoothing is illustrated for the $(11)_{ss}$ and the $(12)_{h1}$ mode shape in figure 4.13. The resulting smoothed mode shapes are depicted in figure 4.14.

It can be seen that the mode shapes are well recognizable for the lower modes. The mode shape sequence is the same as the one calculated with the

improved model. A remarkable difference is observed in the $(11)_h$ and $(12)_h$ modes. The (11) shape of the $(11)_h$ mode appears first on the welded side and then, for a higher frequency, on the unwelded side. The (12) shape of the $(12)_h$ mode, though, appears first on the unwelded side and then on the welded side, as would be expected from the improved model with welds. This is a clear indication that the weld modeling improves the model but is not sufficient to describe the mechanical behavior of the liner.

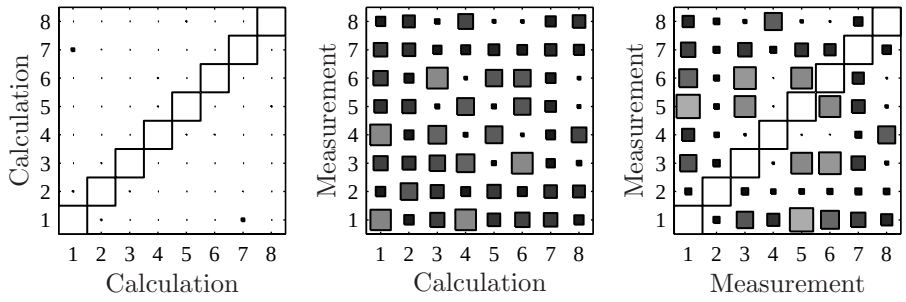

Figure 4.15: MAC values between the calculations evaluated on one side (left), between measured and experimental results (middle) and between the experiments themselves.

To further evaluate the match in mode shapes between calculations and experiments, figure 4.15 shows the MAC values between experimental and numerical results and also the MAC values of the numerical and experimental results compared with themselves. The numerical mode shapes are well distinguishable. The experimental mode shapes are far less distinguishable, as the right figure shows. Two separate measurements were performed without a common reference, and therefore there is no information on the phase between the two sides, which makes it much harder to recognize a mode. Finding a well correlated reference is difficult. When the shaker is mounted on one side of the liner, very little vibration is observed on the other sides and therefore a common reference, that remains on the same side, exhibits very poor coherence when the shaker is mounted and the measurements are made on a different side. The MAC values between measurements and calculations therefore also do not show a clear pattern.

4.4.5 Other structural effects

In this section two other structural effects that are relevant for measurements in the test rig are treated. The first is the influence of temperature on the structural properties and the second is the influence of prestress, which can

arise due to pressure differences over the liner and the not fully unrestrained thermal expansion of the liner in the axial direction.

Influence of temperature on structural properties

The properties of the structure, just as the properties of the acoustics, are a function of temperature. The temperature of the structure can be calculated with a CFD calculation including heat transfer at the wall and including the heat transfer to the cooling air flowing on the outside of the wall. This calculation is far from trivial, because the heat transfer coefficient on the combustion side is difficult to estimate [60]. The most straightforward method of calculating the temperature of structure T_s is just taking it to be the average of the temperature of the air in the combustion chamber T_{comb} and in the cooling passage T_{cool}, so:

$$T_s = \frac{T_{comb} + T_{cool}}{2}, \tag{4.9}$$

The structural material behavior is governed by the Young's modulus E and the Poisson's ratio ν. Values for Poisson's ratio at elevated temperatures are seldomly measured. Measurements at lower temperatures show little temperature dependence, though, with values ranging from 0.29 to 0.31. A constant Poisson's ratio of 0.3 is therefore used.

Figure 4.16(a) shows the dependence of the Young's modulus on temperature for Hastelloy® X [39], which is a high performance alloy used in gas turbines, for SS310 [40], which is used in the test rig and a plot of an expression for a typical stainless steel [107]. All three materials show the same behavior with the Young's modulus dropping slowly from just above 200 GPa to 150 GPa at 800°C.

The eigenfrequencies of a plate (equation (4.6)) scale with the root of Young's modulus. The Young's modulus decreases by approximately 25% for a temperature increase from 20°C to 800°C. This causes a change in eigenfrequency of 13%. A very accurate prediction (better than +/-20°C) of the temperature of the structure is therefore not really important to determine the material properties. However, different temperatures over the structure may lead to thermal stresses, though, which can significantly influence eigenfrequencies and even result in buckling.

In the test setup the thin part of the structure is entirely downstream of the flame and therefore the temperature of the gasses in the combustion chamber is near the adiabatic flame temperature. The cooling air temperature is approximately constant and therefore the temperature of the structure is also taken constant. Previous calculations showed that the gasses in the combustion

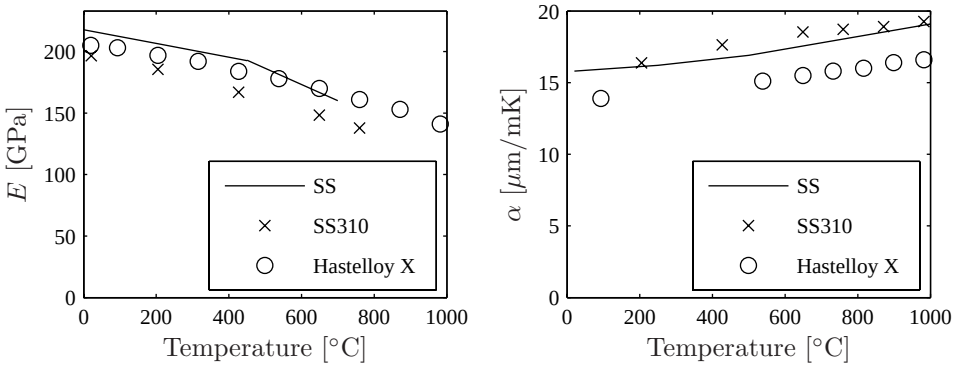

(a) Young's Modulus (b) Coefficient of thermal expansion

Figure 4.16: Temperature dependence of the Young's modulus E and the coefficient of thermal expansion α.

chamber have a temperature of 1680 K (1407°C, see also section 3.3.8). The cooling air enters the cooling passage at 20°C and leaves at around 300°C. The cooling gas temperature is therefore taken as 160°C, which gives a temperature for the structure of 784°C (1057 K). At this temperature, the Young's modulus is approximately 150 GPa and this value is used for the calculations in the presence of combustion.

Figure 4.16(b) shows the temperature dependence of the coefficient of thermal expansion. This depends even less on temperature. A constant value of 17 μm/mK is therefore used. For an increase in temperature from 293 K to 1057 K, the volumetric increase of the steel is just over 1%. The material density is therefore also not taken as a function of temperature.

Figure 4.17 shows the construction for liner temperature measurements schematically and the measured temperature of the liner during a measurement at case 15.4 (see table 3.1). The two thermocouples are mounted on the thick parts of the structural liner, just before the flexible section and just after the flexible section. The thermocouples lie against the liner, but are not embedded in it, and are shielded somewhat from the cooling air by a protective shield. The measured temperature before the flexible section is 580°C and after the flexible section it is 530°C. Because of the lack of embedding in the liner material and the partial protection from the cooling air, these readings are indicative and are likely to be lower than the real values.

As a second measurement technique for the liner temperature, a pyrometer is used, which measures the temperature of the liner on the cooling air side

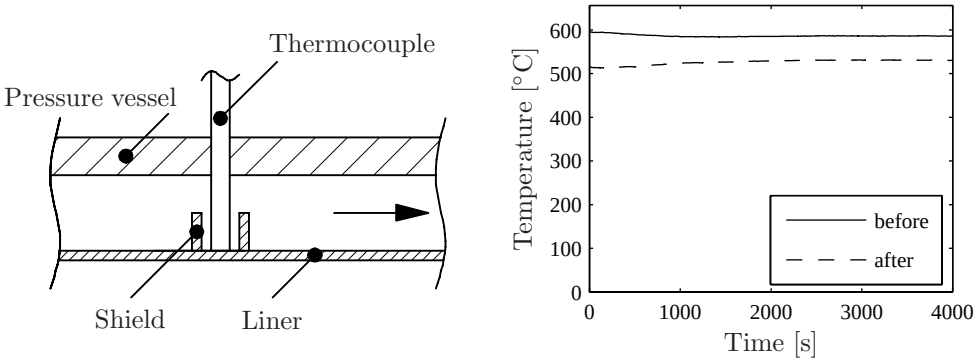

Figure 4.17: Liner temperature measurement construction and the temperature measured for case 15.4.

through the square laser vibrometer window by means of infrared radiation. The temperature measured for case 15.4 was 680°C and for case 15.7 it was 720°C. When the values were measured, a cooling air factor of 1.2 was used, meaning that there is 1.2 times more cooling air than combustion air. A value of 1.0 is also often used and that will result in liner temperatures that are somewhat higher. The estimate of 784°C for the liner temperature is therefore likely to be close to the actual liner temperature. The temperature of the liner in the combustion zone was measured through the windows for the LIF measurements as 1020°C. The liner is hotter here, because the presence of the flame causes a strong increase of heat transfer to the liner.

Influence of prestress on liner behavior

Two different causes of prestress can be distinguished. The first is a pressure difference between liner and cooling passage. During experiments this pressure difference is monitored to assure that the stresses caused are not too high. For a measurement session at a maximum static pressure of 1.5 bar abs, the pressure difference is shown in figure 4.18. The figure shows that the pressure difference remains below 4 mbar. A small overpressure almost always exists in the combustion chamber. This is because the cooling air flows to the water cooler through four hoses, whereas the flue gasses are first forced through the CFD tube (chapter 2) and the pressure drop caused by the CFD tube is slightly higher than that of the hoses due to higher velocities. An additional benefit of the slightly higher pressure in the cooling passage is that if there is leakage (for example at the sliding connection), relatively cold cooling gasses leak into the combustor, but hot flue gasses do not leak to the cooling passage, which

could create hot spots on the structure.

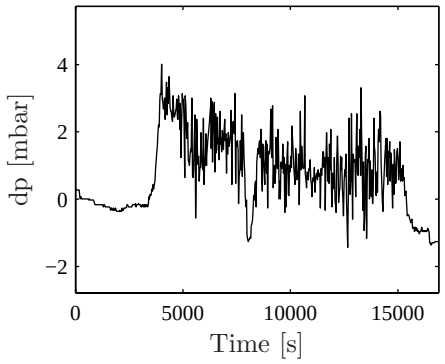

Figure 4.18: Pressure difference (dp) over the liner during a measurements session.

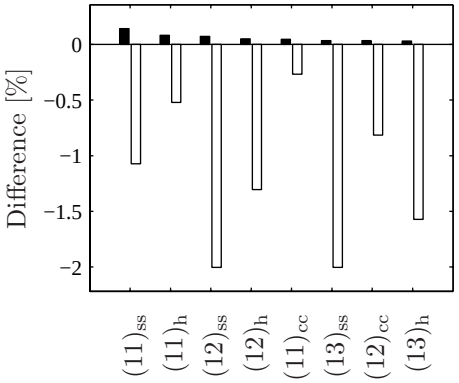

Figure 4.19: Changes in eigenfrequencies due to prestress, black is pressure load, white is thermal load.

A second cause of prestress is constrained thermal expansion of the liner. The test rig has a sliding connection at one side of the structural liner (chapter 2). This partially absorbs the thermal expansion, but prestresses can still exist due to friction.

To evaluate the influence of these two prestresses on structural vibration, the structural eigenfrequencies are calculated for three cases, one without prestress, one with an internal overpressure of 15 mbar and one for a temperature increase of 1°C when the flexible section is constrained (in the test rig the temperature increases are much larger, but the sliding connection can accommodate for much of this expansion). The values are chosen such that the stresses in the structure are of similar magnitude for both preloads. The resulting differences in eigenfrequencies are shown in figure 4.19.

It can be seen that the effect of prestress due to the internal pressure on the structural eigenfrequencies is negligible. Prestress due to friction in the sliding connection, causing in-plane stresses in the plates of the liner, can have a more significant influence on the vibration behavior though. Because these stresses are compressive, they decrease the eigenfrequencies. A complication is that, because the liner goes through a series of stick and slip phases during heat up, the prestresses are unknown at any given time during the measurement. It should be noted that the prestresses in this direction can be smaller as well as larger in the test rig, because the magnitude of the friction forces in the sliding connection is unknown.

The reason for the difference in the effect of prestress is that the pressure

load causes mostly bending prestresses. This gives a stress gradient over the thickness of the liner. Roughly speaking, the compressive stresses on the bottom side decrease the eigenfrequency, but this is compensated by the tension stresses on the top side. Because the liner is a square tube, the pressure load on the side plates of the square cross section cause tension stresses in the top plate. These stresses cause the small increase in eigenfrequency for the pressure load. The stresses caused by thermal expansion have the same direction over the entire thickness and therefore the effect is much more pronounced.

4.5 Fluid-structure interaction in the full rig

4.5.1 Introduction

In chapter 3 acoustic models were developed and the previous section treated structural models. Section 4.3 already introduced fluid-structure coupling. This section will discuss the coupling between models for the structural and acoustic behavior of the test rig without combustion. A strongly simplified, two-dimensional model is first discussed. This model is used to demonstrate the possible influences of acoustic cavities on the structural behavior. The three-dimensional model from section 4.4 is subsequently extended with a simplified acoustic model to study what should be included in the full model. The full models (section 3.3.2 and 4.4) are then coupled and the results are validated using data measured on the test rig. Finally, the influence of flow and turbulent excitation on structural vibration is discussed.

4.5.2 Two-dimensional model

The layout of the two-dimensional model is shown in figure 4.20. The model is a cross section taken from the flexible part of the liner. It consists of an acoustic cavity on the inside, representing the combustion chamber, which is surrounded by the flexible liner. Outside the liner is a cavity representing the cooling passage which is bounded by the pressure vessel. The pressure vessel is assumed to behave as an acoustically hard wall. The properties in table 4.3 are again used, with the additional properties listed in table 4.5. The structural behavior of the two-dimensional liner approximation is treated in appendix D.

Finite element model

To study the behavior of the system of the liner with air on the inside and outside, a finite element model is made. It consists of linear two-dimensional fluid

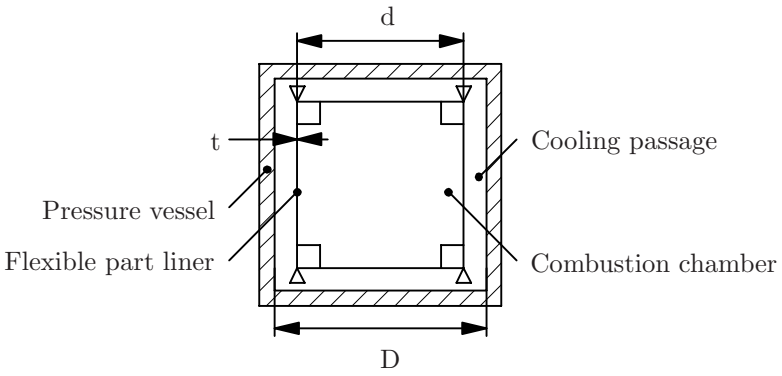

Figure 4.20: Layout of the two-dimensional coupled model.

elements and linear two-dimensional beam elements. The elements are coupled using fluid-structure elements (section 4.2.2) that ensure that the acoustic velocity and the structural velocity are equal in the normal direction of the plate (the hatched elements in figure 4.21).

Because the fluid and the structure share nodes on the fluid-structure interface, two sets of beams are used (the pressure degrees of freedom of the cooling passage and the combustion chamber would otherwise be directly coupled). The displacement and rotational degrees of freedom of these beams are coupled. Because the Young's modulus and mass are taken as half of the real value, these coupled beam elements have the same stiffness and mass as the original beam used in section 4.4. The acoustic cavity elements are coupled to one beam set and the acoustic cooling passage elements to the other.

Influence of the cavities on the eigenmodes

The coupled finite element model is used to study the influence of the cavities on the structural behavior of the liner. The eigenfrequencies and mode shapes are therefore evaluated. Five cases are considered:

Property	**Value**	
Speed of sound	c_0	$343\ \mathrm{m\,s^{-1}}$
Density of air	ρ_0	$1.21\ \mathrm{kg\,m^{-3}}$
Outside dimension cooling passage	D	190 mm

Table 4.5: Material properties and dimensions of the two-dimensional model.

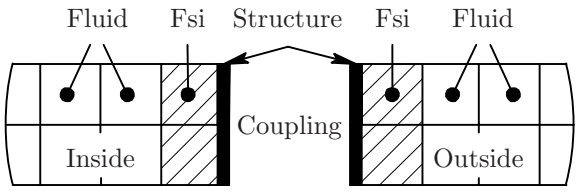

Figure 4.21: Layout of the fluid-structure interface for finite element modeling.

- The structure only.
- The structure and the air in the combustion chamber.
- The structure and the air in the cooling passage.
- The structure with both cooling passage and combustion chamber.
- The cooling passage only.

The eigenfrequencies of the different models are given in table 4.6. The names of the structurally dominated modes are related to beam modes. The vibration of one side of the two-dimensional model always resembles an eigenmode of either a clamped-clamped beam (cc), a pinned-clamped beam (pc) or a pinned-pinned beam (pp) (see also appendix D). Acoustically dominated modes are denoted by 'ac'. Eigenfrequencies 5 and 6 are only present when the cooling passage is included in the model, because this is the first circumferential acoustic mode of the gap (figure 4.22). This circumferential eigenfrequency is approximately given by:

$$f = \frac{c_0}{2\,(D+d)}\,, \tag{4.10}$$

in which it is assumed that the distance that the acoustic wave has to travel is along the center of the cooling passage. With this formula, the first circumferential eigenfrequency becomes 504.4 Hz, which is close to the finite element result. Modes 10 and 11 are the next pair of acoustic cooling passage modes, which would be expected analytically at 1009 Hz.

When examining the eigenfrequencies, it can be observed that the first three slightly decrease by the influence of the acoustic cavities. This is due to the added mass effect of the air surrounding it. The air is pumped between the bulbs of the vibration shape, which increases the effective mass of the vibrating system. The cooling passage has more influence than the combustion chamber in this geometry.

The fourth eigenmode has a somewhat stronger change in eigenfrequency than the first three and this eigenfrequency now increases. The mode shape in figure 4.22 shows that this is a volumetric mode. When the structure vibrates

Model	**1** pp (1)	**2/3** pc (1)	**4** cc (1)	**5/6** ac1	**7** pp (2)	**8/9** pc (2)	**10** pp (3)	**11** ac2
Structure only	164.4	256.9	372.7	-	657.6	832.3	1027	-
Combustion chamber	163.8	255.1	390.4	-	656.0	825.3	1019	-
Cooling passage	161.5	244.9	401.8	537.1	654.1	833.4	955.8	1080
Full model	160.9	243.4	418.0	536.7	652.5	826.2	952.8	1075
Cooling passage only	-	-	-	518.1	-	-	-	1008

Table 4.6: Influence of cavities on the eigenfrequencies of the finite element model.

the volume of the cavity 'breathes'. The cavities act as springs and therefore increase the eigenfrequency. Again, the cooling passage has the strongest influence.

Beyond the first acoustic eigenfrequency (mode 5/6), the interaction between the vibrating structure and the acoustic cavities becomes more complex, because structurally dominated and acoustically dominated modes become more tightly coupled [5]. This can for instance be seen for mode 8/9, the eigenfrequency of which increases due to the cooling passage, but decreases due to the combustion chamber.

Influence of the cavities on the vibration amplitude

To evaluate the influence of the acoustic cavities on the vibration amplitudes, a harmonic force, with the same amplitude for all frequencies, is prescribed at the location shown in figure 4.23. As measure of vibration level, the spatial root-mean-square (rms) value of the velocity of all the nodes on the structure is used (similar to equation (4.8)). These values are calculated using a separate harmonic calculation for each frequency. Figure 4.23 also shows the rms value with and without the acoustic cavities.

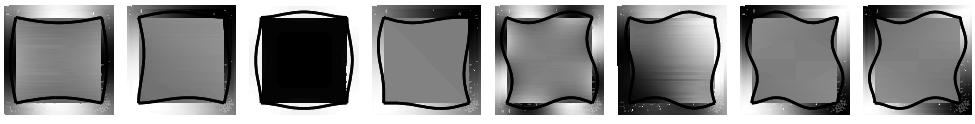

Figure 4.22: Eigenmodes of the two-dimensional system. Black means high acoustic pressure, white low acoustic pressure. The contour represents the vibration shape of the liner.

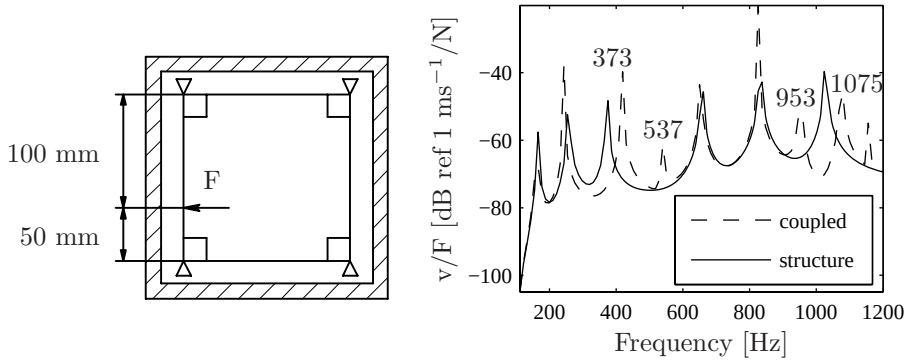

Figure 4.23: Force position (left) and vibration response of liner (right).

It can be seen that the eigenfrequencies at 537 Hz and 1075 Hz are only present for the cases with the cooling passage, because these are eigenfrequencies of the cooling passage. These acoustic eigenfrequencies of the cooling passage lead to sharp increases in the vibration level of the liner around these frequencies.

The structural eigenfrequency at 373 Hz increases due to the presence of the acoustic cavities. The other eigenfrequencies also behave as predicted with the modal analysis. The overall vibration level remains largely the same. In general, the effective mass and stiffness of the system do not change much, they only change around eigenfrequencies of the structure and the acoustics. Furthermore, there is no damping in the model to influence the vibration level.

Around the second resonance of the cooling passage (at 1075 Hz), the influence on the structural behavior is also very strong. The acoustic resonance induces high vibration levels and the high vibration peak without acoustic cavities moves to a different frequency. This strong interaction occurs because acoustic and structural modes match in this frequency region.

Figure 4.24 shows the response of the structure to a prescribed harmonic volume source in the combustion chamber. The first structural eigenfrequency is not visible and the second only slightly. Because the maximum excitation frequency of 1200 Hz is still below the first acoustic eigenfrequency of the two-dimensional combustion chamber, the volume source induces an almost constant pressure field in the cavity. This field does not couple with the vibration shapes of the first two structural eigenfrequencies, which therefore do not show up in the transfer. The volumetric mode 4 is very clearly present, including the increase in frequency when adding the cooling passage, for it matches very well with a constant pressure field.

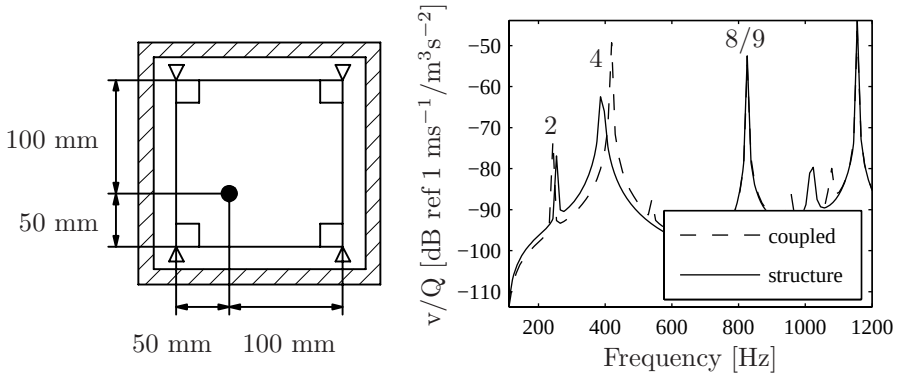

Figure 4.24: Acoustic source position (left) and vibration response of liner (right).

Mode 8/9 is also strongly present at 826 Hz, although this mode does not have a volumetric component. This is because the frequency is such, that the pressure field is not constant over the combustion chamber anymore. An acoustic pattern develops that couples well with the vibration shape and is highly similar to the mode pattern depicted in figure 4.22.

Influence of the structure on the acoustic behavior

Table 4.6 also contains the acoustic eigenfrequencies when the cooling passage is modeled without the structure and all boundaries are modeled as acoustically hard. The acoustic eigenfrequencies of the cooling passage hardly change when adding the structure.

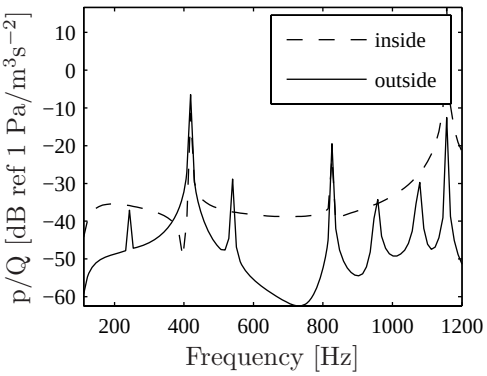

Figure 4.25: Spatial rms pressure in the cooling passage compared with the spatial rms pressure in the combustion chamber.

Figure 4.25 is a result of the two-dimensional model excited by a volume source in the combustion chamber. It shows the spatial rms value of the pressure in the combustion chamber and in the cooling passage. The pressure in the cooling passage is in general substantially lower than in the combustion chamber. The first notable exception is around the fourth eigenfrequency, which belongs to the volumetric structural mode. The pressure on the inside has a peak, but the pressure in the cooling passage also shows a high peak. A second frequency of high acoustic response in the cooling passage is found at the first acoustic eigenfrequency of this passage. For higher frequencies there are more peaks visible, which are associated with eigenfrequencies of the structure and the cooling passage. The reason that this does not happen for lower frequencies is again that the acoustic field hardly couples with the structural vibration pattern. The acoustic pressure in the cooling passage thus depends on the proximity of structural eigenfrequencies to the excitation frequency and the coupling of the pressure field with the structural vibration pattern.

4.5.3 Three-dimensional model

To further examine the behavior of the liner, a simplified three-dimensional model is constructed. It uses the structural model of section 4.4.3, which is the model of only the thin part of the structural liner, clamped at the inlet and outlet side (figure 4.26). This differs from the two-dimensional boundary conditions in the previous section (this model was pinned at the corners, figure 4.20). The acoustic part of the model consists of the acoustic cavities up to the boundaries of the thin section. The acoustic boundaries are modeled as acoustically hard. The dimensions are the same as those of the two-dimensional model (tables 4.3 and 4.5). The eigenmodes and eigenfrequencies of the system are discussed first, after which the response to force excitation and excitation with a volume source is treated. The influence of the assumed acoustically hard boundaries is also discussed.

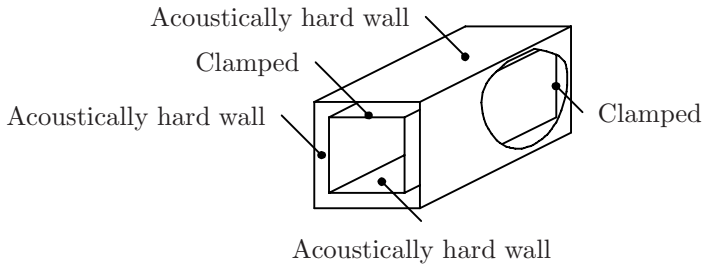

Figure 4.26: Boundary conditions of the three-dimensional model.

Influence of the cavities on the eigenmodes

Analogous to the two-dimensional model, the acoustic cavities at the inside and the outside cause a decrease of the eigenfrequencies (table 4.7), except for the eighth mode, since this is the first volumetric mode. The changes are smaller than in the two-dimensional model. The reason is that the vibration amplitudes are zero at the clamped boundaries in the three-dimensional case. The cavities can therefore only influence the vibration at parts in the lengthwise direction where the vibration amplitudes are high.

Model	**1** $(11)_{ss}$	**2/3** $(11)_{h}$	**4** $(12)_{ss}$	**5/6** $(12)_{h}$	**7** ac1	**8** $(11)_{cc}$	**9** $(13)_{ss}$	**10** $(12)_{cc}$
Structure only	196.8	280.5	287.0	355.3	-	390.3	426.9	448.9
Full model	195.3	275.1	285.2	351.3	392.0	401.7	424.7	474.7
Lower cooling passage	194.3	271.6	284.1	348.6	379.1	409.4	423.5	501.2

Table 4.7: Eigenfrequencies for the three-dimensional model.

The mode shapes (figure 4.27) show that adding the acoustic cavities hardly influences the mode shapes.

Table 4.7 also shows the calculated eigenfrequencies for a model with a cooling passage of 10 mm instead of 20 mm (lower cooling passage). The change in eigenfrequency is now stronger, approximately twice the difference between no cooling passage and the 20 mm passage. No other change in the eigenfrequencies and eigenmodes is observed.

Influence of the cavities on the vibration amplitude

Figure 4.28 shows the rms vibration level of the liner, due to a force on the liner, for the three-dimensional model. The shift in eigenfrequency of the volumetric mode is visible around 400 Hz.

Figure 4.29 shows the vibration response due to a volume source in the combustion chamber with and without the cooling passage. The structural eigenfrequencies are again only slightly visible because they do not couple well with the generated pressure field, whereas the volumetric modes are strongly present. The overall vibration level becomes only slightly lower due to the added stiffness of the cooling passage.

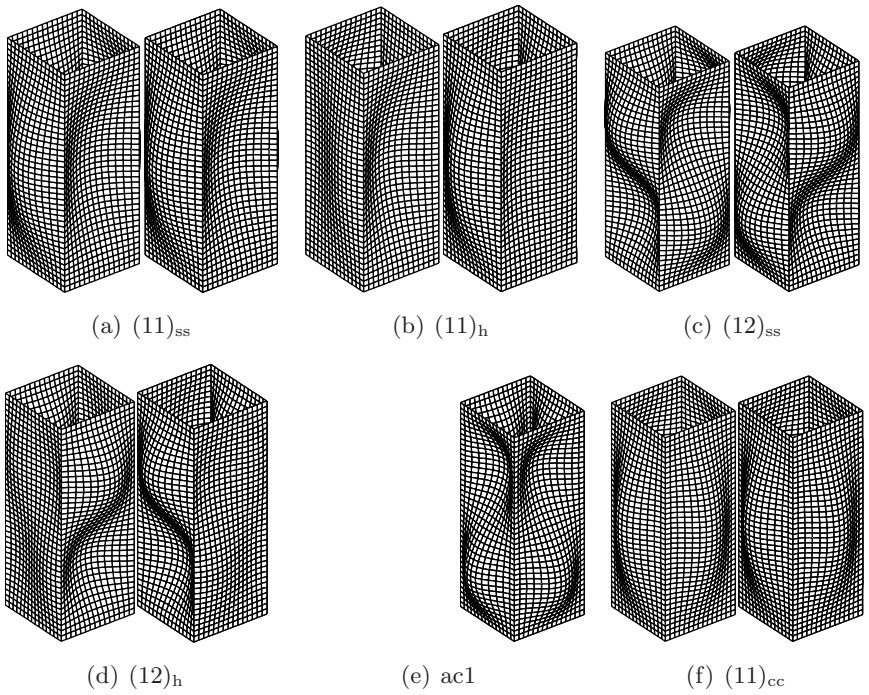

(a) $(11)_{ss}$ (b) $(11)_{h}$ (c) $(12)_{ss}$

(d) $(12)_{h}$ (e) ac1 (f) $(11)_{cc}$

Figure 4.27: Structural displacement for the three-dimensional model, left is the structural model, right is the coupled model.

Influence of the structure on the acoustic behavior

Figure 4.30 shows the acoustic pressure in the combustion chamber and the cooling passage for the three-dimensional model excited by a volume source. Below 400 Hz, the pressure in the cooling passage is lower than in the combustion chamber. Structural modes hardly increase the pressure generated in the cooling passage. This changes around 400 Hz. This is near the first eigenfrequency of a volumetric mode and also near the first acoustic eigenfrequency of the cooling passage. These two effects cause the strong increase in induced pressure. Above 400 Hz the pressure remains high. Therefore, the general conclusion is that high acoustic pressures in the cooling passage are only induced when volumetric structural modes are present or the cooling passage has acoustic eigenfrequencies in the range of the excitation frequency.

For energy losses through the structure, a similar conclusion can be drawn. Assuming that the energy losses in the structure are small, energy can be lost from the combustion chamber through the structure. This is done by

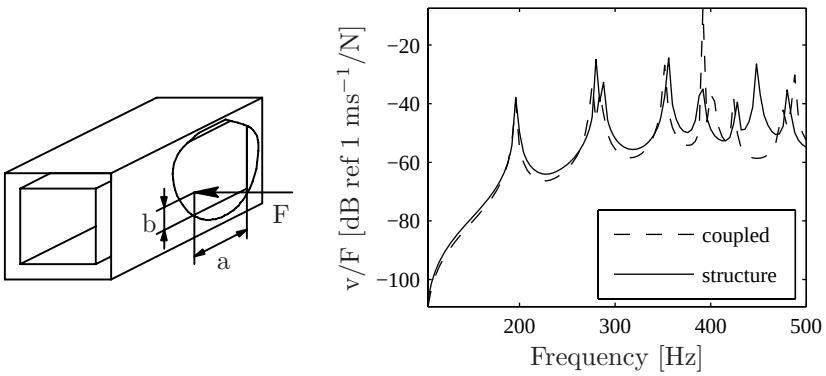

Figure 4.28: Force position (left, a=133.3 mm and b=50 mm) and vibration response of liner to this force (right).

generating an acoustic field in the cooling passage that is dissipated at the boundaries of the cooling passage. This phenomenon is only important when significant pressure levels are induced in the cooling passage.

Influence of acoustic boundary condition on the vibration response

Figure 4.31 shows another response of the structure to a volume source. In the models so far, all acoustic boundaries were acoustically hard. In the model used here, the inlet and outlet of the cooling passage are anechoic, so all acoustic waves are absorbed at this end. The inlet and outlet of the combustion chamber

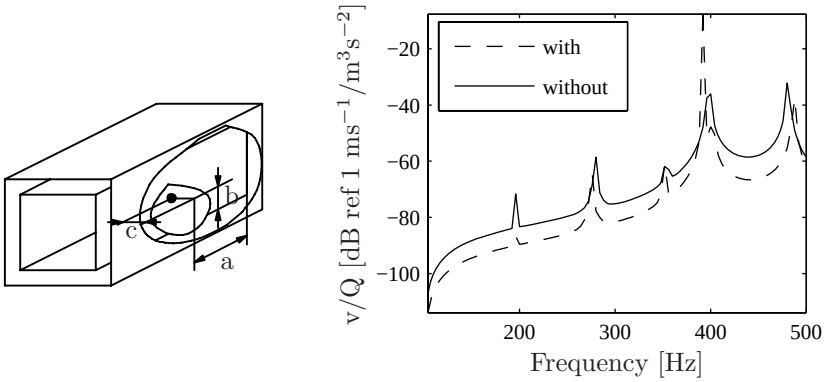

Figure 4.29: Volume source position (left, a=133.3 mm, b=50 mm and c=50 mm) and vibration response of liner to this source with and without the cooling passage (right).

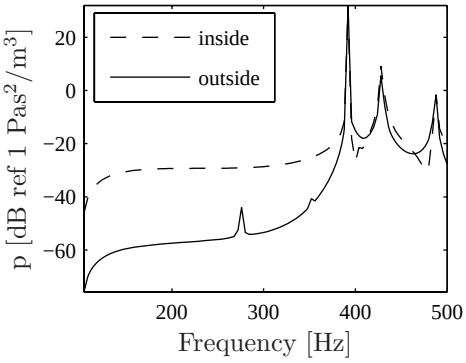

Figure 4.30: The rms pressure in the cooling passage compared with the rms pressure in the combustion chamber for the three-dimensional model.

are kept acoustically hard, to maintain more or less the same acoustic response of the combustion chamber as in figure 4.29. The results for the echoic and the anechoic cooling passage are compared. The reason for this comparison is that the cooling passage of the real setup continues beyond the structural section and therefore there is no full acoustic reflection. Substantial absorption of acoustic waves can take place by turbulent effects, which are modeled by imposing acoustic absorption. It is known from the literature that acoustic absorption can increase structural damping [21].

The figure shows that, below 400 Hz, there is very little difference between the two models. This is because the acoustic pressures induced in the cooling passage are very small below this frequency. Above this frequency the vibration amplitudes are substantially damped, because all pressure waves generated by the structure are absorbed at the anechoic ends. Therefore, it seems that substantial damping can be induced by the cooling passage.

4.5.4 Full geometry

To determine the behavior of the actual setup, a model with a more complex geometry is used. It consists of a combination of the acoustic model developed in chapter 3 (which includes the plenum, burner and water cooler geometry) and the structural model of section 4.4.3, which was also used in the previous sections. As a first check on the correctness of the model, the eigenfrequencies of these separate models are compared with those calculated using the full model.

Table 4.8 lists the acoustic eigenfrequencies of the acoustic model, the coupled model and the experiment. The results for the acoustic model are those of

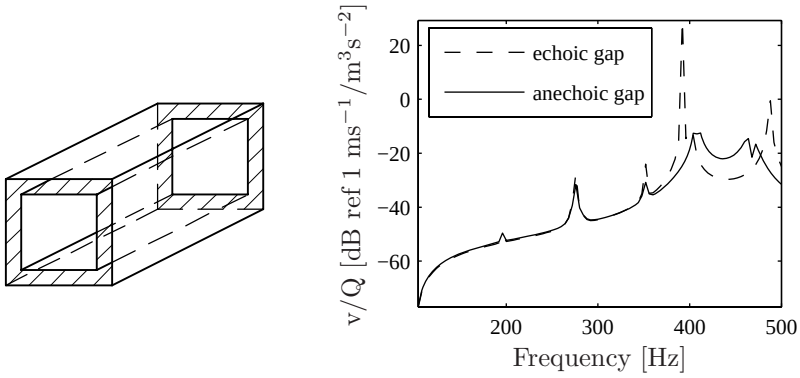

Figure 4.31: Position of the anechoic boundary conditions (hatched, left) and vibration response of liner to a volume source (right).

section 3.3.2 and the experimental results are the same as those in section 3.5. The numerical results are quite similar, with the same modes showing up at similar eigenfrequencies. Most frequencies decrease a little, which is probably due to the slightly different mesh. An exception is the (400) acoustic mode. This mode is very close to a volumetric structural mode ($(11)_{\mathrm{cc}}$), which causes a stronger interaction between these modes. The influence between structure and acoustics, when looking at eigenfrequencies, is only small. It should be noted that the cooling passage is not included in this model. It is likely that the influence of the cooling passage is similar to that of the more simple model in section 4.5.3.

Figure 4.32 shows the numerically calculated mean response of the liner to acoustic excitation (a prescribed pressure at the water cooler is used again, see section 3.5) and also the mean vibration divided by the mean pressure at the sensor locations (p_1, p_2, p_3 and p_4, see also figure 2.10). In the structural response plot, the acoustic eigenfrequencies are depicted by vertical dashed lines. The high vibration levels are all related to the acoustic eigenfrequencies

Model	Cooler	Plenum	$(100)_{\mathrm{a}}$	$(200)_{\mathrm{a}}$	$(300)_{\mathrm{a}}$	$(400)_{\mathrm{a}}$	$(500)_{\mathrm{a}}$
Acoustic	43.4	85.1	131.7	213.2	305.2	391.4	484.0
Coupled	43.2	84.8	131.4	212.4	302.4	385.8	479.9
Experiment	46.0	83.0	130.0	218.0	306.1	396.0	463.0

Table 4.8: Acoustic eigenfrequencies of the combustion chamber for the acoustic model, the coupled model and the experiment.

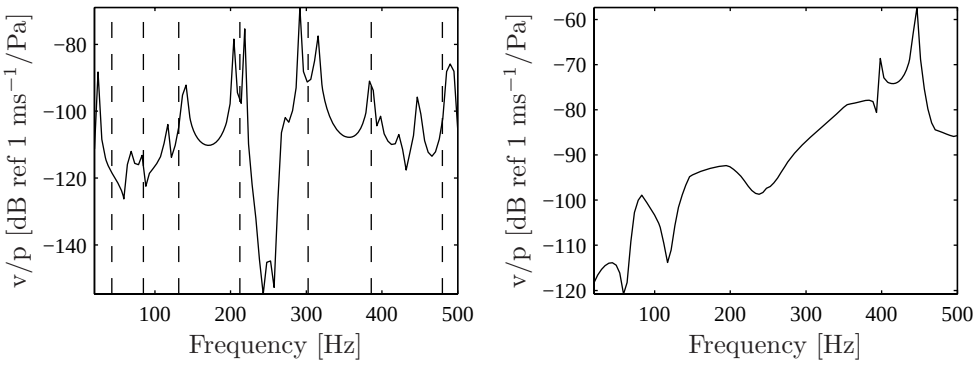

Figure 4.32: Structural response of the full FEM model to a prescribed pressure at the water cooler (left) and the structural response divided by the mean value of the pressure at the locations of the pressure sensors in the combustion chamber (right).

of the combustion chamber. This is confirmed by the mean vibration divided by the average pressure. This spectrum does not show sharp peaks below 400 Hz. The only clear peak is the one at 450 Hz which belongs to the $(12)_{\mathrm{cc}}$ structural mode. It was already shown in section 4.5.3 that only volumetric modes couple well with the pressure field developed.

Model	$(11)_{\mathrm{ss}}$	$(11)_{\mathrm{h}}$	$(12)_{\mathrm{ss}}$	$(12)_{\mathrm{h}}$	$(11)_{\mathrm{cc}}$	$(13)_{\mathrm{ss}}$	$(12)_{\mathrm{cc}}$
Structural	196.8	280.5	287.0	355.3	390.3	426.9	448.9
Coupled	196.3	279.5	286.4	354.2	395.6	426.1	450.7
Acoustic exp.	225	315	300	367	-	414	-
Structural exp.	224		312	-	-	408	-

Table 4.9: Numerical eigenfrequencies for the structural model, coupled model and for the acoustically excited experiment.

4.5.5 Experimental validation

Two experiments made on the test rig are discussed in this section: one with structural excitation, using a shaker, and one with acoustic excitation, similar to the experiment described in section 3.5.

To excite the thin part of the liner inside the pressure vessel structurally, a Plexiglas window was mounted in the setup, in which two holes are available (a schematic drawing is given in figure 4.33). One hole was used to attach a shaker

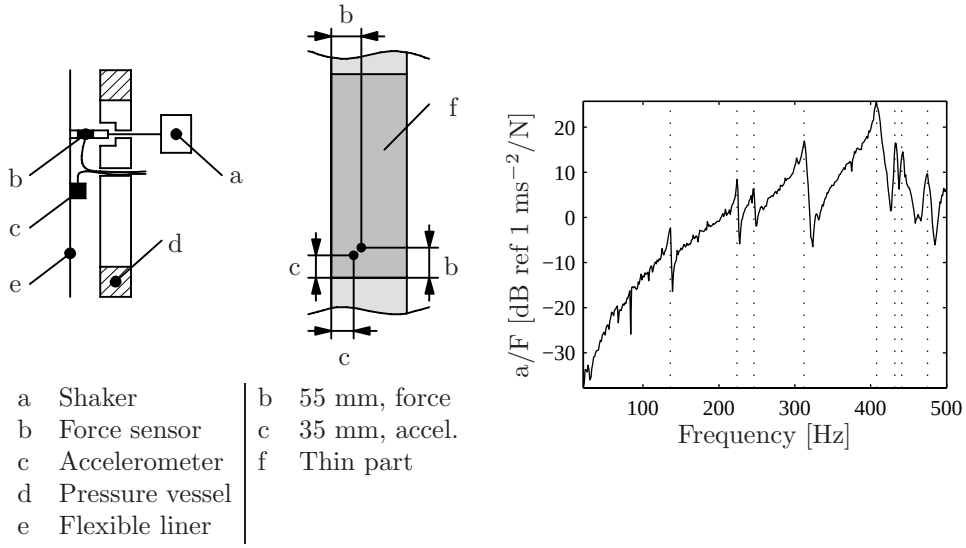

a	Shaker	b	55 mm, force
b	Force sensor	c	35 mm, accel.
c	Accelerometer	f	Thin part
d	Pressure vessel		
e	Flexible liner		

Figure 4.33: Experimental configuration (left) and measured acceleration response on the liner due to force excitation. Dashed lines denote eigenfrequencies.

to a force sensor mounted on the flexible part of the liner. The attachment point is 55 mm above the lower weld and 55 mm away from the left side of the liner (figure 4.33). The second hole was used for the wiring of the force sensor and an acceleration pickup, which is located 35 mm above the lower weld and 35 mm from the side of the liner. This window assured that the liner is still almost fully covered by the pressure vessel. Due to the holes, experiments can only be performed at atmospheric pressure. The transfer from force to acceleration is also depicted in figure 4.33.

For experiments with the liner inside the pressure vessel, excited by an acoustic field, the setup described in section 3.5 is used. The acoustic source mounted at the water cooler generates an acoustic field that propagates from the water cooler to the combustion chamber and excites the liner. Furthermore, the acoustic field also propagates to the cooling channel. The response of the liner is measured on the slit window (section 2.5.3).

Figure 4.34 shows the mean of the acoustic pressure amplitude measured by the sensors in the cooling channel and the combustion chamber. The pressure amplitudes are similar. The reason is that the acoustic source is attached to the water cooler. The acoustic field generated in the water cooler propagates through the CFD tube to the combustion chamber. Subsequently, the induced structural vibration of the liner generates an acoustic field in the cooling chan-

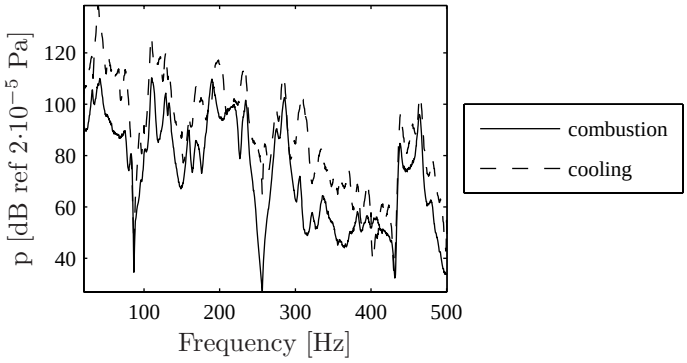

Figure 4.34: Measured pressure in the cooling passage (mean of the amplitudes of p_5 and p_6) and the combustion chamber (mean of the amplitudes of p_1, p_2, p_3 and p_4).

nel. However, acoustic waves can also travel through the bypass through which the cooling air normally flows to the water cooler. The cross-sectional areas of the CFD tube and the cooling air hoses are similar and therefore the acoustic fields generated in the combustion chamber and the cooling passage are of similar magnitude.

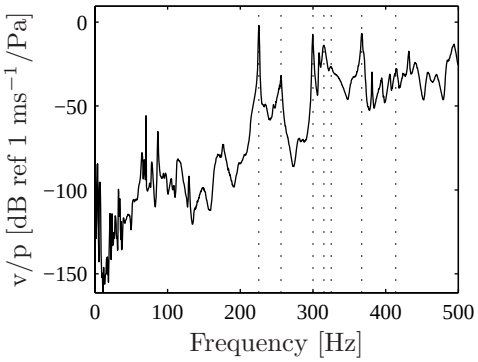

Mode	**f** [Hz]
$(11)_{ss}$	225
Squeeze	256
$(12)_{ss}$	300
$(11)_{h1}$	315
$(11)_{h2}$	325
$(12)_{h1}$	367
$(13)_{ss}$	414

Figure 4.35: Mean value of the vibration level measured through the slit window divided by the mean pressure measured with sensors p_1, p_2, p_3 and p_4, all due to acoustic excitation. Dotted lines are assumed eigenfrequencies.

Figure 4.35 shows the mean value of the vibration level measured through the slit window divided by the mean pressure autospectrum measured with sensors p_1, p_2, p_3 and p_4, which are all located in the combustion chamber. Because the vibration level is divided by the mean pressure, this plot gives an

indication of how strongly the structure responds to an acoustic excitation and therefore peaks in the plot can be related to structural eigenfrequencies. It is difficult to assess which peaks are structural eigenfrequencies of the flexible section. They can also be related to resonances of other parts of the setup, or anti-resonances of the pressure signal. An attempt is made nevertheless. The dotted lines depict the assumed structural eigenfrequencies which are listed in the table next to the figure.

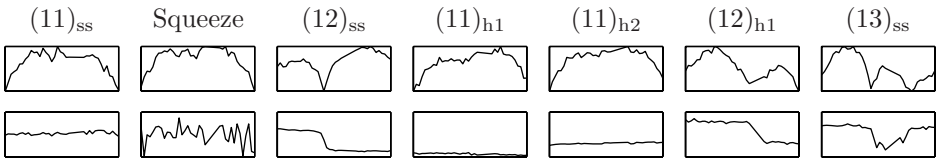

Figure 4.36: Amplitude and phase (with respect to p_1) of the vibration measured through the slit window for the different eigenfrequencies of figure 4.35 (total length of the plot is 35 cm).

The amplitude and phase of the vibration as a function of location in the slit is depicted in figure 4.36. The measured mode shapes correspond fairly well with the calculated shapes.

Comparing the eigenfrequencies found in these experiments with the experimental modal analysis described in section 4.4.4, it can be seen that the resulting eigenfrequencies have changed strongly. There are two reasons for this. The first is that the liner is now mounted inside the setup. The acoustic cavities influence the vibration behavior. Furthermore, the sliding connection between the liner in the combustion section and the structural liner, as well as the pressure sensor mountings on the liner influence the structural behavior. A second reason for the change is that, between the modal analysis of the liner outside the setup and the structural analysis of the liner in the pressure vessel, the setup was fired several times. It is likely that the vibration behavior is influenced by this firing. This second cause can be the reason why even structural excitation and acoustic excitation measurements do not give the same results, because there was substantial time and several firings between these measurements.

The permanent effect of temperature (and probably also vibration [71]) on the vibration behavior of the liner is supported by a measurement made on the liner outside the pressure vessel. The transfer from force to acceleration was measured before and after annealing (a heat treatment used to decrease thermal stresses) the liner. The results are depicted in figure 4.37. The vibration response has already changed substantially, with structural eigenfrequencies

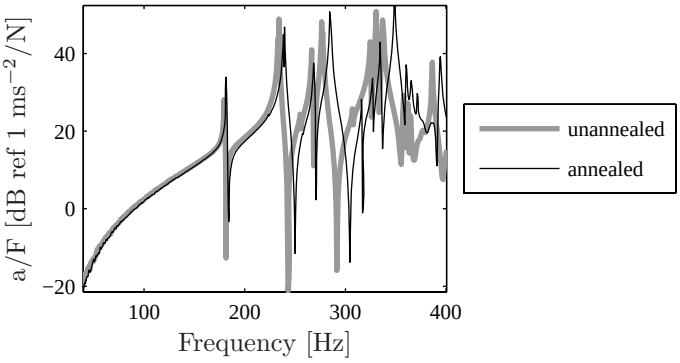

Figure 4.37: Structural response outside the pressure vessel before and after annealing.

moving towards higher frequencies. This can be caused by a decrease in prestresses, oxidization of the surface adding stiffness to the structure or to plastic deformation of the liner by thermal stresses or stresses induced by a pressure difference over the liner.

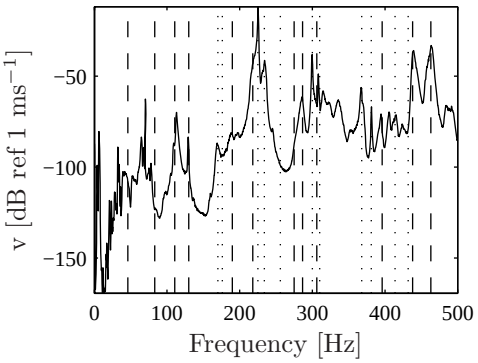

Figure 4.38: Average vibration level of the liner measured through the slit window. Dashed lines denote acoustic eigenfrequencies and dotted lines structural eigenfrequencies.

As last results from the measurements, figure 4.38 shows the average vibration level of the liner. The vibration level around 230 Hz is very high. This is because an acoustic eigenfrequency (the (200) mode of the combustion chamber) is very close to the $(11)_{ss}$ structural modes.

4.5.6 Other interaction effects

This section treats other effects that relate to the interaction between the fluid and the structure. An indication of the influence of flow on the acoustic properties is first given. This is followed by experimental results on turbulent excitation of the structure by the flow without combustion.

Influence of flow

To obtain an indication of the influence of flow on the structural behavior, the setup with the Plexiglas window was used again (section 4.5.5). Because the leakage through the holes in the window is limited, the transfer from force to acceleration could be measured with (cold) flow at atmospheric pressure in the combustion chamber and the cooling passage, and also without flow.

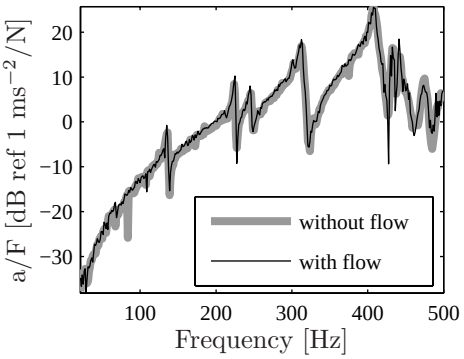

Figure 4.39: Acceleration response due to a force without flow and with a flow equivalent to the 10.4 case (100 kW at 1 bar).

Figure 4.39 shows the measured transfer from force to acceleration for two cases. The first is without flow and the second with flow in the cooling passage and the combustion chamber equivalent to 100 kW thermal power at 1 bar with a ratio of cooling air to combustion air of 1, which is the value normally used in the combustion experiments. At this point the flow speed in the combustion chamber is approximately 2.5 m/s and 4.0 m/s in the cooling channel. The difference between the two measured transfers is hardly visible. The rms value of the transfer from force to acceleration of both measurements is almost identical, being 0.34 without flow and 0.36 with flow. Therefore, it can be concluded that, in this setup, the turbulent flow hardly influences the structural response of the liner.

Turbulent excitation of the structure

The flow inside the combustion chamber and the cooling passage is highly turbulent and therefore the structure can be excited by this turbulence. Figure 4.40 shows the acoustic pressure levels measured with a cold flow (293 K) equivalent to a 100 kW flame at 1 bar. The pressure in the cooling passage is measured using pressure sensor p_6 and the pressure in the combustion channel is the average of the pressures measured by pressure sensors p_1 to p_4.

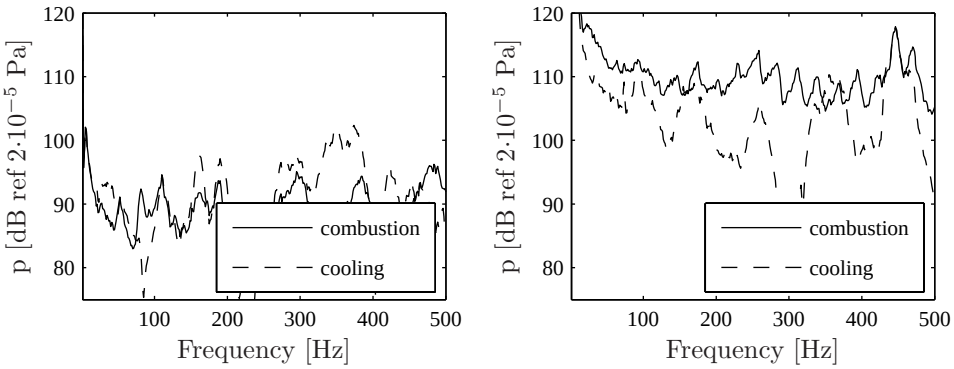

Figure 4.40: Measured turbulent excitation pressure in the combustion chamber and the cooling passage during cold flow (left) and during combustion at case 15.4 (right).

The pressure levels for turbulent excitation are mostly between 90 and 100 dB (figure 4.40), both in the combustion chamber and in the cooling passage. During combustion the pressure levels in the combustion chamber are between 110 and 120 dB, which is a factor ten higher. The turbulent excitation of the structure for cold flow is therefore weaker than the excitation generated by the flame. If the turbulent excitation is similar in the hot flow, then the flame excitation is the dominant excitation mechanism during combustion.

The structural response is depicted in figure 4.41. It can again be seen that the structural response due to turbulent excitation is smaller than the response due to excitation by a force and by the flame.

4.6 Concluding remarks

In this chapter, structural vibration and the interaction with acoustics was discussed. A finite element method with two-way coupling was used. The method was validated on a simple test object; a stiff aluminum box covered

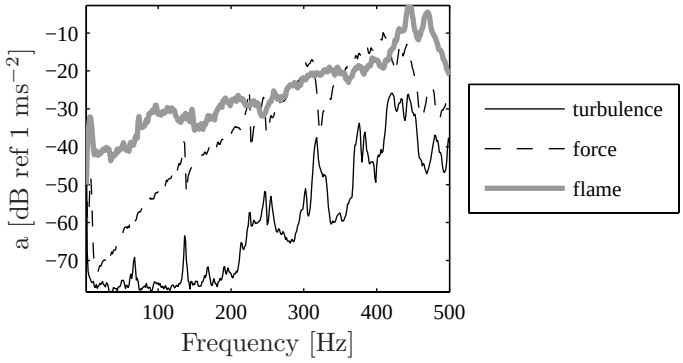

Figure 4.41: Structural response (acceleration) due to different excitations.

by a flexible aluminum plate. The interior acoustics of the box was excited through a hose, giving a boundary with prescribed pressure for the model. The correspondence between the measured and calculated modes, both acoustic and structural, is excellent, which is also the case for the transfer functions between pressure in the box and vibration of the front plate. If the structure and acoustics can be modeled accurately, the results of the coupled finite element model are therefore proven to be accurate.

A structural model was subsequently developed of the liner part on which the vibration is measured. This part consists of a thin, square tube welded between two square, thicker parts. Each of the three square parts is welded out of two bended plates. Experimental modal analysis was performed on this section outside the test rig to determine the mode shapes and eigenfrequencies. The welds make a comparison between the model and the measurement difficult, but both show behavior that is very similar, which makes the model suitable to predict the structural behavior of the test setup. It was also shown that the influence of temperature on the structural vibration is not very strong. Prestress in the structure, caused by a pressure difference over the liner, in general causes bending stresses, which have little influence on the structural vibration. On the other hand, prestresses due to confined thermal expansion cause in-plane stresses, which can influence the behavior of the liner.

The interaction between the vibration behavior of the liner and the acoustics of the combustion chamber and the cooling passage was studied with several models of increasing complexity [44]. A two-dimensional model of a cross section of the test rig and a three-dimensional model of the thin, flexible part of the liner were made. Both models include the acoustics of both the combustion chamber and the cooling passage. The acoustics of the cavities add stiffness

to the structural behavior for volumetric modes and mass for non-symmetric modes. When acoustic modes arise in the cooling passage or combustion chamber, this behavior becomes more complex. The vibration amplitude of the liner can become somewhat lower due to the added stiffness of especially the cooling passage. Damping can be added to the structure if there is significant acoustic dissipation in the cooling passage. This can decrease the vibration amplitudes under structural resonance. Asymmetric structural modes are hardly excited by the acoustics of the combustion chamber, because asymmetric modes do not couple with the more or less one-dimensional pressure field in the combustion chamber.

Matching of the experimental and numerical results is rather difficult. Important reasons for this include the welds in the liner that strongly influence the vibration behavior. Furthermore, when the test rig is fired, the structural behavior of the liner changes permanently. An exact match was therefore not attempted. When the test rig is acoustically excited, the structural behavior is similar to the behavior of the model and similar mode shapes were measured. It is therefore likely that the model can be used to predict trends in behavior, though it may not provide exact quantitative data. Measurements made with flow in the cooling passage showed that there is hardly any difference compared with the structurally excited measurements without flow. The turbulent excitation caused by the flow is also much lower than that of a flame or structural force.

Chapter 5

The fired setup

5.1 Introduction

The purpose of the previous chapter was to gain insight in acousto-elastic interaction. In this chapter, the flame as acoustic volume source is added to the acoustic and coupled models. A numerical model of the temperature field created by the flame and its influence on acoustic behavior was already discussed in 3.3.8. The influence of temperature on vibration behavior was introduced in (section 4.4.5). In section 5.2, combustion noise is discussed, in which the flame is considered as an autonomous source of sound, that is, it does not respond to the acoustic field it produces. Calculated pressure spectra are compared with pressures measured in the test rig during combustion. The acoustic response to a perturbed fuel flow is also discussed, as well as the differences in acoustic behavior of the test rig that were seen between different measurement sessions. Section 5.3 treats the response of the liner during combustion. A comparison is made between the eigenfrequencies for the cold and the hot cases and measured and calculated eigenfrequencies and eigenmodes of the liner are compared. A calculation is also made of the response of the liner to pressures on the wall calculated by large eddy simulation (so-called LES). After the flame as passive source, the flame as active source is considered in section 5.4, in which the flame as source reacts to the acoustic field it causes (this is therefore a form of full coupling, where the flame as passive source is a form of one-way coupling). A transfer function based approach is used to evaluate the influence of feedback on the acoustics of the combustion chamber. The chapter finishes with some remarks on the differences between the test rig used in this thesis and industrial annular combustors.

5.2 Acoustic response during combustion

5.2.1 Introduction

This section treats the acoustic behavior of the combustion chamber during combustion, both numerically and experimentally. The temperature influence on the acoustic behavior was already studied numerically in section 3.3.8. In this section, the eigenmodes that were found are compared with experimental values. The acoustic responses in the plenum and combustion chamber are also treated in this section. The acoustic response when the fuel flow rate is modulated, is treated both numerically and experimentally. The behavior of the liner during combustion is treated in the next section.

5.2.2 Acoustic eigenmodes

In the test rig, pressure signals are measured with the pressure sensor assembly discussed in section 3.4. Autospectra are calculated from the stored time signals. From these autospectra, the acoustic eigenfrequencies of the combustion chamber can be determined. Using the average of the autospectra of all the sensors in the combustion chamber (p_1, p_2, p_3 and p_4, see also figure 2.10) removes the influence of pressure nodes at a sensor. Figure 5.1 shows this average autospectrum for two different operating points, 15.4 and 15.7 (table 3.1). During the measurement for case 15.4 , only sensors p_2 and p_3 were functioning well and only these two sensors are used for the average autospectrum.

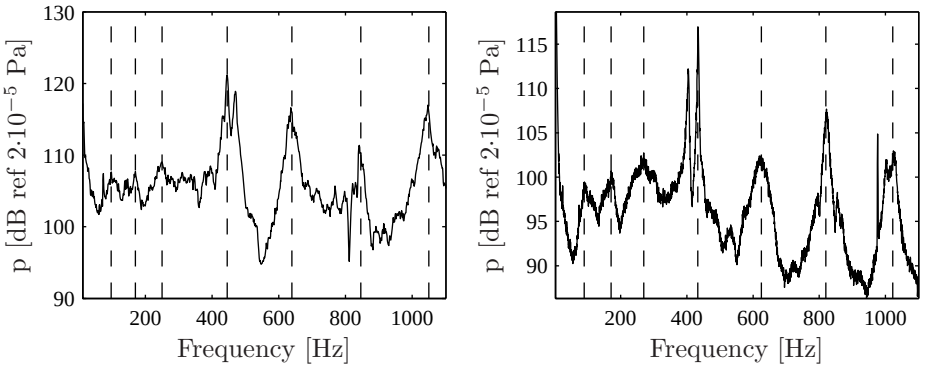

(a) Case 15.4.

(b) Case 15.7.

Figure 5.1: Average pressure measured by the pressure sensors in the combustion chamber. Dashed lines denote measured acoustic eigenfrequencies (table 5.1).

It is expected that only the acoustic modes of the combustion chamber and the Helmholtz-like modes can be identified using the acoustic response in the combustion chamber caused by a steady flame. Figure 3.9 shows the numerically predicted acoustic response to a volume source representing the flame. This figure supports the assumption that the acoustic response is strongly dominated by the acoustic eigenmodes of the combustion chamber.

Table 5.1 lists the acoustic eigenfrequencies of the combustion chamber for three different operating points. The LES results were calculated by CERFACS for the same geometry, but without the water cooler, using the temperature field from an LES calculation including heat losses in a Helmholtz solver [87]. The FEM results are calculated using the model from section 3.3.8, in which the results for operating points 15.7 were already listed.

	15.4		**15.7**			**30.5**
Mode	**FEM**	**Exp.**	**FEM**	**Exp.**	**LES**	**Exp.**
Cooler	79	97	83	90	-	95
Plenum	141	170	146	171	-	175
$(100)_a$	259	250	261	270	250	240
$(200)_a$	432	445	436	433	443	482
$(300)_a$	622	639	627	625	642	632
$(400)_a$	812	846	818	820	844	858
$(500)_a$	1011	1050	1017	1022	1045	1050

Table 5.1: Acoustic eigenfrequencies of the combustion system [Hz] during combustion.

For case 15.7 (125 kW thermal power at 1.5 bar with an equivalence ratio of 1.8), the acoustic eigenfrequencies that are predicted show an excellent match with the experimentally determined ones. The LES results are similar to the results from the combination of RaNS CFD and FEM. The first acoustic eigenfrequency of the combustion chamber is slightly lower, which is due to the slightly different acoustic boundary conditions[1]. The $(100)_a$ mode is sensitive to such changes (section 3.3.4). The other eigenfrequencies are a bit higher in LES, which is caused by slightly higher temperatures in the LES calculation.

For the 15.4 case, which has a thermal power of 150 kW, the results show slightly larger differences, but the match is still good. The numerically predicted eigenfrequencies are slightly lower than those of the 15.7 case, which

[1] In the Helmholtz code, an acoustic particle velocity of zero is prescribed at the inlet of the plenum and a pressure perturbation of zero is prescribed at the outlet of the CFD tube, whereas in the finite element code, the water cooler is included downstream of the CFD tube.

is caused by a small decrease in temperature, because the higher flow speeds increase the heat loss to the wall. The increased flow speed also makes the acoustic boundary conditions in the experiment acoustically harder[1], causing an increase in eigenfrequencies. However, this effect is not accounted for in the finite element model.

For the cases 15.4 and 15.7, figure 5.1 shows that two peaks are visible around the $(200)_a$ mode at about 440 Hz. This is related to unstable behavior, which is discussed in section 5.4.

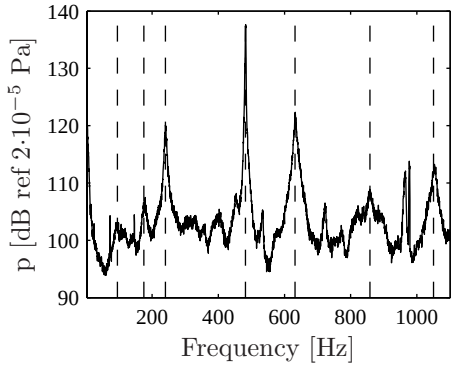

Figure 5.2: Average pressure measured by the pressure sensors in the combustion chamber for case 30.5. Dashed lines denote measured acoustic eigenfrequencies from table 5.1).

The acoustic autospectrum for case 30.5 is shown in figure 5.2. Case 30.5, which has the same flow speeds as 15.4, but a pressure of 3 bar instead of 1.5 bar, has acoustic eigenfrequencies similar to case 15.4. The acoustic equations are not influenced by changes in static pressure, but changes in the heat transfer to the wall, the flame shape and the acoustic boundary conditions cause changes in acoustic eigenfrequencies.

5.2.3 Acoustic response to combustion noise

This section first treats the spectrum of a flame as acoustic source predicted by theory. To extract useful information from sensor signals containing noise, a correlation between two sensors can be applied, which is therefore discussed. Subsequently, measured pressure signals are compared to calculated ones.

[1]Acoustically harder meaning more of the acoustic wave is reflected [3]. This causes a shorter wavelength, as shown in section 3.3.4.

Flame noise theory

The autonomous noise produced by a turbulent flame is caused by the turbulence in the flow. These turbulent fluctuations cause unsteadiness in the reaction rate which causes a volume source (see also section 3.2). Several models exist for the frequency dependence of the heat release rate $\hat{q}$ for combustion noise, which can all be described by:

$$\hat{q} = Bf^n\,, \tag{5.1}$$

in which B is an arbitrary constant and n is the exponent that determines the shape of the spectrum. The relation between the thermoacoustic source term and heat release rate is derived in appendix B. The relation between the acoustic volume source Q used in Ansys and heat release rate $\hat{q}$ is given by:

$$Q = \frac{\mathrm{i}\omega(\gamma-1)}{\rho_0 c_0^2}\hat{q}\,. \tag{5.2}$$

In the literature, the flame noise spectrum is often divided in two frequency ranges, below 1 kHz and above 1 kHz. Using equations (5.1) and (5.2), the Ansys acoustic volume source representation of the flame can therefore be written as:

$$Q = \begin{cases} Bf^{n+1} & \mathrm{f} < 1 \text{ kHz} \\ Cf^{m+1} & \mathrm{f} \geq 1 \text{ kHz} \end{cases}\,, \tag{5.3}$$

in which B and C are arbitrary constants and n and m are the exponents that determine the shape of the spectrum[1]. In appendix B it is shown that for free-field radiation from an acoustic volume source Q, the pressures in the field are proportional to Q. The measured pressure spectrum can therefore be used to determine the exponents m and n. The value of these exponents from different sources in the literature are listed in table 5.2 and figure 5.3 shows the strength of the acoustic volume source representing the flame, as a function of frequency, for three of those models.

Experiments were performed on the Desire test rig measuring CH* radicals using chemiluminescence [48]. The presence of CH* is a qualitative measure of heat release rate [37]. The spectrum created from these measurements is almost flat, suggesting that, for the frequency range measured (up to 400 Hz), the heat release spectrum is flat. The parameter n is therefore taken 0, as suggested by Flemming, Van Kampen and Rajaram and Lieuwen [33, 48, 80]. The volume source for Ansys is therefore given by:

$$Q = Bf\,. \tag{5.4}$$

[1]The exponents are increased by one because of the multiplication with ω in the relation between Q and $\hat{q}$, see also appendix B.

Authors	**Year**	**Ref.**	**Method**	**n**	**m**
Flemming *et al.*	2005	[33]	LES + BEM	0	low
Van Kampen	2006	[48]	Chemiluminescence	0	–
Kok and De Jager	2006	[55]	Imposed	-2.56	-2.56
Rajaram and Lieuwen	2002	[80]	Measured pressure	0	-2.80
Smith and Kilham	1963	[89]	Measured pressure	0.47	-1.41

Table 5.2: Frequency dependence of flame noise from different authors.

Constant B has been obtained by comparing experimental and numerical results for pressure sensor p_2 and is $1{\cdot}10^{-3}$ $\mathrm{m^3 s^{-1}}$. Constant C is not needed, because models and measurements go only slightly above 1 kHz.

The models in table 5.2 are often taken to be valid down to 100 Hz. At frequencies below 50 Hz, the measurements show a strong increase in acoustic pressure levels, which is not studied further, because the structural response is very low at these frequencies (section 4.5).

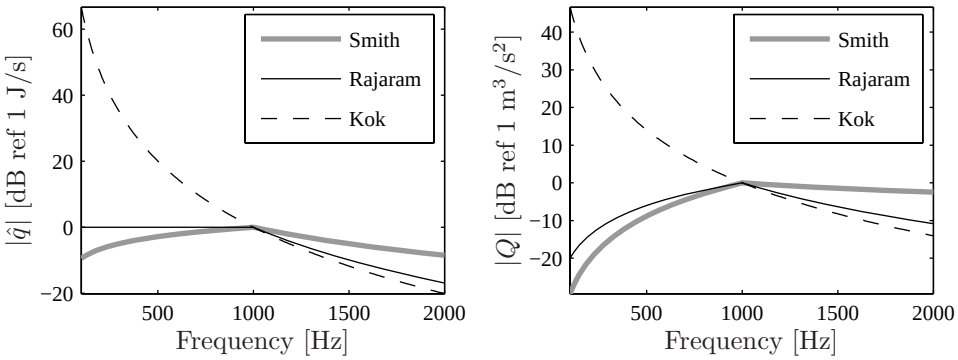

Figure 5.3: Heat release rate (left) and volume source (right) as representation of the flame as autonomous source for several models from table 5.2. The values are normalized to 0 dB at 1 kHz.

Sensor correlation

The signals measured with the pressure sensors in the test rig roughly consist of noise generated by the flame and noise generated by flow. Noise by the flame is measured by all sensors, but flow noise is only correlated very locally and therefore not between the sensors. To suppress flow noise and therefore to obtain only the noise generated by the flame, the coherent part of the autospectrum

is calculated using [1, 59]:

$$G_{ii} = \frac{G_{ij}G_{ji}}{G_{jj}}\,, \tag{5.5}$$

in which G_{ii} is the part of the autospectrum of sensor i coherent with sensor j, G_{ij} is the cross-spectrum between sensors i and j and G_{jj} is the autospectrum of sensor j. As reference sensor j sensor p_3 is used, which is located in the combustion chamber.

Experimental and numerical results

Figure 5.4 shows the pressure measured by sensor p_2, which is located in the combustion chamber (figure 2.10 gives an overview of the sensor locations) and the calculated response of the acoustic finite element model to a volume source representing the flame. In the model, an acoustic absorption factor of 0.5 is prescribed at the outlet through the throttle valve, because significant damping is caused by turbulence effects here (see section 3.4.2 for a description of this acoustic absorption).

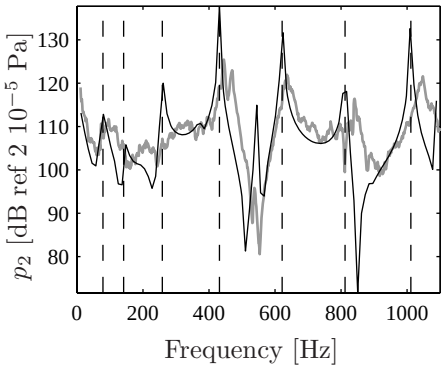

Figure 5.4: Calculated (black) and measured (gray) autospectrum for sensor p_2 (combustion chamber) with flame noise excitation for case 15.4. Dashed lines denote calculated acoustic eigenfrequencies.

For low frequencies, both measurement and calculation show a decreasing acoustic response, followed by several weak resonances related to the water cooler and the plenum. In both measurement and calculation, high acoustic response is found for the second (432 Hz) and higher acoustic eigenmodes of the combustion chamber, which is also observed in the averaged autospectrum in figure 5.1(a). The amplitude of the resonances is higher in the calculations, which is an indication that the damping in the model is lower than in reality. The first acoustic mode of the combustion chamber, which is the $(100)_{\mathrm{a}}$

mode, is not present very strongly, especially in the measurement. This is caused by a feedback mechanism which is treated in section 5.4. Overall, it can be seen that the measured and calculated pressure amplitudes agree well. The acoustic model was already validated in section 3.5. The similar pressure amplitudes therefore prove that the flame model is good for predicting the acoustic response for frequencies below 1 kHz.

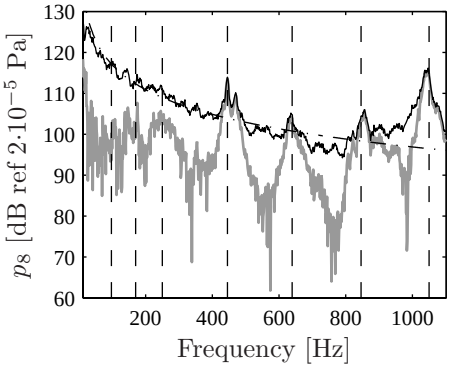

Figure 5.5: Autospectrum for sensor p_8 (plenum) with flame noise excitation for case 15.4. Black denotes the autospectrum, gray the part correlated to sensor p_3 and dash-dotted the noise model. Dashed lines denote measured acoustic eigenfrequencies.

Figure 5.5 shows the pressure measured by sensor p_8, located in the plenum. The autospectrum is dominated by a smooth decline from lower to higher frequencies, which can have two causes. First, such a roll-off is characteristic for turbulent noise. The roll-off is often taken as -10 dB/octave or -14 dB/octave [11, 96]. When a fit is made to the measured data, the roll-off is found to be -6 dB/octave, which is shown with the dashed-dotted line[1]. Noise levels for sensor p_2 are much lower, which can be because sensor p_8 is located directly in the flow and not in a sidetube. A second explanation can be that the cable of sensor p_8 picks up noise. This cable is much longer than those of the other sensors and partially not shielded. When the part coherent with reference sensor p_3, located in the combustion chamber, is taken, the acoustic mode shapes show up again. The signal is therefore still useful.

Figure 5.6 shows the calculated and measured acoustic response to flame noise in the plenum. It again shows that the $(100)_{\mathrm{a}}$ mode at about 250 Hz is hardly present in the measurement. The modes at higher frequencies again match well and the amplitude prediction is also good above 200 Hz. It can

[1] An exponent that is not uncommon for noise [4].

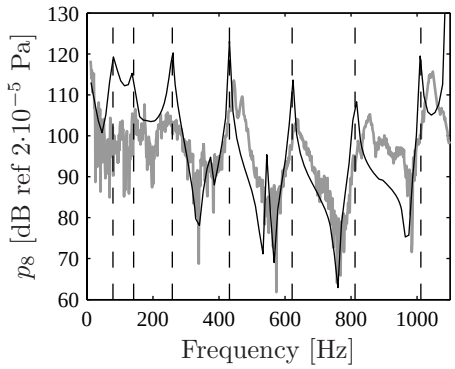

Figure 5.6: Autospectra for sensor p_8 (plenum) with flame noise excitation for case 15.4. Black denotes the calculation and gray the correlated measurement (see figure 5.5). Dashed lines denote calculated eigenfrequencies.

be concluded from the combustion noise measurements that, for case 15.4, the model predicts the behavior of the test rig well. The acoustic eigenfrequencies match well and the acoustic autospectra measured in the combustion chamber and the plenum are similar to those calculated with the model.

5.2.4 Acoustic differences between measurements

The results measured in the test rig are not the same for every measurement, even if the test rig is operated under the same conditions. Figure 5.7 shows the average autospectra measured with the sensors in the combustion chamber for two different measurements. The figure shows that one of the two peaks around 450 Hz has strongly increased in strength. This is caused by a thermoacoustic instability that is building up[1]. The rest of the spectrum is similar, with only a difference in amplitude of roughly 3 dB at lower frequencies. The results can therefore still be used for model validation.

5.2.5 Acoustic response to a pulsated fuel flow

The results in the previous section were measured during steady combustion, which means that the fuel flow is constant. Experiments were also performed with a fuel flow that is perturbed with a MOOG D633-7320 valve [103]. These experiments were performed primarily to determine the flame transfer function. The MOOG valve imposes an oscillation on the fuel flow at the beginning of

[1]Instabilities are caused by a feedback mechanism that is treated in section 5.4.

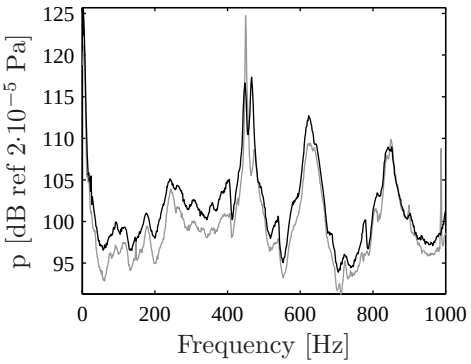

Figure 5.7: Average pressure measured by the pressure sensors in the combustion chamber (p_1, p_2, p_3 and p_4) for case 15.7. Two measurements made during different sessions are shown.

the fuel supply, with a frequency between 0 and 400 Hz. The excitation voltage with which the valve is driven at a specific frequency is chosen such that the fuel perturbation at the fuel injection holes in the swirl tube (see section 2.4.1) is 5% of the total fuel flow. This excitation level can be achieved up to a frequency of 400 Hz.

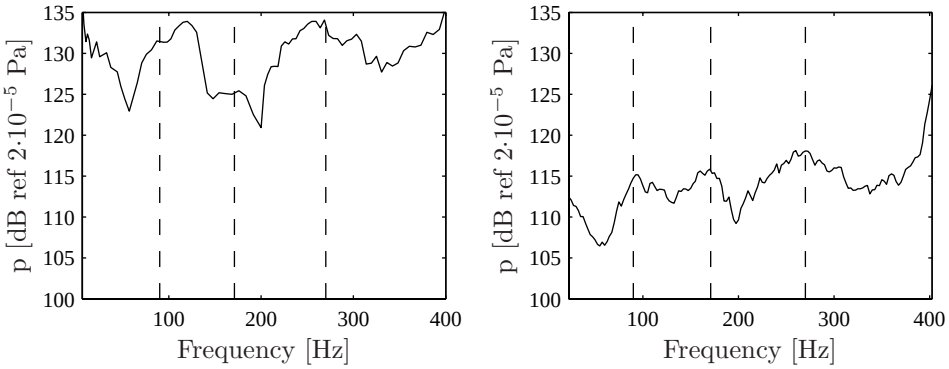

(a) Forced response.

(b) Autonomous response.

Figure 5.8: Average pressure measured by the pressure sensors in the combustion chamber for case 15.7. Dashed lines denote measured acoustic eigenfrequencies (table 5.1).

Figure 5.8 shows the average pressure measured by the pressure sensors in the combustion chamber (p_1, p_2, p_3 and p_4). Note that this plot is for

frequencies up to 400 Hz, whereas previous plots were made up to 1100 Hz, because 400 Hz is the maximum excitation frequency of the MOOG valve. The shape of the spectrum that is measured is somewhat similar, whether the combustion is forced or not. The pressure response range is small, only 15 dB, because the strongly excited combustion chamber modes have eigenfrequencies that are higher than 400 Hz. The response when the fuel flow is pulsated is about 15 dB higher than the response without forcing. In the pulsated measurement, the first acoustic mode of the combustion chamber at 270 Hz is visible. The two Helmholtz eigenfrequencies below 200 Hz do not coincide with the large peak in the forced spectrum, because this peak in the forced spectrum is caused by a resonance in the fuel supply line [48]. It is therefore difficult to draw conclusions from these measurements.

5.3 Structural response

5.3.1 Introduction

This section is devoted to the structural response of the liner during combustion, caused by the acoustic field induced by the flame, as treated in the previous section. The structural eigenfrequencies during combustion are first discussed, followed by the structural response to combustion noise. A second method to predict the response of the liner during combustion, besides the methods used in chapter 4, is also treated. In this method, results from large eddy simulations (LES) are coupled to a structural model to predict vibration. Finally, some results are shown of vibration when the fuel flow is pulsated.

5.3.2 Structural eigenmodes during combustion

The first structural properties that are discussed are the structural eigenmodes and eigenfrequencies during combustion. The eigenfrequencies are obtained from the autospectrum of the laser vibrometer signal, which is averaged over all the measurement points. This assures that modes are not missed due to measurements on a nodal line. The spectrum is divided by the average pressure measured by the sensors in the combustion chamber to suppress the acoustic modes (see also section 4.5.5). The result is shown in figure 5.9, which also lists the measured structural eigenfrequencies for the cold and the hot setup and the relative difference between these. The names of the mode shapes were explained in section 4.4.3.

[1] Taken from a different measurement under the same operating conditions.

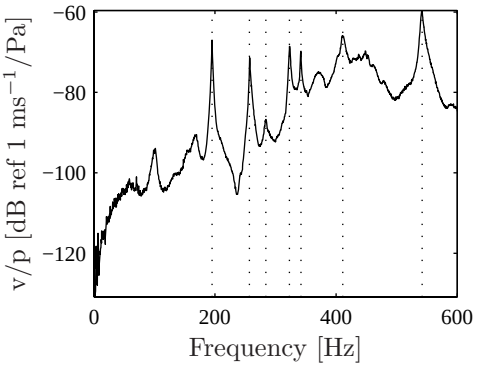

Mode	**Cold** [Hz]	**Hot** [Hz]	**Diff.** [%]
$(11)_{ss}$	225	195	13%
$(12)_{ss}$	300	257	14%
$(11)_{h1}$	315	284	10%
$(11)_{h2}$	325	302[1]	7%
$(12)_{h1}$	367	323	12%
$(13)_{ss}$	414	342	17%
$(11)_{cc}$	-	411	-
$(13)_{h1}$	-	542	-

Figure 5.9: Averaged autospectrum of the laser vibrometer signal divided by the average pressure measured with the pressure sensors in the combustion chamber. The dotted lines are the structural eigenfrequencies listed in the table.

The eigenfrequencies during combustion are lower compared with the eigenfrequencies of the cold setup due to the lower Young's modulus at higher temperatures. The change is not constant. Nevertheless, it matches well with the predicted 15.5% change in eigenfrequency for a liner temperature of 784°C (section 4.4.5). It was already seen earlier that eigenfrequencies can also change due to acousto-elastic coupling (section 4.5), prestress (section 4.4.5) and heating (section 4.5.5), which can be an explanation for the differences in the change of eigenfrequencies.

The mode shapes behind the slit window are depicted in figure 5.10. The figure shows that the mode shapes can mostly be identified clearly, except for the $(13)_{ss}$ mode, for which its measured shape looks like a (12) type of mode. In the structural experiments in section 4.4.4 it was already seen that this mode shape propagates into the thicker parts of the structural liner, which are not visible behind the slit window. This could be an explanation for the fact that the shape seen behind the slit does not really look like the $(13)_{ss}$ shape. Another explanation could be that the mode shape has been changed due to, for instance, thermal prestress.

To evaluate if the acousto-elastic interaction for the hot case is different compared with the cold case, the structural eigenfrequencies for the cold model (taken from section 4.5.4) and those for the hot model are compared. The differences between the models are the different density of the fluid, the different speed of sound and the different Young's modulus of the structure. The resulting calculated structural eigenfrequencies are shown in table 5.3. The difference

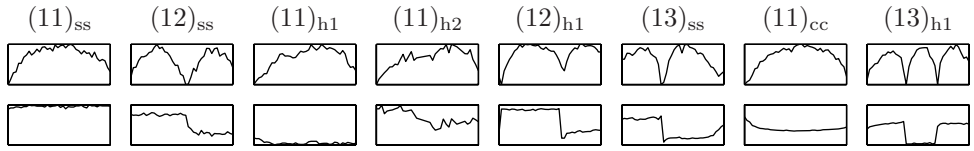

Figure 5.10: Amplitude (top) and phase (bottom) of the mode shapes measured during combustion at case 15.7.

in eigenfrequency is almost fully determined by the different Young's modulus, which is 150 GPa for the hot model and 210 GPa for the cold model. The relative difference in eigenfrequency is almost the same for most modes. Two modes, $(11)_{cc}$ and $(12)_{cc}$, show a larger difference. For these modes, the fluid in the combustion chamber and the cooling passage causes an increase in eigenfrequency compared with the model of only the structure (section 4.5.3). In the hot model, the fluid has a lower density and higher speed of sound, giving a lower increase in eigenfrequency caused by the fluid. This gives, besides the lower Young's modulus, an additional decrease in eigenfrequency and therefore the difference is somewhat larger.

Model	$(11)_{ss}$	$(11)_{h}$	$(12)_{ss}$	$(12)_{h}$	$(11)_{cc}$	$(13)_{ss}$	$(12)_{cc}$
Cold [Hz]	196.3	279.5	286.4	354.2	395.6	426.1	450.7
Hot [Hz]	166.2	236.9	242.4	300.1	329.2	360.6	378.1
Difference	15.3%	15.2%	15.4%	15.3%	16.8%	15.4%	16.1%

Table 5.3: Numerically determined structural eigenfrequencies for the full model of the cold setup and the hot setup.

5.3.3 Structural response to combustion noise

Figure 5.11(a) shows the vibration level measured through the slit window, averaged over all 40 equidistant measurement points. The high acoustic pressure level at low frequencies does not lead to a high level of vibration. This is because the liner is not compliant below the first eigenfrequency. Below 100 Hz the level is below the noise floor of the laser vibrometer.

Above 200 Hz the signals are very coherent, which shows that the structure responds to the acoustic field generated in the combustion chamber by the flame. The vibration level compares well between the measurement and the calculation, starting near -120 dB (1 μm/s) for low frequencies and increasing to -60 dB (1 mm/s) around 500 Hz, after which it decreases again.

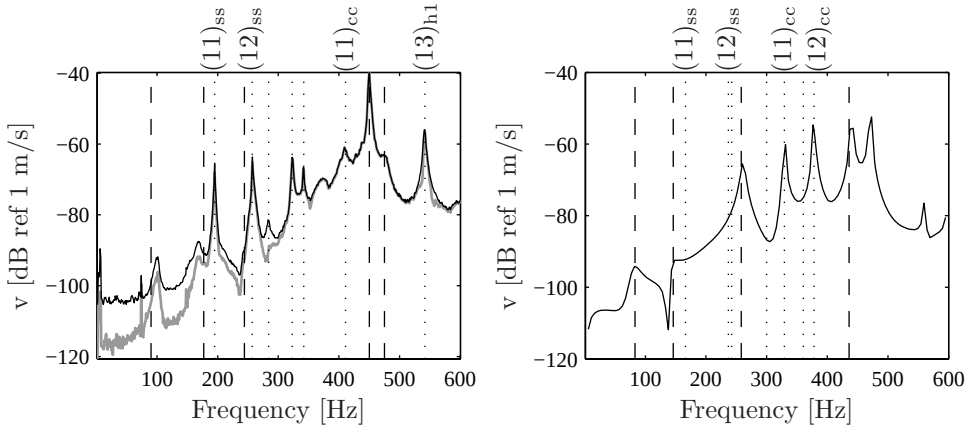

(a) Measured. (b) Calculated.

Figure 5.11: Measured (gray is the part correlated with p_3) and calculated autospectrum of the mean vibration of the liner. Dashed lines denote acoustic eigenfrequencies, dotted lines denote structural eigenfrequencies.

The structural eigenfrequencies are depicted by dotted lines, whereas acoustic eigenfrequencies are denoted by dashed lines. The first two structural eigenfrequencies, $(11)_{ss}$ and $(12)_{ss}$, show very distinct vibration peaks in the measurement. In the calculation (figure 5.11(b)), the peaks are not visible at all. This is caused by the structural model, which does not have any welds or other asymmetry. Because the acoustic field is almost one-dimensional in the model, the symmetric acoustic pressure load on the liner does not couple with these asymmetric structural mode shapes and therefore these modes are not excited. In the experiment, the acoustic excitation is not entirely symmetric and the mode shapes are not symmetric either (because of the welding). Therefore these modes are excited. To get an indication of this influence, figure 5.12 shows the calculated response when the structural model is made asymmetric by giving the elements at the weld location a Young's modulus of 2100 GPa. In this model, the $(11)_{ss}$ mode has an eigenfrequency of 183 Hz and the $(12)_{ss}$ has an eigenfrequency of 274 Hz. It is clear that this model shows the high vibration amplitude for these modes seen in the measurement.

In the symmetric model, a very high structural response is found for the symmetric breathing modes, $(11)_{cc}$ and $(12)_{cc}$. The reason is that these structural modes match very well with the one-dimensional pressure load. In section 5.3.2 on structural eigenmodes, only the $(11)_{cc}$ mode was identified in the experiments. Looking at the calculations, the eigenfrequency of the $(11)_{cc}$ is twice that of the $(11)_{ss}$ mode, which is also the case for the experiment. For

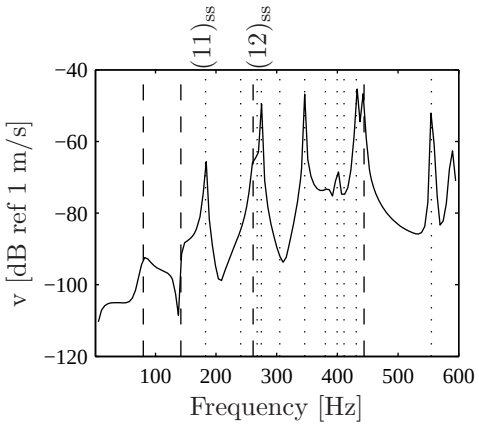

Figure 5.12: Calculated autospectrum of the mean vibration of the liner for an asymmetric structure.

the $(12)_{ss}$ and $(12)_{cc}$ mode, this factor is 1.56 in the calculation, which means that, in the experiment, the $(12)_{cc}$ would be at 401 Hz, which is very near the $(11)_{cc}$. It is therefore not unlogical that it is not clearly visible. The $(11)_{cc}$ mode still shows a high vibration level in the measurement, as predicted by the calculation.

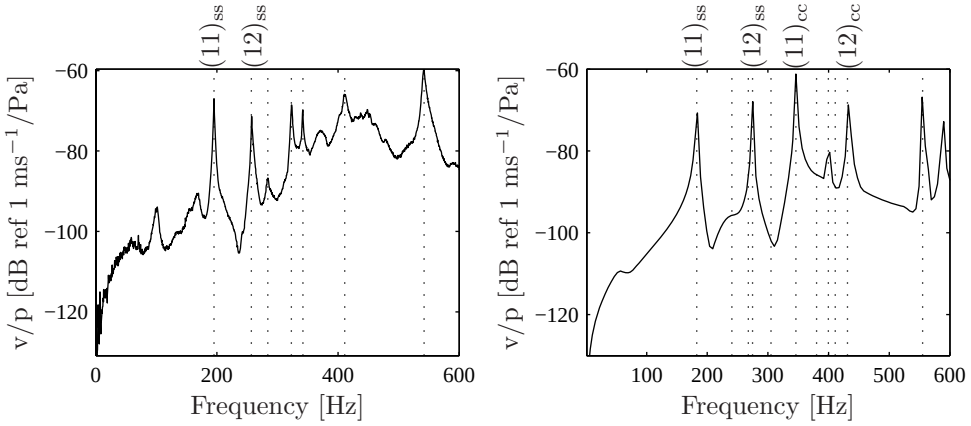

(a) Measured. (b) Calculated.

Figure 5.13: Mean vibration divided by the average pressure measured in the combustion chamber.

Figure 5.13 shows the average vibration level of the liner divided by the average pressure in the combustion chamber. This suppresses the acoustic eigenfrequencies from the plot. The asymmetric model is used again. It leads

to similar conclusions as the autospectra. The $(11)_{ss}$ and $(12)_{ss}$ modes have a large contribution. Furthermore, the $(11)_{cc}$ mode at 346 Hz and the $(12)_{cc}$ mode at 431 Hz have a strong transfer in the model. The figure also shows that the model and the measurement give the same spectrum shape, starting low and reaching a similar high amplitude above 250 Hz.

To evaluate the acoustic pressures in the cooling passage induced by liner vibration, figure 5.14 shows the acoustic pressure measured with sensor p_6, which is located in the cooling passage. At very low frequencies the signal is strong and decreases with frequency. The vibration level of the liner is very low at low frequencies and therefore it is unlikely that, at low frequencies, the flame noise propagates through structural vibration of the liner to the cooling passage. Section 4.5.6 showed a similar shape and amplitude of the pressure spectrum in the cooling passage at low frequencies without combustion. The measured pressure spectrum is then strongly dominated by turbulent noise and it is therefore likely that these high levels with combustion at low frequencies are also caused by turbulent flow noise.

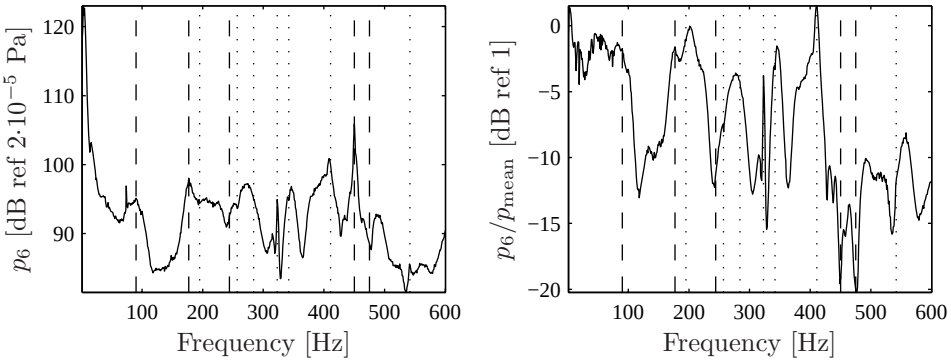

Figure 5.14: Measured autospectrum for sensor p_6 (cooling passage) with flame noise excitation (left) and this spectrum divided by the mean pressure in the combustion chamber for case 15.7.

Besides turbulent noise by the flow, there are two main paths through which pressure waves can enter the cooling channel. The first is through (mainly the flexible part of) the liner and the second is from the water cooler in which the cooling channel ends. The right-hand graph in figure 5.14 shows p_6 divided by the mean pressure in the combustion chamber. The frequencies of high acoustic transfer are all related to structural eigenfrequencies (dotted lines). The induced pressure is almost always lower than the pressure levels in the combustion chamber, especially around the acoustic eigenfrequencies of the combustion chamber. Substantial acoustic damping of the combustion cham-

ber through the structure is therefore not expected. This can be changed by bringing structural eigenfrequencies near the acoustic eigenfrequencies, but this will severely limit the life of the combustor.

5.3.4 Coupling of LES and FEM

In LES calculations, made by CERFACS [87], the variations in pressure are solved (see also section 3.2.4). The calculated pressures on the liner of the combustion chamber can therefore be used as fluid loading on a structural model. This is one-way coupling, because vibration data are not fed back to the LES simulations.

The LES data are calculated on a very fine grid and with very small time steps, which is not practical for structural calculations. The LES data are therefore remapped onto a coarser grid with equidistant nodes spaced 10 mm apart. A data set is made every 0.15 ms over a total time of 21 ms, giving 140 samples. The very short total time is caused by the extremely high computational costs of LES. The data used in this section are for the 15.7 case without fuel forcing.

The LES data are in the time domain. For comparison, time signals describing acoustic pressures and vibrations are also created from the harmonic acousto-elastic model calculations in this thesis. A time signal is created from the spectrum using:

$$p'(t) = \mathrm{Re}\left[\hat{p}(\omega)e^{\mathrm{i}\omega t}\right] , \tag{5.6}$$

in which Re denotes the real part. The reconstructed time signal has the same length as the LES calculation, being 21 ms. Frequency data up to a frequency of 600 Hz were calculated, which causes a smooth response.

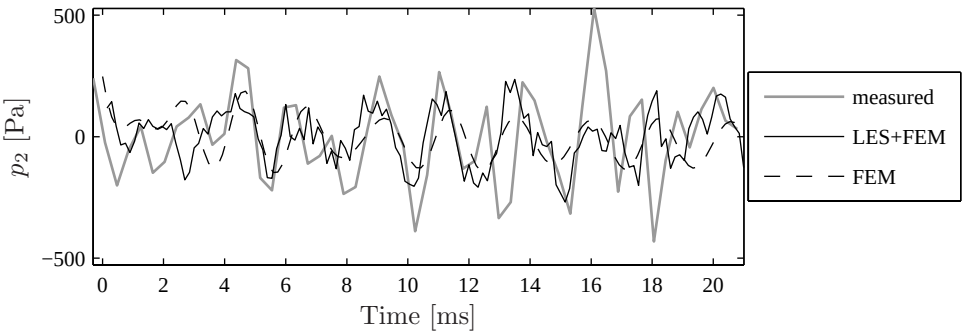

Figure 5.15: Calculated and measured pressure of sensor p_2 for case 15.7 during steady combustion.

Figure 5.15 shows the acoustic pressure at the position of sensor p_2, from the LES calculation, the FEM model developed in this thesis and from the measurement. The sample rate for the measurement was only 2.56 kHz and therefore there is only a limited amount of samples in the plotted data set. Measurement and calculations show a strong harmonic component near 400 Hz (period 2.5 ms, see also figures 5.4 and 5.16(a)), which is related to the $(200)_a$ mode. The pressure amplitude of the calculation and the measurement matches well, which indicates that the calculated pressures on the wall are correct.

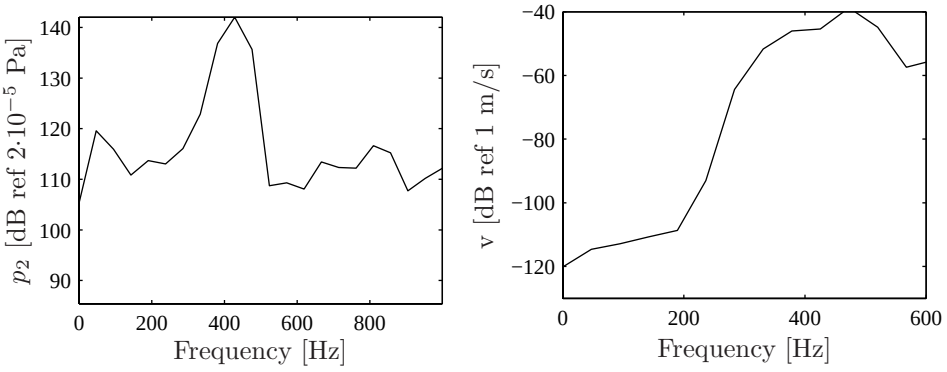

(a) Pressure. (b) Structural velocity.

Figure 5.16: Pressure spectrum calculated with LES for pressure sensor p_2 and the velocity calculated using the combination of LES and FEM.

The pressures on the wall calculated with LES can be used as loads for a structural model. For each element in the mesh, the 140 pressure results from LES were translated to 140 pressure loads at different times for the finite element model. A transient analysis was performed subsequently to calculate the resulting displacements as a function of time. A fixed time step of 0.03 ms was used, with linear interpolation of the pressure loads between the 0.15 ms samples. To compare the results with velocity data measured in the experiment, the finite element results are approximated as:

$$v_{i+1/2} = \frac{x_{i+1} - x_i}{t_{i+1} - t_i}\,, \tag{5.7}$$

in which $v_{i+1/2}$ is the velocity at $t_{i+1/2}$ and x_i is the displacement at time t_i.

Figure 5.17 shows the calculated and the measured vibration velocity at the laser vibrometer measurement point, which is again behind the slit window,

50 mm above the lower thick part. The figure shows a good match between the calculated and the measured vibration amplitude. Furthermore, it clearly shows that the structure responds mostly to the $(200)_a$ acoustic mode, which was also seen in the measured spectrum in figure 5.11(a) and the calculated spectrum using LES loads in figure 5.16(b). This calculated spectrum also matches well with the measured spectrum in figure 5.9 (which is for case 15.4 and not 15.7, but those cases are similar).

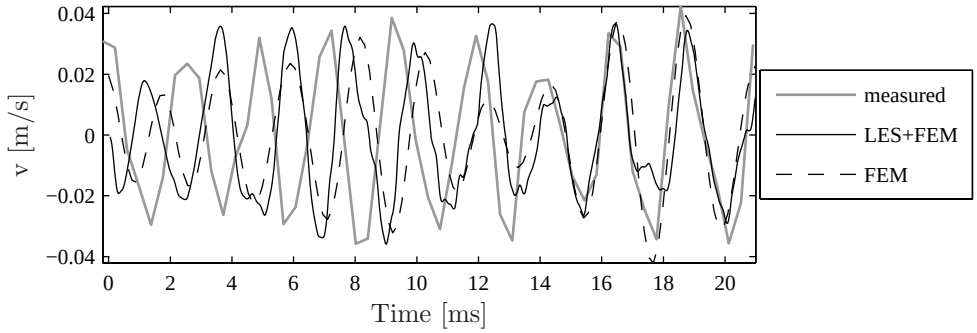

Figure 5.17: Calculated and measured velocity for case 15.7 during steady combustion.

5.3.5 Structural response to a pulsated fuel flow

For the structural response during combustion with a pulsated fuel flow, case 15.7 is used with a fuel forcing at 300 Hz. The LES calculations use a 15% fuel forcing. The measurement data were measured with an 8.5% perturbation on the fuel, because this is the maximum fuel forcing achievable in the DESIRE test rig. To make the measured data comparable with the calculated data, linear flame behavior is assumed [87] and therefore the measured pressures have been scaled linearly by a factor of 1.76, the ratio between the imposed numerical and experimental fuel perturbation. This also amplifies the flame as an autonomous source of sound, but the forced component is assumed to be dominant.

To calculate the forced response with the finite element models, the ANSYS acoustic volume source as function of the forcing is needed. This can be found by combining the flame transfer function of equation (3.10) and the relation between heat release and the ANSYS volume source from equation (3.5):

$$Q = \frac{\mathrm{i}\omega(\gamma-1)q_0}{\rho_0 c_0^2}\left[\frac{1}{1+\mathrm{i}\omega\tau_1}\right]^m\left[\frac{\hat{v}_B}{v_{B,0}}\right]\mathrm{e}^{\mathrm{i}\omega(t-\tau)}\,. \tag{5.8}$$

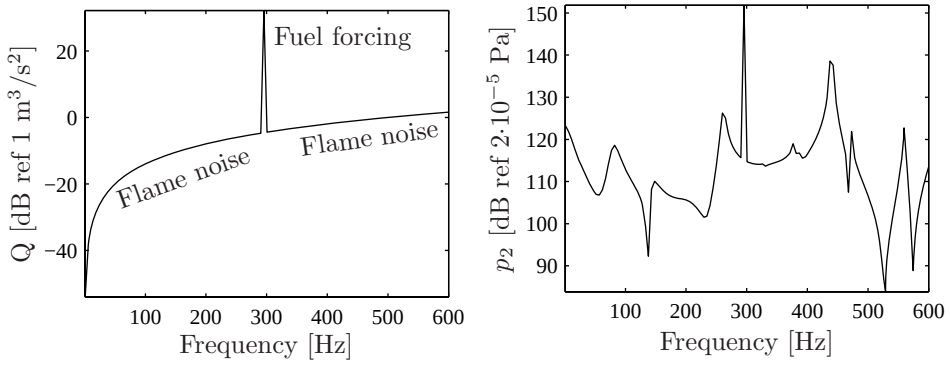

(a) Q. (b) p_2.

Figure 5.18: Numerically predicted acoustic volume source and the resulting pressure at sensor p_2.

The acoustic source is now a summation of the autonomous source from equation (5.4) and a 15% fuel forcing at 300 Hz. Figure 5.18 shows this source as a function of frequency. There is a strong harmonic response at 300 Hz in a noise spectrum that is much weaker. The predicted acoustic spectrum is also shown. It still has the strong peak at 300 Hz, but the difference with other frequencies than 300 Hz is less, which is caused by the high acoustic amplification at acoustic eigenfrequencies.

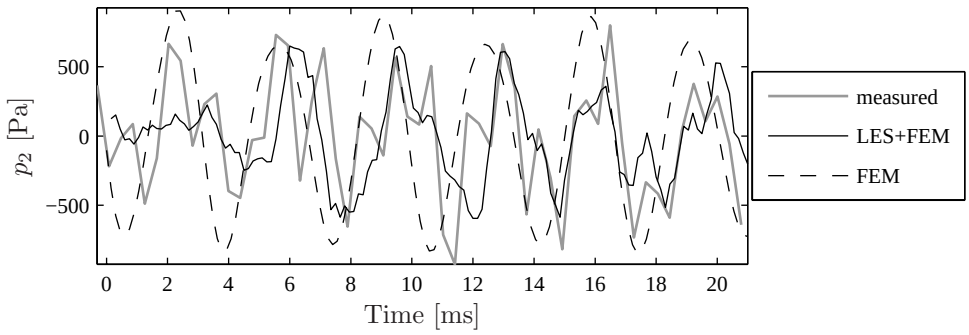

Figure 5.19: Calculated and measured pressure of sensor p_2 for case 15.7 with 15% fuel forcing at 300 Hz.

The time signals for pressure sensor p_2 are depicted in figure 5.19. The first part (about 3 ms) of the LES calculation does not show a clear perturbation. This is because the perturbation is imposed at the location where the fuel

enters the swirl passage. This perturbation first has to travel to the flame front before it causes a perturbation in the heat release and therefore a pressure perturbation (this time delay is discussed in section 3.2.3). After this delay, both the measured and the calculated time signal contain a strong 300 Hz response.

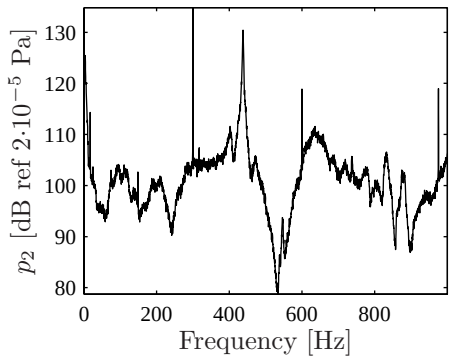

Figure 5.20: Experimentally determined autospectrum of sensor p_2 for case 15.7 with 8.5% fuel forcing at 300 Hz.

A second harmonic pressure perturbation is also visible in the time signal. Figure 5.20 shows the autospectrum of sensor p_2 for the measurement and figure 5.21(a) for the LES calculation. The figure for the measurement shows that, besides the harmonic response at 300 Hz, a second harmonic signal is present at 438 Hz, caused by the $(200)_a$ acoustic eigenmode. The LES calculation is very short and therefore the autospectrum has a low frequency resolution[1], but the second component can still be seen and it is also slightly visible in the LES time signal. The predicted pressure is similar to the measured one, especially when considering that turbulent noise and autonomous flame noise distort the active response of the flame.

Figure 5.22 shows the calculated and measured vibration velocity at the laser vibrometer measurement point. The figure shows that the calculated and measured amplitudes are close to each other, which corresponds with the good match at 300 Hz found in figure 5.11. The LES based calculation starts with a low velocity level, which rapidly increases to a more or less steady vibration amplitude. This is because in the transient finite element calculations no displacement and velocity are used as initial conditions and therefore the vibration has to build up first. Figure 5.21(b) shows the velocity spectrum for

[1]The visibility of the peaks is made even worse by the Hanning window that is applied, which causes spillover [81].

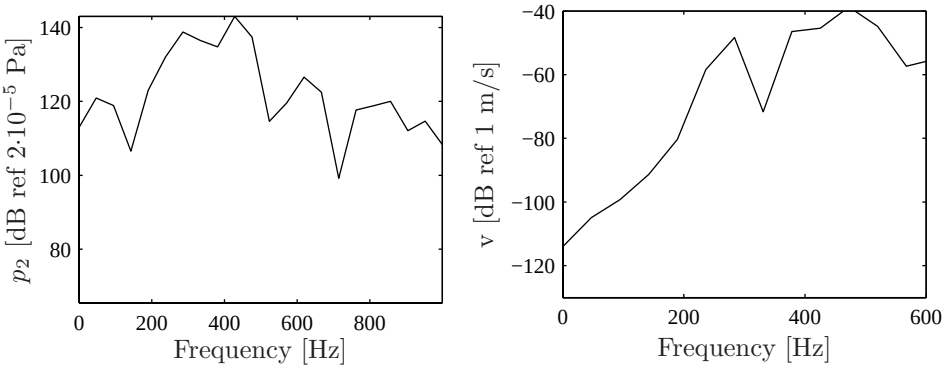

(a) Pressure. (b) Velocity.

Figure 5.21: Autospectrum of sensor p_2 for case 15.7 with 15% fuel forcing at 300 Hz from LES (left) and the corresponding structural velocity (right).

the FEM calculation using LES results. This spectrum also obtains a peak at 300 Hz, compared to the response to the flame as an autonomous source (figure 5.16(b)).

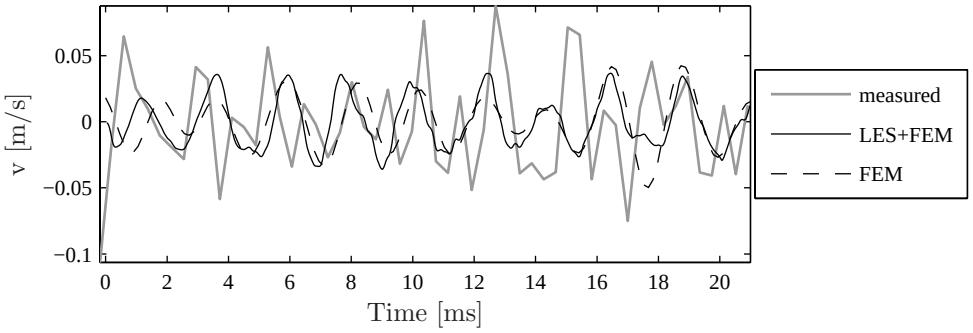

Figure 5.22: Calculated and measured structural velocity for case 15.7 with 15% fuel forcing at 300 Hz.

5.4 Unstable behavior

5.4.1 Introduction

In the previous sections, the coupling between combustion and acoustics was considered as one-way, in which unsteady combustion acts as a thermoacoustic

source and therefore creates pressure perturbations and structural vibrations. In this section, a method to include two-way interaction is presented, because in the measurements, high acoustic pressures are seen caused by two-way interaction between flame and acoustics (section 5.2.2).

5.4.2 Thermoacoustic instability

Frequencies where high acoustic pressures are caused by the interaction between the acoustic field in the combustor and the flame are related to so-called thermoacoustic instabilities. A thermoacoustic instability arises when heat release and the acoustic field amplify each other. The first explanation of this was given by Lord Rayleigh [82]. He stated that when heat is added at greatest compression and taken at greatest rarefaction, then the acoustic field can grow in time and an instability develops. In other words, when pressure and heat release are in phase, the flame acts as a sound amplifier and when the pressure and heat release are out of phase, the flame dampens the acoustic pressure oscillations. In an integral formulation, this can be written as [25]:

$$\frac{\gamma - 1}{c_0^2} \int_t \int_V p' \frac{\partial q'}{\partial t} dV dt > \int_t \int_S p' v' dS dt \,, \tag{5.9}$$

in which V is the volume of the domain, S is the boundary of the domain and time integration is performed over one period of oscillation. The work done by the flame should thus exceed the losses at the boundaries to develop an instability.

5.4.3 Transfer function approach

Figure 5.23 shows the feedback loop describing the two-way interaction between combustion and acoustics, as it is used here. A perturbation of the burner outlet velocity $\hat{v}_B$ flows to the flame front and causes a heat release perturbation $\hat{q}$. The relation between $\hat{v}_B$ and $\hat{q}$ is called the Flame Transfer Function or FTF, which was treated in section 3.2. The unsteady heat release acts as acoustic volume source Q, as described in appendix B. The acoustic volume source creates an acoustic field, causing perturbations on the amount of mixture that flows from the burner exit into the combustion chamber. The burner exit is assumed to be small compared with the acoustic wavelength and therefore the acoustic particle velocity normal to the burner exit $\hat{v}_B$ is taken constant over the burner exit area. The relation between Q and $\hat{v}_B$ is called the Acoustic Transfer Function or ATF and was treated in section 3.3. The loop is a negative feedback loop, because the burner velocity perturbations are calculated such

that a positive perturbation decreases the fuel flow to the flame. The Bode stability criterion [34] states that the loop becomes unstable when, for the open loop system, the gain is higher than one and the phase is -π radians minus an integer multiple of 2π radians. The gain and phase are therefore important properties that have to be determined. Because the flame acts as a low pass filter, the gain of the flame is, for higher frequencies, too low for the open loop to have a gain above one. Unstable behavior is therefore limited to lower frequencies.

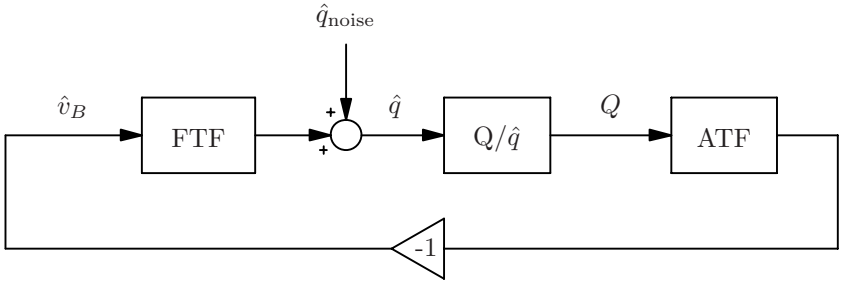

Figure 5.23: The feedback loop between combustion and acoustics.

The open loop of figure 5.23 was already used in sections 5.2.5 and 5.3.5, which treated the response to a fuel flow forcing. It includes the path from velocity perturbation $\hat{v}_B$ to heat release $\hat{q}$ by the flame transfer function, the translation to acoustic volume source and the acoustic response to this source, calculated using the finite element method. With the finite element package used, the closed loop cannot be implemented. A direct calculation of the feedback loop is therefore not possible and a different approach is used. The coupling is achieved by creating linear transfer function descriptions for the flame transfer function and the acoustic transfer function [43]. It is common in classical control theory to use the Laplace transform. The advantage over the Fourier transform is that it can also be used to describe unstable systems [74] and therefore it is used in this section. The flame transfer function is thus given according to equation (3.10) by:

$$H_f(s) = \frac{\hat{q}}{\hat{v}_B} = \left[\frac{1}{1+s\tau_1}\right]^m \left[\frac{q_0}{v_{B,0}}\right] \mathrm{e}^{-T_d s}\,, \tag{5.10}$$

in which T_d is the time delay. The order of the low-pass filter m was taken as 6. To implement the time delay in a linear model, a (4,4) Padé approximation [34] is used:

$$\tilde{H}_f(s) = \left[\frac{1}{1+s\tau_1}\right]^m \left[\frac{q_0}{v_{B,0}}\right] P_{(4,4)}(T_d)\,, \tag{5.11}$$

in which $P_{(4,4)}(T_d)$ denotes the (4,4) Padé approximation of T_d. In the frequency domain, the Padé approximation has properties similar to a time delay for low frequencies [97]. If the flame transfer function H_f is used in the transfer function approach, the burner exit velocity and mean heat release have to be known. For case 15.7, the burner exit velocity is 64 m/s [48] and the mean thermal power is 150 kW. Figure 5.24 shows the flame transfer function H_f and the Padé approximation $\tilde{H}_f$ (a similar flame transfer function as depicted in figure 3.4). The figure shows that the Padé approximation is exact for the amplitude and the phase is accurate in the frequency domain up to a frequency of 1000 Hz.

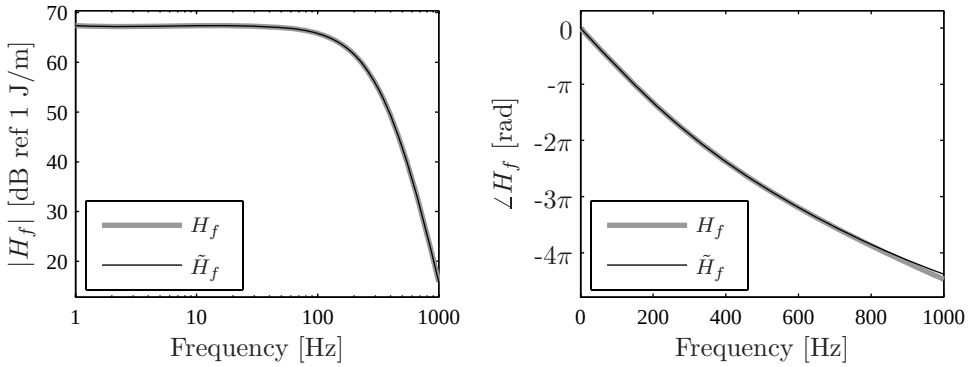

Figure 5.24: The flame transfer function H_f from burner exit velocity $\hat{v}_B$ to volume integrated heat release rate $\hat{q}$ and the Padé approximation $\tilde{H}_f$ of this transfer.

The relation between $\hat{q}$ and Q is, following equation (3.5), given by:

$$H_q(s) = \frac{Q}{\hat{q}} = \frac{(\gamma - 1)}{\rho_0 c_0^2} s \,. \tag{5.12}$$

Figure 5.25 shows the frequency properties of this transfer function. A differentiation is present (the term $\mathrm{i}\omega$), causing the monotonically increasing amplitude with +20 dB per decade and the constant phase of $\pi/2$ radians.

The acoustic transfer function was calculated with a series of harmonic analyses. The finite element code calculates the nodal pressures for these discrete frequencies. Appendix C describes how the acoustic particle velocity can be calculated from these nodal pressures. The resulting response at discrete frequencies must be translated to a transfer function description with poles

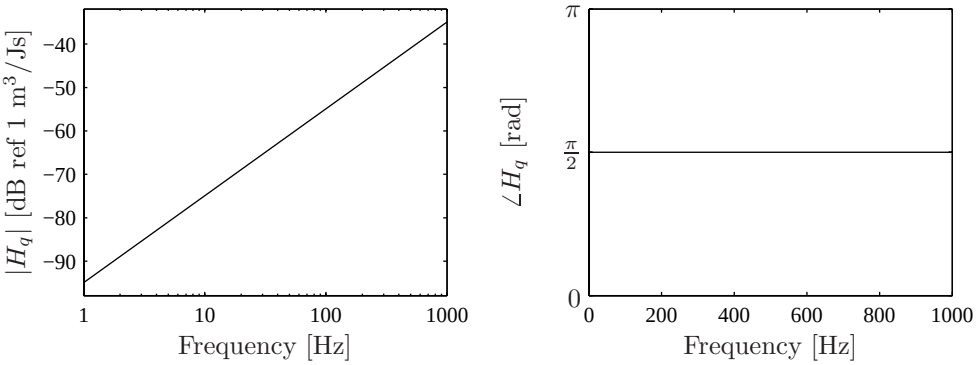

Figure 5.25: The transfer function H_q from volume integrated heat release rate $\hat{q}$ to volume flow rate Q.

and zeros. The transfer function is given by:

$$H_a(s) = \frac{\hat{v}_B}{Q} = B\frac{\prod_{i=1}^{m}(s - z_i)}{\prod_{j=1}^{n}(s - p_j)}, \tag{5.13}$$

in which $H_a(s)$ is the frequency response function, B denotes the gain, z_i denotes zero i, p_j pole j, m the number of zeros and n the number of poles. By fitting the poles, zeros and gain of this general transfer function to the response calculated with the finite element model, the linear acoustic transfer function can be determined. Methods exist to automate the curve fit procedure [30], but for the results in this thesis, the values were matched by trial and error.

The burner exit velocity v_B has dimensions m/s and the acoustic volume source Q has dimensions m^3/s^2. The acoustic transfer function H_a should therefore contain a time integration (a term 1/s). This causes a value of zero for one of the values of p_i in equation (5.13). The other values of p_i and z_i are all complex conjugate pairs of poles and zeros, in which the pairs of poles give eigenfrequencies and the pairs of zeros antiresonances. The gain of the transfer function also has to be determined. The result of the fit is depicted in figure 5.26. It shows that the fit approximates the calculated response very well.

5.4.4 Results

The transfer functions derived in section 5.4.3 can be used to study the influence of feedback on the behavior of the system. This response is analyzed with root locus plots, frequency response functions and responses in the time domain.

Figure 5.27 shows the root locus plot of the open loop system. The loci in the figure show the pole locations for a feedback gain increasing from zero (no

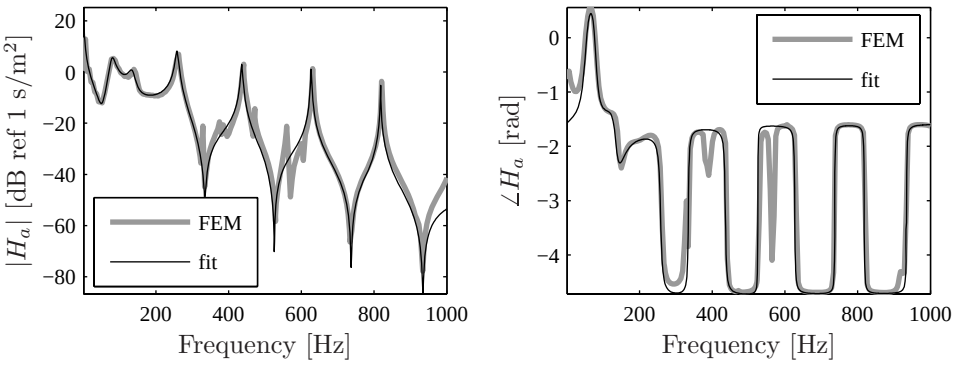

Figure 5.26: The acoustic transfer function H_a from volume source Q to acoustic particle velocity at the burner outlet $\hat{v}_B$.

.

feedback) to one (the closed loop system). The end of the loci are therefore the pole locations for the closed loop system. The poles and zeros near the imaginary axis come from the acoustic transfer function. The poles on the real axis are caused by the low pass behavior of the flame and those further away from the axes are related to the Padé approximation of the time delay. The zero at the origin is caused by the differentiation in H_q, which is compensated by a pole in zero caused by the integration in H_a.

The figure shows that the first acoustic eigenfrequency of the combustion chamber is damped by the feedback loop, because the pole moves into the left half plane. The numerically predicted acoustic response to flame noise (section

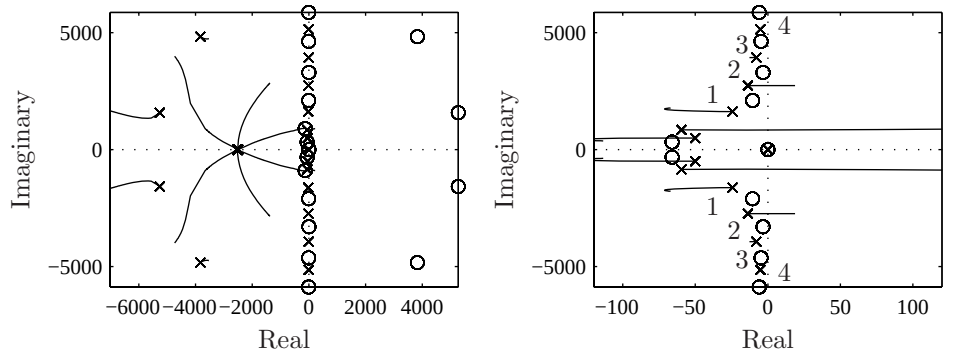

Figure 5.27: Root locus plot for the open loop system; the right figure is a zoom near the imaginary axis of the left figure. The numbers correspond to the acoustic eigenmodes of the combustion chamber.

5.2.3) showed a much higher response at this first eigenfrequency than the measurements. The calculation was made for the system without feedback. The feedback damps the first acoustic eigenmode and therefore the response with feedback is lower. The pole of the second acoustic eigenmode moves into the right half plane and therefore it becomes unstable, which is also sometimes seen in the measurements for cases 15.4 and 15.7 (figure 5.1). The poles from higher acoustic modes only move slightly, visible by their very short loci, which is caused by the low pass behavior of the flame. If no damping is present in the system, some of these poles can still move into the right half plane and become unstable. Damping is therefore also an important property in the stability analysis of a combustor.

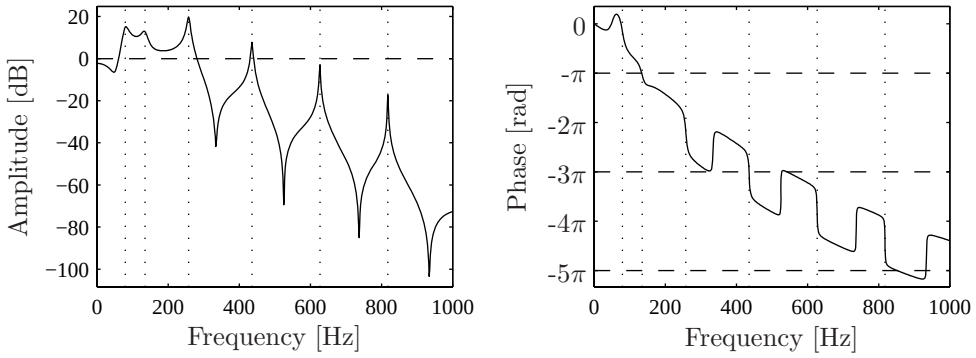

Figure 5.28: Open loop frequency response of the system. Dotted lines denote acoustic eigenfrequencies, dashed lines indicate the critical 0 dB and -π-2$n\pi$ radians lines.

Figure 5.28 shows the frequency response of the open loop system. The amplitude shows that the amplitude is higher than or near one for the first three eigenfrequencies of the combustion chamber. Unstable behavior arises when the phase in this region is -π-2$n\pi$ radians, with n an integer (the dashed lines in the figure). The phase plot shows that this is the case for the second acoustic eigenmode, confirming the observations made with the root locus plot. Above the third eigenfrequency, the loop gain is always below one (because damping causes finite amplitudes at eigenfrequencies) and therefore unstable behavior does not occur at higher frequencies. For frequencies below 200 Hz, the calculated loop gain is always above one. The phase becomes -π in this region and this leads to an instability, which was also seen in the root locus plot (figure 5.27), in which a loci moves into the right half plane around 150 Hz. The gain of both the flame transfer function H_f and the acoustic transfer function H_q is not very accurate in this region though, which can explain this

instability not occurring in the experiments.

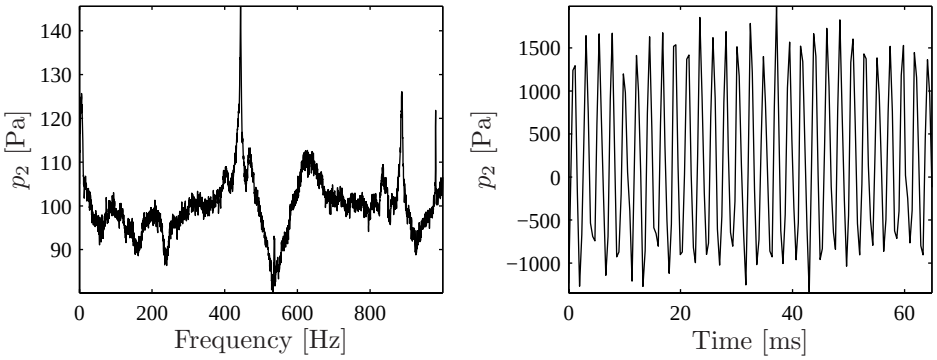

(a) Autospectrum of sensor p_2.

(b) Time signal of sensor p_2.

Figure 5.29: Experimental data from the unstable operation for case 15.7.

Figure 5.29 shows a measurement made during unstable operation at operating point 15.7. It can be seen clearly that the second acoustic eigenmode dominates the acoustic spectrum and the time signal is strongly harmonic. The third acoustic mode is damped again and the fourth seems a little amplified. This is consistent with figure 5.28, which shows the third mode is not near a critical phase, whereas the fourth mode is again. Nevertheless, the calculations show some margin, both in phase (which is slightly above 5π radians) and in gain (which is slightly below one, figure 5.28).

5.5 Differences with industrial combustors

This thesis deals with the test rig developed at the University of Twente. It was designed to have properties similar to a real gas turbine combustor. Nevertheless, because the test rig is a scaled-down version of a real combustor, the properties of the test rig differ from those of a real combustor. This section discusses several of these differences.

Flame size

Section 3.3.8 treated the influence of temperature on the acoustic behavior of the test rig. It showed that the flame is located at the beginning of the combustion chamber. In an industrial combustor, the combustion chamber length is similar to that of the test rig, but the size of the burner and the width of the combustion chamber is much larger, because the thermal power is higher.

This means that the length of the flame is also larger. The flame zone occupies almost the entire combustion chamber. Using a correct temperature field is therefore more important for an industrial combustor than in the calculations for the test rig. A second consequence of the larger flame is related to the compactness of the source. In the test rig, the flame is much smaller than the acoustic wavelength. If the flame occupies almost the entire combustion chamber, the flame is no longer compact. This means the flame as acoustic source cannot be lumped at one point. A possible solution is to use a multipole expansion of the source [65].

Structural properties

The structure of the test rig has been designed for simple modeling. In an industrial combustor, other requirements are more important, such as resistance to thermal and structural loads and efficient cooling of the structure. The design of an industrial annular combustor is therefore much more complex, increasing the difficulties in accurately modeling the structure. Besides eigenfrequencies and mode shapes that are more difficult to determine, the damping properties of the structure are also more complex. Where the test rig liner is a welded construction, the liner of an industrial combustor is likely to contain bolted and clamped liner parts. This introduces frictional damping, which is more complex to model accurately.

A second difference is that, in the test rig, the thin part of the structural liner is located after the flame zone. Because the flame zone is much larger in an industrial combustor, most of the liner is in the flame zone. The heat transfer to the liner and therefore the temperature distribution on it will be more complex.

A further difference lies in the scale of industrial combustors. They are much larger than the combustor used in the test rig. This means that the vibration displacements can be much larger. In this thesis, the assumption was made that the flame does not react directly on the vibrating walls, and the CFD can therefore be performed using non-moving boundaries. For larger combustors there may be a relevant influence.

Annular combustors

In annular combustors, several burners are present around the circumference of the combustor. This makes modeling the flame much more difficult, because of the interaction between the flames [86]. For the acoustic model, this means that several acoustic sources are present. The acoustic behavior of the test rig

also differs from an annular combustor. The test rig behavior is dominated by longitudinal modes, which makes the acoustic field almost one-dimensional. In an annular combustor, circumferential modes are also present [91, 29], as well as combinations of longitudinal and circumferential modes. This will make the acoustic behavior more complex and increase the acoustic modal density. The finite element technique applied in this thesis can nevertheless include these effects [16].

Model applicability

Several differences between industrial combustion systems and the test rig and the calculations made in this thesis were introduced in this section. These differences nevertheless can be included using the same modeling procedure. This procedure was shown to be valid using setups of different complexity. It can therefore now be used to build more accurate models of the current test rig as well as models of setups that include one or more of the differences mentioned before.

5.6 Concluding remarks

In this chapter, the models of the flame, the acoustic behavior of the test rig and the interaction with the structure were brought together to describe the behavior of the test rig during combustion. The acoustic response of the combustion chamber of the test rig during combustion was discussed first. The measured and predicted eigenfrequencies matched well. A simple model for the spectrum of the autonomous flame source was subsequently developed, which assumes a constant amplitude of the heat release rate perturbation. This amplitude was fitted to measured results. Using this autonomous flame model, the pressures caused by this autonomous flame source were calculated using the acoustic model. The numerical results agree well both in shape and in level with the experimental results. However, differences in the acoustic amplitude at acoustic eigenfrequencies were seen, indicating that the acoustic damping was not modeled accurately.

The structural eigenfrequencies decrease with an increase in temperature. The calculated relative decrease is 15%, which is similar to the decrease seen in the experiments. The measured and calculated structural mode shapes can be matched. In the cold measurements differences between the measured and calculated structural behavior, caused by the welds, were already seen. These are obviously still present in the hot measurements treated in this chapter.

In the calculations, the symmetric structural eigenmodes are not excited, because they do not couple with the one-dimensional pressure field, whereas in the experiment, these modes are excited. This can be solved by making the structural model slightly asymmetric. The calculated behavior is then similar to the measured behavior. It was shown that the acoustic pressures induced in the cooling passage by vibration of the liner are much lower than the acoustic pressures in the combustion chamber. Because the damping of the structure itself is also low, acoustic losses through the structure will be low. As a second method to calculate the structural response of the liner, it was determined by coupling LES results to a finite element model that only includes the structure. The results are similar to those found with the models developed in this thesis and compare very well with measurements.

Attention was also paid to the feedback between flame and acoustics. An approach from control theory was used, based on transfer functions. It was shown that the acoustic response is substantially influenced by this feedback loop, which can both amplify and dampen acoustic modes. The results of the closed loop model agree with experimental observations and at least partially explain the differences in acoustic response found with the autonomous flame model. However, the results of the closed loop model are sensitive to small changes in the flame transfer function, so the predictive capabilities may not be high.

Finally, some remarks were made on the differences between an industrial combustor and the test rig and the numerical models developed in this thesis. The modeling procedure developed in this thesis can include these differences. Its validity was shown using test setups of different complexity. The next step can now be to apply it to more complex setups, such as the annular combustors used in industry.

Chapter 6

Conclusions and recommendations

6.1 Conclusions

In this thesis, models and experiments are described to obtain insight in the interaction between combustion, acoustics and vibration. Combustion and acoustics are combined in the field of thermoacoustics, whereas acoustics and vibration are combined in the field of acousto-elastic interaction. For the modeling, results from computational fluid dynamics and semi-analytical relations for the flame as acoustic source were combined with acousto-elastic finite element models. A test rig was built to provide experimental insight in the interaction and to validate the models. By increasing the complexity of the models and experiments step by step, different aspects of the problem could be isolated. The comparison of experimental and numerical results was used to further understand the experimental results. From this range of models and experiments, the following conclusions can be drawn:

- The influence of the acoustic cavities of the combustion chamber and the cooling passage on the eigenmodes and eigenfrequencies of the liner is only minor. The only modes for which substantial influence was seen are so-called volumetric modes which cause a change in the volume of the combustion chamber. This change causes an added stiffness that increases the eigenfrequencies.

- The influence of structural vibration on the acoustic behavior of the combustion chamber is small. Although structural resonances cause sharp peaks over a small frequency range in the modeled acoustic response

of the combustion chamber, these peaks are not found in experiments. The reason is that in the real setup, structural modes are always slightly damped. The vibration amplitude in resonance is therefore large, but not large enough to exert substantial influence on the acoustic behavior.

- The temperature profile in the combustion chamber is important for accurately determining the acoustic behavior. In the test rig, dividing the temperature field in a cold zone before the flame front and a hot zone behind is insufficient, due to the temperature gradient caused by the substantial heat loss to the liner. Using the full temperature field from CFD calculations, a very accurate prediction of the acoustic behavior of the combustion chamber of the test rig was obtained. The exact temperature of the liner in the test rig is less important, because, for the temperatures examined, the properties of the structure do not depend strongly on temperature.

- The finite element code used can produce very accurate predictions of acousto-elastic behavior when the fluid is stagnant. An almost perfect match between models and experiments on a separate test setup was obtained.

- Using a simple model of the flame as autonomous acoustic source, a good indication can be obtained of the vibration level of the liner. Applying pressures on the wall, calculated with large eddy simulation, to a structural model gives similar results.

- The flame as active source of sound, reacting to the acoustic field in the combustor, has a substantial influence on the acoustic response. The system can become unstable, which results in one very dominant frequency in the acoustic spectrum. If the system is stable, feedback still increases or decreases the damping of different acoustic modes.

- A relatively low-cost pressure measuring system was developed based on sidetubes with acoustic damping and a back pressure facility. This system allows accurate measurements under high temperatures and elevated pressures using relatively cheap pressure transducers.

- If proper data acquisition is applied, laser vibrometry can be applied to obtain accurate vibration data on the hot surface of the liner. Optical access using windows has to be provided.

- The modeling procedure developed in this thesis was validated on a combustion setup that is representative for an industrial combustor. The

procedure can therefore be used to predict the acousto-elastic behavior of larger combustion systems, such as those used in industry.

6.2 Recommendations

- The structural liner used in this thesis has been welded from several plates. These welds were not included in the structural model, which gives differences between model and experiment in eigenfrequencies and the symmetry of eigenmodes. Differences in structural behavior caused by heat transfer through the liner and flow along the liner are also hard to distinguish due to the difference in structural behavior. It is therefore recommended to either manufacture a liner that has better defined properties, for instance using laser welding, or to improve the weld modeling such that a better match between the structural model and the actual structure is obtained.

- In this thesis, the structural behavior was mostly studied using eigenfrequencies, eigenmodes and frequency response functions. For fatigue calculations the exact vibration amplitude is very important. In a structural resonance peak, this amplitude depends strongly on the damping of the structure. Additional attention should be paid to measuring and predicting this damping.

- In this thesis, pressures on the wall from a large eddy simulation were applied to a structural model to calculate the mechanical vibration of the liner, which is a form of one-way coupling. Extending this to two-way coupling can provide further insight in the interaction between structural vibration and turbulent flow. For instance, it could be possible to predict the damping of the structure caused by turbulent flow.

- The test rig used in this thesis is a medium sized one. It is much smaller than an industrial system and therefore cheaper and easier to operate. On the other hand, it already has a complexity and size that makes it difficult to isolate physical effects. Building smaller and better defined setups can therefore be beneficial for code validation and isolating the influence of different physical phenomena, such as heat transfer and damping by flow.

- All the calculations and measurements in this thesis were made on a test setup, which is a scaled-down version of an industrial combustor. Section 5.5 summarized several differences with an industrial combustion system. Models should be made using an industrial geometry, to see if

this exhibits the same behavior. Results can be compared with (limited) experimental data on an industrial system for validation and be used for evaluation whether the conclusions based on the test rig geometry also hold for an industrial combustion system.

List of Symbols

General

The symbols that are used throughout this thesis are divided into several classes: Roman, Greek, superscripts and subscripts and miscellaneous. Additionally, a list of abbreviations is included after the definition of the symbols. The arrangement of the list is as follows, first the symbol is written, then the description and finally the dimensions, if applicable.

Roman

A	Cross-sectional area	[m^2]
a	Width of the plate	[m]
a	Acceleration	[m/s^2]
a_c	Cavity dimension	[m]
a_s	Radius of the sphere	[m]
a_i^j	Polynomial coefficient for species j	[-]
B	Constant	[-]
b	Height of the plate	[m]
b_c	Cavity dimension	[m]
b^j	Moles of species j	[-]
C	Constant	[-]
c_0	Speed of sound	[m/s]
c_c	Cavity dimension	[m]
c_p	Specific heat at constant pressure	J/kgK
c_v	Specific heat at constant volume	J/kgK
D	Outside dimension cooling passage	[m]
d	Liner width	[m]
E	Modulus of elasticity	[Pa]
$\mathbf{F}$	Structural external loads	[N]

$\mathbf{F^p}$	Loads by acoustic pressures	[N]
$\mathbf{F^t}$	All the external loads	[N]
f	Frequency	[Hz]
f_c	Cut-off frequency	[Hz]
f_i	Force in direction i	[N]
G_{ii}	Coherent part of an autospectrum	[-]
G_{ij}	Cross-spectrum	[-]
G_{jj}	Autospectrum	[-]
H_{12}	Transfer between sensor 1 and 2	[-]
H_a	Acoustic transfer function	[s/m^2]
H_f	Flame transfer function	[J/m]
H_q	Transfer function from $\hat{q}$ to Q	[m^3/Js]
$H(s)$	General transfer function	[-]
h	Thickness	[m]
I_{zz}	Area moment of inertia about the neutral axis	[m^4]
$\mathbf{I}$	Identity matrix	[-]
$\mathbf{K}$	Stiffness matrix	[N/m]
$\mathbf{K^{fs}}$	Stiffness coupling matrix	[N/m]
$\mathbf{K^k}$	Acoustic stiffness matrix	[N/m]
$\mathbf{K^w}$	Structural stiffness matrix	[N/m]
k	Wavenumber	[m^{-1}]
k_h	Number of half waves in a direction	[-]
L_{FL}	Length of the flame	[m]
L_s	Characteristic dimension of the source	[m]
L	Length	[m]
l_b	Distance between burner outlet and sensor 1	[m]
l_s	Distance between sensor 1 and sensor 2	[m]
l_h	Number of half waves in a direction	[-]
$\mathbf{M}$	Mass matrix	[kg]
$\mathbf{M^{fs}}$	Mass coupling matrix	[kg]
$\mathbf{M^k}$	Acoustic mass matrix	[kg]
$\mathbf{M^w}$	Structural mass matrix	[kg]
m	Exponent	[-]
m_a	Mass injection rate per unit volume	[kgs/m^3]
m_b	Mass per unit length of a beam	[kg/m]
m_h	Number of half waves in a direction	[-]
m_p	Mass per unit area of a plate	[kg/m^2]
N	Shape function	[-]
N_n	Number of nodes	[-]

n	Exponent	[-]
n_c	Number of cycles	[-]
$\mathbf{p}$	Vector containing the nodal pressures	[Pa]
p	Pressure	[Pa]
p_A	Forward traveling wave	[Pa]
p_B	Backward traveling wave	[Pa]
$\hat{p}_B$	Harmonic pressure amplitude at the burner outlet	[Pa]
p_b	Pressure in the box	[Pa]
p_s	Excitation pressure	[Pa]
Q	Volume flow rate	[m^3/s^2]
Q_i	Mass flux on node i	[m^3/s]
q	Specific heat release	[J/kg]
$\bar{q}$	Volume integrated heat release rate	[J/s]
$\hat{q}$	Harmonic amplitude volume integrated heat release rate	[J/s]
R	Gas constant	[J/kgK]
r	Characteristic impedance	[-]
r_s	Distance to the source	[m]
S	Boundary of the domain	[m^2]
St	Strouhal number	[-]
s	Entropy	[J/kgK]
T	Temperature	[K]
T_{comb}	Combustion air temperature	[K]
T_{cool}	Cooling air temperature	[K]
T_d	Time delay	[s]
t	Time	[s]
t_1	Thickness of the thick liner parts	[m]
t_2	Thickness of the thin liner parts	[m]
V	Volume	[m^3]
v	Velocity	[m/s]
v_B	Velocity perpendicular to the burner outlet	[m/s]
v_i	Velocity in direction i	[m/s]
v_f	Convection speed through the flame	[m/s]
v_n	Normal velocity	[m/s]
v_s	Surface velocity	[m/s]
$\mathbf{w}$	Vector containing the nodal displacements	[m]
X_i	Response at cycle i	[m]
x	Coordinate	[m]
x_i	Coordinate in direction i	[m]
y_a	Air mass flow	[kg/s]

y_f	Fuel mass flow	[kg/s]
y_j	Local coordinate in direction j	[m]
Z	Impedance	[Pas/m]
z_i	Value for zero i	[-]

Greek

α	Coefficient of thermal expansion	[-]
β	Angle	[rad]
γ	Ratio of specific heats	[-]
ζ	Dimensionless impedance	[-]
λ_i	Tabulated eigenfrequency factor for beams	[-]
λ_{ij}	Tabulated eigenfrequency factor for plates	[-]
ν	Poisson's ratio	[-]
ξ	Damping	[-]
ρ	Density	[kg/m^3]
σ	Stress	[Pa]
τ_i	Inverse of the angular cut-off frequency	[s]
τ_{ij}	Viscous stress tensor	[Pa]
$\mathbf{\Phi}$	Matrix containing displacement vectors	[m]
$\boldsymbol{\phi}_i$	Vector containing the displacements of mode i	[m]
ϕ	Equivalence ratio	[-]
$\mathbf{\Omega}$	Diagonal matrix	[-]
ω	Angular frequency	[rad/s]

Superscripts and subscripts

$()^{(i)}$	Belonging to node i
$()^{st}$	Stoichiometric values
$()^T$	Transpose
$()'$	Perturbation
$\dot{()}$	Time derivative
$\hat{()}$	Harmonic amplitude
$()_0$	Mean value
$()_{,0}$	Mean value
$()_B$	At the burner outlet

$()_{L2}$	Spatial L_2 norm
$()_{\mathrm{pp}}$	Shape like boundary condition pinned-pinned
$()_{\mathrm{pc}}$	Shape like boundary condition pinned-clamped
$()_{\mathrm{cc}}$	Shape like boundary condition clamped-clamped
$()_{\mathrm{ss}}$	Shape like boundary condition all sides simply supported
$()_{\mathrm{h}}$	Different shapes on different sides
$()_{\mathrm{h1}}$	Different shapes on different sides, first occurrence
$()_{\mathrm{h2}}$	Different shapes on different sides, second occurrence

Miscellaneous

$\|\|$	Absolute value
Δ	Difference
$\mathrm{i} = \sqrt{-1}$	Imaginary unit
δ_{ij}	Kronecker delta
∂	Partial derivative
Re()	Real part

Abbreviations

ATF	Acoustic Transfer Function
CERFACS	Centre Européen de Recherche et de Formation Avancée en Calcul Scientifique
CFD	Computational Fluid Dynamics
DESIRE	Design and demonstration of highly reliable low NO_x combustion systems for gas turbines
FEM	Finite Element Method
FTF	Flame Transfer Function
LES	Large Eddy Simulation
RaNS	Reynolds averaged Navier Stokes
TMF	Transfer Matrix Formulation
rms	Root Mean Square

Appendix A

A basic flame temperature calculation

The acoustic behavior of a combustion setup is strongly influenced by the temperature of the combustor. The main effect is the change in speed of sound, which is included in the acoustic models in this thesis. Different methods to include the temperature field are discussed in section 3.3.8. The most straightforward method is to divide the combustion chamber in a section upstream of the flame, which has the air inlet temperature T_i and a section downstream of the flame, which has the flame temperature T_o. To calculate the heat released by the flame needed to increase the temperature from T_i to T_o, the specific heat at constant pressure c_p is needed as function of temperature. A polynomial approximation is used for this function [14]:

$$c_p(T) = a_0 + a_1 T + a_2 T^2 + a_3 T^3 \,. \tag{A.1}$$

The coefficients a_i for this polynomial approximation for the gasses used are listed in table A.1.

Species	a_0	a_1	a_2	a_3
N_2	28.90	$-0.1571 \cdot 10^{-2}$	$0.8081 \cdot 10^{-5}$	$-2.873 \cdot 10^{-9}$
O_2	25.48	$1.5200 \cdot 10^{-2}$	$-0.7155 \cdot 10^{-5}$	$1.312 \cdot 10^{-9}$
CO_2	22.26	$5.9810 \cdot 10^{-2}$	$-3.5010 \cdot 10^{-5}$	$7.469 \cdot 10^{-9}$
H_2O	32.24	$0.1923 \cdot 10^{-2}$	$1.0550 \cdot 10^{-5}$	$-3.595 \cdot 10^{-9}$

Table A.1: Coefficients of the c_p polynomial, giving c_p in kJ/kmol·K. The coefficients are accurate (average error $< 0.5\%$) up to 1800 K.

To obtain the total heat absorbed during the temperature increase of the combustion gasses $\bar{q}$, the polynomial has to be integrated, which leads to:

$$\bar{q} = \int_{T=T_i}^{T_o} c_p(T)dT = a_0(T_o - T_i) + \frac{a_1}{2}(T_o^2 - T_i^2) + \frac{a_2}{3}(T_o^3 - T_i^3) + \frac{a_3}{4}(T_o^4 - T_i^4) \tag{A.2}$$

The heat released by combusting a fuel $\bar{q}$ can be calculated from the formation enthalpy. Natural gas, which is used as fuel, consists mostly of methane (CH_4), and this gas is therefore used in the calculation[1]. The reaction for combustion of methane with air is:

$$CH_4 + \left(\frac{2}{\phi}\right) O_2 + \left(\frac{7.52}{\phi}\right) N_2 \Rightarrow CO_2 + 2H_2O + \left(\frac{7.52}{\phi}\right) N_2 + \left(\frac{2}{\phi} - 2\right) O_2 \tag{A.3}$$

in which ϕ denotes the equivalence ratio. This equation is only valid for equivalence ratios below one, when there is an excess amount of air. In environmentally friendly combustion this is always the case, because otherwise unburned hydrocarbons would be emitted to the atmosphere. The formation enthalpies for the substances in reaction (A.3) are listed in table A.2 [14].

Species	**Formation enthalpy**
CH_4	74.850
H_2O	241.818
O_2	0
N_2	0
CO_2	393.509

Table A.2: Formation enthalpy of the combustion gasses in MJ/kmol.

Using these values and the reaction in equation (A.3), the energy released by combusting 1 kmol CH_4 can be calculated as 802.3 MJ/kmol. This energy is absorbed by the temperature increase of the combustion gasses according to equation (A.2), which can thus be used to calculate the flame temperature. The polynomial coefficients for $c_p(T)$ are weighed by the composition of the flue gasses to obtain a polynomial approximation for $c_p(T)$ of the flue gasses as:

$$a_i^n = \frac{\sum_{j=1}^{m} a_i^j b^j}{\sum_{j=1}^{m} b^j} \tag{A.4}$$

[1]The natural gas used in the test rig has a heating value that is approximately 20% lower [61], which will lead to a slightly lower flame temperature.

in which a_i^n is the ith coefficient of the resulting polynomial, m is the number of species, a_i^j is the ith coefficient for species j and b^j is the number of moles of species j in the combustion gas. The flame temperature can now be calculated using equation (A.2). The flame temperature as function of the equivalence ratio, for an inlet temperature of 573 K and a methane flame, is depicted in figure A.1.

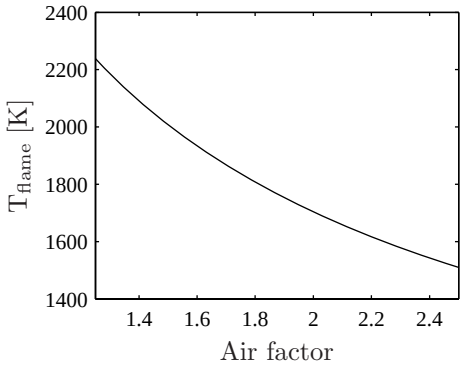

Figure A.1: Flame temperature for a methane flame as function of equivalence ratio for a combustion air temperature of 573 K.

Reference case 15.7 has an air inlet temperature of 573 K (300°C) and an air factor of 1.8. The predicted flame temperature is 1808 K (1535°C). The speed of sound at this temperature is 852 m/s, compared with 480 m/s for the inlet air at 573 K. The density decreases by a factor of 3.2 from 0.62 kg/m^3 to 0.20 kg/m^3.

Appendix B

The thermoacoustic source term

In this appendix, the basis of the flame as an acoustic source is derived. This is done by starting with the basic equations of fluid dynamics and then using the classic Lighthill analogy [67]. This leads to a description consisting of the wave equation with sound sources on the right-hand side. The relevant sound source is then expressed in terms of the unsteady heat release rate. The section ends with information on how the flame as an acoustic source is used in a finite element model.

B.1 Lighthill's analogy

The conservation of momentum can be written as [77]:

$$\frac{\partial}{\partial t}(\rho v_i) + \frac{\partial}{\partial x_j}(p\delta_{ij} - \tau_{ij} + \rho v_j v_i) = f_i \,, \tag{B.1}$$

in which t is time, ρ is the density, v_i is the velocity in direction i, x_i is the coordinate, p is the pressure, τ_{ij} is the viscous stress tensor, f_i is the force exerted on the fluid in direction i and δ_{ij} is the Kronecker delta. Differentiation with respect to x_i gives:

$$\frac{\partial^2}{\partial x_i \partial t}(\rho v_i) + \frac{\partial^2}{\partial x_i \partial x_j}(p\delta_{ij} - \tau_{ij} + \rho v_j v_i) = \frac{\partial f_i}{\partial x_i} \,. \tag{B.2}$$

The first term on the left-hand side can be eliminated by using conservation of mass, which is given by:

$$\frac{\partial \rho}{\partial t} + \frac{\partial}{\partial x_i}(\rho v_i) = m_a \,, \tag{B.3}$$

in which m_a is the mass injection rate per unit volume. When this equation is differentiated with respect to time it becomes:

$$\frac{\partial^2}{\partial x_i \partial t}(\rho v_i) = \frac{\partial m_a}{\partial t} - \frac{\partial^2 \rho}{\partial t^2}\,. \tag{B.4}$$

Substitution of equation (B.4) in equation (B.2) yields:

$$\frac{\partial m_a}{\partial t} - \frac{\partial^2 \rho}{\partial t^2} + \frac{\partial^2}{\partial x_i \partial x_j}(p\delta_{ij} - \tau_{ij} + \rho v_j v_i) = \frac{\partial f_i}{\partial x_i}\,. \tag{B.5}$$

If no unsteady mass injection into the system is assumed, the acoustic equation becomes:

$$-\frac{\partial^2 \rho}{\partial t^2} + \frac{\partial^2}{\partial x_i \partial x_j}(p\delta_{ij} - \tau_{ij} + \rho v_j v_i) = \frac{\partial f_i}{\partial x_i}\,, \tag{B.6}$$

which equals, after rewriting the term with the Kronecker delta:

$$\frac{\partial^2 p}{\partial x_i^2} - \frac{\partial^2 \rho}{\partial t^2} = \frac{\partial^2}{\partial x_i \partial x_j}(\tau_{ij} - \rho v_j v_i) + \frac{\partial f_i}{\partial x_i}\,. \tag{B.7}$$

In acoustics, small perturbations around the mean values are considered. The pressure is therefore written as $p_0 + p'$, in which p_0 is the mean pressure, and p' is the pressure perturbation, which can be a function of space and time. Similarly the density is written as $\rho_0 + \rho'$, which leads to:

$$\frac{\partial^2 p'}{\partial x_i^2} - \frac{\partial^2 \rho'}{\partial t^2} = \frac{\partial^2}{\partial x_i \partial x_j}(\tau_{ij} - \rho v_j v_i) + \frac{\partial f_i}{\partial x_i}\,. \tag{B.8}$$

Subtracting a term $1/c_0^2 \cdot \partial^2 p'/\partial t^2$ on both sides of the equation leads, after some rewriting, to:

$$\frac{\partial^2 p'}{\partial x_i^2} - \frac{1}{c_0^2}\frac{\partial^2 p'}{\partial t^2} = \frac{\partial^2}{\partial x_i \partial x_j}(\tau_{ij} - \rho v_j v_i) + \frac{\partial f_i}{\partial x_i} + \frac{\partial^2}{\partial t^2}\left(\rho' - \frac{p'}{c_0^2}\right)\,. \tag{B.9}$$

If c_0 is taken as the speed of sound and the right-hand side is taken as zero, this is the homogeneous wave equation. All effects not compliant with the homogeneous wave equation are treated as acoustic sources and are placed on the right-hand side of this equation. The first term describes quadrupole sources (two spatial derivatives), for instance due to flow noise. The second term describes dipole sources (one spatial derivative), for instance due to forces acting on the fluid and the third term describes monopole sources such as

unsteady combustion. The equation that is used in this thesis, leaving out the dipole and quadrupole terms, becomes:

$$\frac{\partial^2 p'}{\partial x_i^2} - \frac{1}{c_0^2}\frac{\partial^2 p'}{\partial t^2} = \frac{\partial^2}{\partial t^2}\left(\rho' - \frac{p'}{c_0^2}\right) . \tag{B.10}$$

The right-hand side term in this equation has to be expressed in combustion related parameters. This is done in the next section.

B.2 Unsteady heat release rate as source

In the previous section of this appendix, an acoustic source term for a monopole source was derived in equation (B.10). The basic acoustic property of unsteady combustion is the unsteady heat release rate [53], so a relation is needed between this acoustic source term and heat release rate. This is often done using the basic laws of thermodynamics. A more heuristic approach is taken here [42].

The term needed is the thermoacoustic source term in the right-hand side of Lighthill's equation, equation (B.10). From thermodynamics it is known [14] that any thermodynamic variable can be expressed as a function of two other independent variables. If the pressure p is taken as a function of density ρ and heat release q, a small change in pressure $\mathrm{d}p$ is given by:

$$\mathrm{d}p = \left(\frac{\partial p}{\partial \rho}\right)_q \mathrm{d}\rho + \left(\frac{\partial p}{\partial q}\right)_\rho \mathrm{d}q\,. \tag{B.11}$$

For a reversible process, heat release and entropy s are related by:

$$\mathrm{d}q = T\mathrm{d}s\,, \tag{B.12}$$

in which T is the absolute temperature. Constant heat release is therefore the same condition as constant entropy. The isentropic relations for an ideal gas can therefore be used for the first partial derivative in equation (B.11). The relation between pressure and density is therefore:

$$p = B\rho^\gamma\,, \tag{B.13}$$

in which γ is the ratio between specific heats and B is an arbitrary constant. Using the equation of state for an ideal gas, $p = \rho RT$, with R the gas constant, the first partial derivative can now be obtained in a straightforward manner as:

$$\left(\frac{\partial p}{\partial \rho}\right)_s = \gamma B\rho^{\gamma-1} = \gamma\frac{p}{\rho} = \gamma RT\,. \tag{B.14}$$

Using the definition of the speed of sound, $c_0^2 = \gamma RT$, finally gives:

$$\left(\frac{\partial p}{\partial \rho}\right)_q = c_0^2 \,. \tag{B.15}$$

The second partial derivative in equation (B.11) is evaluated at constant density (or constant specific volume). The relation between heat release and temperature is then given by:

$$\mathrm{d}q = c_v \mathrm{d}T \,, \tag{B.16}$$

in which c_v is the specific heat at constant volume. Using the equation of state for an ideal gas, the partial derivative can be written as:

$$\left(\frac{\partial p}{\partial q}\right)_\rho = \frac{1}{c_v}\left(\frac{\partial p}{\partial T}\right)_\rho = \frac{\rho_0 R}{c_v} \,. \tag{B.17}$$

For an ideal gas, the specific gas constant R, the specific heat at constant volume c_v, the specific heat at constant pressure c_p and the ratio of specific heats γ are related by:

$$R = c_p - c_v \,, \tag{B.18}$$

$$\gamma = \frac{c_p}{c_v} \,. \tag{B.19}$$

Using these two equations gives:

$$\frac{\rho_0 R}{c_v} = \frac{\rho_0 (c_p - c_v)}{c_v} = \rho_0(\gamma - 1) \,. \tag{B.20}$$

Using the expressions derived for the partial derivatives in equation (B.11), equations (B.15) and (B.20), gives:

$$dp = c_0^2 d\rho + \rho_0(\gamma - 1) dq \,. \tag{B.21}$$

Substituting this for p' in the right-hand side term in equation (B.10) gives:

$$\frac{1}{c_0^2}\frac{\partial^2 p'}{\partial t^2} - \frac{\partial^2 p'}{\partial x_i^2} = \frac{\rho_0(\gamma - 1)}{c_0^2}\frac{\partial^2 q'}{\partial t^2} \,. \tag{B.22}$$

Because the heat release q is of dimension J/kg and not J/m^3, there is a ρ_0 in the source term and a second derivative to time is found because q is defined as heat release and not heat release rate, in contrast with some well-known publications [23, 53]. Furthermore, there are two constants, namely ρ_0 and c_0. These are the local density and the local speed of sound. These values strongly depend on the local temperature. Good correspondence with measurements is found if the mean density ρ_0 and speed of sound c_0 are used at the adiabatic flame temperature [48].

B.3 Compactness of the source

A common assumption in thermoacoustic modeling is that the source is compact, which means that the source is much smaller than the acoustic wavelength:

$$L_s \ll \frac{c_0}{f_{max}}\,, \tag{B.23}$$

in which L_s is a characteristic dimension of the source and f_{max} is the maximum frequency of interest. For case 15.7 (125 kW at 1.5 bar, table 3.1), the flame temperature is 1808 K (appendix A) and therefore the speed of sound is 852 m/s. The maximum frequency of interest is 500 Hz (section 1.2), which means that the source should be much smaller than 1.7 meter. Figure B.1 shows the numerically calculated rate of consumption of methane, which is an indication of the heat release rate. These results were experimentally validated [48]. In the length direction, the heat release is concentrated in less than the first one diameter (0.15 meter) of the combustion chamber.

Rayleigh's criterion (subsection 3.2.2) states that when heat is added at high acoustic pressures and taken at low acoustic pressures, then the system experiences a driving force and, in the absence of damping, acoustic pressure amplitudes grow. The position of heat release within a standing wave is therefore very important. The flame dimension is approximately 6% of a wavelength and therefore the location is fairly well defined, but it should be realized that the flame is not all that compact.

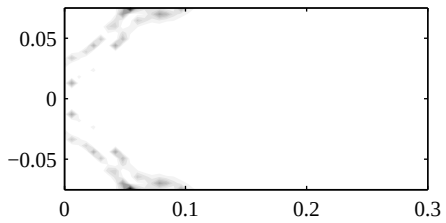

Figure B.1: Numerically calculated rate of consumption of methane (CH_4), which is an indication of heat release rate. White denotes no consumption, black high consumption. Only the first 0.3 meter of the almost 2 meter long combustion chamber is shown.

In the radial direction (the vertical direction in figure B.1) the acoustic field is one-dimensional and therefore the flame is compact by definition. Moreover, the flame is almost axi-symmetric, despite the square combustion chamber geometry, and therefore the acoustic source can be lumped on the axis of the combustion chamber if near-field effects are neglected.

B.4 Finite element implementation

In the previous parts of this appendix it was shown that the flame acts as a monopole source. There are several methods to implement this in a finite element code. The method used depends on the code used. Nowak [72] and Fannin [31] both use SYSNOISE and apply the same technique. They move a surface at the boundary of the acoustic domain, at the location of the flame front, such that it generates a volume source that is equivalent to the unsteady heat release of the flame. Pankiewitz [75] employs COMSOL FemLab which allows for more control on the way the finite element code works. He discretizes the source term caused by unsteady heat release together with the wave equation (B.22).

In this thesis the commercial finite element code ANSYS is used, which does not allow for a direct implementation like Pankiewitz used. To model unsteady heat release, a volume source Q is used, which is defined as a nodal flow rate [2] with dimensions [m^3/s^2] and which acts as a monopole source. Equation (B.10) has a monopole source on the right-hand side, which was rewritten in heat release terms in equation (B.22). Therefore, it can be expected that a similar relation exists between the nodal flow rate in ANSYS and the heat release. Because the source is lumped to one node, the heat release has to be integrated over the volume of the flame. Heat release is therefore expressed as the volume integrated heat release rate $\bar{q}$ with dimension [J/s]. The relation between the specific heat release q' and the volume integrated heat release rate $\bar{q}$ is given by:

$$\bar{q} = \rho_0 \int_V \frac{\partial q'}{\partial t} dV \,, \tag{B.24}$$

in which V is the total volume of the flame. Making a volume integrated term of the right-hand side of equation (B.22) gives:

$$\int_V \frac{\rho_0(\gamma-1)}{c_0^2} \frac{\partial^2 q'}{\partial t^2} dV = \frac{\rho_0(\gamma-1)}{c_0^2} \frac{\partial}{\partial t} \int_V \frac{\partial q'}{\partial t} dV \,. \tag{B.25}$$

Using equation (B.24) leads to the volume integrated source term:

$$\frac{\rho_0(\gamma-1)}{c_0^2} \frac{\partial}{\partial t} \int_V \frac{\partial q'}{\partial t} dV = \frac{(\gamma-1)}{c_0^2} \frac{\partial \bar{q}}{\partial t} \,. \tag{B.26}$$

A relation between the nodal flow rate and this volume integrated heat release rate is now needed, which should include the term of equation (B.26). The dimensions of the term are [kg/s^2]. The nodal flow rate is expressed in [m^3/s^2]

and therefore a division by the mean density is still needed. The nodal flow rate can therefore be expressed in the volume integrated heat release rate as:

$$Q = \frac{(\gamma - 1)}{\rho_0 c_0^2} \frac{\partial \bar{q}}{\partial t} \,. \tag{B.27}$$

Transformation to the frequency domain, again assuming harmonic perturbations as $\bar{q} = \hat{q} e^{\mathrm{i}\omega t}$, is straightforward and gives:

$$Q = \frac{\mathrm{i}\omega(\gamma - 1)}{\rho_0 c_0^2} \hat{q} \,. \tag{B.28}$$

The term $\mathrm{i}\omega$ is a direct consequence of the ANSYS implementation, in which a volume flow rate is prescribed and not volume flow. Therefore, it is often not found in the literature.

B.5 Free field pressure from a volume source

In ANSYS the acoustic volume source Q with dimension $\mathrm{m}^3/\mathrm{s}^2$ is used. This section derives the free field response from this source, to be able to translate pressures measured in the free field to the corresponding source strength. The pressure field caused by a pulsating sphere is given by [7, 102]:

$$\hat{p}(r_s) = \frac{\mathrm{i}\rho_0 c_0 k a_s^2 \hat{v}_s}{(1 + \mathrm{i}ka_s) r_s} e^{-\mathrm{i}k(r_s - a_s)} \,, \tag{B.29}$$

in which r_s is the distance to the source, a_s is the radius of the sphere and $\hat{v}_s$ is the complex amplitude of the surface velocity. If the sphere is much smaller than the acoustic wavelength ($a_s \ll 1/k$), this can be written as:

$$\hat{p}(r_s) = \frac{\mathrm{i}\rho_0 c_0 k a_s^2 \hat{v}_s}{r_s} e^{-\mathrm{i}k(r_s - a_s)} \,. \tag{B.30}$$

Only an amplitude relation is needed, and therefore this equation can be simplified further to:

$$|\hat{p}(r_s)| = \frac{\rho_0 c_0 k a_s^2 |\hat{v}_s|}{r_s} \,. \tag{B.31}$$

Assuming harmonic perturbations, the acoustic volume source Q used in the finite element calculations can be written as a pulsating sphere according to:

$$|Q| = 4\pi a_s^2 \omega |\hat{v}_s| \,. \tag{B.32}$$

Combining equations (B.32) and (B.31) results in:

$$|\hat{p}(r_s)| = \frac{\rho_0}{4\pi r_s}|Q|\,. \tag{B.33}$$

This equation shows that, for free field radiation, the acoustic pressure in the field is proportional to the acoustic volume source used in the finite element code. The frequency dependence of the pressure generated by a flame under free field conditions is therefore the same as the frequency dependence of the acoustic volume source.

Appendix C

Acoustic particle velocity in FEM

The variable solved in the acoustic finite element formulation is the pressure. This appendix explains how to obtain the acoustic particle velocity from this pressure data for linear, isoparametric, tetrahedral elements.

To obtain the acoustic particle velocity from the nodal pressures, the relation between particle velocity and pressure gradient in the frequency domain (the Helmholtz equation) can be applied:

$$-\rho_0 \mathrm{i}\omega \hat{v}_i = \frac{\partial \hat{p}}{\partial x_i}\,, \tag{C.1}$$

in which ρ_0 is density, i is the imaginary unit, ω is angular frequency, $\hat{v}_i$ is the amplitude of the particle velocity in direction i, $\hat{p}$ is the amplitude of the pressure and x_i is the coordinate in that direction. Pressure gradient information is not directly available in the finite element solution extracted from the finite element code, but can be obtained within an element using the shape functions. Using isoparametric elements gives the same shape functions for location and field variable, or:

$$x_i = \sum_{k=1}^{4} N^{(k)} x_i^{(k)} \tag{C.2}$$

$$\hat{p} = \sum_{k=1}^{4} N^{(k)} \hat{p}^{(k)}\,, \tag{C.3}$$

in which $x_i^{(k)}$ and $\hat{p}^{(k)}$ are the coordinates of and the amplitudes of the pressure on node k of the element and $N^{(k)}$ are the shape functions. The derivatives

of the pressure with respect to the global coordinates x_i can be written in derivatives with respect to the element coordinates y_j as:

$$\frac{\partial \hat{p}}{\partial x_i} = \sum_{j=1}^{3} \frac{\partial \hat{p}}{\partial y_j} \frac{\partial y_j}{\partial x_i} \,. \tag{C.4}$$

The derivatives of $\hat{p}$ to the local coordinates follow directly from equation (C.3) as:

$$\frac{\partial \hat{p}}{\partial y_j} = \sum_{k=1}^{4} \frac{\partial N^{(k)}}{\partial y_j} \hat{p}^{(k)} \,. \tag{C.5}$$

The derivatives of the local coordinates y_j to the global coordinates x_i follow from (C.2) as:

$$\frac{\partial y_j}{\partial x_i} = 1 / \sum_{k=1}^{4} \frac{\partial N^{(k)}}{\partial y_j} x_i^{(k)} \,, \tag{C.6}$$

with which the derivatives of the pressure $\hat{p}$ to the global coordinates x_i can be written as:

$$\frac{\partial \hat{p}}{\partial x_i} = \sum_{j=1}^{3} \left(\sum_{k=1}^{4} \frac{\partial N^{(k)}}{\partial y_j} \hat{p}^{(k)} / \sum_{k=1}^{4} \frac{\partial N^{(k)}}{\partial y_j} x_i^{(k)} \right) . \tag{C.7}$$

For a tetrahedral isoparametric linear element, the shape functions are given by [20]:

$$N^{(1)} = 1 - y_1 - y_2 - y_3 \,, \tag{C.8a}$$

$$N^{(2)} = y_1 \,, \tag{C.8b}$$

$$N^{(3)} = y_2 \,, \tag{C.8c}$$

$$N^{(4)} = y_3 \,, \tag{C.8d}$$

which means that, in matrix vector notation, the pressure gradients are obtained with:

$$\begin{Bmatrix} \frac{\partial \hat{p}}{\partial x_1} \\ \frac{\partial \hat{p}}{\partial x_2} \\ \frac{\partial \hat{p}}{\partial x_3} \end{Bmatrix} = \left[\begin{bmatrix} -1 & 1 & 0 & 0 \\ -1 & 0 & 1 & 0 \\ -1 & 0 & 0 & 1 \end{bmatrix} \cdot \begin{bmatrix} x_1^{(1)} & x_2^{(1)} & x_3^{(1)} \\ x_1^{(2)} & x_2^{(2)} & x_3^{(2)} \\ x_1^{(3)} & x_2^{(3)} & x_3^{(3)} \\ x_1^{(4)} & x_2^{(4)} & x_3^{(4)} \end{bmatrix} \right]^{-1} \begin{bmatrix} -1 & 1 & 0 & 0 \\ -1 & 0 & 1 & 0 \\ -1 & 0 & 0 & 1 \end{bmatrix} \begin{Bmatrix} \hat{p}^{(1)} \\ \hat{p}^{(2)} \\ \hat{p}^{(3)} \\ \hat{p}^{(4)} \end{Bmatrix} . \tag{C.9}$$

It can be seen that the pressure gradient is independent of the location in the element, which is a consequence of the element formulation.

Appendix D

Approximate liner models

In this appendix several approximate models of the liner are presented. In this thesis, they are used for numerical validation or as a basis for more advanced models. A two-dimensional structural model of the liner is constructed first, because its results are easier to interpret than those of a three-dimensional model. Furthermore, it is used to explain the influence of acoustic cavities on the structural behavior in section 4.5.2. A two-dimensional finite element model is described, after which an analytical approximation of the results is shown. An analytical approximation of the three-dimensional finite element liner model from section 4.4.3 is also given.

D.1 Two-dimensional finite element model

The two-dimensional model consists of linear beam elements. It is expected that the corners of the liner will not move much in the three-dimensional tube when the tube is not very long (because the bending stiffness along the length of the liner is much higher than the local stiffness of the side plates of the tube). The corners are therefore modeled as pinned boundary conditions which only allow for rotation (figure D.1). Furthermore, the corners are assumed to remain right-angled. A term $(1-\nu^2)$ with ν Poisson's ratio is used for the area moment of inertia about the neutral axis I_{zz}, to account for the fact that the sides are, in reality, plates and not beams, so they cannot contract in the direction not included in the model. In equation:

$$I_{zz} = \frac{L_2 t_2^3}{12(1-\nu^2)}\,, \tag{D.1}$$

in which t_2 is the thickness and L_2 is the length (see section 4.4.2). The element size used is 10 mm. The dimensions and material properties from the liner of the test rig, listed in table 4.3, are used. The resulting eigenfrequencies are listed in table D.2.

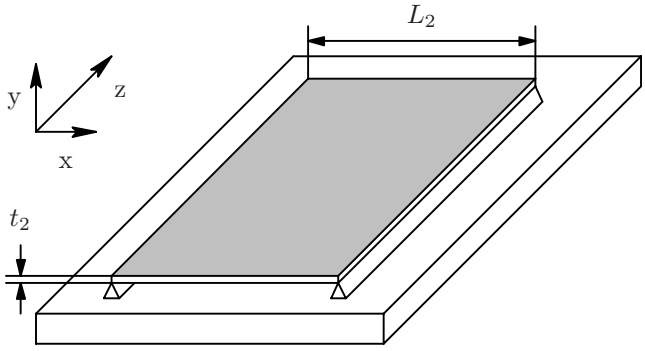

Figure D.1: Schematic representation of one side of the two-dimensional model for pinned boundary conditions. Four of these together form the square liner.

D.2 Two-dimensional analytical model

The behavior of the square section can also be described analytically by beam modes of each of the sides. All four beams have to vibrate in the same mode shape, because they all vibrate at the same frequency and have the same dimensions. Because the boundary conditions applied externally to the model are pinned connections, a side cannot behave like it has a free end condition. The three possible beam mode shapes remaining are clamped-clamped (cc), clamped-pinned (cp) and pinned-pinned (pp), with the clamped condition for a side being imposed by the side around the corner. Because the corners have to remain right-angled, these beam mode shapes give, for the first beam modes, the eigenmodes shown in figure D.2. Higher modes of the two-dimensional model, which consist of the higher beam modes, are denoted by a number between brackets. The second pinned-pinned mode for instance is denoted by 'pp (2)'.

The eigenfrequencies for the beam modes are [8]:

$$f_i = \frac{\lambda_i^2}{2\pi d^2}\sqrt{\frac{EI_{zz}}{m_b}}\,, \tag{D.2}$$

in which f_i denotes an eigenfrequency, E is Young's modulus, d is the length

of a beam and m_b is the mass per unit length of the beam. The parameter λ_i is given in table D.1 (see e.g. Blevins [8]). The resulting eigenfrequencies are listed in table D.2. The modes consisting of clamped-pinned beams are

Mode	**pp**	**pc**	**cc**
1	π	3.93	4.73
2	2π	7.07	7.85
3	3π	10.21	11.00

Table D.1: Value of parameter λ_i in equation (D.2).

listed twice, because the shape of this beam mode is not symmetric. There are therefore two possible geometric compositions, one being a 90 degrees rotated version of the other, which is shown in the right-hand two images in figure D.2. If the setup is not entirely symmetric due to manufacturing, for instance, these two modes both show up separately.

Mode	1	2/3	4	5	6/7
Shape	pp (1)	pc (1)	cc (1)	pp (2)	pc (2)
FEM	164.4 Hz	256.9 Hz	372.7 Hz	657.6 Hz	832.3 Hz
Analytic	164.4 Hz	256.9 Hz	372.7 Hz	657.7 Hz	832.4 Hz

Table D.2: Finite element and analytical eigenfrequencies for the two-dimensional model. Shapes are shown in figure D.2.

Table D.2 shows that the structural finite element model and the analytical description give practically the same results. The structural finite element model used in this appendix is extended in section 4.5.2 with acoustic cavities to study the influence of these on the structural behavior.

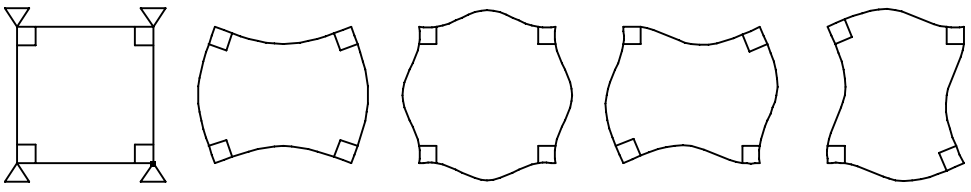

Figure D.2: The two-dimensional structural model (left) and the analytic structural mode shapes. The two figures on the right are 90 degrees rotated versions of the same mode.

D.3 Three-dimensional analytical model

The two-dimensional model showed that the eigenmodes of the square section consist of three types of beam modes, namely pinned-pinned, pinned-clamped and clamped-clamped. In the three-dimensional model, the inlet side and the outlet side are clamped. It can therefore be expected that the eigenmodes now consist of plate modes with two opposite sides clamped and the other two sides either simply supported (ss), clamped (cc) or one clamped and one simply supported (cs). The (cs) modes do not show a match with finite element results for the tube and therefore these are not used. The eigenfrequencies for plates with different boundary conditions are given by:

$$f_{ij} = \frac{\lambda_{ij}^2}{2\pi a^2}\sqrt{\frac{Eh^3}{12\gamma(1-\nu^2)}}\,. \tag{D.3}$$

The parameter λ_{ij} is tabulated for different length to width ratios. For the

Mode	cc	ss
1	23.34	11.64
2	26.52	16.77
3	31.44	24.78

Table D.3: Values for λ_{ij} in equation (D.3) for a plate with an aspect ratio of 0.375.

geometry used in this thesis, with a ratio of 0.375, the values are extrapolated from the values at a ratio of 0.4 and at a ratio of 2/3. These extrapolated

Mode	Analytic	FEM	Description
1	193.9	196.8	$(11)_{\mathrm{ss}}$
2/3		280.5	$(11)_{\mathrm{h}}$
4	279.4	287.0	$(12)_{\mathrm{ss}}$
5/6		355.3	$(12)_{\mathrm{h}}$
7	388.8	390.3	$(11)_{\mathrm{cc}}$
8	412.8	426.9	$(13)_{\mathrm{ss}}$
9	441.8	448.9	$(12)_{\mathrm{cc}}$
10/11		481.1	$(13)_{\mathrm{h}}$

Table D.4: Eigenfrequencies in Hz for the three-dimensional structural models.

values are given in table D.3. The resulting eigenfrequencies are listed in table D.4 together with the results that were obtained in section 4.4.

The main difference between the two-dimensional and the three-dimensional model is that the modal density has increased considerably. This is because additional modes are present in the third direction. In table D.4 it can be seen that the eigenfrequencies of the cc and cs modes show fairly good agreement between the analytical and numerical model. The differences are mostly caused by the approximated value of λ_{ij}. This was also observed in section 4.3.2 on the simplified model.

Appendix E

Mode identification

In the test rig, the modes can be measured on one side only, because the laser vibrometer has to be positioned at one of the sides (see chapter 2). To compare measured and calculated modes, the corresponding modes should be identified. This can be done using the Modal Assurance Criterion or MAC value [68] given by:

$$\mathrm{MAC_{ij}} = \frac{\left(\boldsymbol{\phi}_i^T \boldsymbol{\phi}_j\right)^2}{\left(\boldsymbol{\phi}_i^T \boldsymbol{\phi}_i\right)\left(\boldsymbol{\phi}_j^T \boldsymbol{\phi}_j\right)}\,, \tag{E.1}$$

in which $\boldsymbol{\phi}_i$ is the vector containing the displacements for mode i and $\mathrm{MAC_{ij}}$ is the MAC value between modes i and j. The MAC value is a derivation from the angle β between two vectors, which is defined by:

$$\cos(\beta) = \frac{\boldsymbol{\phi}_i \cdot \boldsymbol{\phi}_j}{|\boldsymbol{\phi}_i||\boldsymbol{\phi}_j|}\,, \tag{E.2}$$

from which it can be seen that the MAC value is the squared cosine from the angle between the vectors describing the mode shapes. If the measured and calculated mode are the same, the MAC value is one, whereas uncorrelated modes result in a MAC value of zero. The values do not have to be zero though. Eigenmodes are orthogonal to the mass and stiffness matrix, so the following equations hold:

$$\boldsymbol{\Phi}^T \mathbf{M} \boldsymbol{\Phi} = \mathbf{I} \qquad \boldsymbol{\Phi}^T \mathbf{K} \boldsymbol{\Phi} = \boldsymbol{\Omega}\,, \tag{E.3}$$

in which $\mathbf{M}$ is the mass matrix, $\mathbf{K}$ is the stiffness matrix, $\boldsymbol{\Phi}$ is the matrix containing the vectors $\boldsymbol{\phi}$, $\mathbf{I}$ is the identity matrix and $\boldsymbol{\Omega}$ is a diagonal matrix. The MAC criterion includes neither the mass nor the stiffness matrix, because they are often not available. Therefore, if the stiffness or the mass are not

equally distributed, the off-diagonal values in the MAC-matrix do not have to be zero. As a first indication of what results to expect from the MAC values, the values are determined for the numerical mode shapes on the finite element grid compared with themselves. The results are depicted in figure E.1. It

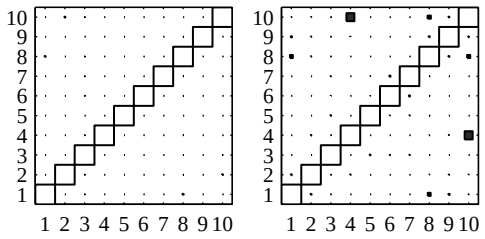

(a) Flexible part. (b) Full liner.

$1 = (11)_{ss}$ $7 = (11)_{cc}$
$2/3 = (11)_{h}$ $8 = (13)_{ss}$
$4 = (12)_{ss}$ $9 = (12)_{cc}$
$5/6 = (12)_{h}$ $10 = (13)_{h}$

Figure E.1: MAC values of the numerical modes for the finite element grid and the mode numbering used in this appendix.

can be clearly seen in figure E.1 that a mode obtains a MAC value of one (a white block) when compared with itself. What the other values are depends on which data are used. When only the data on the thin section are used, the other values are very small (only small dots are visible), because all nodes have approximately the same associated mass. This is not the case when the entire liner model is used, including the thick end parts. The nodes on the thick part have a higher associated mass and therefore the other values do not have to become zero anymore. This can be seen in the right figure, where non-zero values are observed for modes 8 and 10 (shown as black squares), which have substantial vibration on the thick end parts (they are modes with a (31) shape).

Measurement limitations

In the test setup, only a limited part of the liner is visible, limiting the structural vibration data that can be obtained. Furthermore, substantial time is needed to make a point measurement, because of the random and unknown excitation the combustion process generates. Only a limited set of measurements can therefore be made. These two limitations require an investigation of how well the visible parts show the vibration behavior and how many measurement points are needed to measure this behavior. Clearly distinguishable MAC values are a first requirement for this, though it may not be enough [70]. This is because a really strong assumption is used, namely that the calculated and measured mode shapes are the same. If this is the case, then it is pos-

sible to identify corresponding modes based on the MAC values. However, if the mode shapes are not exactly the same due to differences between model and experiment, which always exist to some extent, measurements made on a finer grid can give valuable information on the differences between the model of the structure and the structure itself. Furthermore, not all measurement points generate good data, which also justifies using more points than strictly necessary.

MAC values through the windows

To evaluate how well mode shapes can be distinguished, the full liner model is used (appendix F). The MAC values for the numerical mode shapes are calculated for a grid of 5x5 points on the square window and for a grid of 10x1 points on a slit window. The windows are located at the same position as they are in the test rig (section 2.4.2). The results are depicted in figure E.2.

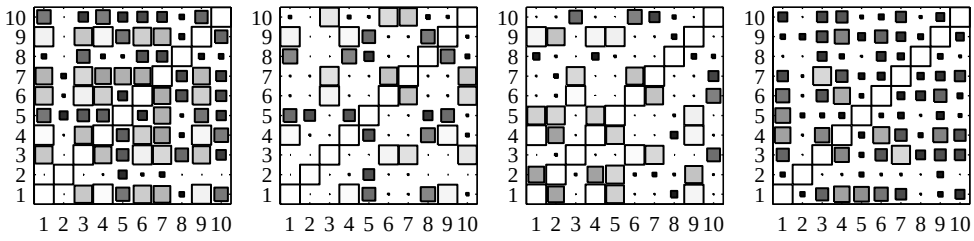

(a) Square window top. (b) Square window middle. (c) Slit window. (d) Slit window and square window.

Figure E.2: MAC values for different measurement windows.

Figure E.2(a) shows the MAC values for a square liner window as it is located in the test rig, covering the first part of the flexible section, directly after the welded connection to the thick part (see section 2.5.3 for the precise location of the windows with respect to the thin section). It can be seen that many modes become hard to distinguish. This is because all modes, starting from the weld, first increase in amplitude, so the first part of the modes looks pretty much the same. Figure E.2(b) shows the values when the window is moved to the middle of the flexible part. It is now easier to distinguish the modes because they differ more in this region. A $(21)_{ss}$ mode, for instance, has a nodal line where a $(11)_{ss}$ mode has only high amplitudes. Mode identification is still not really clear though. This is because information is available on one side of the liner only. Different types of, for instance, a (11) mode (which are $(11)_{ss}$, $(11)_{cc}$ and $(11)_{h}$) cannot be distinguished, because they give the same

vibration pattern behind the window. Figure E.2(c) shows the MAC values for 10 measurement points on a 35 cm slit window located 5 cm from the side of the liner, which is also present in the DESIRE rig. Distinction between for instance a $(11)_{ss}$ and $(21)_{ss}$ mode is very clear now, whereas distinction between different variants of (11) modes is hardly possible, because they simply all look the same on a line measurement. Also, the asymmetric variants of a mode are hard to distinguish using a line measurement. A combination of the square window at the top and the slit window on the side, which are both present in the test rig, gives the results shown in figure E.2(d). The modes can be identified somewhat better, but this option is hard to implement in the test rig, because the laser vibrometer has to measure around the corner.

The above may give the impression that it will be very difficult to extract useful information from the measurements. This is not necessarily the case, though. Because similar modes (like the $(11)_s$ modes) appear in a fixed sequence, the first time a certain pattern is observed is therefore likely to be the first mode seen in calculations (the cs case). Because the slit measurements give fair results and are easy to implement, these are used most in this thesis. Mode identification is then based on recognition of the shapes combined with an assumption, based on numerical results, of the sequence in which modes should appear.

Measurement grid density evaluation

It is preferable to decrease the number of measurement points in a grid, because experimental time is expensive for the test rig used in this thesis. The grid can be determined adaptively during the measurement [98] to refine the measurement at locations with a high level of detail, but because only mode shape data are required, a limited number of measurements is needed. The measurement locations are therefore determined offline. To evaluate the ef-

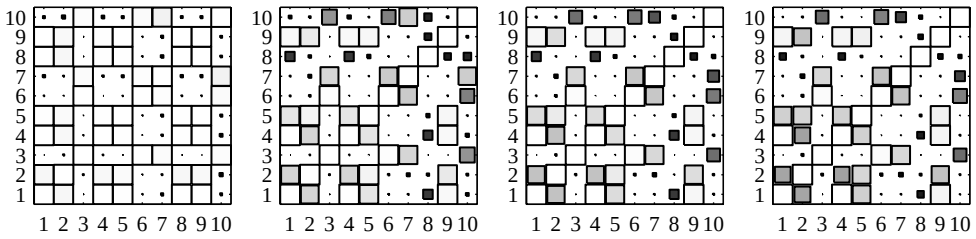

(a) One point. (b) Two points. (c) Three points. (d) Ten points.

Figure E.3: MAC values for different grid densities.

fect of coarser grids on the identification of modes based on their mode shape, figure E.3 shows the MAC values for different grid densities using data on a slit. It can be seen that using more than three points does not improve the identification further. This again assumes that the measured and calculated modes are actually the same. The reason is that three points already give a distinct pattern for the modes in the range considered.

Appendix F

Improved structural model

In section 4.4, a three-dimensional, but still simplified, model of the flexible liner was described. To give an indication of how the structural results can be improved, a more elaborative model is developed in this appendix, which is closer to the manufactured setup. The main differences between this improved structural model and the structural model in section 4.4 are:

- The thick parts are also included. The boundary conditions for the flexible part were taken as clamped, but they are not entirely stiff, since they are only 4.0 mm thick. Equation 4.6 shows that the eigenfrequency scales with the thickness to the power 1.5, which means that the eigenfrequencies using the thick material are only 4.4 times higher than those using the thin material. The so-called eigenfrequencies of the thin part are therefore also influenced by the vibration of the thick part.

- The corners of the tube are taken as rounded, which they are because the tube has been bent from plate material (see also section 4.4.2).

- An approximation of the weld on the thin part of the liner is added. These welds (figure 4.7) are needed for the production of the liner and influence the dynamic behavior. There is some literature on methods to model spot welds that proposes rigidly connecting an area approximating the spot size from both parts together in the finite element model [58]. Following this approach, the welds on the thin part are modeled as stiffened areas in the flexible plate by making the Young's modulus much larger than in the rest of the thin liner part, to accommodate for thickness, stiffness and curves that exist around the weld.

- The welds between the thick and the thin section are accounted for by

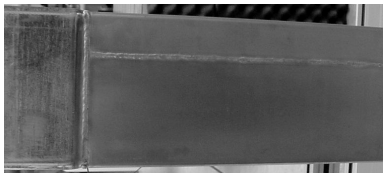

Property	Value
Young's modulus	190 GPa
Flexible section length	460 mm
Young's modulus weld	2000 GPa
Weld width	10 mm

Table F.1: Picture of the weld and the properties of the full model.

changing the length of the flexible section.

Because the exact properties of the liner, such as the stiffness of the weld, are unknown, the eigenfrequencies of the finite element model are fitted to the experimental results (section 4.4.4). A genetic algorithm was used to determine the Young's modulus, stiffness and width of the weld on the flexible section and the precise length of the flexible section (to accommodate for the welds at the ends, which cause a transition zone between thick and thin). The resulting values are listed in table F.1 and the eigenfrequencies found with this model are listed in table F.2. There are better and more advanced methods for improving the similarity between measurements and calculations [22], but it is probably wiser to first gain more understanding of the behavior of the welded liner, or else manufacture a liner with more well-defined properties.

Mode	Analytic	FEM	FEM fit	Measured	Description
1	193.9	196.8	182.5	181.5	$(11)_{ss}$
2/3		280.5	269.0 / 279.1	257.5/269.0	$(11)_{h}$
4	279.4	287.0	243.6	239.0	$(12)_{ss}$
5/6		355.3	318.0 / 337.6	285.0/327.0	$(12)_{h}$
7	388.8	390.3	394.8	-	$(11)_{cc}$
8	412.8	426.9	321.2	316.5	$(13)_{ss}$
9	441.8	448.9	441.0	-	$(12)_{cc}$
10/11		481.1	393.4 / 427.1	-	$(13)_{h}$

Table F.2: Eigenfrequencies in Hz for the three-dimensional structural models.

Bibliography

[1] S. Allam and H. Bodén. Signal-to-noise ratio enhancement in experimental characterisation of ic-engine exhaust and intake systems. In *Proceedings of the International Congress on Sound and Vibration 11*, 2004.

[2] AnsysHTML Online Documentation. Ansys*8.1*. Ansysinc., 2004.

[3] Y. Aurégan and G. Ajello. Scattering matrix measurements of circular diaphragm with superimposed flow. In Fülöp Augusztinovicz, editor, *Proceedings of Internoise*, volume 1, pages 383–386. OPAKFI, 1997.

[4] P. Bak, C. Tang, and K. Wiesenfeld. Self-organized criticality: An explanation of 1/f noise. *Physical Review Letters*, 59(4):381–384, 1987.

[5] T.G.H. Basten. *Noise reduction by viscothermal acousto-elastic interaction in double wall panels*. PhD thesis, University of Twente, 2001.

[6] D. Bernier, S. Ducruix, , F. Lacas, S. Candel, N. Robart, and T. Poinsot. Transfer function measurements in a model combustor: application to adaptive instability control. *Combustion Science and Technology*, 175:993–1013, 2003.

[7] D.A. Bies and C.H. Hansen. *Engineering noise control, theory and practice*. E&FN Spon, an imprint of Chapman & Hall, 2nd edition, 1996.

[8] R.D. Blevins. *Formulas for natural frequency and mode shape*. Robert E. Krieger publishing company, 1984.

[9] G.J. Bloxsidge, A.P. Dowling, and P.J. Langhorne. Reheat buzz, and acoustically coupled combustion instability. Part 2. Theory. *Journal of Fluid Mechanics*, 193:445–473, 1988.

[10] D. Bohn, G. Deutsch, and U. Krüger. Numerical prediction of the dynamic behavior of turbulent diffusion flames. *Journal of Engineering for Gas Turbines and Power*, 120:713–720, 1998.

[11] V. Borue. Inverse energy cascade in stationary two-dimensional homogeneous turbulence. *Physical Review Letters*, 72(10):1475–1479, 1994.

[12] C. Bréard, A.I. Sayma, M. Vahdati, and M. Imregun. Aeroelasticity analysis of an industrial gas turbine combustor using a simplified combustion model. *Journal of Fluids and Structures*, 16(8):1111–1126, 2002.

[13] S.J. Brookes, R.S. Cant, I.D.J. Dupère, and A.P. Dowling. Computational modeling of self-excited combustion instabilities. *Journal of Engineering for Gas Turbines and Power*, 123(2):322–326, 2001.

[14] Y.A. Çengel and R.H. Turner. *Fundamentals of Thermal-Fluid Sciences*. McGraw-Hill, 2001.

[15] W.S. Cheung, G.J.M. Sims, J.R. Copplestone, R.W. Tilston, C.W. Wilson, S.R. Stow, and A.P. Dowling. Measurements and analysis of flame transfer function in a sector combustor under high pressure conditions. In *Proceedings of the ASME TURBO EXPO 2003*, 2003. GT2003-38219.

[16] H.G. Choi, S.W. Yoo, J.D. Jeong, and J.M. Lee. Acoustic characteristics of annular cavities with locally non-uniform media. *Journal of Sound and Vibration*, 266:967–980, 2003.

[17] J.Y. Chung and D.A. Blaser. Transfer function method of measuring in-duct acoustic properties: I. theory. *Journal of the Acoustical Society of America*, 68:907–913, 1980.

[18] J.Y. Chung and D.A. Blaser. Transfer function method of measuring in-duct acoustic properties: II. experiment. *Journal of the Acoustical Society of America*, 68:914–921, 1980.

[19] R.D. Ciskowski and C.A. Brebbia. *Boundary element methods in acoustics*. Computational Mechanics Publications, 1991.

[20] R.D. Cook, D.S. Malkus, M.E. Plesha, and R.J. Witt. *Concepts and Applications of Finite Element Analysis*. John Wiley & Sons, 2002.

[21] A. Cummings, H.J. Rice, and R. Wilson. Radiation damping in plaes, induced by porous media. *Journal of Sound and Vibration*, 221(1):143–167, 1999.

[22] W. D'Ambrogio and A. Fregolent. The use of antiresonances for robust model updating. *Journal of Sound and Vibration*, 236(2):227–243, 2000.

[23] A.P. Dowling. The calculation of thermoacoustic oscillations. *Journal of Sound and Vibration*, 180(4):557–581, 1995.

[24] A.P. Dowling. Nonlinear self-excited oscillations of a ducted flame. *Journal of Fluid Mechanics*, 346:271–290, 1997.

[25] A.P. Dowling. Singing flames - the coupling of acoustics and combustion. In *Proceedings of the International Congress on Sound and Vibration 10*, 2003.

[26] P. Durrieu, G. Hofmans, G. Ajello, R. Boot, Y. Auregan, A. Hirschberg, and M.C.A.M. Peters. Quasisteady aero-acoustic response of orifices. *Journal of the Acoustical Society of America*, 110(4):1859–1872, 2001.

[27] F.J.M. van der Eerden. *Noise reduction with coupled prismatic tubes.* PhD thesis, University of Twente, 2000.

[28] G.C. Everstine. A symmetric potential formulation for fluid-structure interaction. *Journal of Sound and Vibration*, 79(1):157–160, 1981. Letter to the editor.

[29] S. Evesque, W. Polifke, and C. Pankiewitz. Spinning and azimuthally standing acoustic modes in annular combustors. In *Proceedings of the AIAA/CEAS Aeroacoustics Conference and Exhibit 9*, 2003.

[30] D.J. Ewins and P.T. Gleeson. A method for modal indentification of lightly damped structures. *Journal of Sound and Vibration*, 84(1):57–79, 1982.

[31] C.A. Fannin. *Linear modeling and analysis of thermoacoustic instabilities in a gas turbine combustor.* PhD thesis, Virginina Polytechnic Institute and State University, 2000.

[32] E.C. Fernandes. The design of sound probes. In *Proceedings of the International Congress on Sound and Vibration 12*, 2005.

[33] F. Flemming, A. Nauert, A. Sadiki, J. Janicka, H. Brick, R. Piscoya, M. Ochmann, and P. Költzsch. A hybrid approach for the evaluation of the radiated noise from a turbulent non-premixed jet flame based on large eddy simulation and equivalent source & boundary element methods. In

Proceedings of the International Congress on Sound and Vibration 12, 2005.

[34] G.F. Franklin, J.D. Powell, and A. Emami-Naeini. *Feedback control of dynamic systems*. Addison-Wesley Publishing Company, 1994.

[35] L.P. Franzoni and C.M. Elliott. An innovative design of a probe-tube attachment for a 1/2 in. microphone. *Journal of the Acoustical Society of America*, 5:2903–2910, 1998.

[36] T.M. Geerssen. *Physical properties of natural gases*. N.V. Nederlandse Gasunie, 1988.

[37] Y. Hardalupas and M. Orain. Local measurements of the time-dependent heat release rate and equivalence ratio using chemiluminescent emission from a flame. *Combustion and Flame*, 139:188–207, 2004.

[38] M. Harleman. Characterizing flame behavior in a lean premixed turbulent methane burner with optical techniques. Master's thesis, University of Twente, Faculty of Mechanical Engineering, Enschede, The Netherlands, 2005.

[39] Haynes International. *Hastelloy X®*. Haynes International, 2005.

[40] Haynes International. *Haynes® HR-120™*. Haynes International, 2005.

[41] R.C. Heinemeijer. Verification of acoustic source localization methods. Master's thesis, University of Twente, Faculty of Mechanical Engineering, Enschede, The Netherlands, 2003.

[42] A. Hirschberg and C. Schram. A primitive approach to aeroacoustics. *Lecture Notes in Physics*, 586:1–30, 2002.

[43] R.A. Huls, A. de Boer, and J.B.W. Kok. A transfer function approach to structural vibrations induced by thermoacoustic sources. In *Proceedings of the International Congress on Sound and Vibration 11*, 2004.

[44] R.A. Huls, A. de Boer, J.B.W. Kok, and P.G.M. van der Hoogt. Experimental validation of the interaction between combustion and structural vibration. In *Proceedings of the International Congress on Sound and Vibration 12*, 2005.

[45] R.A. Huls, J.F. van Kampen, J.B.W. Kok, and A. de Boer. Fluid structure interaction to predict liner vibrations in an industrial combustion

system. In *Proceedings of the International Congress on Sound and Vibration 10*, 2003.

[46] J.G. Ih, C.M. Park, and H.J. Kim. A model for sound propagation in capillary ducts with mean flow. *Journal of Sound and Vibration*, 190(2):163–175, 1996.

[47] U. Ingard and V.K. Singhal. Sound attenuation in turbulent pipe flow. *Journal of the Acoustical Society of America*, 55(3):535–538, 1974.

[48] J.F. van Kampen. *Acoustic pressure oscillations induced by confined turbulent premixed natural gas flames*. PhD thesis, University of Twente, 2006.

[49] J.F. van Kampen, R.A. Huls, J.B.W. Kok, and T.H. van der Meer. One-dimensional acoustic modeling of thermoacoustic instabilities. In *Proceedings of the International Congress on Sound and Vibration 10*, 2003.

[50] J.F. van Kampen, J.B.W. Kok, and T.H. van der Meer. Prediction of thermo-acoustic spectra in gas turbine combustors using unsteady RaNS CFD simulations. In *Proceedings of the International Congress on Sound and Vibration 11*, 2004.

[51] J.F. van Kampen, J.B.W. Kok, and T.H. van der Meer. Efficient retrieval of a flame transfer function from a steady-state CFD simulation. In *Proceedings of the International Congress on Sound and Vibration 12*, 2005.

[52] J.S. Kim and F.A. Williams. Effects of non-homogeneities on the eigenmodes of acoustic pressure in combustion chambers. *Journal of Sound and Vibration*, 209(5):821–843, 1998.

[53] S.A. Klein. *On the acoustics of turbulent non-premixed flames*. PhD thesis, University of Twente, 2000.

[54] K. Kohse-Höinghaus. Laser techniques for the quantitative detection of reactive intermediates in combustion systems. *Progress in Energy and Combustion Science*, 20:203–279, 1994.

[55] J.B.W. Kok and B. de Jager. Modeling of combustion noise in turbulent, premixed flames. In *Proceedings of the ASME TURBO EXPO*, 2006. GT2006-90567, submitted.

[56] H. Kromdijk. Desired experiments, experimental analysis of a burner test rig. Master's thesis, University of Twente, Faculty of Mechanical Engineering, Enschede, The Netherlands, 2004.

[57] U. Krüger, J. Hüren, S. Hoffman, W. Krebs, P. Flohr, and D. Bohn. Prediction and measurement of thermoacoustic improvements in gas turbine with annular combustion systems. *Journal of Engineering for Gas Turbines and Power*, 123:557–566, 2001.

[58] P. Lardeur, E. Lacouture, and E. Blain. Spot weld modelling techniques and performances of finite element models for the vibrational behaviour of automotive structures. In P. Sas and D. Moens, editors, *Proceedings of ISMA 25*, volume 1, pages 387–394, 2000.

[59] J. Lavrentjev, M. Åbom, and H. Bodén. A measurement method for determining the source data of acoustic two-port sources. *Journal of Sound and Vibration*, 183(3):517–531, 1995.

[60] A.H. Lefebvre. *Gas Turbine combustion*. Taylor and Francis, 2nd edition, 1999.

[61] P.H.H. Leijendeckers, J.B. Fortuin, F. van Herwijnen, and H. Leegwater, editors. *Polytechnisch zakboekje*. Koninklijke PBNA, 48 edition, 1997. in Dutch.

[62] T. Lieuwen. Modeling of premixed combustion-acoustic wave interactions: A review. *Journal of Propulsion and Power*, 19(5):765–781, 2003.

[63] T. Lieuwen and Y. Neumeier. Nonlinear pressure heat-release transfer function measurements in a premixed combustor. *Proceedings of the Combustion Institute*, 29:99–105, 2002.

[64] T. Lieuwen, H. Torres, C. Johnson, and B.T. Zinn. A mechanism of combustion instability in lean premixed gas turbine combustors. *Journal of Engineering for Gas Turbines and Power*, 123(1):182–189, 2001.

[65] T. Lieuwen and B.T. Zinn. Application of multipole expansions to sound generation from ducted unsteady combustion processes. *Journal of Sound and Vibration*, 235:405–414, 2000.

[66] T.C. Lieuwen. *Investigation of combustion instability mechanisms in premixed gas turbines*. PhD thesis, Georgia Institute of Technology, 1999.

[67] M.J. Lighthill. On sound generated aerodynamically. I. general theory. *Royal Society of London Proceedings Series A*, 211:564–587, 1952.

[68] N.M.M. Maia and J.M.M. Silva, editors. *Theoretical and Experimental Modal Analysis*. Research Studies Press LTD., 1997.

[69] K.R. McManus, T. Poinsot, and S.M. Candel. A review of active control of combustion instabilities. *Progress in Energy and Combustion Science*, 19:1–29, 1993.

[70] M.E. McNelis, T.W. Goodnight, K.S. Carney, and K.D. Otten. Lessons learned from CM-2 modal testing and analysis. In *Proceedings of the International Congress on Sound and Vibration 9*, 2002.

[71] A.S.M.Y. Munsi, A.J. Waddell, and C.A. Walker. Modification of residual stress by post-weld vibration. *Materials Science and Technology*, 17:601–605, 2001.

[72] D. Nowak, V. Bellucci, J. Cerny, and M. Toqan. Numerical modeling of thermoacoustic oscillations in a gas turbine combustion chamber. In *Proceedings of the International Congress on Sound and Vibration 11*, 2004.

[73] L.G. Olson and K. Bathe. Analysis of fluid-structure interactions. a direct symmetric coupled formulation based on the fluid velocity potential. *Computers & Structures*, 21(1/2):21–32, 1985.

[74] M. Oude Nijhuis. *Analysis tools for the design of active structural acoustic control systems*. PhD thesis, University of Twente, 2003.

[75] C. Pankiewitz and T. Sattelmayer. Time domain simulation of combustion instabilities in annular combustors. *Journal of Engineering for Gas Turbines and Power*, 125(3):677–685, 2003.

[76] C.O. Paschereit, B. Schuermans, W. Polifke, and O. Mattson. Measurement of transfer matrices and source terms of premixed flames. *Journal of Engineering for Gas Turbines and Power*, 124:239–247, 2002.

[77] A.D. Pierce. *Acoustics, An Introduction to its Physical Principles and Applications*. Acoustical Society of America, 1994.

[78] W. Polifke, C.O. Paschereit, and K. Döbbeling. Suppression of combustion instabilities through destructive interference of acoustic and entropy

waves. In *Proceedings of the International Congress on Sound and Vibration 6*, 1999.

[79] Polytec. Principles of vibrometry, 2003.

[80] R. Rajaram and T. Lieuwen. Parametric studies of acoustic radiation from turbulent flames. In *Proceedings of the AIAA/AME/SAE/ASEE Joint Propulsion Conference and Exhibit*. American institute of aeronautics and astronautics, 2002. AIAA-2002-3864.

[81] R.W. Ramirez. *The FFT, Fundamentals and Concepts*. Prentice-Hall, 1985.

[82] J.W.S. Rayleigh. *The theory of sound*. Macmillan, London, 1896.

[83] S.W. Rienstra and A. Hirschberg. An introduction to acoustics. Technical report, Eindhoven University of Technology, 2001.

[84] T. Sattelmayer. Influence of the combustor aerodynamics on combustion instabilities from equivalence ratio fluctuations. *Journal of Engineering for Gas Turbines and Power*, 125:11–19, 2003.

[85] T. Scarinci and J.L. Halpin. Industrial trent combustor—combustion noise characteristics. *Journal of Engineering for Gas Turbines and Power*, 122(2):280–286, 2000.

[86] B. Schuermans, V. Bellucci, and C.O. Paschereit. Thermoacoustic modeling and control of multi burner combustion systems. In *Proceedings of the ASME TURBO EXPO*, 2003. 2003-GT-38688.

[87] A.X. Sengissen, T.J. Poinsot, J.F. van Kampen, and J.B.W. Kok. Response of a swirled non-premixed burner to fuel flow rate modulation. In *Proceedings of Complex Effects in Large Eddy Simulation*, 2005.

[88] A.X. Sengissen, J.F. van Kampen, R.A. Huls, G.G.M. Stoffels, J.B.W. Kok, and T. Poinsot. Response of a swirled non-premixed burner to fuel flow rate modulation. *Combustion and Flame*, 2006. To be submitted.

[89] T.J.B. Smith and J.K. Kilham. Noise generation by open turbulent flames. *Journal of the Acoustical Society of America*, 35(5):715–724, 1963.

[90] T. ter Steeg. Ontwikkelen van een meetopstelling voor het bepalen van akoestische impedanties. Master's thesis, University of Twente, Faculty of Mechanical Engineering, Enschede, The Netherlands, 1994. in Dutch.

[91] S.R. Stow and A.P. Dowling. Thermoacoustic oscillations in an annular combustor. In *Proceedings of the ASME TURBO EXPO*, 2001. 2001-GT-0037.

[92] W.C. Strahle. On combustion generated noise. *Journal of Fluid Mechanics*, 49(2):399–414, 1971.

[93] R.I. Sujith, G.A. Waldherr, and B.T. Zinn. An exact solution for one-dimensional acoustic fields in ducts with an axial temperature gradient. *Journal of Sound and Vibration*, 184(3):389–402, 1995.

[94] H. Tijdeman. On the propagation of sound waves in cylindrical tubes. *Journal of Sound and Vibration*, 39:1–33, 1975.

[95] T. Tinga and G.A. Kool. Mechanical aspects of gas turbines, an introduction to loads, design criteria and material selection. Technical report, National Aerospace Laboratory NLR, 2004.

[96] Y. Tsuji and T. Ishihara. Similarity scaling of pressure fluctuation in turbulence. *Physical Review E*, 68(2), 2003.

[97] M. Vajta. Some remarks on Padé approximations. In *Proceedings of the 3rd TEMPUS-INTCOM Symposium*, 2000.

[98] S. Vanlanduit and P. Guillaume. An automatic scanning algorithm for high spatial resolution laser vibrometer measurements. *Mechanical Systems and Signal Processing*, 18:79–88, 2004.

[99] S. Vanlanduit, P. Guillaume, and J. Schoukens. Robust data reduction of high spatial resolution optical vibration measurements. *Journal of Sound and Vibration*, 274(1-2):369–384, 2004.

[100] D. Veynante and T. Poinsot. Large eddy simulation of combustion instabilities in turbulent premixed burners. *Annual Research Briefs*, pages 253–274, 1997.

[101] D. Veynante and L. Vervisch. Turbulent combustion modeling. *Progress in Energy and Combustion Science*, 28:193–266, 2002.

[102] R. Visser. *A boundary element approach to acoustic radiation and source identification.* PhD thesis, University of Twente, 2004.

[103] A. Wachsman, S. Park, A.M. Annaswamy, and A.F. Ghoniem. Sensors and actuators for combustion control. In *Proceeding of the 2004 American control conference*, pages 5496–5501, 2004.

[104] J. Warnatz, U. Maas, and R.W. Dibble. *Combustion: physical and chemical fundamentals, modeling and simulation, experiments, pollutant formation*. Springer, 2001.

[105] D.C. Wilcox. *Turbulence modeling for CFD*. DCW Industries Inc., 1998.

[106] O.C. Zienkiewicz and R.L. Taylor. *The finite element method*. Butterworth-Heinemann, 2000.

[107] S.J. Zinkle, J.P. Robertson, and R.L. Klueh. Thermophysical and mechanical properties of Fe-(8-9)%Cr reduced activation steels (4/25/98 draft). Technical report, Oak Ridge National Laboratory, 1998.

Nawoord

Dat was hem dan. Na bijna een jaar als afstudeerder en vier jaar als promovendus bij de vakgroep Technische Mechanica is het toch gekomen tot een proefschrift. En dat is zeker niet alleen mijn eigen verdienste geweest, vele mensen hebben hier direct dan wel indirect aan meegewerkt.

Ten eerste gaat mijn dank uit naar mijn promotor André de Boer voor de inhoudelijke begeleiding tijdens het promotietraject en tijdens het schrijven van het proefschrift, maar zeker ook voor de onvoorwaardelijke steun. Bedankt!

In proefschriften van mijn voorgangers wordt de vakgroep altijd geroemd om de goede sfeer en leuke collega's. En ik moet nu eerlijk bekennen dat dat terecht is. Ondanks dat er een complete lichting promovendi afzwaaide gedurende mijn promotietijd en er een compleet nieuwe lichting voor in de plaats kwam, is het al die tijd een leuke groep geweest. Geregeld activiteiten, van een middagje klootschieten, via regelmatig bioscoopbezoek tot wintersport hebben daar zeker aan bijgedragen. Grote dank hiervoor aan de mensen die gedurende kortere of langere tijd mijn naaste collega-promovendi waren: Marco Oude Nijhuis, René Visser, Clemens Beijers, Marco Derksen, Edwin de Korte, Marieke Hannink, Ekke Oosterhuis, Marten Nijhof, Peter Sloetjes, Loes van Haaren, Bert Koopman, Maarten van Riel, Jelmer Wind en Ronald Kampinga.

This thesis was written within the DESIRE project and therefore there were project meetings every six months. These meetings were not only a great way to get to know other people working on similar problems, but they were also a valuable source of comments on my work. I would like to thank all the people that participated in this project. It would go too far to mention all these people, but a special thanks should go to Alois Sengissen from CERFACS, who did the LES calculations that were used in this thesis.

Natuurlijk zijn er binnen de Universiteit Twente buiten de vakgroep ook vele mensen geweest die een bijdrage hebben geleverd aan de totstandkoming van dit proefschrift. Bij het ontwerp van de testopstelling zijn de adviezen en ondersteuning van Jan Bossink en Nutte Dijkstra zeer waardevol geweest. Vanuit de vakgroep Thermische Werktuigbouwkunde is de ondersteuning van Jim Kok,

Theo van der Meer en Genie Stoffels ook zeker waardevol geweest. Daarnaast heeft een aantal studenten meegewerkt aan het DESIRE project en daarmee ook indirect aan dit proefschrift, te weten Harmen Kromdijk, Marc Harleman, Uros Lekic en Rob Kleinlugtenbelt. Verder heeft mijn directe collega-promovendus binnen het DESIRE project, Jaap van Kampen, aan vele stukken van dit proefschrift direct of indirect een bijdrage geleverd, of het nu gaat om het ontwerp van de testopstelling of de CFD berekeningen. Voor alle hulp en ondersteuning van deze mensen: hartelijk dank!

Verder gaat mijn dank uit naar alle mensen van de vakgroep Technische Mechanica, waarbinnen ik heb mogen werken. Naar de secretaresses Debbie Vrieze en Tanja van Scherpenzeel, voor het afhandelen van de administratieve zaken, een luisterend oor en de broodnodige kaffeine. En aan de medewerkers van de vakgroep, Ruud Spiering, Ysbrand Wijnant, Bert Wolbert en mijn assistent-promotor Peter van der Hoogt.

Tot slot gaat mijn dank uit naar mijn vrienden en familie, voor onvoorwaardelijke steun voor mijn werk, ondanks dat voor velen nooit duidelijk is geworden wat ik nu zoal de hele dag uitspookte. Mensen, bedankt!

Enschede, Mei 2006

Rob Huls